MARTIN MARIETTA ENERGY SYSTEMS LIBRARIES
3 4456 0286763 6

ORNL-2842
Physics and Mathematics
TID-4500 (15th ed.)

NEUTRON PHYSICS DIVISION

ANNUAL PROGRESS REPORT

FOR PERIOD ENDING SEPTEMBER 1, 1959

CENTRAL RESEARCH LIBRARY
DOCUMENT COLLECTION
LIBRARY LOAN COPY
DO NOT TRANSFER TO ANOTHER PERSON
If you wish someone else to see this document, send in name with document and the library will arrange a loan.

OAK RIDGE NATIONAL LABORATORY
operated by
UNION CARBIDE CORPORATION
for the
U.S. ATOMIC ENERGY COMMISSION

Printed in USA. Price $4.00 . Available from the
Office of Technical Services
Department of Commerce
Washington 25, D. C.

LEGAL NOTICE

This report was prepared as an account of Government sponsored work. Neither the United States, nor the Commission, nor any person acting on behalf of the Commission:

A. Makes any warranty or representation, expressed or implied, with respect to the accuracy, completeness, or usefulness of the information contained in this report, or that the use of any information, apparatus, method, or process disclosed in this report may not infringe privately owned rights; or

B. Assumes any liabilities with respect to the use of, or for damages resulting from the use of any information, apparatus, method, or process disclosed in this report.

As used in the above, "person acting on behalf of the Commission" includes any employee or contractor of the Commission, or employee of such contractor, to the extent that such employee or contractor of the Commission, or employee of such contractor prepares, disseminates, or provides access to, any information pursuant to his employment or contract with the Commission, or his employment with such contractor.

ORNL-2842
Physics and Mathematics
TID-4500 (15th ed.)

Contract No. W-7405-eng-26

NEUTRON PHYSICS DIVISION ANNUAL PROGRESS REPORT

for Period Ending September 1, 1959

E. P. Blizard, Director
A. Simon, Associate Director

A. D. Callihan, Leader, Critical Experiments Facility
L. B. Holland, Leader, Tower Shielding Facility
F. C. Maienschein, Leader, Bulk Shielding Facility
F. J. Muckenthaler, Leader, Lid Tank Shielding Facility

DATE ISSUED

NOV 9 1959

OAK RIDGE NATIONAL LABORATORY
Oak Ridge, Tennessee
operated by
UNION CARBIDE CORPORATION
for the
U. S. ATOMIC ENERGY COMMISSION

MARTIN MARIETTA ENERGY SYSTEMS LIBRARIES

3 4456 0286763 6

TABLE OF CONTENTS AND SUMMARY

1. RESEARCH FOR LIGHT-WATER-MODERATED REACTORS

1.1. *REACTIVITY EFFECTS OF LARGE VOIDS IN THE REFLECTOR OF THE POOL CRITICAL ASSEMBLY*

A. B. Reynolds, K. M. Henry, and E. B. Johnson 3

Reactivity effects of large voids in the reflector of a pool-type reactor were investigated. The variation of reactivity with void size and position on the core-reflector interface was studied and correlated by a statistical weight correlation. The variation of reactivity with the distance between the void and the core was also determined. In an additional study of the superposability of void effects, it was found that voids separated by 4 in. or more were superposable; however, for a separation of only 2 in., the sum of the individual effects was greater than the combined effect. On the other hand, for a zero separation distance the sum of the effects of individual voids was less than the effect of the large void alone. An approximate theoretical method based on two-group diffusion theory was developed for calculating the reactivity effect of a void covering one entire face of a reactor having a parallelepiped core. The calculated effect was in reasonable agreement with experimental results.

1.2. *CRITICAL MASS CALCULATIONS FOR POOL-TYPE RESEARCH REACTORS*

E. G. Silver and W. Etzel 6

The 32-group, one-dimensional diffusion theory reactor code, GNU-II, and the two-dimensional few-group diffusion theory code, PDQ, both for the IBM-704 computer, have been employed for a number of critical mass calculations on 20% U^{235}-enriched and highly enriched pool-type research reactors. Loadings of the Bulk Shielding Reactor I, the Geneva Reactor, the Oak Ridge Research Reactor, and the Puerto Rican Research Reactor have been investigated. In general, this work indicates that these codes are capable of excellent results in predicting critical masses of compact cores of such reactor types.

2. NEW REACTORS FOR THE BULK SHIELDING AND TOWER SHIELDING FACILITIES

2.1. *BULK SHIELDING REACTOR II: STATUS REPORT*

K. M. Henry, E. G. Silver, and E. B. Johnson 21

The fabrication of the stainless steel-UO_2 core (BSR-II) for the Bulk Shielding Facility has been completed and initial critical tests have been performed in the Pool Critical Assembly (PCA). The critical mass of the initial loading was about 5.84 kg of U^{235}. Other loadings required from 5.59 to 6.20 kg of U^{235}. Machine calculations with the GNU-II and PDQ codes for the IBM-704 were made to determine the reactivity worths of the control plates and a double-ended reactivity-insertion device, to ascertain the effect of the steel structure below the core, and to obtain plots of the flux within the reactor. The worths of the control plates and the reactivity-insertion device were also determined experimentally, as was the time response of the insertion device. The core and auxiliary equipment have now been shipped to the SPERT-I Facility in Idaho, where extensive static and dynamic tests with the reactor have begun.

2.2. *MEASUREMENT OF THE RATIO OF THE PROMPT-NEUTRON GENERATION TIME TO THE EFFECTIVE DELAYED-NEUTRON FRACTION OF THE BSR-II*

E. G. Silver, G. deSaussure, K. M. Henry, E. B. Johnson, and R. Perez-Belles 35

The ratio of the prompt-neutron generation time, L, to the effective delayed-neutron fraction, β_{eff}, has been measured for the BSR-II by the use of the pulsed-neutron method. The BSR-I and an adjacent D_2O-filled tank served as a thermal-neutron source, and a rotating chopper produced the neutron pulses. By means of this method a value of L/β_{eff} of 3.2 ± 0.16 msec was obtained. Using this value, measurements of multidollar negative reactivity effects of control rods in BSR-II have been performed, and results are given.

2.3. *THE TOW SHIELDING REACTOR II: STATUS REPORT*
L. B. Holland, V. R. Cain, J. L. Hull, J. Lewin, and D. R. Ward 39

Fabrication of the Tower Shielding Reactor II (TSR-II), the spherically symmetric reactor that will be operated at the TSF, is nearing completion. The final design includes modifications that have resulted from critical experiments and component development work. The control system and water cooling system have been installed and tested at the TSF, and a beam shield that will be used with the reactor has been completed. Plans are being made to operate the reactor at powers up to 100 kw in order to determine its nuclear characteristics and leakage spectra.

3. CRITICAL EXPERIMENTS

3.1. *MULTIPLICATION MEASUREMENTS WITH SLABS OF ENRICHED URANIUM*
J. T. Mihalczo and J. J. Lynn 67

A series of neutron multiplication measurements with arrays of 1 × 8 × 10 in. slabs of 93.4% U^{235}-enriched uranium metal have been made to provide data from which safety criteria for the storage of these fissile units can be established. A maximum of 125 units was assembled, each slab containing 22.9 kg of U^{235}. The arrays studied were cubic lattices of the units and were usually parallelepipedal in shape. Arrays were both unmoderated and Plexiglas-moderated and were surrounded in most cases by a 1-in.-thick Plexiglas reflector. The lattice densities (ratio of fissile unit volume to lattice cell volume) were between 0.023 and 0.06. Unmoderated lattices with a density of 0.06 would require 145 ± 5 units for criticality, while approximately 27 units would be required for a moderated array.

3.2. *RADIAL FLUX MEASUREMENTS IN A CYLINDRICAL ANNULAR CRITICAL ASSEMBLY OF $U^{235}O_2F_2$-H_2O*
R. Gwin and D. W. Magnuson 69

Radial flux measurements with bare gold foils have been made in a water-reflected cylindrical annular critical assembly of $U^{235}O_2F_2$-H_2O. A comparison with unreflected gold foil measurements made in a previous experiment is given in tabular and graphical form.

3.3. *CRITICAL PARAMETERS OF SLIGHTLY ENRICHED ANNULAR CYLINDRICAL URANIUM METAL SLUGS*
J. K. Fox and L. W. Gilley 71

A study of some of the critical parameters for water-moderated and -reflected 0.94% U^{235}-enriched annular cylindrical uranium metal slugs is in progress. Data for triangular lattices of two different spacings indicate that the critical mass for regular lattices of these slugs varies from 5.04 to 12.40 tons of uranium, depending upon lattice spacing, while a random array containing 18.8 tons of uranium showed an apparent source neutron multiplication of about three.

3.4. *THE POISONING EFFECT OF COPPER LATTICES IN AQUEOUS SOLUTIONS OF ENRICHED URANYL OXYFLUORIDE*
J. K. Fox and L. W. Gilley 73

Experiments on the poisoning effect of various lattices of copper tubing and rods in aqueous solutions of 93.2% U^{235}-enriched UO_2F_2 having an $H:U^{235}$ atomic ratio of 52.6 have been completed. Comparison of copper-tube data with data obtained by substitution of aluminum tubes indicates that the most important effect is produced by the displacement of the solution by the copper tubing, rather than by neutron absorption in the metal.

3.5. *CRITICAL PARAMETERS OF U^{235} AND U^{233} SOLUTIONS IN SIMPLE GEOMETRY*
J. K. Fox, L. W. Gilley, R. Gwin, and D. W. Magnuson 76

Some data describing the critical conditions of cylindrical volumes of aqueous solutions of U^{235} and U^{233} are presented. The critical parameters of one spherical volume of solution are also given.

3.6. *CRITICAL PARAMETERS FOR 20-in.-dia STAINLESS STEEL CYLINDERS CONTAINING AQUEOUS SOLUTIONS OF U^{235} POISONED WITH PYREX GLASS*

J. K. Fox and L. W. Gilley 78

Experiments were performed to determine the poisoning effect of Pyrex glass pipe inserted in large vessels containing aqueous solutions of uranium compounds enriched in U^{235}. The data indicate that a U^{235} solution in a 20-in.-dia by 36-in.-long stainless steel cylinder, water-reflected on sides and bottom and containing a volume of 2-in.-dia Pyrex pipe lattice equal to 15% of the total cylinder volume, will remain subcritical even for $H:U^{235}$ atomic ratios near those for minimum critical volume. For the unreflected system, the required glass content is about 12 vol % for 2-in.-dia glass pipe and 14 vol % for 3-in.-dia pipe. Using shorter pieces of smaller-diameter pipe (Raschig rings) will reduce the percentage of glass required to about 11% for reflected systems.

3.7. *CRITICAL PARAMETERS OF UNREFLECTED ARRAYS OF INTERACTING CYLINDERS CONTAINING AQUEOUS SOLUTIONS OF U^{235}*

J. K. Fox and L. W. Gilley 82

Previous studies of the critical parameters of aqueous solutions of 93.2% U^{235}-enriched uranyl fluoride have been extended to include solutions with $H:U^{235}$ atomic ratios of 297 and 309. The solutions were contained in unreflected 6-, 8-, and 9.5-in.-dia cylinders in line, square, hexagonal, and triangular arrays. Results are given in both tabular and graphical form.

3.8. *HOMOGENEOUS CRITICAL ASSEMBLIES OF 2% U^{235}-ENRICHED UF_4 IN PARAFFIN*

J. T. Mihalczo and J. J. Lynn 85

Additional critical experiments have been performed with a homogeneous mixture of 2% U^{235}-enriched UF_4 and paraffin, the $H:U^{235}$ atomic ratio for these later experiments being 404. The results have been combined with those of earlier experiments, in which $H:U^{235}$ ratios of 195 and 294 were used, to present plots of minimum critical masses and volumes.

3.9. *DETERMINATION OF THE INFINITE MEDIUM MULTIPLICATION FACTOR FOR 2% U^{235}-ENRICHED UF_4 IN PARAFFIN*

J. T. Mihalczo 86

The infinite medium multiplication factor for a homogeneous mixture of 2% U^{235}-enriched UF_4 in paraffin was determined from a series of critical experiments in which known changes in the buckling were made and the resulting stable periods measured. The interpretation was based on the critical equation $k_\infty P(B) = 1$, where $P(B)$, the nonleakage probability for all neutrons from fission, were obtained from both one- and two-group models. Values computed for an assembly with base dimensions of 71.5 by 71.5 cm were 1.197 ± 0.015 with the one-group model and 1.197 ± 0.015 with the two-group model. Corresponding values for an assembly with base dimensions of 86.7 by 81.7 cm were 1.200 ± 0.016 and 1.202 ± 0.016, respectively.

3.10. *CRITICAL MASSES OF 93% U^{235}-ENRICHED URANIUM METAL "BUTTONS" AND "BRIQUETTES"*

J. K. Fox and L. W. Gilley 88

A series of experiments has been performed to provide data for the safe handling of 4-in.-dia by 1-in.-thick 93% U^{235}-enriched uranium metal buttons and 4-in.-dia briquettes 2 to 4 in. thick. The experiments were performed in 7- to 12-in.-dia graphite crucibles and were moderated with water. Both water-reflected and unreflected cases were investigated. The estimated minimum critical mass for a reflected button assembly is about 22 kg of U^{235}. The corresponding value for a reflected briquette assembly is approximately 23 kg of U^{235}.

4. FISSION PHYSICS

4.1. PRELIMINARY RESULTS FROM A DETERMINATION OF THE LOW-ENERGY PORTION OF THE GAMMA-RAY SPECTRUM EMITTED PROMPTLY AFTER FISSION OF U^{235} BY THERMAL NEUTRONS

T. A. Love, F. C. Maienschein, and R. W. Peelle 93

Previous measurements of the gamma-ray spectrum closely associated in time with the fission of U^{235} by thermal neutrons have been extended down to 10 kev. A time-of-flight requirement was used with a single-crystal gamma-ray spectrometer to obtain a pulse-height spectrum free of pulses caused by fast prompt neutrons. The results show several apparent peaks in the gamma-ray spectrum, including two which correspond to the x rays from the light and heavy fission fragments. After a very rough correction for the spectrometer sensitivity as a function of energy, the photon yield varies between 6 and 15 photons·fission^{-1}·Mev^{-1} for all energies from 10 to $\sim$600 kev, except at the heavy-fragment x-ray peak, where the yield rises to $\sim$24. These results are tentative until a final analysis is completed.

4.2. THE DETERMINATION OF η OF U^{233} BY DIRECT COMPARISON OF CRITICAL EXPERIMENTS IN LARGE SPHERES

D. W. Magnuson and R. Gwin 96

Critical assemblies of uranyl nitrate solutions of U^{235} and U^{233} in identical spherical geometry have been compared to determine the value of η of U^{233} relative to the value of η of U^{235}. Measurements were made for four U^{235} solution concentrations and five U^{233} concentrations in a 69.2-cm-dia sphere, as well as for one U^{235} concentration and one U^{233} concentration in a 122-cm-dia sphere. The value of η of U^{233} determined from the data obtained in the larger sphere is 2.295 ± 0.036.

4.3. CALCULATIONS OF η OF U^{235} AND U^{233} FROM CRITICAL EXPERIMENTS IN CYLINDRICAL GEOMETRY

D. W. Magnuson and R. Gwin 98

Data from a series of critical experiments utilizing aqueous solutions of U^{235} and U^{233} in 5- and 9-ft-dia cylinders have been analyzed to obtain values of η of U^{235} and η of U^{233}. The η values for U^{235} range from 2.049 ± 0.014 to 2.072 ± 0.025; the U^{233} values vary from 2.281 ± 0.016 to 2.290 ± 0.025.

4.4. MEASUREMENTS OF η OF U^{233} AND U^{235} BY A MANGANESE BATH TECHNIQUE

G. deSaussure, J. D. Kington, R. L. Macklin, and W. S. Lyon 99

Absolute values of η for U^{233} and U^{235} were measured directly by a method of total absorption which involves relative counting and some minor corrections. A thermal-neutron beam was introduced into the center of a 1-m-dia sphere filled with a solution of manganous sulfate in water, and the direct activation of the bath by the beam was determined. The beam was then totally absorbed in a sample of the isotope under investigation, and the activation of the bath by fission neutrons from the isotope was measured. The ratio of the two activities is equal to η, except for small corrections. The values obtained, corrected to a neutron velocity of 2200 m/sec, are 2.30 ± 0.02 for η of U^{233} and 2.07 ± 0.02 for η of U^{235}.

4.5. PRELIMINARY MEASUREMENT OF THE GROSS SPECTRUM OF GAMMA RAYS ASSOCIATED WITH THE INTERACTION OF THERMAL NEUTRONS AND U^{235}

F. C. Maienschein, T. A. Love, and R. W. Peelle 103

A preliminary measurement of the gross spectrum of gamma rays associated with the interaction between thermal neutrons and U^{235} has been made, using a three-crystal pair spectrometer and an irradiated U^{235} foil. The measurement is preliminary because the absolute fission rate was not determined, only energies above 1.6 Mev were examined, correction was not made for the nonunique response of the spectrometer, and the possible neutron-induced backgrounds were not fully explored. Within these limitations the results agreed in spectral shape with those obtained by Motz and also with a summation of the earlier prompt-fission and fission-product data.

5. EXPERIMENTAL REACTOR PHYSICS

5.1. *AN INVESTIGATION OF THE SLOWING DOWN OF FISSION NEUTRONS IN WATER*

T. V. Blosser and D. K. Trubey 109

An experiment to measure the slowing down of U^{235} fission neutrons to indium resonance energy has been continued. The major portion of the experiment involves a determination of the magnitude of various perturbations not examined in previous measurements. The effect of the source position in the experimental arrangement, the source strength distribution as a function of diameter, and the effect of cadmium covers has been investigated. A preliminary 30-mil-cadmium 5-mil-indium age has been computed to be 26.7 cm^2, in good agreement with recent results of other experimenters.

5.2. *NONLEAKAGE PROBABILITIES IN CRITICAL EXPERIMENTS AND THEIR RELATION TO NEUTRON AGE*

R. Gwin and D. W. Magnuson 112

A brief outline of the theory of unreflected reactors is given, and the theory is employed for the analysis of some experimental data obtained at the ORNL Critical Experiments Facility. A neutron age to thermal of 25.7 cm^2 and an age to indium of 24.7 ± 1.2 cm^2 are indicated by the analysis.

5.3. *MEASUREMENTS OF THE TRANSPORT MEAN FREE PATH OF THERMAL NEUTRONS IN BERYLLIUM AS A FUNCTION OF TEMPERATURE*

G. deSaussure and E. G. Silver 115

The variation of the transport mean free path of thermal neutrons in beryllium with temperature has been investigated for various temperatures higher than room temperature, and for one temperature below room temperature, by the pulsed-neutron technique. Measured values of λ_{tr} for temperatures from ~225 to ~790°K are compared with values calculated by Singwi and Kothari, and good agreement is found.

6. REACTOR THEORY

6.1. *FAST MULTIPLICATION EFFECT OF BERYLLIUM*

W. Häfele 121

The beryllium $(n,2n)$ reaction produces neutrons which can be used to increase the available reactivity margin in a multiplying assembly. An investigation of the magnitude of this effect has been carried out. To this end reviews of similar investigations and the relevant cross-section data were made, and upper and lower limits for the $(n,2n)$ cross section were estimated. The fast multiplication effect was then determined by calculating the spectrum in an infinite homogeneous beryllium moderator, assuming that the source neutrons had a fission-neutron distribution, and considering the whole angular distribution of the elastically scattered neutrons. The upper limit of the net multiplication effect is 7.6%, the lower limit 5.1%; however, after about 2 years, poisoning by the daughter products of the (n,α) reaction would lower the reactivity by 5% for fluxes of about 5×10^{13} neutrons/cm^2/sec.

6.2. *ON THE THEORY OF THE DIFFUSION COOLING EFFECT IN HOMOGENEOUS AND HETEROGENEOUS ASSEMBLIES*

W. Häfele and L. Dresner 124

The flux distribution of a homogeneous pulsed-neutron assembly has been expanded in terms of eigenfunctions with respect to both energy and space. The diffusion cooling constant was determined exactly in terms of matrix elements with respect to these eigenfunctions. The matrix elements and the diffusion cooling constant have been evaluated for the special case of a heavy gas moderator. It is also possible to develop the theory for heterogeneous assemblies. There, in addition to the normal diffusion cooling effect, a second cooling effect appeared which has been ascribed to the diffusion of neutrons into the lumped absorbers.

6.3. *COMPARISON THEOREMS FOR THE ESTIMATION OF AVERAGE COLLISION PROBABILITIES*
L. Dresner 128

Theorems are given which permit the estimation of average collision probabilities for convex solids of irregular shape by comparison with solids for which the average collision probability is known.

6.4. *FIRST-FLIGHT NONESCAPE PROBABILITIES FOR NEUTRONS IN A SPHERE*
E. Inönü 134

First-flight nonescape probabilities for both a uniform and a persisting neutron distribution in a spherical bare homogeneous reactor have been calculated by the second fundamental theorem of reactor theory in order to test its accuracy for small reactors. Results are compared to accurate values obtained from transport theory and to previously published values for infinite slab reactors.

6.5. *INFLUENCE OF THE GEOMETRIC SYMMETRIES OF A HETEROGENEOUS REACTOR ON THE FLUX DISTRIBUTION*
L. Dresner 138

In a bare, homogeneous reactor the space and energy dependences of the flux are separable under quite general assumptions. This theorem has been extended to some heterogeneous reactors. It is found that for certain heterogeneous reactors of special shape and geometric symmetry, there are eight networks of points, each with the following properties: (1) the space and energy dependences of the flux are separable at these points, and thus the spectrum is the same at all points of a network; and (2) the space dependence of the flux over a network is the same as that of the flux in a homogeneous reactor lying inside the same boundary.

6.6. *THERMALIZATION OF PULSED NEUTRONS IN A NONMULTIPLYING MODERATING MEDIUM*
S. N. Purohit 141

The time behavior of the thermal-neutron energy spectrum of neutrons from a monoenergetic pulsed source in beryllium assemblies with various geometric bucklings has been calculated using the heavy gas model.

6.7. *MONTE CARLO NEUTRON ESCAPE PROBABILITY CODES*
R. R. Coveyou, W. E. Kinney, and J. G. Sullivan 142

Two codes have been written to compute the escape probability of neutrons from solids. One of the codes, identified as Lump I, considers a disk with sources distributed exponentially along the axis. The radial distribution results from collimating neutrons from an isotropic disk source and is roughly Gaussian. The other code, Lump II, computes escape probabilities from parallelepipeds, cylinders, spheres, or ellipsoids and considers the source to be uniformly distributed throughout the solid.

6.8. *ADDITIONS TO CORN PONE – A MULTIGROUP, MULTIREGION REACTOR CODE*
W. E. Kinney 143

Several additions have been made to Corn Pone Reactor Code. They include a program to compute neutron absorptions and fissions in specified elements, the option of using a fixed or variable transverse buckling, the option of specifying the thermal constants and number of space points in each region, the availability of a number of initial source guesses, the option of punching the converged source on paper tape, and the ability to treat vacuum regions.

6.9. *NEUTRON REACTION RATE CODES*
R. R. Coveyou and W. E. Kinney 144

Neutron thermal cross sections in a medium at a certain temperature may be computed from data taken at a lower temperature. Codes to perform the calculation have been written for the IBM-704 computer.

6.10. *RESONANCE ABSORPTION OF NEUTRONS IN A LUMP*
K. Hasegawa 146

A new integral equation governing the slowing down of neutrons in a lump, assuming a spatially uniform neutron flux inside the lump, has been derived from the Boltzmann equation. In the first approximation the equation is solved by using the asymptotic energy dependence of the neutron flux and proposing a new resonance integral formula. In the limits of both the narrow resonance and the wide resonance, the

formula tends to be equal to that derived in the conventional narrow and wide resonance approximations. In the second approximation the effects of the deviation of the Placzek function from its asymptotic form are calculated by a method similar to that used by Weinberg and Wigner for homogeneous systems. It is shown that the resonance integrals of the usual narrow and wide resonance approximations become equal for a certain value of Γ_n/Γ, irrespective of the resonance width. Some numerical results are given.

6.11. CALCULATION OF THE PROMPT NEUTRON GENERATION TIME FOR THE BSR-II

R. Perez-Belles 148

A theoretical calculation, based on a two-group treatment, of the prompt-neutron generation time in the BSR-II has been made. The computed result is 21.3 μsec, which is in good agreement with the experimental result reported in Sec 2.2.

6.12. A CORN PONE CALCULATION OF THE ENERGY-DEPENDENT NEUTRON FLUX IN AN UNREFLECTED 69.2-cm-dia SPHERE

D. W. Magnuson, R. Gwin, and W. E. Kinney 151

The first of a series of calculations of parameters of an unreflected 69.2-cm-dia critical sphere, based on the use of the consistent P_1 approximation of the Corn Pone code, has been completed. Values of the square root of the buckling, the extrapolated radius, and the extrapolated length are given for several energy groups, and the effective extrapolated length is plotted as a function of energy group for the neutron source and flux.

6.13. REACTION CROSS SECTIONS USING THE STATISTICAL MODEL OF THE COMPOUND NUCLEUS

S. K. Penny 153

Hauser and Feshbach used the statistical model to consider the total cross section for the inelastic scattering of neutrons. They further suggested that their formalism might be altered to include competition from other reactions and also to consider the possibility of charged particles as incident and emergent particles. These changes have now been written explicitly for the total reaction cross section for the case in which the statistical model applies to the compound nucleus only. (Abstract only published here, with reference).

6.14. EFFECTS OF CHEMICAL BINDING ON NEUTRON SCATTERING

F. S. Alsmiller 154

A study of the effects of chemical binding on the scattering of low-energy neutrons in crystals and in fluids is in progress. Application of existing standard formulations to the materials under study (ice, heavy ice) does not appear appropriate because of difficulties with the H_2O and D_2O lattice structures. A suitable modification of the theory is being sought.

6.15. SLINKY: A MONTE CARLO CODE TO SOLVE MULTIGROUP, MULTIREGION DIFFUSION EQUATIONS

R. R. Coveyou and D. J. Irving 154

An IBM-704 code, called SLINKY, has been developed in an attempt to solve the equations of diffusion theory by the Monte Carlo method. The code is essentially complete and will be tested to determine its value.

7. SHIELDING RESEARCH

7.1. *PULSE-HEIGHT SPECTRA OF THERMAL-NEUTRON-CAPTURE GAMMA RAYS IN VARIOUS MATERIALS*

F. J. Muckenthaler 157

Pulse-height spectra resulting from thermal-neutron-capture gamma rays produced in aluminum, lead, and iron have been measured. Samples were exposed to thermalized neutrons from a Po-Be source, and gamma-ray spectra were measured from the bare sample and a boron-Plexiglas-covered sample. The difference between the curves was attributed to thermal-neutron-capture gamma rays. Observed peaks are in agreement with published data.

7.2. *PREDICTION OF THERMAL-NEUTRON FLUXES IN THE BSF FROM LTSF DATA*

A. D. MacKellar 162

Predictions of the thermal-neutron fluxes to be expected near the Bulk Shielding Reactor were made on the basis of Lid Tank Shielding Facility experimental data transformed to the BSR geometry. The predicted fluxes are higher than the measured fluxes by 15 to 25% for distances closer than 60 cm, but they are essentially in agreement for larger distances. At a distance of 125 cm the predicted flux was only 1% too low.

7.3. *RADIATION ATTENUATION PROPERTIES OF BARYTES CONCRETE AND ITS COMPONENTS*

W. J. Grantham, Jr. 164

A series of measurements of fast-neutron dose rates, gamma-ray dose rates, and thermal-neutron fluxes in water behind samples of barytes aggregate, barytes aggregate plus portland cement, and barytes concrete has been completed at the Lid Tank Shielding Facility. The fast-neutron mass attenuation coefficient for barytes concrete was found to be 0.0301 cm^2/g, which is in good agreement with a calculated value of 0.0313 cm^2/g based on chemical analysis of the concrete.

7.4. *EFFECTIVE NEUTRON REMOVAL CROSS SECTION OF ZIRCONIUM*

J. M. Miller 168

The effective removal cross section of zirconium has been determined as 2.36 ± 0.12 barns on the basis of thermal-neutron flux measurements made at the LTSF beyond two slabs of zirconium (1.8 wt % hafnium), each 54 × 49 × 2 in. A mass attenuation coefficient (Σ_R/ρ) based upon the removal cross section and a measured density of 6.54 g/cm^3 is $(1.56 \pm 0.08) \times 10^{-2}$ cm^2/g.

7.5. *RECHECKS AND EXTENSIONS OF THE 2π EXPERIMENTS AT THE TSF*

D. R. Ward, F. J. Muckenthaler, and S. C. Dominey 169

The 2π experiments performed by the General Electric Company at the Tower Shielding Facility in 1956 were checked and extended in late 1958 by ORNL personnel. Most of the experiments consisted in measurements of radiation in the G-E crew compartment as a function of altitude for various shield configurations on the TSR-I 64 ft away. The fast-neutron dose rates observed in the two series were in agreement for all cases in which the 2π borated water shield was on the bottom of the reactor; for some cases in which the 2π shield was removed the ORNL fast-neutron measurements agreed to within 15% with the G-E data. Thermal-neutron and gamma-ray measurements were essentially in agreement in the two series. The extensions to the measurements largely consisted in mapping the radiation around the reactor shield and measuring the spectra of gamma rays in the crew compartment.

7.6 *THE HIGH-ENERGY ACCELERATOR SHIELDING PROGRAM*

C. D. Zerby and H. W. Bertini 176

The conditional Monte Carlo method has been selected for calculating the deep penetrations of particles through high-energy accelerator shields. This method was chosen because of its adaptability to various shield geometries and because complex chains of secondary radiation can be handled with relative ease. An intranuclear cascade calculation to compute the inelastic differential cross sections for complex nuclei required for the penetration calculation is being coded for the IBM-704.

7.7. MONTE CARLO CODE FOR THE CALCULATION OF DEEP PENETRATIONS OF GAMMA RAYS: STATUS REPORT

S. K. Penny 177

During the development of the Monte Carlo code for deep penetrations of gamma rays, several methods were investigated, the most successful being the "conditional Monte Carlo" method. In a calculation with this method the results for fictitious particles were within 20% of those obtained by an exact calculation, but for gamma-ray sources the results fluctuated badly. More work on the code will be required.

7.8. NEUTRON YIELDS FROM (α,n) REACTIONS IN VARIOUS MATERIALS

F. S. Alsmiller and G. M. Estabrook 177

A program has been initiated to calculate the neutron yields from (α,n) reactions in certain uranium isotopes (U^{232} through U^{236}), Th^{228} and its daughters, and other elements often present in fabricated uranium. A method for the calculation has been developed.

8. RADIATION DETECTOR STUDIES

8.1. THE MODEL IV GAMMA-RAY SPECTROMETER: STATUS REPORT

G. T. Chapman and T. A. Love 181

All components for the model IV gamma-ray spectrometer have been received at the Bulk Shielding Facility, and the assembly of the components is almost complete. An extensive radiation survey is being made of the lead-lithium housing in order to determine whether any voids might have occurred during the pouring and solidification of the material.

8.2. NONPROPORTIONALITY OF RESPONSE OF AN NaI(Tl) SCINTILLATION CRYSTAL TO GAMMA RAYS

R. W. Peelle and T. A. Love 181

The nonproportionality of response of a 3-in.-dia by 3-in. NaI(Tl) crystal to gamma rays has been studied briefly in a manner which does not depend critically on the performance of the pulse-height discriminator system. "Sum" pulse-height distributions which corresponded to the simultaneous detection of cascade gamma rays were observed and compared with the sum of peaks representing the individual gamma rays. In the experiment performed, cascade gamma-ray transitions of Y^{88} and Bi^{207} were used, and the results showed that the "sum peaks" occurred at pulse heights higher than would have been expected on the hypothesis that the integrated pulse output of the phototube was proportional to the absorbed gamma-ray energy. The difference corresponded to an average of 30 ± 6 kev.

8.3. MONTE CARLO CODE FOR CALCULATIONS OF RESPONSE FUNCTIONS OF GAMMA-RAY SCINTILLATION DETECTORS

C. D. Zerby and H. S. Moran 185

A Monte Carlo code has been written for the IBM-704 computer for calculations of the gamma-ray response functions of NaI and xylene scintillation detectors. The detector geometry can be either a right cylinder or a right cylinder with one conical end. The source is restricted to a monoenergetic source of arbitrarily chosen energy in the range from 0.005 to 10.0 Mev. The treatment of the primary incident radiation takes into account Compton scattering, pair production, and the photoelectric effect; however, secondary bremsstrahlung and annihilation radiation are not considered. The particular Monte Carlo method used is designed for minimum statistical error in the so-called "Compton tail" of the spectrum.

8.4. *MONTE CARLO CALCULATIONS OF GAMMA-RAY ENERGY-LOSS SPECTRA IN LARGE NaI(Tl) SCINTILLATORS*

R. W. Peelle, C. D. Zerby, G. T. Chapman, and H. S. Moran 187

The recently written IBM-704 code for Monte Carlo calculations of the gamma-ray responses of scintillation detectors which is described in Sec 8.3 has been used to predict the effects of several variations in the parameters of a large, "total-absorption" NaI(Tl) scintillator. Inclusion of axial wells of various depths and variations in crystal length and diameter were separately considered. Since the code as presently written does not include effects due to bremsstrahlung, pair-annihilation quanta, or electron escape from the crystal, only incident gamma-ray energies of 2 Mev and below are included.

8.5. *COMPARISON OF EXPERIMENTAL GAMMA-RAY RESPONSES OF AN 8-in.-dia NaI(Tl) CRYSTAL WITH CALCULATED RESPONSES*

G. T. Chapman, T. A. Love, and R. W. Peelle 191

The gamma-ray response functions of an 8-in.-dia by 8-in.-long cylindrical NaI(Tl) scintillation crystal have been investigated experimentally at the Bulk Shielding Facility. The crystal was formed by optically coupling two smaller crystals, each 8 in. in diameter and 4 in. long, together in such a way that the composite gave results comparable to those for a single crystal. By mounting an additional 4-in.-dia by 2-in.-long crystal, which had a ½-in.-dia axial hole, on the end of the composite crystal and taking the anticoincidence spectrum from the large crystal, it was shown that the ratio of the peak area to the total area could be improved by the addition of a well in the crystal. The experimental data were compared with the results of Monte Carlo calculations for a crystal of the same size.

8.6. *RESPONSE OF END-WINDOW PHOTOMULTIPLIER TUBES AS A FUNCTION OF TEMPERATURE*

R. B. Murray and J. J. Manning 193

The variation with temperature of the response to monochromatic light of four standard and two modified end-window photomultiplier tubes has been investigated over the range from 25 to −195°C for wavelengths from 4000 to 7000 Å. The temperature-dependent effects observed are discussed in terms of effects associated with the spectral sensitivity and the electrical resistivity of the photocathode.

8.7. *SCINTILLATION PROPERTIES OF NONACTIVATED LITHIUM IODIDE*

R. B. Murray, H. G. Hanson, and J. J. Manning 197

Previous investigations of the factors influencing the scintillation response of Li^6I and $Li^6I(Eu)$ crystals to both gamma rays and to the alpha-triton pair resulting from slow-neutron capture have been extended. For nonactivated Li^6I, the light intensity and the decay time of light pulses have been studied as functions of crystal temperatures from +25 to −196°C. The relative response to gamma rays and to slow-neutron capture has been compared as a function of temperature, and the two distinct bands previously observed in the emission spectra have been correlated to two exponentially decaying components of the light intensity. It is concluded that nonactivated Li^6I offers no advantages over $Li^6I(Eu)$ as a practical detector for either fast or slow neutrons.

8.8. *DETERMINATION OF EXPERIMENTAL FLUX DEPRESSION AND OTHER CORRECTIONS FOR GOLD FOILS EXPOSED IN WATER*

W. Zobel 202

An investigation is under way at the LTSF to determine the depression of the thermal-neutron flux in a medium caused by the presence of a gold foil detector and also to determine other corrections which should be applied to foil measurements. Attempts are being made to include all the corrections in one factor, the ratio of the flux measured with infinitely thin foils to the flux measured with the commonly used 0.002-in.-thick foils. From exposures of foils of various thicknesses, the experimental ratio of the saturated activity per unit mass of a "zero"-thickness foil exposed in water to that of a 0.002-in.-thick foil has been determined to be 1.22 ± 0.16. Several calculated values vary from 1.08 to 1.30.

8.9. *CORRECTION FACTORS FOR FOIL-ACTIVATION MEASUREMENTS OF NEUTRON FLUXES IN WATER AND GRAPHITE*

D. K. Trubey, T. V. Blosser, and G. M. Estabrook 204

A study has been made of the various perturbing factors encountered in the use of foil-activation techniques for measurement of neutron fluxes in water and graphite. Values of $f(T)$, the self-shielding factor, have been calculated for both resonance and thermal-neutron detectors and are compared with experimental data with good agreement. Data is also given concerning the effects of flux depression, cadmium covers, and angular distribution.

9. THERMONUCLEAR RESEARCH

9.1. *ORBIT PRECESSION IN DCX*

T. K. Fowler 219

The possibility of causing ions in the DCX to avoid the arc, once trapped, by introducing precession into their orbits has been investigated. It appears to be impractical to reduce the time spent in the arc by more than a factor of 10.

9.2. *ABSOLUTE CONTAINMENT OF IONS IN DCX*

T. K. Fowler and M. Rankin 219

The study of orbits of single ions in the azimuthally symmetric DCX magnetic field is being carried out, and a detailed report concerning the absolute containment of ions encircling the symmetry axis of the field has been issued. In summary, the report presents a derivation of the absolute-containment criterion together with plots of the regions in space and momentum space to which absolutely contained particles are confined.

9.3. *CODE FOR CALCULATIONS OF ENERGY DISTRIBUTIONS OF PARTICLES IN THE DCX*

T. K. Fowler and M. Rankin 219

An IBM-704 code is being designed to solve coupled Fokker-Planck transport equations for the steady-state energy distributions of ions and electrons in the DCX.

9.4. *MICROWAVE DIAGNOSTICS UTILIZING THE FARADAY EFFECT*

T. K. Fowler 220

An analysis is presented which indicates the possibility of determining the low electron densities in the DCX plasma from measurements of the Faraday rotation of the polarization plane of microwaves in resonance with the electron cyclotron motion. The electron collision frequency can also be determined.

9.5. *CRITICAL CURRENT FOR BURNOUT IN AN OGRA-TYPE DEVICE*

A. Simon 221

A complete algebraic analysis has been obtained for the variation of the steady-state ion density n_+ with injected current I in an OGRA-type fusion device (i.e., a device based on trapping of ions by breakup of energetic molecular ions on collision with either the background gas or trapped ions). The most general variation of n_+ with I is shown to be an s curve with at most three roots of n_+ for a given input I. A physical interpretation of these three roots has been obtained. In addition, algebraic expressions have been derived for the two currents at which the bends in the s curve occur. It will be necessary to attain the larger current in order to build up a high-density plasma when the density is being increased from below. On the other hand, once the high density has been achieved, it may be maintained by steady injection of a current larger than the lower value.

9.6. COHERENT RADIATION FROM A PLASMA

E. G. Harris and A. Simon 221

By beginning with the Liouville equation and treating both the plasma particles and the electromagnetic field in a completely statistical fashion (the single approximation involved being that all pair correlations vanish), the so-called "collisionless Boltzmann equation" or "Vlasov equation" is deduced, as well as a companion equation for each field oscillator. It is shown, as a consequence of this companion equation, that the entropy of the electromagnetic field is a constant and that, in general, a plasma obeying the Vlasov equation can only radiate coherently.

9.7. PLASMA INSTABILITIES ASSOCIATED WITH ANISOTROPIC VELOCITY DISTRIBUTION

E. G. Harris 221

An earlier study of the instabilities of an infinite homogeneous plasma in a uniform magnetic field due to anisotropic velocity distributions suffered from the failure to use the complete set of Maxwell equations. This limited the treatment to longitudinal waves and precluded any consideration of coupling between longitudinal and transverse waves. The work has now been extended to remedy these defects.

9.8. CALCULATION OF THE CROSS SECTION FOR DISSOCIATION OF D_2^+ BY A CARBON ARC

R. G. Alsmiller, Jr. 224

A calculation of the cross section for the dissociation of the D_2^+ molecule by a particle of charge ze has been carried out in Born approximation.

9.9. DIFFUSION OF PLASMA PARTICLES ACROSS A MAGNETIC FIELD

A. Isihara and A. Simon 224

A previous calculation of the rate of diffusion of like charged particles across a magnetic field has been generalized. No a priori assumption as to the relative magnitude of certain terms was made, and spatial density gradients were permitted in both directions perpendicular to the field. The final result agrees with that given earlier.

9.10. SOME EXACT RADIATING SOLUTIONS IN VLASOV'S EQUATIONS

L. C. Biedenharn 225

A class of exact solutions to Vlasov equations which show electro magnetic radiation has been constructed. Since velocities larger than c appear to be possibly of importance in these solutions, an exact radiating solution to the relativistic Vlasov equations was constructed, which, though much more specialized than the nonrelativistic solutions, shows that "unphysically" large velocities in the nonrelativistic solutions are not essential for the radiation there obtained.

10. THEORETICAL NUCLEAR PHYSICS

10.1. SPACINGS OF NUCLEAR ENERGY LEVELS

L. Dresner 229

A simple statistical model, in terms of which the general features of the level spacing distribution can be understood, has been suggested; it involves no special assumptions other than that of Porter and Thomas. The model is described in another publication.

10.2. OPTICAL MODEL OF INELASTIC SCATTERING FROM NUCLEI

T. K. Fowler 230

It is found that the magnitude of the real part of the optical potential, from which distorted waves in direct interactions with nuclei are to be calculated, should be less than that appropriate to elastic scattering. The correction derived agrees with corrections of this sort found to be necessary in some phenomenological fits to experimental inelastic scattering data.

10.3. THE QUASI-ELASTIC SCATTERING OF FAST PARTICLES BY ATOMIC NUCLEI

T. K. Fowler and K. M. Watson 231

The scattering of fast particles by atomic nuclei for large momentum transfers and small energy loss is studied. The cross sections may be expanded in inverse powers of the energy of the incident particle, using methods due to Placzek and Wick. The resulting cross sections, when applied to analysis of experiments, may be used to study short-range order in nuclei. An analysis of electron, pion, and proton experiments shows consistent results and also shows in a striking way the effects of the "repulsive core" in two-body forces.

11. EXPERIMENTAL NUCLEAR PHYSICS

11.1. MEASUREMENTS OF Y^{88}, Zn^{65}, AND Mn^{54} GAMMA-RAY ENERGIES BY SCINTILLATION SPECTROSCOPY TECHNIQUES

R. W. Peelle and T. A. Love 235

A series of experiments is described in which the energies of the intense gamma rays in the decay of Y^{88} have been carefully measured, using NaI(Tl) scintillation counters in a variety of geometries and with various combinations of known energy sources. Less complete measurements were performed for the gamma rays in the decay of Zn^{65} and Mn^{54}. Care was taken to avoid effects from drifts and to correct for nonlinearities of the system. Average values obtained were 1.840 $\pm$ 0.002 and 0.8988 $\pm$ 0.0012 Mev for Y^{88}, 0.8347 $\pm$ 0.0011 Mev for Mn^{54}, and 1.114 $\pm$ 0.004 Mev for Zn^{65}. Energy determinations obtained for well-known gamma-ray transitions gave results consistent with recorded values within similar errors.

11.2. CROSS SECTION FOR THE $Li^6(n,\alpha)H^3$ REACTION FOR $1.2 \leqq E_n \leqq 8.0$ Mev

R. B. Murray, H. W. Schmitt, and J. J. Manning 238

The previously measured cross section for the reaction $Li^6(n,\alpha)H^3$ has been re-evaluated in terms of a recent remeasurement of the Np^{237} fission cross section. The major difference with the previous result occurs in the 1- to 3-Mev region. The revised cross section is in good agreement with that measured by Ribe and slightly higher than that reported by Gabbard *et al.*

11.3. NEUTRON-INDUCED FISSION CROSS SECTION OF Np^{237}

H. W. Schmitt, R. B. Murray, and J. J. Manning 240

The Np^{237} fission cross section has been measured as a function of neutron energy in the range $0.9 \leqq E_n \leqq 8.0$ Mev. The basis of the measurement is a determination of the ratio $\sigma_f(Np^{237})/\sigma_f(U^{238})$ combined with previously determined values of $\sigma_f(U^{238})$. The uncertainty in absolute value of $\sigma_f(Np^{237})$ is estimated to be $\pm$7%. The results from this experiment differ somewhat from a corrected cross-section curve reported previously, and considerable difference exists in both low- and high-energy regions between these results and uncorrected cross sections given in standard compilations.

Part 1

RESEARCH FOR LIGHT-WATER-MODERATED REACTORS

1.1. REACTIVITY EFFECTS OF LARGE VOIDS IN THE REFLECTOR OF THE POOL CRITICAL ASSEMBLY

A. B. Reynolds[1] K. M. Henry E. B. Johnson

A method for simulating voids in the reflector of a pool-type reactor was described previously.[2] Briefly, it consisted in placing a large aluminum tank against one face of the core and forming voids within the tank by separating water-filled Plexiglas boxes which were positioned in two adjacent layers inside the tank. The experimental arrangement is shown in Fig. 1.1.1.

[1]Massachusetts Institute of Technology.

[2]A. B. Reynolds, *Neutron Phys. Ann. Prog. Rep. Sept. 1, 1958*, ORNL-2609, p 7.

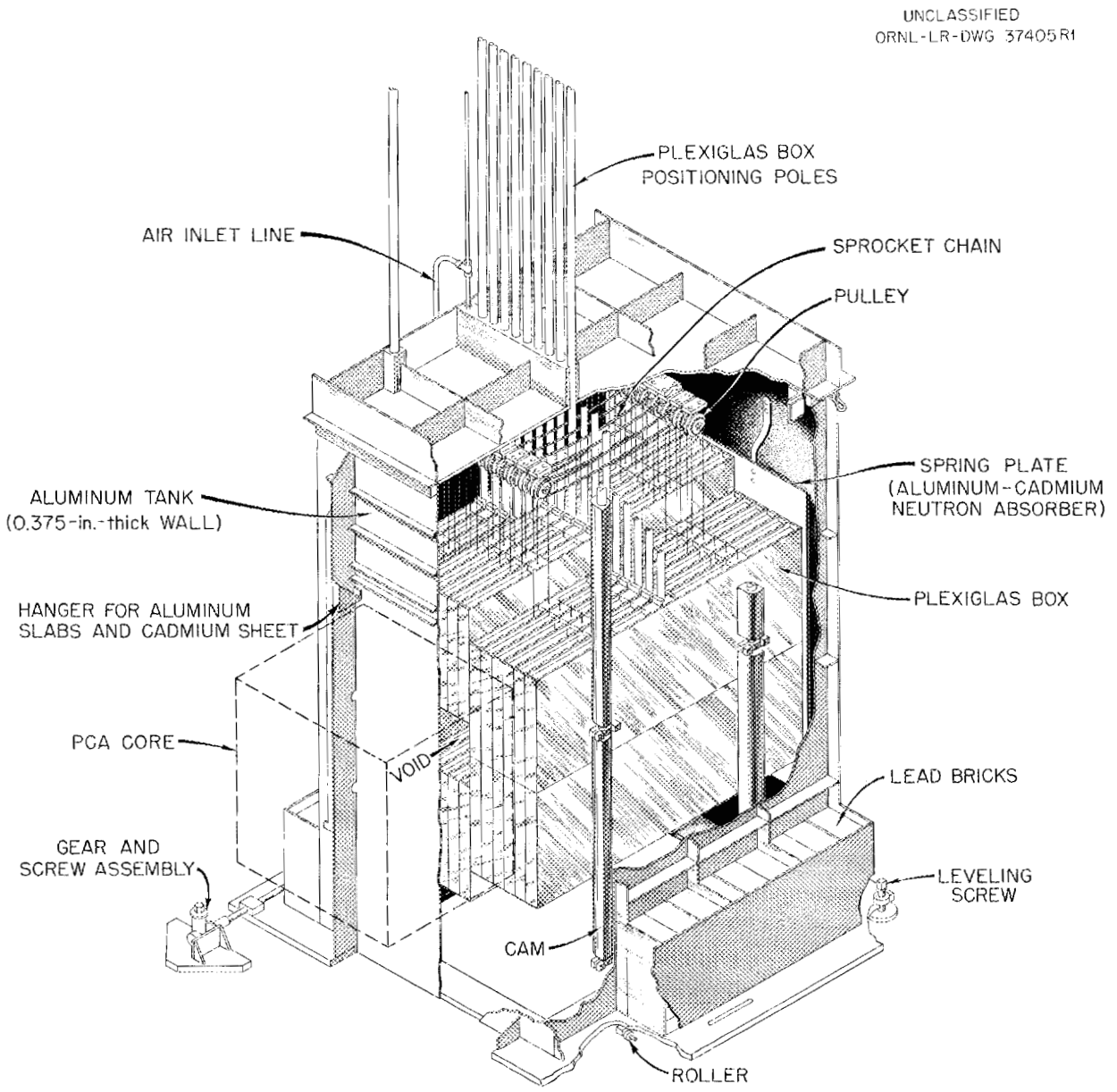

Fig. 1.1.1. Schematic Illustration of Tank Used to Form Voids.

This method was recently used in a study of the effect on the reactivity of introducing voids in the reflector of the Pool Critical Assembly (PCA).[3] The variation of reactivity with void was studied first, with voids of approximately square cross section being located at the center of the core face. In order to determine the effect of the 0.375-in.-thick aluminum tank wall between the core and the void, that is, in order to separate the void effect from the wall effect, measurements of reactivity were made with two additional thicknesses of aluminum between the tank and the core. The results could then be extrapolated to a zero wall thickness. The measurements for the three wall thicknesses and the extrapolated values are shown in Fig. 1.1.2.

The dashed curve in Fig. 1.1.2 is a statistical weight correlation which was obtained by assuming that the effect of a void at the core-reflector interface is the same as the effect of a gray absorbing plane. The reactivity effect, ρ, of the void would then be, within the limits of first-order, one-velocity perturbation theory, proportional to the "statistical weight," α, of the portion of the interface covered by the void; that is, $\rho = m\alpha$, where m is a proportionality factor. The statistical weight of the void area in contact with an interface in the y,z plane is defined as

$$\alpha = \frac{\iint_{\text{void-core interface}} \phi(y,z)\, \phi^*(y,z)\, dy\, dz}{\iint_{\text{entire core face}} \phi(y,z)\, \phi^*(y,z)\, dy\, dz} ,$$

where y and z are the horizontal and vertical directions, respectively, in the plane of the core-void interface, ϕ is the real neutron flux, ϕ^* is the adjoint flux, and the integration in the denominator includes the extrapolated distances. It is evident, of course, that a void actually differs from a gray absorbing medium because of neutron transport across the void surfaces to regions of higher or lower importance.

In the statistical weight correlation shown in Fig. 1.1.2, cosine distributions were assumed for both the real and the adjoint fluxes, and the curve was normalized to the zero wall-thickness curve at a void area of 235 in.^{2}. The probable cause for the lower values in the experimental curve for large voids is the introduction of second-order perturbation effects caused by the large voids.

The variation of reactivity with the position of a void on the core-reflector interface was also observed. Voids of two different heights and 2 in. wide were placed at various positions in the y direction. The results are compared with the statistical weight correlation in Fig. 1.1.3. In this case the values of ϕ used in the statistical weight expression were measured fluxes.

In a study of void effects as a function of the water thickness between the void and the core, two different voids, one 22 by 24 in. in cross section and the other 6 by 6 in., were placed at various distances from the reactor. The results are shown in Fig. 1.1.4. Loadings A and C refer to the reactor core configurations. (Loading A included $2\frac{1}{2}$ more elements than loading C, each element containing 140 g of U^{235}.)

The superposability of multiple voids was also studied. It was found that the reactivity effects

[3] E. B. Johnson and K. M. Henry, *Neutron Phys. Ann. Prog. Rep. Sept. 1, 1958*, ORNL-2609, p 3.

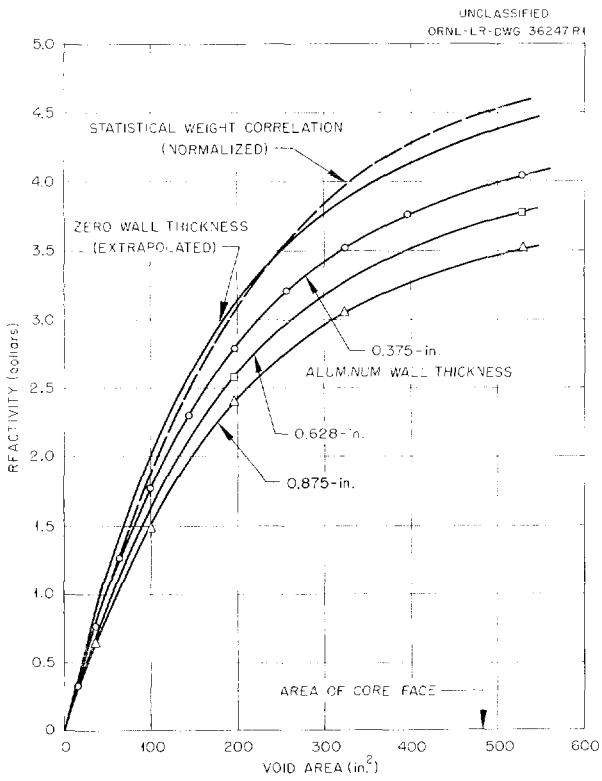

Fig. 1.1.2. Reactivity Effects of Centrally Located Voids as a Function of Void Area.

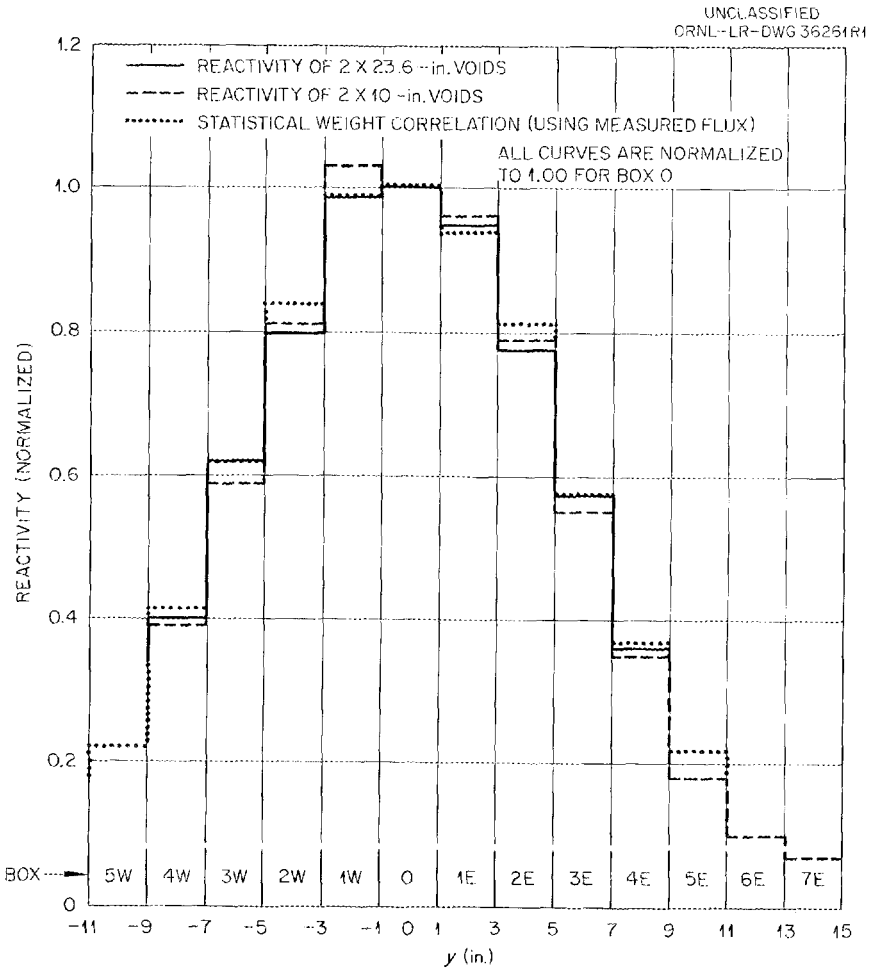

Fig. 1.1.3. Reactivity Effects of Voids Located in Various y Positions: Comparison with Statistical Weight Correlation.

of voids separated by 4 in. or more are superposable. In each case in which the water separation was only 2 in., however, the sum of the individual void effects was greater than the effect of the voids measured together. A partial explanation for the lower effect of multiple voids is the introduction of second-order effects. Each individual void views a higher flux alone than it views when other voids are nearby. On the other hand, it was found that for a zero separation distance the sum of the effects of individual voids was less than the effect of the large void alone. Hence at some separation distance, possibly of about a thermal diffusion length in water, other effects which oppose the second-order perturbation effect apparently become important.

A method based on two-group diffusion theory was developed for calculating the reactivity effect of a void which covers one entire face of a reactor with a rectangular parallelepiped core. The calculated value for loading A of the PCA is 4.6 ± 0.3 dollars. This is to be compared with an experimental value of 4.4 ± 0.1 dollars.

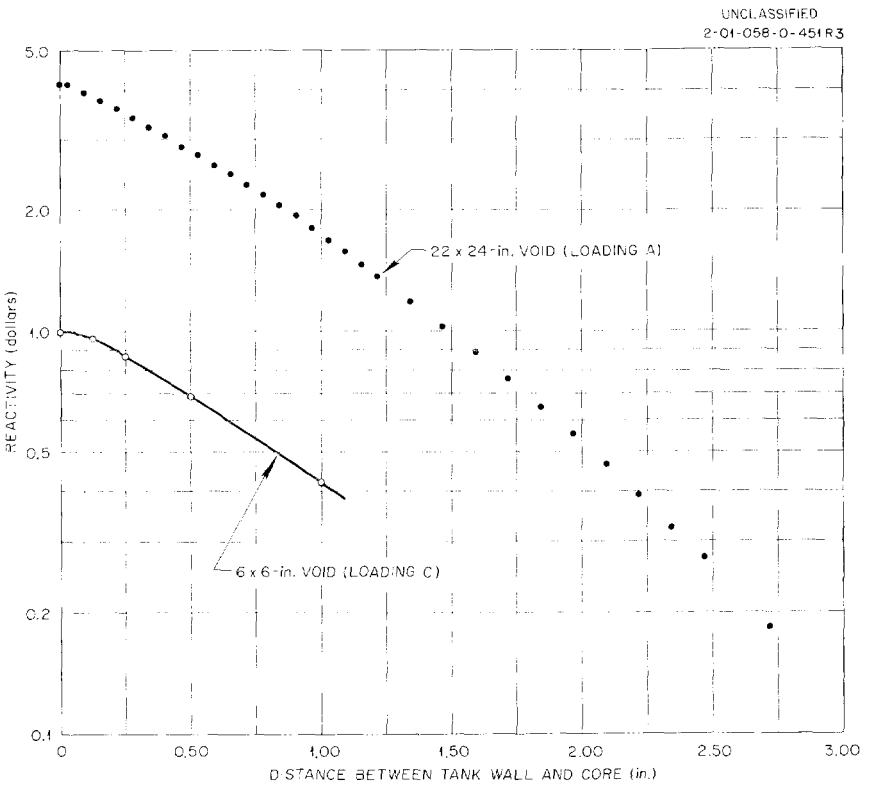

Fig. 1.1.4. Variation of Reactivity with Distance Between Void and Core (0.375-in.-thick Aluminum Wall Between Void and Core).

1.2. CRITICAL MASS CALCULATIONS FOR POOL-TYPE RESEARCH REACTORS

E. G. Silver W. Etzel

Calculations of critical masses for various loadings of the pool-type Bulk Shielding Reactor I (BSR-I) with two different reactor codes have been presented previously.[1-3] One of the codes used was the Oracle 3G3R, a one-dimensional diffusion theory code limited to three energy groups and three regions. For it to be applicable, it was necessary for the BSR-I to have specially symmetric and simple loadings. The other was the UNIVAC Eyewash code. It improved the nuclear model so that 30 energy groups were included and the Goertzel-Selengut slowing down in hydrogen was considered, but it was limited to spherically symmetric geometry.

The geometric limitations of these two codes have been largely overcome by the new two-dimensional codes, one of which is the PDQ[4] for the IBM-704 computer. The PDQ code not only makes it possible to use realistic loading shapes but also allows control rods and small water voids, such as those left by withdrawn rods, to be considered even in arbitrary locations.

As an extension to the earlier work, the PDQ code has been used to calculate the multiplication

[1] E. G. Silver, *Appl. Nuclear Phys. Ann. Prog. Rep. Sept. 10, 1956*, ORNL-2081, p 47.

[2] E. G. Silver, *Appl. Nuclear Phys. Ann. Prog. Rep. Sept. 1, 1957*, ORNL-2389, p 25.

[3] E. G. Silver, *Comparison of BSR Critical Experiments with Two-Group and Thirty-Group Calculations*, ORNL-2499 (1958).

[4] E. G. Bilodeau *et al.*, *PDQ – An IBM-704 Code to Solve the Two-Dimensional Few-Group Neutron Diffusion Equations*, WAPD-TM-70 (1957).

constants (k) of four pool-type reactors: the Geneva Reactor, the Puerto Rican Research Reactor (PRR), the BSR-I, and the Oak Ridge Research Reactor (ORR). The Geneva Reactor and the PRR contain U_3O_8-Al cores enriched to 20% in U^{235}, while the BSR-I and the ORR have highly enriched U-Al cores. The calculations for these four reactors are discussed below. Calculations for a fifth reactor, the BSR-II, are described in Sec 2.1.

Method of Calculation

The input constants for the PDQ calculations were obtained from calculations with the GNU-II code,[5] a one-dimensional 32-group diffusion theory code which utilizes the Goertzel-Selengut slowing-down model for hydrogenous material and provides for inelastic scattering from any lethargy group to any lower group. For these calculations a spherically equivalent model for each reactor case was set up by using the Prohammer method[6] to determine the outer core radius and setting the volume fractions in the actual core and the model core equal to obtain the radii of the interior regions.

The GNU-II code has provisions for calculating few-group constants for up to four energy groups for each region of the reactor. For example, the absorption cross section $(\Sigma_a)_j^G$ for the jth region and few-group interval G is given by

$$(\Sigma_a)_j^G = \frac{\int_{g_a}^{g_b}\int_{r_a}^{r_b} \Sigma_a(u,r)\ \phi(u,r)\ dV\ du}{\int_{g_a}^{g_b}\int_{r_a}^{r_b} \phi(u,r)\ dV\ du} ,$$

where g_a and g_b are the lethargy group limits of the few-group interval G, and r_a and r_b are the region limits of the jth region.

The removal cross sections for the few-group intervals are calculated from "manufactured" removal cross sections, $(\Sigma_R)_j^g$, for each of the 32 lethargy groups, g_j, obtained by

$$(\Sigma_R)_j^g = (\zeta\bar{\Sigma}_t - \zeta\bar{\Sigma}_a)_j^g .$$

These $(\Sigma_R)_j^g$'s are used to calculate $(\Sigma_R)_j^G$ as shown above for $(\Sigma_a)_j^G$.

In the work reported here inelastic scattering cross sections were employed only in those cases involving stainless steel or 20%-enriched fuel.

The elemental cross sections from which the region cross sections were calculated were used as furnished with the GNU-II code. In computing the region averages, no account was taken of binding effects or of self-shielding in heterogeneous fuel pieces; in other words, the materials were treated as homogeneous mixtures of monatomic gases. In the cases where water spaces exist in the core interior, the cross sections for the interior water regions were calculated separately from the cross sections for the exterior water region (reflector), since the difference between the epithermal spectrum in the core interior and in the reflector causes considerable weighting differences in the two locations, leading to significantly different fast few-group cross sections.

As mentioned above, the few-group cross sections obtained from the GNU-II calculations were used as input to the PDQ code. Both three- and four-group models were used for the PDQ calculations, and both X-Y and R-Z calculations were performed. The output of the PDQ code includes the fluxes for each mesh point (maximum number, 2500) for each energy group, as well as the source strength at each mesh point. In a typical case, using about 2000 mesh points and four energy groups, the total computing time for each problem is of the order of 2 hr. The convergence criterion is set so as to limit the convergence error to less than 0.1% in the multiplication constant.

Geneva Reactor Calculations

The calculations for the Geneva Reactor were undertaken as a step preliminary to calculating the multiplication constants of the proposed U^{235} loadings of the PRR. This step was included because the PDQ code had not previously been used for a 20%-enriched reactor, and, since an experimental loading of the Geneva Reactor was available, the applicability of the code could be tested. A GNU-II calculation was first carried

---

[5] C. L. Davis, J. M. Bookston, and B. E. Smith, *GNU-II, a Multigroup One-Dimension Diffusion Program*, GMR-101 (1957).

[6] F. G. Prohammer, *A Comparison of One-Dimensional Critical Mass Computations with Experiments for Completely Reflected Reactors*, ORNL-2007 (1956).

out for four regions to obtain the four-group constants. Descriptions of the regions and the results of the calculation are shown in Table 1.2.1. The PDQ calculation was then performed for the actual X-Y (horizontal plane) geometry of the first critical loading of the reactor. The two-dimensional model is shown in Fig. 1.2.1, and the results of the PDQ calculation are given in Table 1.2.2. The calculated k value of 0.997 is in good agreement with the experimental value of 1.0 and thus validates the usefulness of the PDQ code for PRR calculations.

PRR Calculations

As mentioned above, the PRR calculations were performed in order to predict the multiplication constants for the proposed loadings. A series of five GNU-II calculations was first carried out for PRR loading No. 1 in order to study the effect of various fuel element loadings. The assumed reactor regions and the results of the calculations are shown in Table 1.2.1. A curve of the multiplication constant as a function of the fuel element content is presented in Fig. 1.2.2. Shown in the figure for the PDQ code is an adjusted curve resulting from a normalization of the GNU-II curve to the results of a PDQ calculation for the 178-g loading. The model used for the PDQ calculation is given in Fig. 1.2.3*a*, and the k result is shown in Table 1.2.2. The top curve shown in Fig. 1.2.2 was obtained from a report issued by AMF-Atomics.[7]

An additional PDQ calculation was performed to determine the amount of excess reactivity that could be obtained by replacing the partial elements in PRR loading No. 1 with full elements, assuming that the full elements each contained 178 g of U^{235}. As shown in Table 1.2.2, using only full elements increased the k value from 1.0050 to 1.0512, a difference of $\delta k/k = 4.6\%$.

On the basis of these results, a fuel loading of 192 g of U^{235} per element was chosen, and an additional PDQ calculation was carried out for the 192-g elements in the arrangement shown in Fig. 1.2.3*b* (designated as loading No. 5). The result of this calculation was $k = 1.0042$. Loading No. 5 was selected because the results of an AMF calculation[7] indicated that it should be a critical loading.

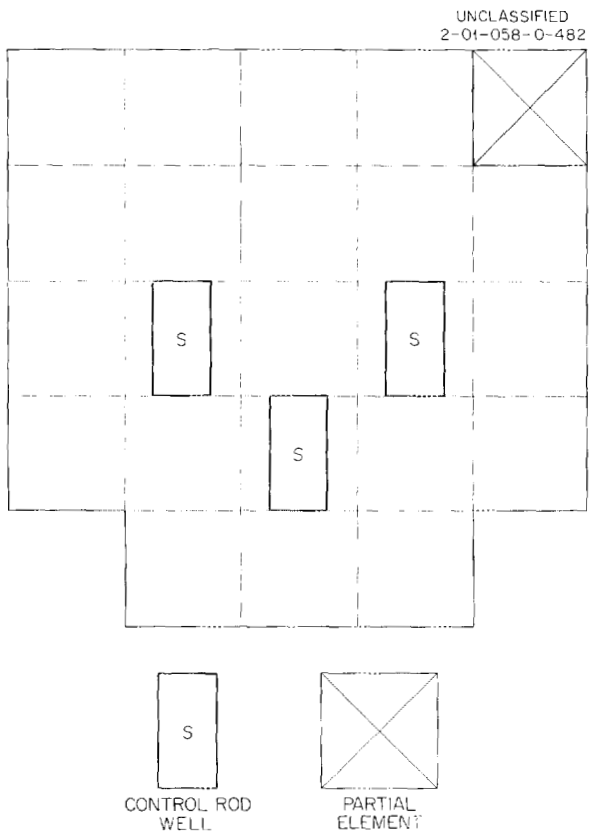

Fig. 1.2.1. Two-Dimensional Model for PDQ Calculation of Geneva Reactor Loading No. 1.

BSR-I Calculations

In order to determine the validity of the calculational methods for highly enriched cores, calculations were made for the 5 × 5 BSR-I loading which had previously been calculated by the Oracle 3G3R code and the UNIVAC Eyewash code.[1-3] As before, a GNU-II calculation was first performed to obtain three-group parameters for the six regions of this reactor, the six regions consisting of (1) interior water spaces, (2) 140-g inner fuel elements, (3) a control-rod well, (4) outer 140-g fuel elements, (5) 70-g partial elements, and (6) the reflector water. The thicknesses of the various regions in the spherical model are given in Table 1.2.1. Accuracy of representation of the model was sacrificed in

[7] R. Powell, *Design for U_3O_8 Core Fuel Loading for the Puerto Rico Nuclear Center*, Reactor Engineering Section, AMF-Atomics (n.d.).

Table 1.2.1. Descriptions and Results of GNU-II Calculations for Various Pool-Type Reactors

Reactor Description	No. of Regions	Region Descriptions and Outer Radii	No. of Few-Groups	Few-Group Lethargy Limits*	k
Geneva Reactor loading No. 1	4	Control rod well, 5.78 cm; core, 23.92 cm; partial element, 24.46 cm; water, 49.46 cm	4	0, 7, 16.6, 19.8 (19.8)	1.0298
Puerto Rican Reactor loading No. 1					
128 g of U^{235} per element	4	Control rod well, 12.26 cm; partial elements, 17.68 cm; core, 28.07 cm; water, 53.1 cm	4	0, 7, 16.6, 19.8 (19.8)	0.8985
153 g of U^{235} per element	4	Control rod well, 12.26 cm; partial elements, 17.68 cm; core, 28.07 cm; water, 53.1 cm	4	0, 7, 16.6, 19.8 (19.8)	0.9491
178 g of U^{235} per element	4	Control rod well, 12.26 cm; partial elements, 17.68 cm; core, 28.07 cm; water, 53.1 cm	4	0, 7, 16.6, 19.8 (19.8)	0.9891
203 g of U^{235} per element	4	Control rod well, 12.26 cm; partial elements, 17.68 cm; core, 28.07 cm; water, 53.1 cm	4	0, 7, 16.6, 19.8 (19.8)	1.0211
228 g of U^{235} per element	4	Control rod well, 12.26 cm; partial elements, 17.68 cm; core, 28.07 cm; water, 53.1 cm	4	0, 7, 16.6, 19.8 (19.8)	1.0476
Bulk Shielding Reactor I, 5 by 5 loading	6	Water, 8.98 cm; core, 22.63 cm; control rod well, 23.54 cm; core, 26.26 cm; partial elements, 27.60 cm; water, 52.60 cm	3	0, 16.6, 19.8 (19.8)	1.0157
Oak Ridge Research Reactor					
Fuel section of ORR rod inserted	9	Control rod fuel, 8.04 cm; control rod structure, 9.89 cm; core, 22.11 cm; partial elements, 26.16 cm; Al, 26.41 cm; Be I,** 31.55 cm; Be II,** 35.97 cm; Al, 36.22 cm; water, 61.22 cm	3	0, 16.6, 19.8 (19.8)	1.1996
Poison section of ORR rod inserted	9	Control rod structure, 9.51 cm; control rod cadmium, 9.89 cm; remainder as above	3	0, 16.6, 19.8 (19.8)	1.0006
Fuel section of PCA rod inserted	10	Control rod water, 7.76 cm; control rod poison and Al, 7.79 cm; control rod fuel, 9.89 cm; remainder as above	3	0, 16.6, 19.8 (19.8)	1.3229

*The lethargy zero is at 10^7 ev; the number in parentheses in this column is the lethargy of the thermal group.

**The Be I region contains more water for cooling than does the Be II region. Both of these are standard Be elements.

Table 1.2.2. Descriptions and Results of PDQ Calculations for Various Pool-Type Reactors

Reactor Description	No. of Groups	No. of Regions	Region Descriptions	B_z^2, Vertical Buckling (cm^{-2})	Mesh	Axes of Symmetry*	k
Geneva Reactor loading No. 1	4	4	Water, core, partial element, control rod well	0.002056	48 × 43	None	0.9970
Puerto Rican Reactor							
Loading No. 1 (with partials)	4	4	Water, core, partial elements, control rod well	0.002037	35 × 70	Y	1.0050
Loading No. 1 (with full elements only)	4	3	Water, core, control rod well	0.002037	35 × 70	Y	1.0512
Loading No. 5	4	3	Water, core, control rod well	0.002037	50 × 42	None	1.00420
Bulk Shielding Reactor I							
5 by 5 loading	3	5	Water, core, partial elements, Al, central water	0.002029	39 × 42	X,Y	1.0002
Loading No. 20	3	4	Water, core, control rod well, central water	0.002029	46 × 39	X,Y	1.0356
Oak Ridge Research Reactor							
Fuel section of ORR rod inserted	3	5	Water, Be with water, core, control rod structure, control rod fuel	0.002003	38 × 38	X,Y	1.2095
Poison section of ORR rod inserted							
Cadmium taken as diffusing medium	3	5	Water, Be with water, core, control rod structure, control rod poison	0.002003	46 × 46	X,Y	0.8317
Cadmium taken as black	3	5	Water, Be with water, core, control rod structure, control rod poison	0.002003	46 × 46	X,Y	0.8502
Fuel section of PCA rod inserted	3	5	Water, Be with water, core, control rod fuel, control rod structure	0.002003	39 × 39	X,Y	1.1782
Poison section of PCA rod inserted	3	6	Water, Be with water, core, control rod structure, control rod poison, control rod water	0.002003	47 × 47	X,Y	0.9333

*All cases used X,Y geometry.

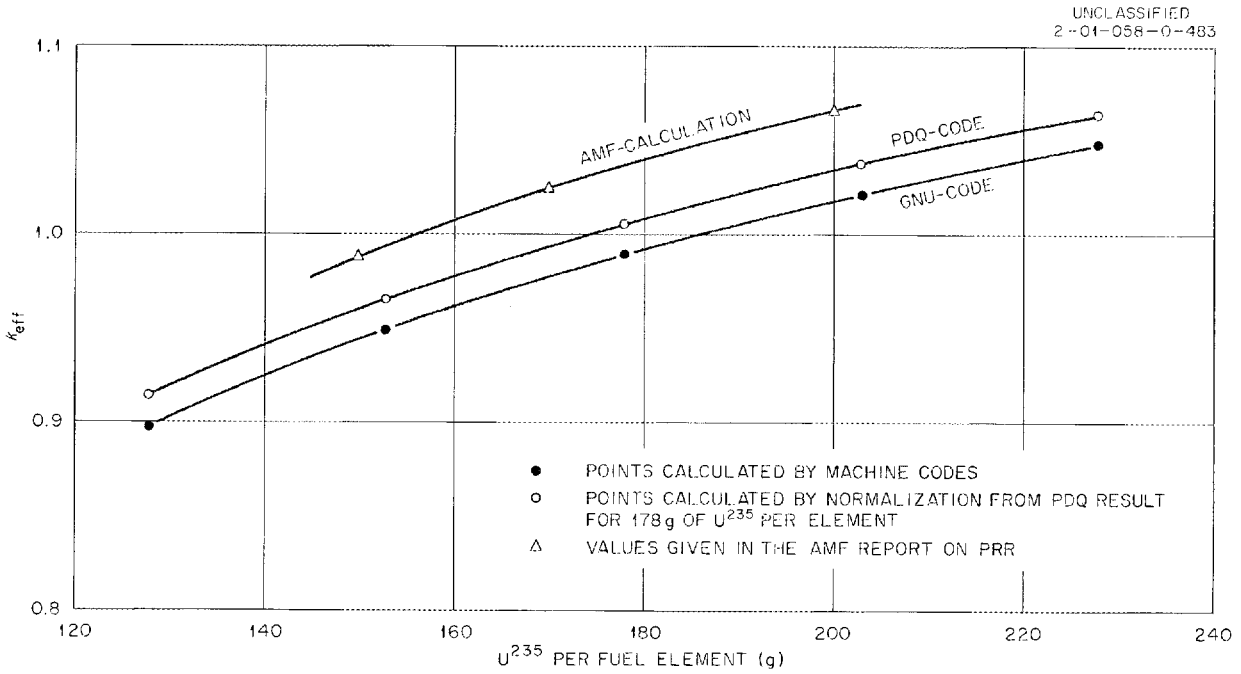

Fig. 1.2.2. Effective Multiplication Constant, k_{eff}, as a Function of Individual Fuel Element Loading for PRR Loading No. 1. Comparison of results of three calculations.

this calculation in order to obtain all the few-group parameters desired for BSR-I work in one GNU-II calculation, and the calculated value of $k = 1.0157$ therefore has little significance except to indicate that the model approximates the actual reactor well enough to make the few-group parameters obtained meaningful.

A PDQ calculation in X,Y geometry was then carried out for the model shown in Fig. 1.2.3*c*. The resulting k value of 1.0002 (Table 1.2.2) is in excellent agreement with the experiment. In view of this, another PDQ calculation was performed for BSR-I loading No. 20, which is a cold, clean critical loading having a one-element water void in its center. The two-dimensional model is shown in Fig. 1.2.3*d*, and the results of the calculation are included in Table 1.2.2. The k value of 1.0356 differs by a suprisingly large amount from the experimental value, and the discrepancy is not well understood at this time. Further investigation is planned.

ORR Calculations

The ORR calculations were performed to determine the worths of double-ended control rods in the ORR, and more particularly, to evaluate a proposed design for double-ended control rods intended for ORR mockup experiments in the Pool Critical Assembly (PCA). Cross sections of the fuel and poison sections for both the ORR and the PCA rods are shown in Fig. 1.2.4. The calculational method consisted in computing the worth of standard ORR control rods in a given loading and then computing the worth of the proposed control rod in the same loading. Accordingly, three GNU-II calculations were made to obtain three-group cross sections for all compositions required for the proposed calculations. The fuel cross sections were separately computed with and without the poison sections of the control rods in the core in order to correctly take account of the spectrum changes imposed by the cadmium control elements. Descriptions of the assumed reactor regions and the results of the calculations are included in Table 1.2.1.

The ORR model for the PDQ calculations was a rectangular loading, surrounded by a layer of beryllium reflector elements, with four control elements symmetrically located in the core as

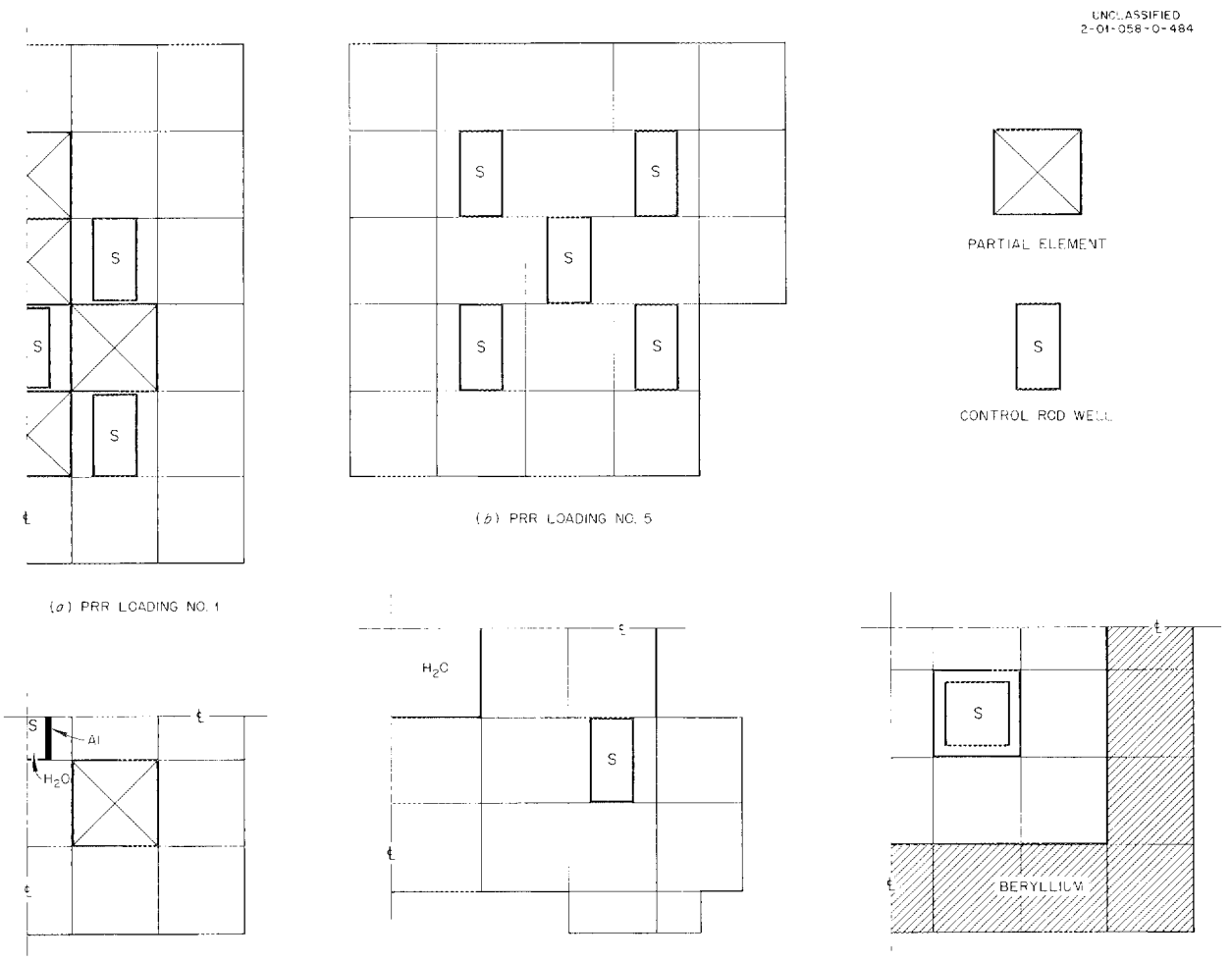

Fig. 1.2.3. Two-Dimensional Models for PDQ Calculations of PRR, BSR-I, and ORR. (*a*) PRR loading No. 1, (*b*) PRR loading No. 5, (*c*) 5 by 5 BSR-I loading, (*d*) BSR-I loading No. 20, (*e*) ORR.

shown in Fig. 1.2.3*e*. With this model a large number of mesh points were made available for calculating accurate flux shapes in the vicinity of the control elements without an excessive total number of mesh points.

The PDQ computation for which it was assumed that the fuel section of the standard ORR double-ended control element was inserted in the core resulted in a k value of 1.2095. For the case in which the cadmium poison section was inserted, it was questionable whether the intermediate-energy group constants for the cadmium region should be used, thus treating the cadmium in the energy range from thermal up to about 0.9 ev as a diffusing medium, or whether the cadmium in this energy group should be treated as "black" with a specification of the flux gradient at the region surface. The calculation was therefore done by both methods as shown in Table 1.2.2. The difference between the two k values is small enough so that it was not considered necessary to investigate this problem further. The total calculated reactivity worth of the standard ORR control rods in the positions shown in Fig. 1.2.3*e* was thus calculated to be $\Delta k/k_{\text{fuel in}} = 30.4\%$.

The PDQ calculations to determine the effectiveness of the proposed double-ended PCA control rods resulted in a k value of 1.178 for the fuel section inserted and a k value of 0.933 for the poison section inserted. This gives a control element reactivity worth of $\Delta k/k_{\text{fuel in}} = 24.5\%$,

UNCLASSIFIED
2-01-058-0-485

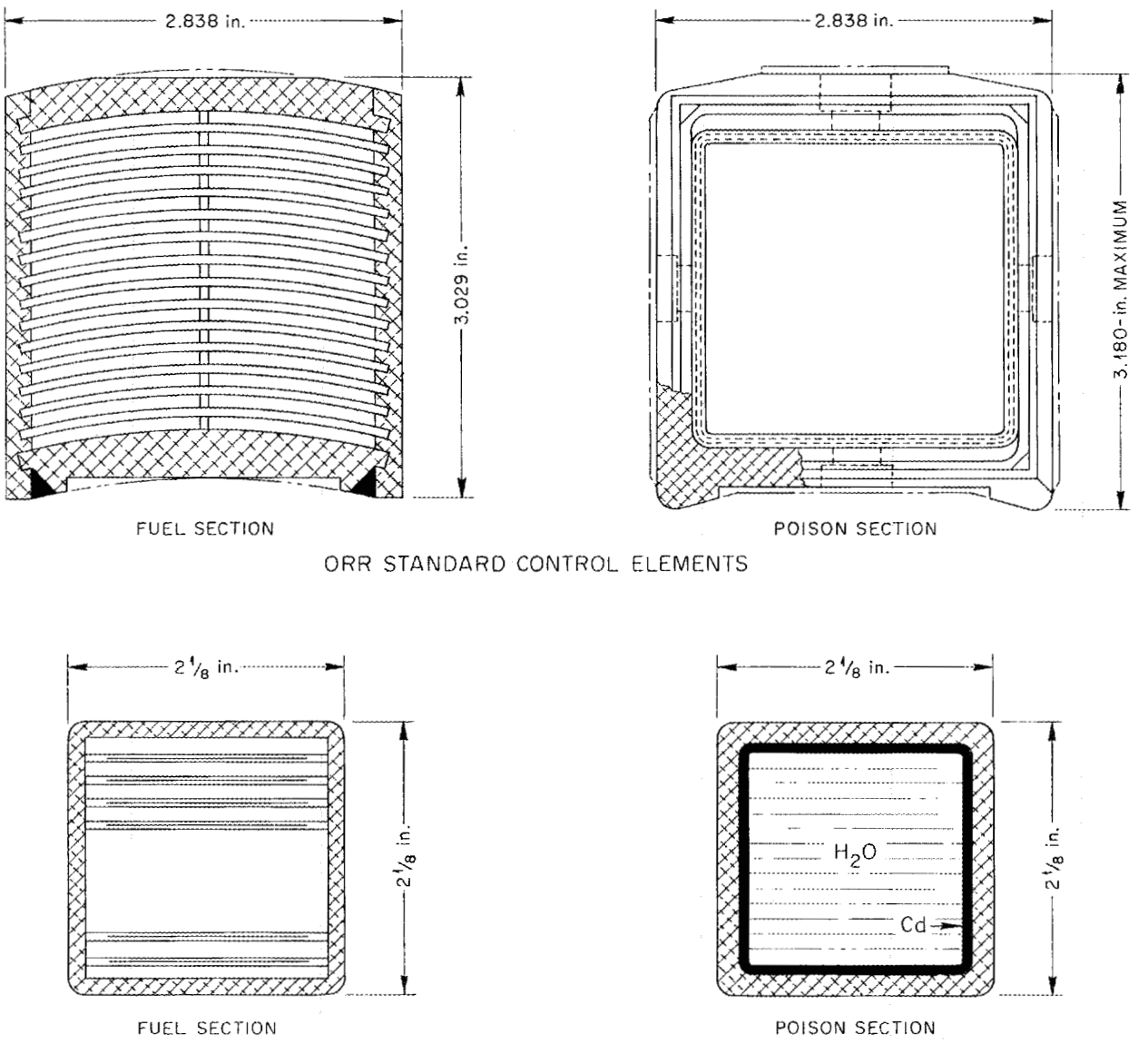

Fig. 1.2.4. Cross Sections of Fuel and Poison Sections of ORR Double-Ended Control Rods and PCA Mockup Rods.

which is 5.9% less than the worth of the standard ORR control rod in the same core configuration. This difference is due to the smaller poison area of the PCA rod.

Flux Plots

As a result of a PDQ calculation, the neutron flux distribution in the plane of the calculation is obtained. It is frequently of interest to observe how core shapes affect these flux distributions; therefore contour plots have been made of the flux distributions in the X,Y plane of several of the calculated reactor configurations.

Figure 1.2.5 shows the thermal-neutron flux contour map for a portion of the PRR loading No. 5. The flux shape in the vicinity of the

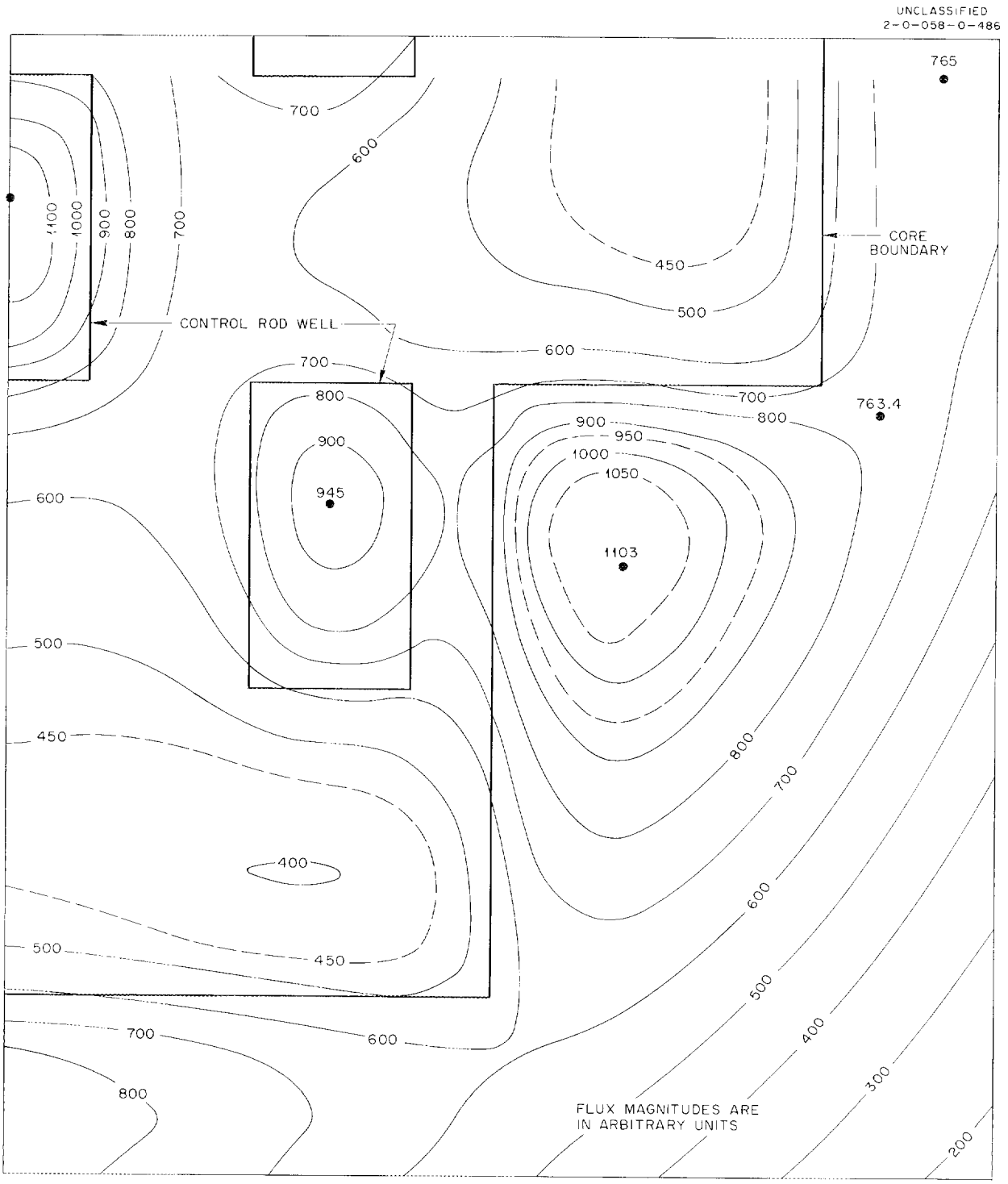

Fig. 1.2.5. Isoflux Contours Calculated by the PDQ Code for the Thermal-Neutron Flux in PRR Loading No. 5.

concave corner is of interest, as are the flux peaks in the water voids formed by the control rod wells.

A contour plot for the thermal flux in BSR-I loading No. 20 is shown in Fig. 1.2.6. The nonsymmetric corner elements were approximated in this calculation by half elements and quarter elements in the corner position, so that biaxial symmetry, with its attendant meshpoint economy, could be preserved. Figure 1.2.7 shows the intermediate-energy flux contour for this same BSR-I case.

Summary and Future Plans

Since the GNU-II and PDQ codes yielded satisfactory agreement in most cases where direct comparisons with experimental data could be made, it may be concluded that for compact core loadings such calculations may be relied upon to furnish useful critical mass predictions. However, a number of problems remain to be investigated more adequately. There is first the question of the effect of large water regions in the core, and also the question of the best approximation for heavily absorbing materials such as appear in control rods. The latter problem is necessarily involved with the basic inadequacy of diffusion theory to deal with such regions. However, by proper choice of boundary conditions, improvements may well be possible. Future calculations to investigate these problems are planned. Calculations on partially and completely inserted control rods in nonsymmetric configurations are also planned, since it will be possible to make direct comparisons of the results of such calculations with experimental information obtained by the pulsed-neutron method, which is discussed in Sec 2.2 of this report.

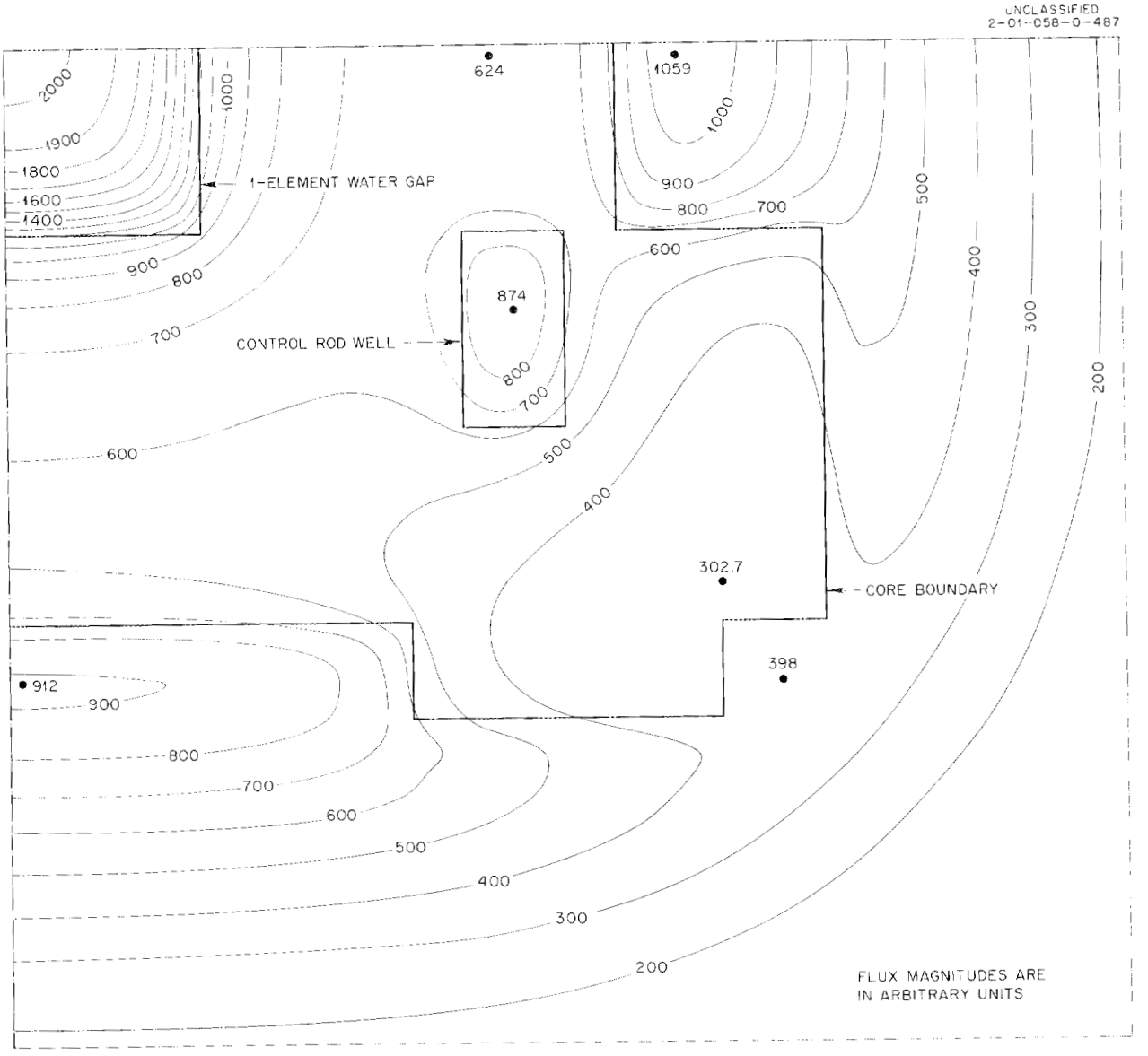

Fig. 1.2.6. Isoflux Contours Calculated by the PDQ Code for the Thermal-Neutron Flux in BSR-I Loading No. 20. The half- and quarter-sized elements in the corner represent asymmetrically placed elements symmetrized for the purpose of achieving a configuration with two axes of symmetry.

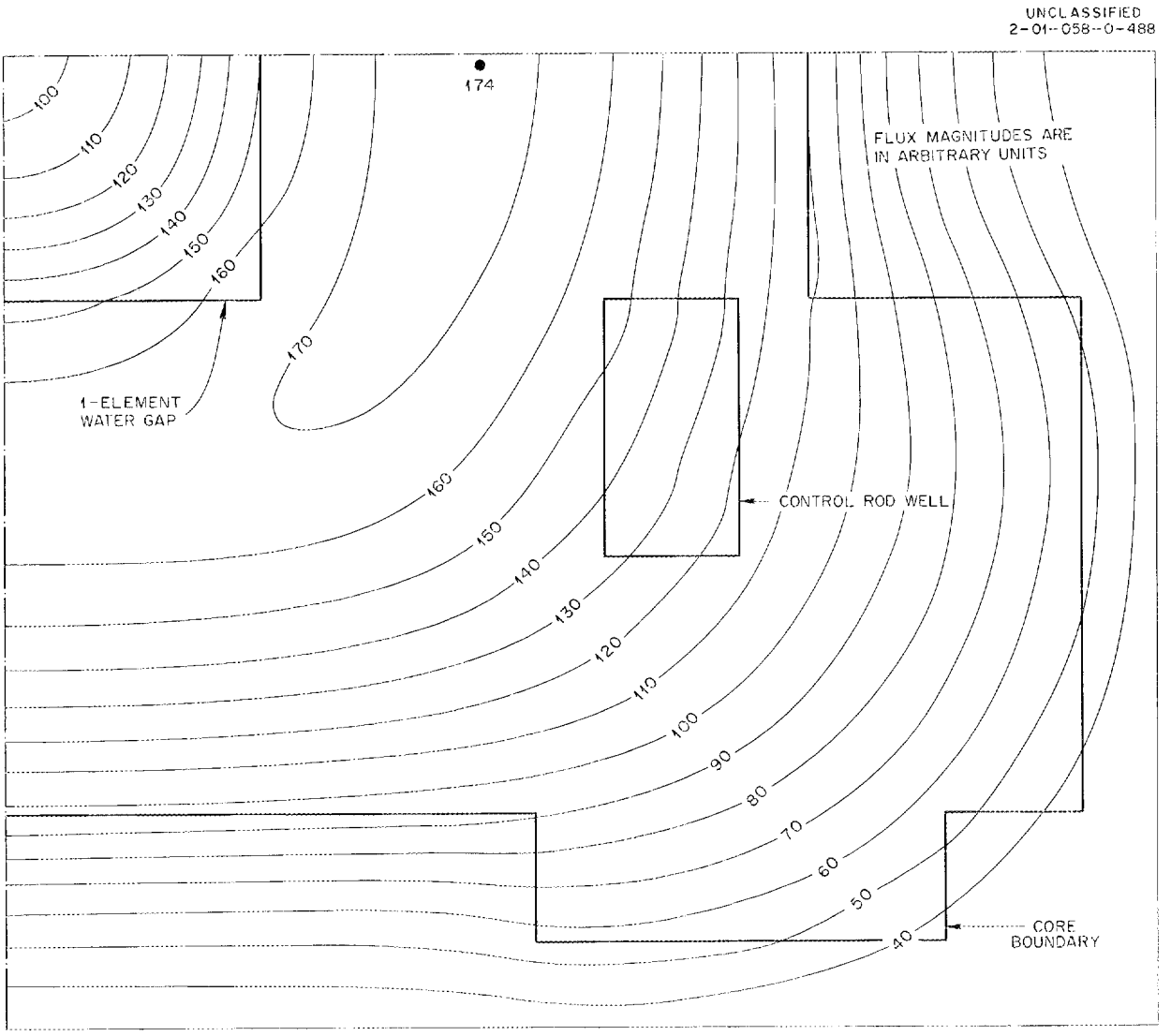

Fig. 1.2.7. Isoflux Contours Calculated by the PDQ Code for the Intermediate-Energy Flux (Thermal to 0.9 *ev*) in BSR-I Loading No. 20. The half- and quarter-sized elements in the corner represent asymmetrically placed elements symmetrized for the purpose of achieving a configuration with two axes of symmetry.

Part 2

NEW REACTORS FOR THE BULK SHIELDING AND TOWER SHIELDING FACILITIES

2.1. BULK SHIELDING REACTOR II: STATUS REPORT

K. M. Henry E. G. Silver
E. B. Johnson

Previous reports[1-3] have covered rather thoroughly the design and logic of the Bulk Shielding Reactor (BSR-II), the UO_2–stainless steel reactor core for the Bulk Shielding Facility. Subsequent to the most recent of these reports, minor modifications have been made in the design, and the fabrication of the reactor has been completed. The BSR-II has now undergone preliminary critical tests in the Pool Critical Assembly (PCA). The tests have included several critical loadings and experimental determinations of the prompt-neutron lifetime, the reactivity worth of the control plates, and the worth of a double-ended reactivity-insertion device. The insertion device was designed for use in the tests on the reactor at the SPERT-I Facility at the National Reactor Testing Station in Idaho Falls, Idaho.

Additional calculations have also been performed for the reactor. These calculations utilized the recently available GNU-II and PDQ codes for the IBM-704, the latter code allowing calculations in *R-Z* geometry.

The BSR-II and associated components have now been shipped to the SPERT-I Facility where static tests with the reactor have begun. These will be followed by dynamic excursion tests designed to determine the inherent self-limiting characteristics of the reactor and the effectiveness of its control system.

In the discussion that follows, only the design changes are presented, and only the most recent calculations are described. The SPERT-I test plans are also discussed briefly.

Mechanical Design

The mechanical design of the BSR-II is essentially as previously reported.[1-3] In order to accommodate the double-ended reactivity-insertion plates necessary for the SPERT-I tests, which will be described below, two 0.4 by 3 in. rectangular slots were machined in the grid plate. They are located 1.3 in. from the grid plate center line, on opposite sides of the central element hole, and permit the passage of the pair of double-length rods through the plate into the space beneath. Design dimensions of the grid plate were successfully retained after heat treatment to Rockwell hardness 42.

The design of the fuel elements is unchanged. A standard 20-plate element contains 290 g of U^{235} in a cermet (~75 wt % stainless steel). Four half elements, each containing 145 g of U^{235}, and four quarter elements, each containing 72 g of U^{235}, have been fabricated by modifying the proportions of uranium and stainless steel in the cermet. Dimensions of the partial elements are identical with those of standard fuel elements.

A standard control-plate element contains 223 g of U^{235} in the same cermet as the standard fuel element, the lower loading resulting from the use of narrower plates. The standard control plates (two per control element) now contain 6.0 g of 85% B^{10} enriched boron dispersed in iron powder. The finished plate contains a core 2.5 × 0.025 × 15 in. and has over-all dimensions of 2.8 × 0.085 × 18 in. The chafing strips that previously extended the full length of the plate on the center line have been moved toward the edges and reduced in size to 0.05 by $^5/_{16}$ by 16.5 in. They serve to stiffen the poison plate and position it in the element channel so that coolant passages are assured. The 3 by 3 in. coaxial control-plate drives, patterned after the standard BSF drive, have been modified by the addition of a thrust bearing on the drive to the lead screw to facilitate compressing the 66-lb spring that accelerates the scramming action. The drive magnets are designed to release within 10 msec after application of a scram signal to the sigma bus.

In order to provide the necessary rate and amount of positive reactivity insertion for the current SPERT-I tests, a pair of reactivity insertion blades has been designed. The upper section of these is composed of three control element fuel plates held 0.094 in. apart by side plates. A

---

[1] E. G. Silver and J. Lewin, *Appl. Nuclear Phys. Ann. Prog. Rep. Sept. 1, 1957*, ORNL-2389, p 33.

[2] E. G. Silver and J. Lewin, *Safeguard Report for a Stainless Steel Research Reactor for the BSF (BSR-II)*, ORNL-2470 (1958).

[3] E. G. Silver, *Neutron Phys. Ann. Prog. Rep. Sept. 1, 1958*, ORNL-2609, p 15.

lower section, attached to the bottom of the upper section by a 1-in. spacer, is a single steel box containing 28 g of 90 wt % B^{10} powder. Tie pins are located every 2 in. on the center line to assist in the maintenance of geometry under the proposed acceleration and shock conditions. No provision for cooling passages within the boron was deemed necessary, since during the time of operation at high power the poison is to be out of the core, hence out of the high-flux region of the reactor.

For the PCA tests the electromagnet was replaced by a positively attached rod so that the possibility of rapid insertion of reactivity was excluded.

Recent Calculations

The critical mass calculations employing the Eyewash code for the UNIVAC have been described previously.[1-3] More recent calculations, discussed in the following paragraphs, have been made with the GNU-II and PDQ codes for the IBM-704. A detailed discussion of the theory and reliability of the GNU-II and PDQ codes is given in Sec 1.2.

One of the calculations was performed to determine the worth of the control plates in a 5 by 5 BSR-II loading containing four control elements in the four positions adjacent to the corners of the central fuel element. With water in the control plate wells, the calculation yielded a multiplication constant $k = 1.02$, while with control plates in the fully inserted position $k = 0.899$. The reactivity worth is therefore 12.0% $\Delta k/k$. By using the delayed neutron data of Keepin *et al.*[4] and assuming the relative effectiveness of prompt and delayed neutrons, γ, to be 1.1 ± 0.1, the value of β_{eff} is determined to be 0.0070 ± 0.0007. The value of the total reactivity worth of the control system is thus determined to be 17.1 ± 1.7 dollars. For comparison, experimental measurements were made on BSR-II loading No. 14A, which has no corner elements and has a half element adjacent to one empty corner. This loading was supercritical by 44 cents with all control plates fully withdrawn, as determined by the inhour method. With all plates fully inserted, a negative reactivity of 7.78 dollars was measured by the pulsed-neutron method. The total control plate worth was therefore 8.22 dollars. The absence of corner elements, however, diminished the control plate worth, the worth of the plates in one control element being 2.87 dollars with the adjacent corner filled, but only 2.50 dollars with the adjacent corner empty. No direct measurement of the effect of the half element adjacent to the corner was made, but examination of the reactivity worth of the half element in this position indicates that the worth of the control plates in the nearby control element is diminished by a factor reasonably estimated at 1.1. A combination of the experimental data gives a total worth of ($8.22/4) (2.87/2.50) (3 + 1.1) = 9.70 ± 1.0 dollars.

It was originally expected that the desired reactivity worth of the SPERT-I reactivity-insertion device would be obtained by merely inserting three fuel plates into each of two water spaces. PDQ calculations based on this model were therefore performed, giving a $k = 1.012$ for water in the insertion slots, and a $k = 1.021$ for fuel plates in the slots. Since the difference was insufficient, the double-ended device described above was designed. A calculation of the effect of the fully inserted poison sections of these devices gave a result of $k = 0.965$. A comparison of this with $k = 1.021$ for fuel plates inserted indicates a $\Delta k/k = 5.6\%$, which is equivalent to 7.9 ± 0.8 dollars, based on the assumptions previously employed for the value of γ. Experimental verifications using the pulsed-neutron technique produced a value of 5.41 ± 0.5 dollars. Since the model for the calculation employed an early design using two dispersed-poison plates per channel, while the experiment used the later single thick plate filled with powder described above, this difference is not surprising.

Because the BSR-II has a 0.85-in.-thick steel grid plate, as well as relatively massive steel lower end boxes in very close proximity to the fuel region (much closer than in the corresponding aluminum structures of the BSR-I), a calculation of the effect of this steel on the flux and multiplication of the BSR-II was performed. A PDQ calculation in R-Z geometry was made both with and without the steel members. For calculational ease the grid plate and end boxes were assumed to be ring-shaped structures of stainless steel

[4] G. R. Keepin, T. F. Wimett, and R. K. Zeigler, *J. Nuclear Eng.* 6, 1 (1958); see also G. R. Keepin, T. F. Wimett *et al.*, *Delayed Neutrons from Fissionable Isotopes of Uranium Plutonium and Thorium*, LA-2118 (1957).

and water, as shown in Fig. 2.1.1, with metal-to-water ratios maintained as in the reactor. The result of the calculation without the steel members was $k = 1.019$, while the calculation including the steel gave a result of $k = 1.015$. The small difference in the values is attributed to the fact that steel is a good neutron reflector. Figure 2.1.2 shows flux plots along the reactor axis (passing through a water space in the grid plate and end boxes) and along a vertical line displaced from the axis by 3.83 cm, so as to pass through the steel portion of both the grid plate and the end boxes. It is evident that the flux shape in the core region is perturbed very little by the presence of the steel, thus accounting for the small effect on the multiplication.

UNCLASSIFIED
2-01-058-0-492

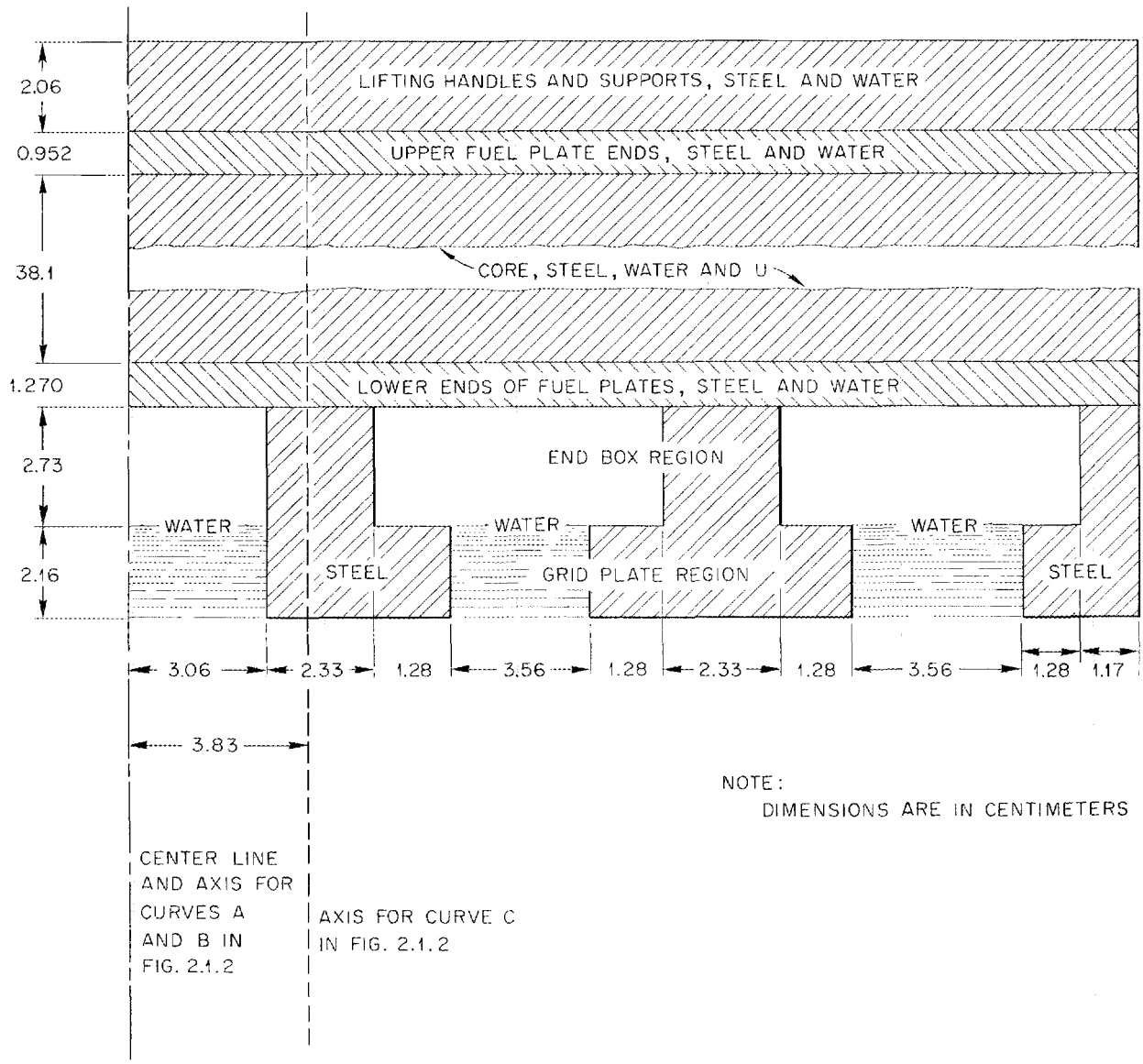

Fig. 2.1.1. BSR-II Model Used for PDQ Calculations (R-Z Geometry).

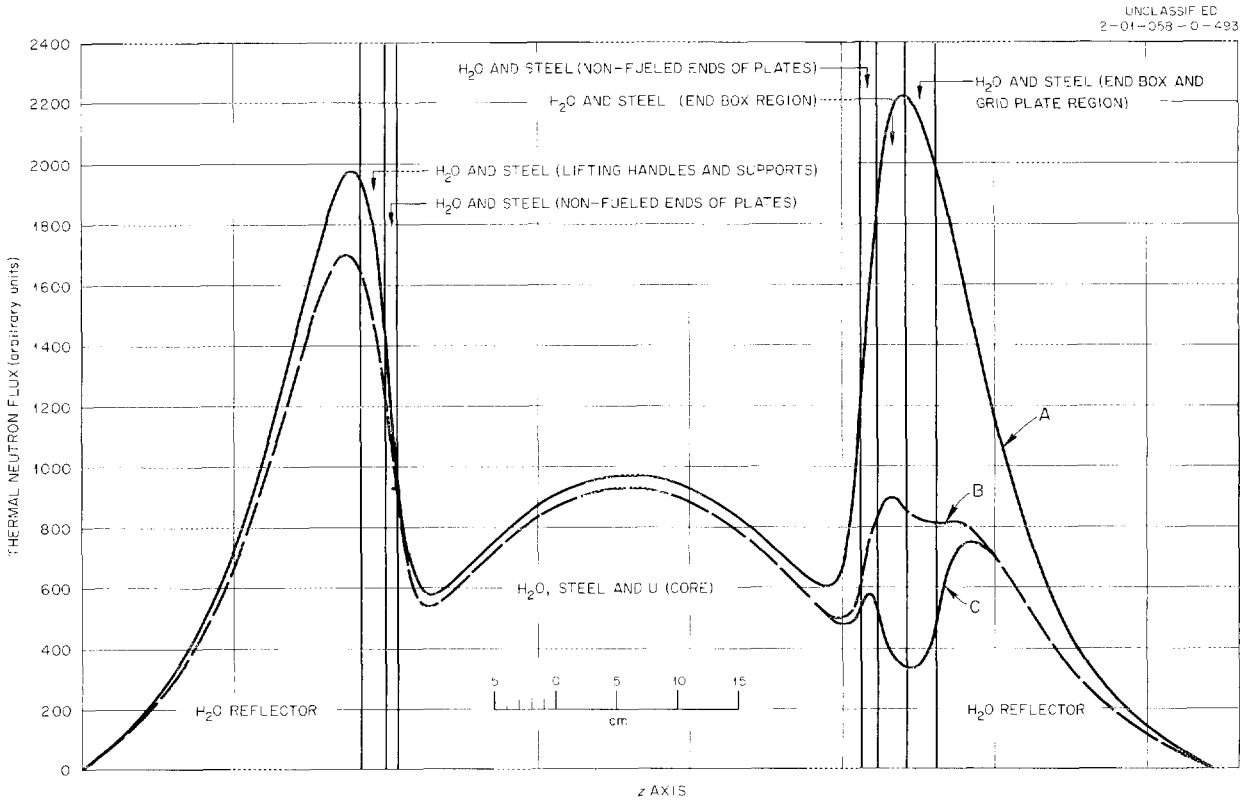

Fig. 2.1.2. Thermal-Neutron Fluxes Along Vertical Lines Through BSR-II (PDQ Code Calculation in *R-Z* Geometry). Curve A: Along *z* axis, no end boxes or grid plate present. Curve B: Along *z* axis, end boxes and grid plate present. Curve C: 3.8 cm from *z* axis, end boxes and grid plate present. Refer to Fig. 2.1.1 for calculation model. Flux values are independently arbitrary.

Isoflux plots of the thermal-neutron flux in the BSR-II in *X-Y* geometry have also been calculated by the PDQ code and are presented in Figs. 2.1.3–2.1.6. The large flux peaks in regions of low absorption adjacent to the core are notable. Figure 2.1.3 gives isoflux curves for the core interior of the BSR-II without the control plates inserted, while Fig. 2.1.4 shows the flux contours with the plates inserted. Figure 2.1.5 gives the thermal-neutron flux exterior to the core. This region is little affected by details of the core conditions. The isoflux contours for the low epithermal flux in the reactor without the control plates inserted are shown in Fig. 2.1.6.

Experimental Measurements

Critical loadings of the BSR-II were made in the PCA facility at the BSF. The existing three PCA safety-rod control circuits were used to control three of the four BSR-II safety rods, while the fourth was controlled by one of two recently installed guillotine drive control circuits. (The second guillotine drive control was used to control the drive of the reactivity-insertion device when used.) Since the BSR-II has no "regulating rod," the PCA servo channel was deactivated, and flux level was controlled manually by adjustment of the shim-safety rods. (The term "rod" here refers to a pair of the BSR-II control plates.) The remainder of the control circuits and all of the safety circuits were left as normally designed for PCA operation. An aluminum support stand elevated the BSR-II grid plate 20 in. above the PCA grid plate, positioning the core near the control chambers and leaving room under the core for use with the double-ended reactivity-insertion device.

The initial critical loading (Fig. 2.1.7) contained 5.877 kg of U^{235} and had an excess reactivity of 16.5 cents with the shim-safety rods

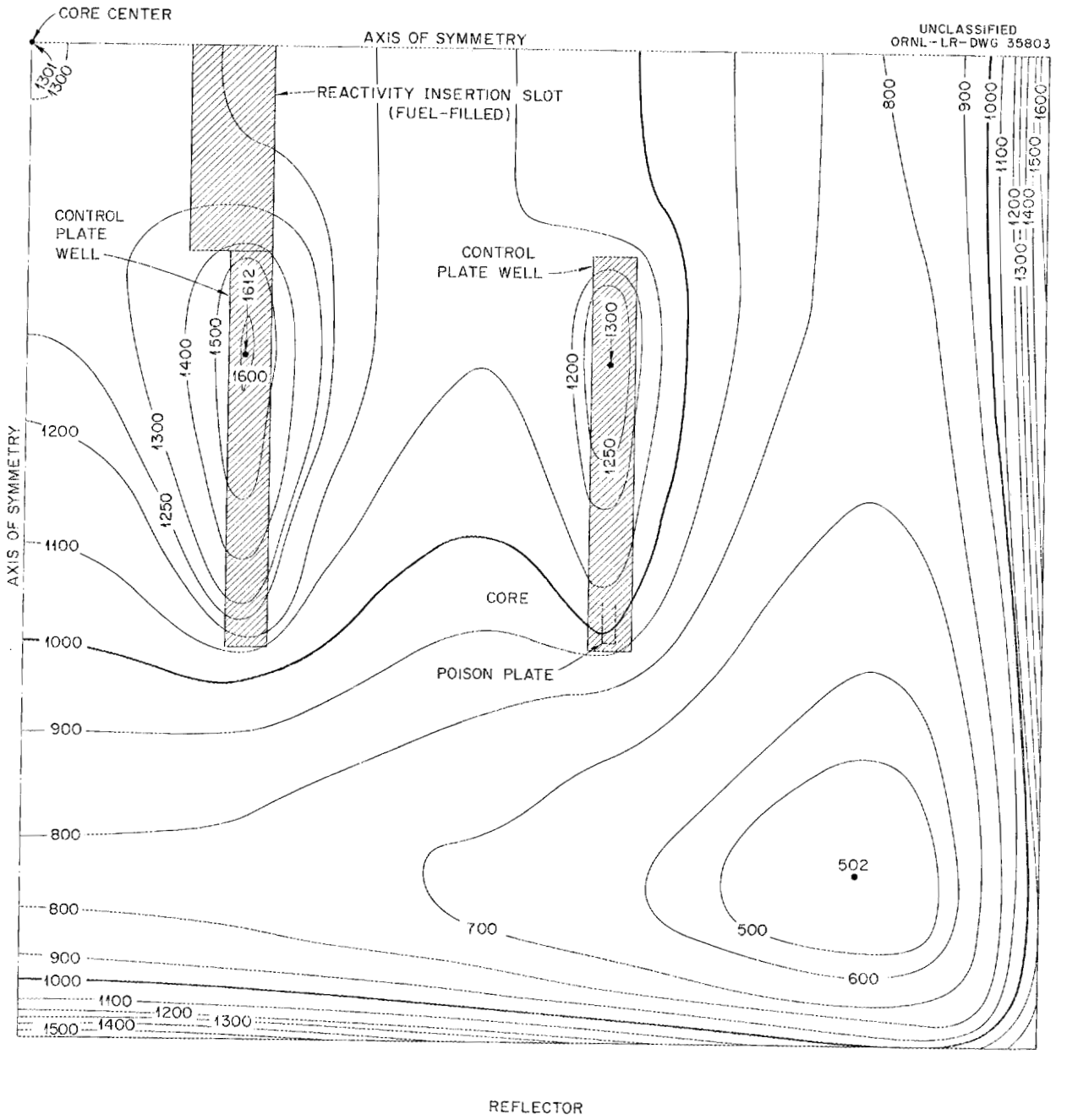

Fig. 2.1.3. Isoflux Contours Calculated by the PDQ Code for the Thermal-Neutron Flux in the X-Y Plane of One Quarter of the BSR-II Core: No Control Plates, Fuel in Reactivity Insertion Slots.

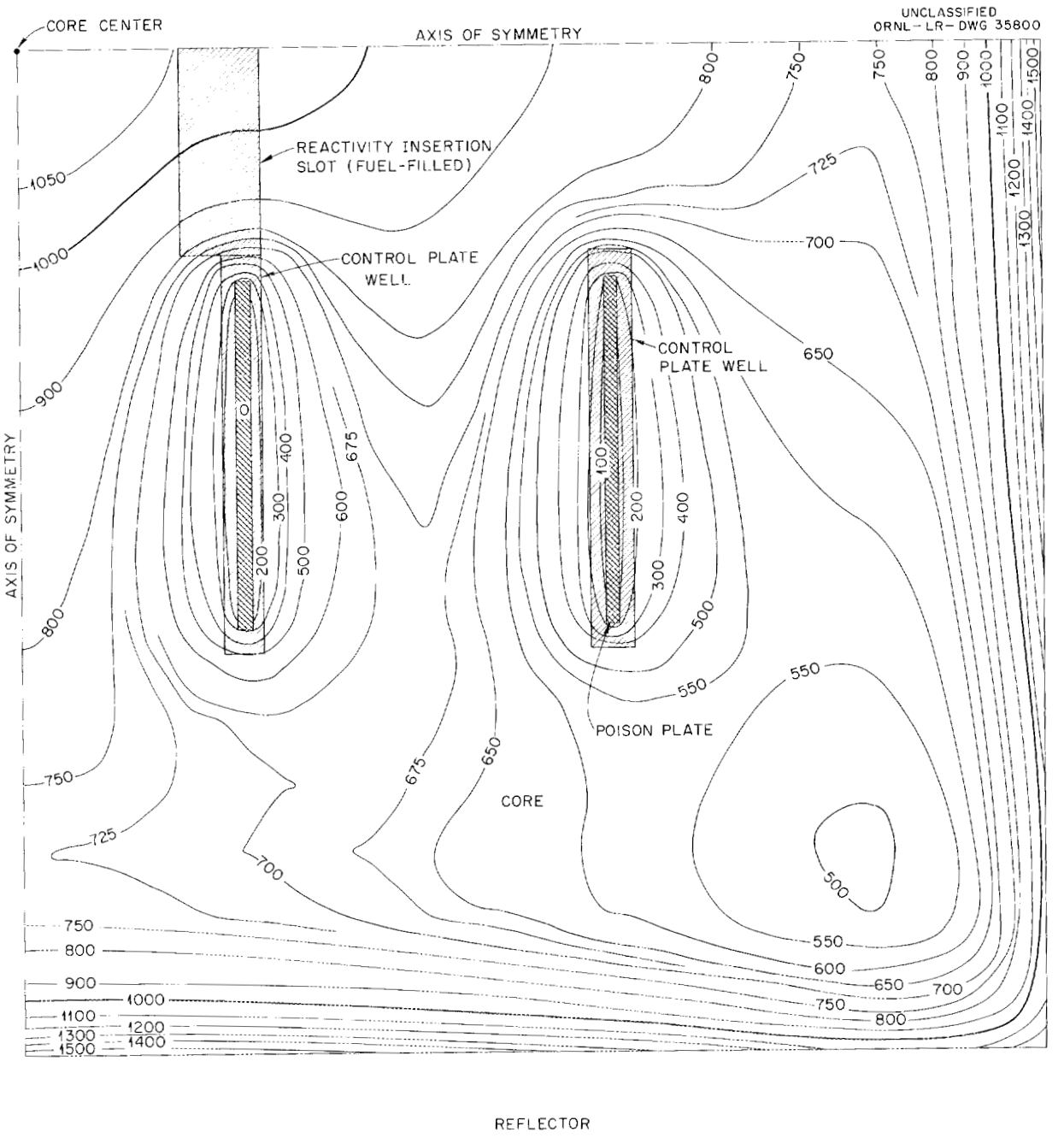

Fig. 2.1.4. Isoflux Contours Calculated by the PDQ Code for the Thermal-Neutron Flux in the *X-Y* Plane of One Quarter of the BSR-II Core: Control Plates Fully Inserted, Fuel in Reactivity Insertion Slots.

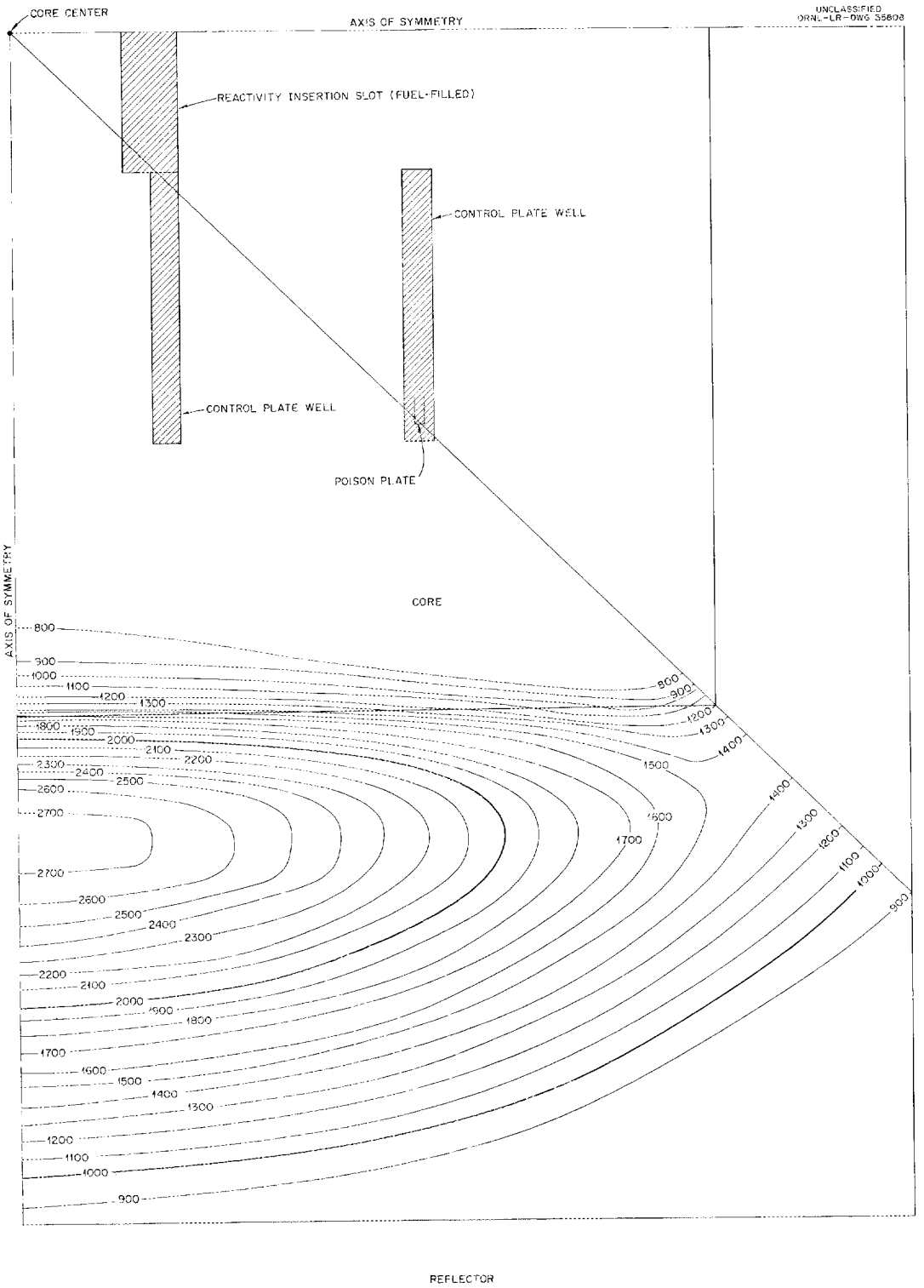

Fig. 2.1.5. Isoflux Contours Calculated by the PDQ Code for the Thermal-Neutron Flux Exterior to the BSR-II Core.

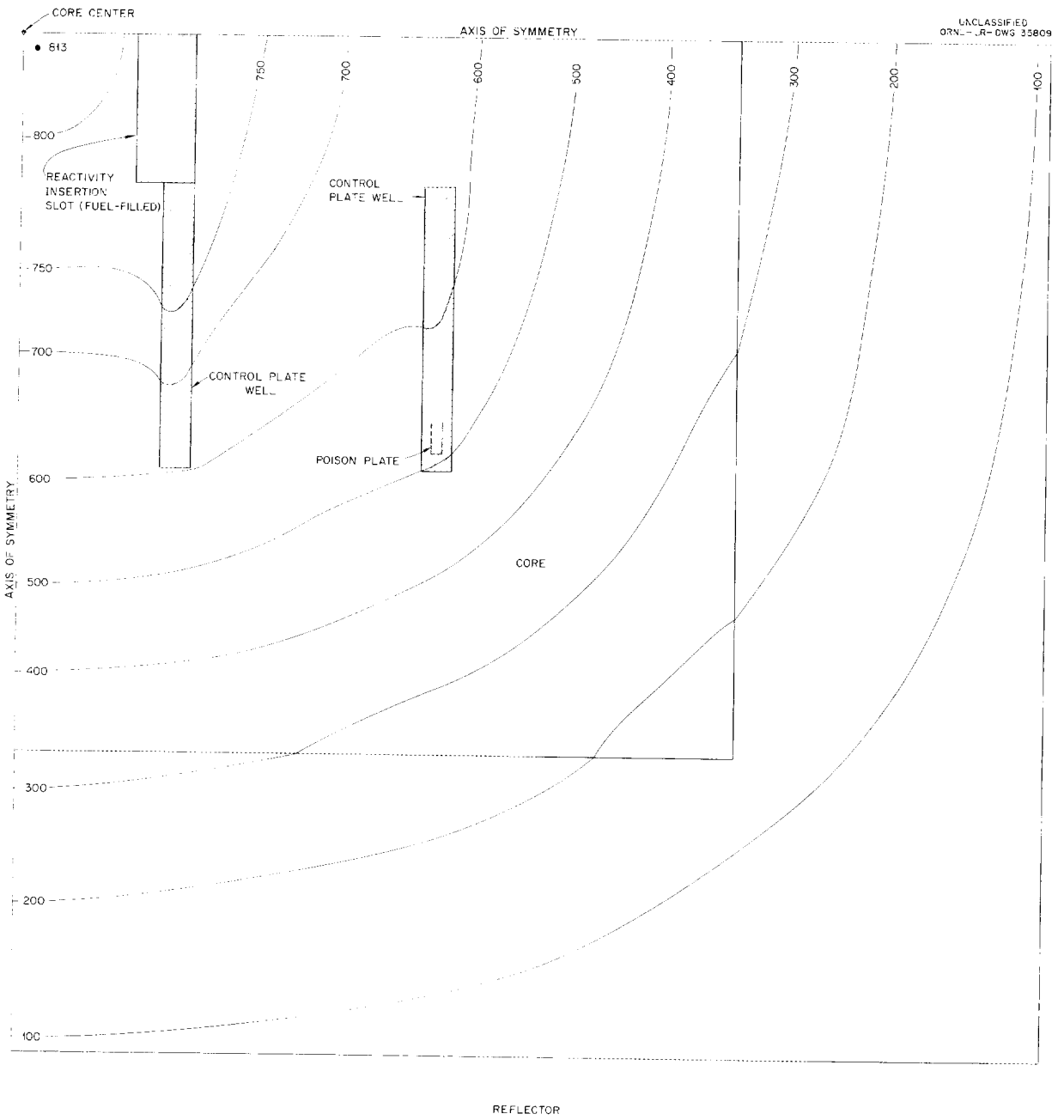

Fig. 2.1.6. Isoflux Curves for the Low Epithermal Flux in the X-Y Plane in One Quarter of the BSR-II Core: Control Plates Fully Withdrawn, Fuel in Reactivity Insertion Slots.

UNCLASSIFIED
2-01-058-0-494

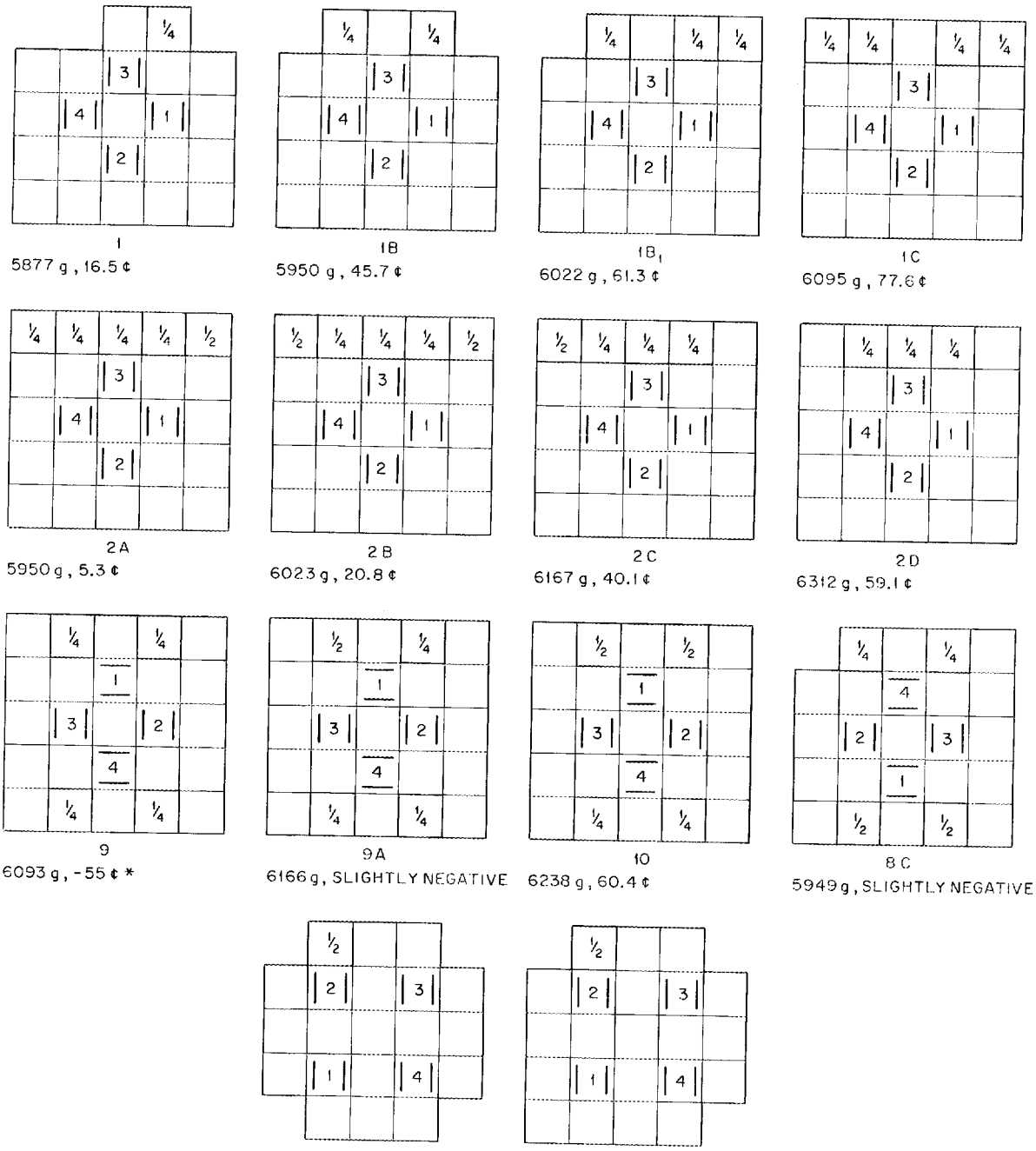

* VALUE DETERMINED BY PULSED-NEUTRON METHOD.
** THE CORNER ELEMENT WAS IN THE CORE ONLY WHILE THE ELECTROMAGNET AND DRIVE MOTOR WERE REMOVED FROM ROD NO. 3.

Fig. 2.1.7. BSR-II Core Loadings.

withdrawn to their 1-in. preinsertion stops. The extrapolated experimental critical mass is about 5.84 kg. The previously calculated critical mass for a 5 by 5 element core was 6.02 kg of U^{235}, a difference of 3% in mass and 80 cents in reactivity.

The other loadings shown in Fig. 2.1.7 permitted reactivity calibration of safety rods and a limited knowledge of element importance as a function of position. They also demonstrate the effectiveness of additional fuel as the mass was increased. The reactivities were obtained by inhour calibrations of the control rods, unless otherwise indicated, and were reproducible to ~1%. The loadings were restricted to an excess reactivity of <1.0 dollar. Flexibility of loading was restricted by the unavailability of three-quarter elements.

Other core loadings were assembled in order to achieve configurations suitable for use in the determination of the prompt-neutron lifetime by the pulsed-neutron technique. This measurement, needed to calculate the step and ramp rates of the reactivity insertion device, is reported in Sec 2.2. The data, together with the delayed neutron data of Keepin *et al.*,[4] was used to plot the inhour equation for the BSR-II shown in Fig. 2.1.8.

The reactivity worth of the shim-safety rods was determined by both the positive period inhour method and the pulsed-neutron method. Use of the inhour method was restricted to values of less than 1.00 dollar. Figure 2.1.9 shows the result of an attempt to evaluate the worth of a control rod and to determine the shape of the control-rod

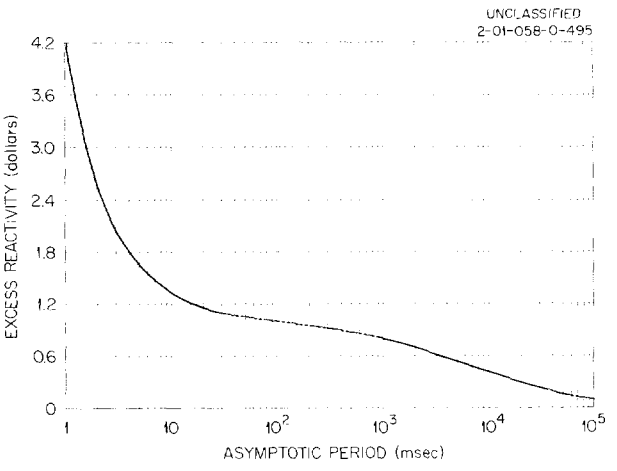

Fig. 2.1.8. Asymptotic Positive Period for the BSR-II as a Function of Excess Reactivity (Inhour Curve).

calibration curve when the rod is placed in core positions of such low importance that the total worth of the rod is less than the 1.00-dollar reactivity limit. The worth of the rod in a conventional position is included for comparison.

Since the use of the pulsed-neutron method on subcritical systems is not restricted by reactivity limits, reactivity worth measurements could be made to full-shutdown reactivity directly by this method. A series of measurements, restricted by the limited time available, gave data on shading and the reactivity worths shown in Table 2.1.1. As the table shows, the worth of the No. 1 rod for full travel was 2.50 dollars in loading No. 14A and 2.87 dollars in loading No. 14B. The worth of the full element placed in the corner next to rod No. 1 (which converts loading No. 14A to 14B) is 0.99 dollar when the rod is fully withdrawn and 0.62 dollar when the rod is at its lower limit. The change is the result of flux depression by the poison.

As noted above, a double-ended reactivity-insertion device will be used during the SPERT-I tests outlined below. High-speed (Fastax) motion pictures have been used to analyze the drop-time response of this device, and the results are plotted in Fig. 2.1.10. The curves show that the plate achieved a velocity of ~6 fps after 30 msec, and that the total time required to drop the full 12-in. stroke was ~175 msec.

The pulsed-neutron method was used to measure the reactivity worth of the reactivity insertion device, and the results are shown in Fig. 2.1.11. The reactor was brought critical with the fuel section of the device fully inserted, and then a series of measurements was made for various amounts of poison insertion. This information, coupled with the data on drop-time response, was used to determine the amount of inserted reactivity as a function of time after initiation of a proposed excursion. This data is plotted in Fig. 2.1.12, where it is seen that enough reactivity to give a 3-msec positive period can be inserted in ~100 msec, and a period of 1 msec can be achieved ~150 msec after initiation of the excursion.

SPERT-I Tests

As noted in the early portion of this report, the BSR-II is now at the SPERT-I Facility of the NRTS at Idaho Falls for extensive testing. The primary objective of the tests is to determine

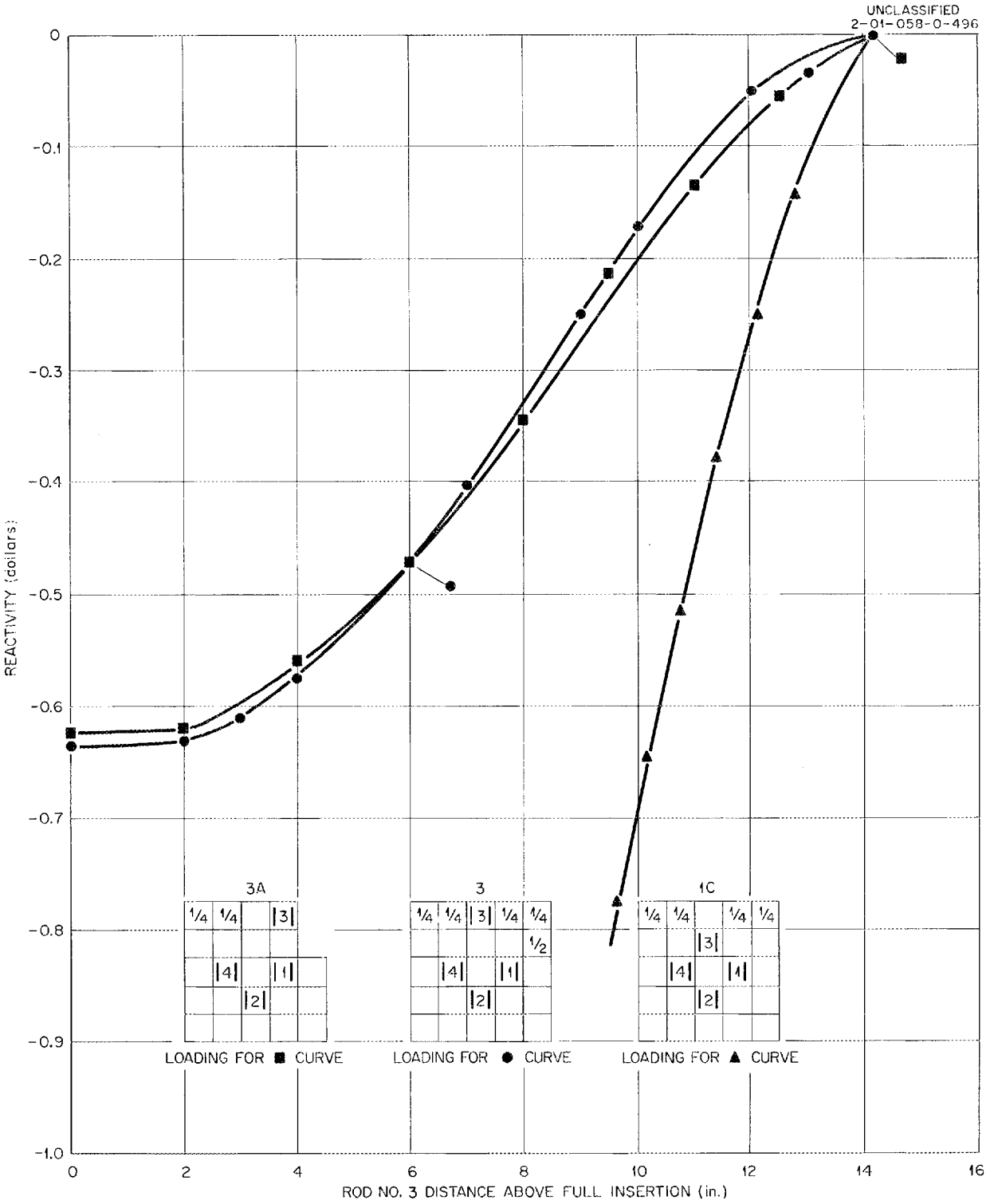

Fig. 2.1.9. Reactivity as a Function of Position of No. 3 Shim-Safety Rod for Three Loadings of the BSR-II Core. Reactivity values based on calibration of Rod No. 2 in Loading 1C.

Table 2.1.1. BSR-II Reactivities for Three Core Loadings* and Various Rod Positions

Distance Above Full Insertion** (in.)				Core Reactivity (dollars)	
Rod 1	Rod 2	Rod 3	Rod 4	Pulsed-Neutron Method	Inhour Calibration Method
			Loading 10		
UL	UL	11.42	UL		Critical
UL	12.00	11.42	UL	0.427	0.42
11.68	12.00	11.42	UL	0.934	0.92
UL	LL	11.42	UL	3.285	
LL	LL	11.42	UL	5.60	
			Loading 14A		
UL	UL	UL	UL		0.44
UL	UL	LL	UL	2.08	
LL	UL	LL	UL	4.58	
UL	UL	LL	LL	4.22	
LL	LL	LL	LL	7.78	
			Loading 14B		
UL	UL	UL	UL		1.43 (est)
UL	UL	LL	UL	1.09	
LL	UL	LL	UL	3.96	

*Core loadings are shown in Fig. 2.1.7.

**UL = upper limit; LL = lower limit.

whether the core, from the nature of its self-regulating characteristics, can be safely operated in an uncontained research reactor facility with sufficient potential excess reactivity to override the effects of xenon poisoning, fuel burnup, temperature coefficient and small beam tubes. A secondary objective will be to evaluate the performance of a typical control system for a pool-type reactor. For this purpose the control system which has been installed for the SPERT-I tests will be evaluated by using it to limit some of the proposed excursions. A final objective will be to provide data that can be compared with data previously obtained at the SPERT-I Facility for other cores, as a further aid in the interpretation of reactor excursions.

The current static tests on the BSR-II employ a 5 by 5 element core containing an excess reactivity of over 3.00 dollars. Control rods will be calibrated for this loading by the inhour method. The reactivity-insertion device will also be calibrated to the extent of the available excess. Void-coefficient measurements, using aluminum or magnesium as the void material, will be made to

obtain information about the effect on reactivity of steam-void formation, and the temperature coefficients of the core and reflector will be determined.

Following the static tests, thermocouples and pressure-sensing devices will be attached to the core. Power excursions of increasing severity will be induced by both linear ramp and step insertions of reactivity, with the power surge controlled either by standard ORNL reactor-control instruments or by the self-limiting traits of the core. An attempt will be made to schedule the degree of burst severity so that the maximum amount of information can be obtained before core damage occurs.

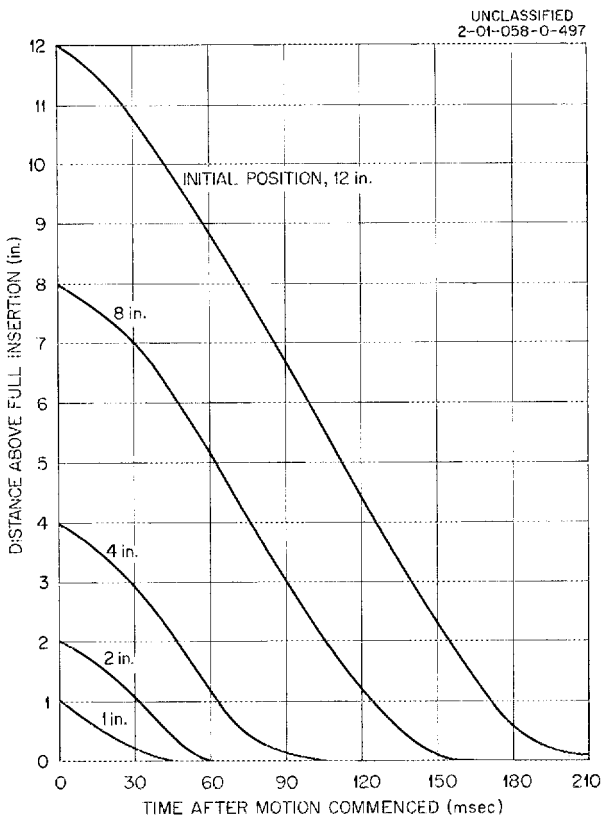

Fig. 2.1.10. Drop-Time Curves for the Double-Ended Reactivity-Insertion Device.

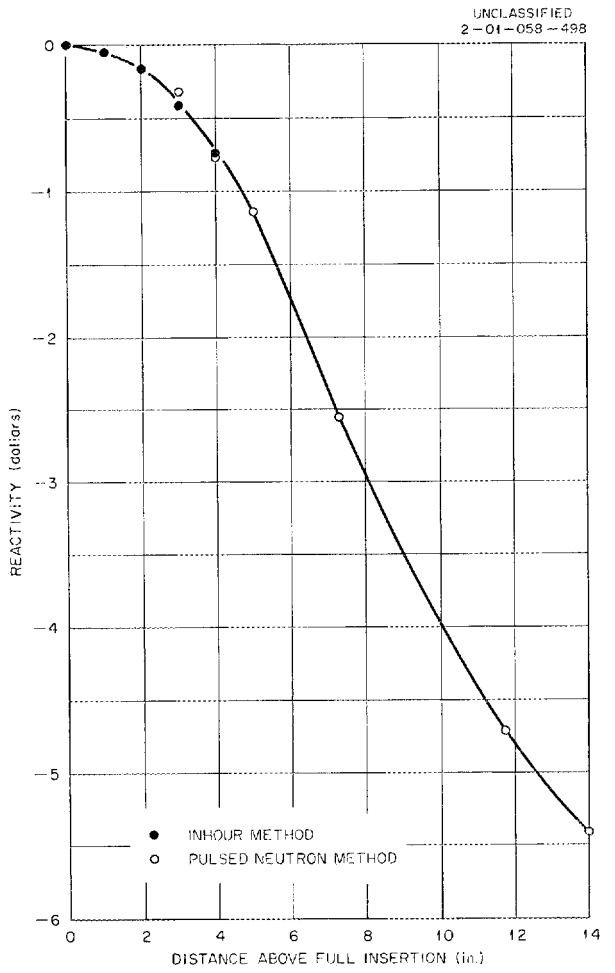

Fig. 2.1.11. Reactivity as a Function of the Vertical Position of the Reactivity-Insertion Device at the Center of the BSR-II.

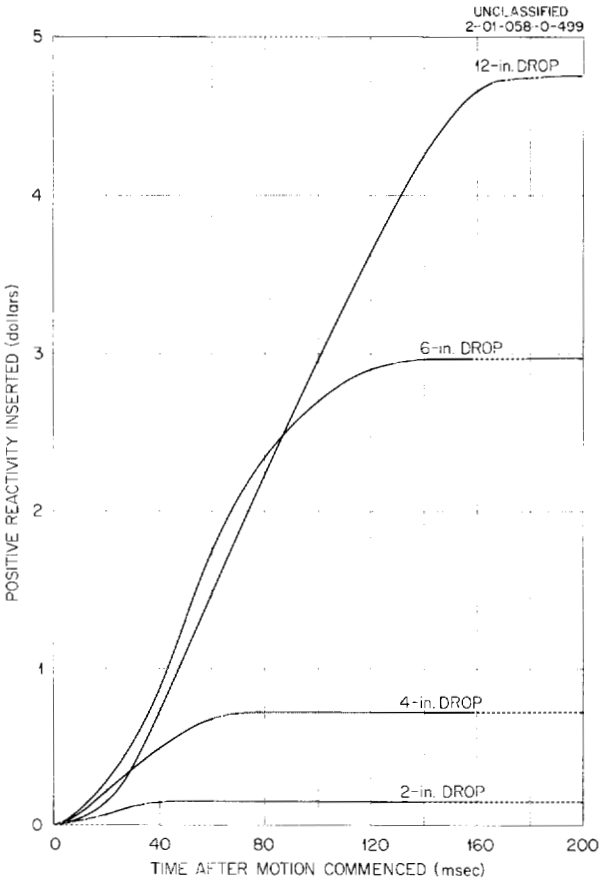

Fig. 2.1.12. Reactivity as a Function of Time After Start of Movement of the Reactivity-Insertion Device for Various Initial Positions (Inches from Fully Inserted Position).

2.2. MEASUREMENT OF THE RATIO OF THE PROMPT-NEUTRON GENERATION TIME TO THE EFFECTIVE DELAYED-NEUTRON FRACTION OF THE BSR-II

E. G. Silver K. M. Henry
G. deSaussure E. B. Johnson
R. Perez-Belles

A method for determining the ratio of the prompt-neutron generation time of a reactor to its effective delayed-neutron fraction (i.e., L/β_{eff}) consists in pulsing neutrons into the reactor, either at delayed critical or with a known amount of negative reactivity, and measuring the decay of the neutron density following the pulse. This technique was used recently to determine L/β_{eff} for the Bulk Shielding Reactor II (BSR-II) (see Sec 2.1). In the experiment short bursts of neutrons from the BSR-I impinged on the face of the BSR-II, and the decay of the neutron population in the BSR-II was observed after each burst.

Experimental Arrangement

A plan view of the experimental arrangement is shown in Fig. 2.2.1. Neutrons from the BSR-I were thermalized in the D_2O-filled aluminum tank adjacent to the core and then collimated through the long air-filled pipe coupling the tank with the BSR-II. A motor-driven, rotary-type chopper,[1] made of aluminum and filled with boron powder enriched to ~90% in B^{10}, was located 106 in. from the D_2O tank and 12 in. from the BSR-II. Three slits in the rotor permitted the passage of thermal neutrons into the south face of the BSR-II for approximately 10% of each of the two cycles per turn of the rotor. The rotor was directly driven by a reversible, shunt-wound, variable-speed d-c motor having a maximum speed of 1800 rpm. With this speed 60 neutron pulses per second were attainable; however, in this experiment only about 30 pulses per second were used.

An aluminum disk integral with the rotor carried two ferrous studs which furnished a time signal of known relationship to the rotor position as they passed a magnetic pickup. Both the motor-rotor assembly and the magnetic phase-signal pickup were enclosed in an aluminum housing, completely lined with boral except for the collimator entrance and exit. The entire assembly was pressurized with air for underwater operation.

The detector used to observe the neutron decay in the BSR-II consisted of a 1-in.-dia by 3-mm-thick $Li^6I(Eu)$ scintillation crystal mounted on an RCA 6655 photomultiplier tube. The detector and its preamplifier were housed in a watertight container whose forward portion was made of Lucite. The entire assembly was suspended from a tube and positioned at the center of one of the lateral faces of the BSR-II.

[1] The chopper was designed by F. R. Duncan of the Instrumentation and Controls Division.

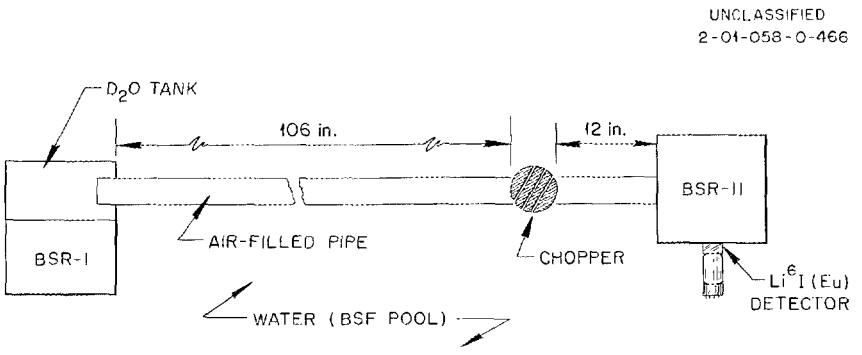

Fig. 2.2.1. Plan View of Experimental Arrangement for the Measurement of L/β_{eff} in the BSR-II.

The analysis equipment was primarily an 18-channel time analyzer described by Glass[2] and modified[3] as follows: A signal from the magnetic pickup initiated a counting cycle, which began with an adjustable waiting time of n time-base pulses, after which each of the 18 counting channels was in turn gated open for the duration of one time-base pulse. The circuit then was quiescent until the next signal from the magnetic pickup was received. The time-base frequency, u, was arbitrarily determinable except that it had to be such that $(n + 18)/u$ was less than $1/U$, where U was the neutron burst repetition frequency.

Theory of the Experiment

The interpretation of the experiment was based on the inhour equation. In its familiar form,[4] the inhour equation is written as

$$\rho = \frac{L}{Tk_{\text{eff}}} + \sum_i \frac{\beta_i \gamma_i}{1 + \lambda_i T} . \qquad (1)$$

Dividing this equation by $\sum_i \beta_i \gamma_i$, where β_i is the delayed neutron fraction of the ith decay group and γ_i is the relative probability for a delayed neutron to yield a further fission as compared to a prompt neutron, gives

$$\frac{\rho}{\beta\gamma} = \frac{L}{\beta\gamma}\frac{1}{Tk_{\text{eff}}} + \frac{1}{\beta\gamma}\sum_i \frac{\beta_i \gamma_i}{1 + \lambda_i T} . \qquad (2)$$

In theory, if a small change in reactivity is made on a critical system there will be an asymptotic period, T_r, which is given to very good approximation by the second term on the right-hand side of (2). This term depends only on the relative delay fraction $\beta_i \gamma_i/\beta\gamma$ and is thus independent of the absolute value of $\beta\gamma$. In practice, a series of measurements is made with positive periods $(T_r)_j$ and additivity is assumed for obtaining:

$$\frac{\rho}{\beta\gamma} = \sum_j \left[\frac{1}{\beta\gamma} \sum_i \frac{\beta_i \gamma_i}{1 + \lambda_i (T_r)_j} \right]$$

$$= \frac{1}{\beta\gamma} \sum_i \frac{\beta_i \gamma_i}{1 + \lambda_i T_r} . \qquad (3)$$

Then the further assumption is made that the rod displacement corresponding to the final positive reactivity can also insert the same amount of negative reactivity, starting from a critical core. It is assumed that the multiplication can be changed by using other control rods or making other core changes in such a way as not to alter the measured calibration. Thus a measurement of T_r yields a value of $\rho/\beta\gamma$.

By using a short burst of neutrons, the decay of flux at times small compared to the delayed neutron periods may be observed, and this decay is given by the limiting value of (2) for $T \to 0$, designated as T_p. Thus,

$$\frac{\rho}{\beta\gamma} = \frac{L}{\beta\gamma T_p k_{\text{eff}}} + 1 ,$$

or

$$\left(\frac{\rho}{\beta\gamma} - 1 \right) = \frac{L}{\beta\gamma T_p k_{\text{eff}}} . \qquad (4)$$

If the reactor is close to critical, k_{eff} is almost unity, and (4) can be written simply as

$$\left(\frac{\rho}{\beta\gamma} - 1 \right) = \frac{L}{\beta\gamma} \cdot \frac{1}{T_p} . \qquad (4a)$$

Since the value of $\rho/\beta\gamma$ is known from the measurements of $(T_r)_j$, a measurement of T_p, the period measured by the pulsed method, immediately gives a value of $L/\beta\gamma$ or L/β_{eff}, which is the desired quantity.

Conversely, once $L/\beta\gamma$ is known, any other reactivity may be measured by measuring T_p in the new configuration and solving for $\rho/\beta\gamma$ in (4a).

Experimental Procedure and Results

The method for obtaining the decay constants consisted first in observing the counts per channel without any delay between the arrival of the timing

---

[2] F. Glass, *Instrumentation and Controls Ann. Prog. Rep. July 1, 1957*, ORNL-2480, p 22.

[3] The modifications to the time-base analyzer were designed by F. Glass and H. Wilson of the Instrumentation and Controls Division.

[4] S. Glasstone and M. C. Edlund, *The Elements of Nuclear Reactor Theory*, p 301, Van Nostrand, New York, 1952.

pulse and the start of counting. In this fashion the buildup of flux during the pulse and the subsequent establishment of the decay curve could be observed, and the proper delay for optimum observation of the decay chosen. Figure 2.2.2 shows a typical curve of this type. The upper curve is the data that was actually recorded, and the lower curve represents the data after the flat background was subtracted. It will be noted that the decay curve becomes a clean exponential very soon after the peak of the neutron flux intensity is passed.

After a proper delay, 3 to 4 million counts were then obtained for each case, and the results analyzed by the method of Cornell[5] into the sum of a constant background and a single decay exponential.

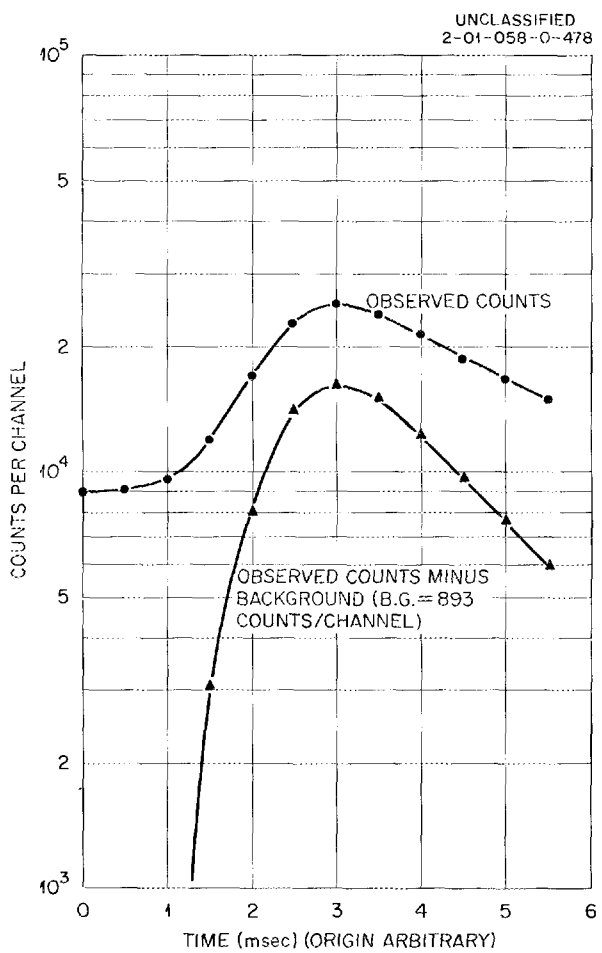

Fig. 2.2.2. Thermal-Neutron Flux Pulse Shape Measured in the BSR-II at a Reactivity of −0.548 dollar.

The value of L/β_{eff} was determined by inserting three reactivities, ranging from $-\frac{1}{2}$ to $-\frac{3}{2}$ dollars, into the BSR-II by means of control rods calibrated with positive periods using the inhour method. The decay curves obtained are shown as the top three curves of Fig. 2.2.3. The corresponding decay constants and L/β_{eff} values are given in Table 2.2.1.

The measured value of L/β_{eff} was then used to obtain the reactivity worth of control-rod configurations having more negative reactivity than

[5] R. G. Cornell, *A New Estimation Procedure for Linear Combinations of Exponentials*, ORNL-2120 (1956).

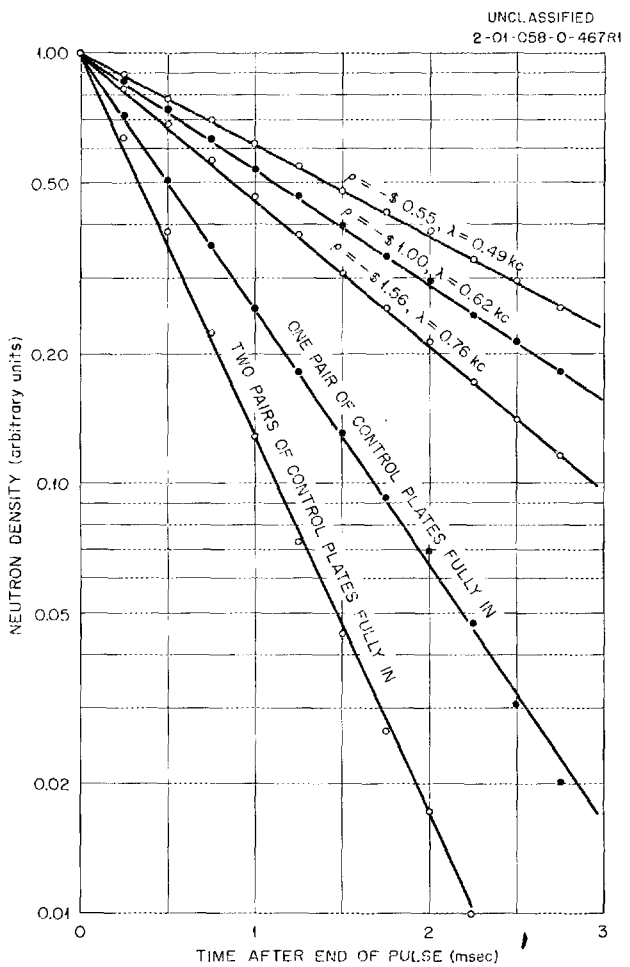

Fig. 2.2.3. Decay of the Thermal-Neutron Density in the BSR-II as a Function of Time After End of Pulse, for Various Subcritical Conditions. In each curve the flat background has been subtracted.

Table 2.2.1. Measurement of L/β_{eff} for BSR-II*

ρ/β_{eff}, Reactivity Measured by Inhour Method (dollars)	Decay Constant (kc)	L/β_{eff} (msec)
-0.55 ± 0.02	0.480 ± 0.010	3.17 ± 0.16
-1.00 ± 0.04	0.618 ± 0.012	3.23 ± 0.16
-1.56 ± 0.07	0.783 ± 0.016	3.27 ± 0.16
	Avg:	3.2 ± 0.2

*The data above were obtained over a limited time interval due to scheduling of the BSR-II; therefore, a complete analysis of possible biasing factors was not possible. In particular, a small dependence of L/β_{eff} or ρ/β_{eff} was not ruled out, and hence the uncertainty given for the average of L/β_{eff} is that due to each separate measurement.

could be measured by the inhour positive-period method. The fuel loading configuration of the BSR-II used in all the experimental work reported here is shown in Fig. 2.2.4, as are the locations of four pairs of control plates used in the BSR-II core. The worths of one and two pairs of these plates, marked (1) and (2) in Fig. 2.2.4, were measured by the pulsed-neutron method. The resulting decay curves are shown as the two lowest curves in Fig. 2.2.3. The reactivity worth of No. 2 control plate pair inserted ($\lambda = 1.36 \pm 0.03$ kc) was -3.3 ± 0.2 dollars, and that of Nos. 1 and 2 control plate pairs inserted ($\lambda = 2.11 \pm 0.04$ kc) was -5.6 ± 0.3 dollars. Comparison of these results shows that shadowing effects occur when two pairs of plates are used. The usefulness of the pulsed-neutron method for this type of measurement is therefore apparent.

UNCLASSIFIED
2-01-058-0-477

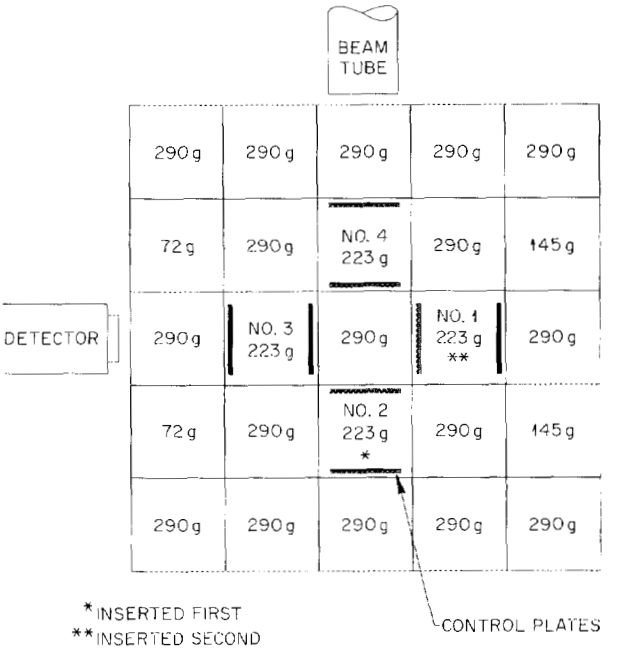

Fig. 2.2.4. BSR-II Core Configurations for Pulsed-Neutron Measurements.

Summary and Future Plans

By use of the BSR-I as a radiation source, it has been possible to make consistent measurements of the ratio of the prompt neutron generation time to the effective delayed neutron fraction in the BSR-II. The same experimental technique was used to measure shutdown multiplication constants from which control-rod worths were obtained for configurations not readily measurable by other means. Future work is planned to investigate these parameters for BSR-I-type cores, and also to extend the application of this technique to the exploration of reactor configurations involving multidollar subcritical reactivities.

2.3. THE TOWER SHIELDING REACTOR II: STATUS REPORT

L. B. Holland J. L. Hull
V. R. Cain J. Lewin
D. R. Ward

The design of the Tower Shielding Reactor II (TSR-II), the spherically symmetric reactor that will be operated at the Tower Shielding Facility, has been presented previously.[1,2] A few modifications have been necessary as a result of critical experiments and component development work, and the present discussion of the design is limited to a description of these changes. The critical experiments and development work that dictated the modifications are also presented, with a discussion of the status of the reactor and a description of an associated "beam" shield.

Mechanical Design[3]

The latest design of the TSR-II is shown in Fig. 2.3.1. The major changes have been made in the spherical internal reflector region. The entire control mechanism assembly is now operated in a 17-in.-dia aluminum sphere that almost completely fills the internal reflector region, and much of the water inside the sphere itself is displaced with aluminum. This sphere is shown in the left of Fig. 2.3.2 and the aluminum within the sphere is shown at the right. Much of the aluminum consists of plugs attached to the framework. The addition of this extra aluminum was necessary to increase the reactivity of the reactor after the first set of critical experiments (see below) showed that the water-reflected fuel annulus alone was subcritical. The reactivity was further increased by loading the aluminum cover plates that form the 17-in.-dia sphere with 220 g of U^{235}. (The fuel annulus contains 8.1 kg of U^{235}.)

The spherical housing for the control mechanism was also required for another purpose. It is used to restrict the water flow through the internal reflector region to the small annulus between the fuel and the sphere. This eliminates the possibility of dangerous void formations within the reactor, since any voids which are formed in the annulus will be too small to cause severe reactivity effects.

An exploded view of the control mechanism, its housing, and the six control rods[4] is shown in Fig. 2.3.3. Except for the top rod, which is the regulating rod, each rod is keyed so that it can move over four aluminum plugs without making contact.

Another design change consisted in the substitution of a $\frac{3}{4}$-in.-dia fission chamber for the $2\frac{1}{4}$-in.-dia chamber previously included in the lead shot and water region above the core. This will minimize the leakage of gamma rays through this region.

Status of the Reactor

All the major components of the reactor have been fabricated and shop assembly is under way. In Fig. 2.3.4 a technician is assembling the annular fuel elements on the central cylinder. In Fig. 2.3.5 all the elements are in place and an aluminum baffle plate (see discussion of flow distribution studies below) covers the upper half of the elements. Figure 2.3.6 shows the ionization guide assembly being lowered into the central cylinder, which has already been mounted in the reactor tank. The tank is shown suspended from the reactor support platform.

The water cooling system and reactor control system have been installed and tested insofar as they can be without the reactor. The water cooling system is shown in Fig. 2.3.7. At the left of the photograph are the air-blast water coolers, and immediately to the right is the pumphouse, which is partially obscured by the building housing the emergency pump system. The 6-in. hoses that carry water to the reactor can be seen suspended from the towers.

---

[1] C. E. Clifford and L. B. Holland, *Neutron Phys. Ann. Prog. Rep. Sept. 1, 1958*, ORNL-2609, p 16.

[2] L. B. Holland and C. E. Clifford, *Description of the Tower Shielding Reactor II and Proposed Preliminary Experiments*, ORNL-2747 (1959).

[3] The mechanical design of the reactor was done by members of a design group in the Engineering and Mechanical Division, in particular by F. L. Hannon under the supervision of C. W. Angel.

[4] The term "control rod" is used for all references to a neutron-absorbing device in the TSR-II since it has been almost universally used in this manner. In the case of the TSR-II, each control rod consists of dished, hermetically sealed plates of stainless steel filled with boron carbide.

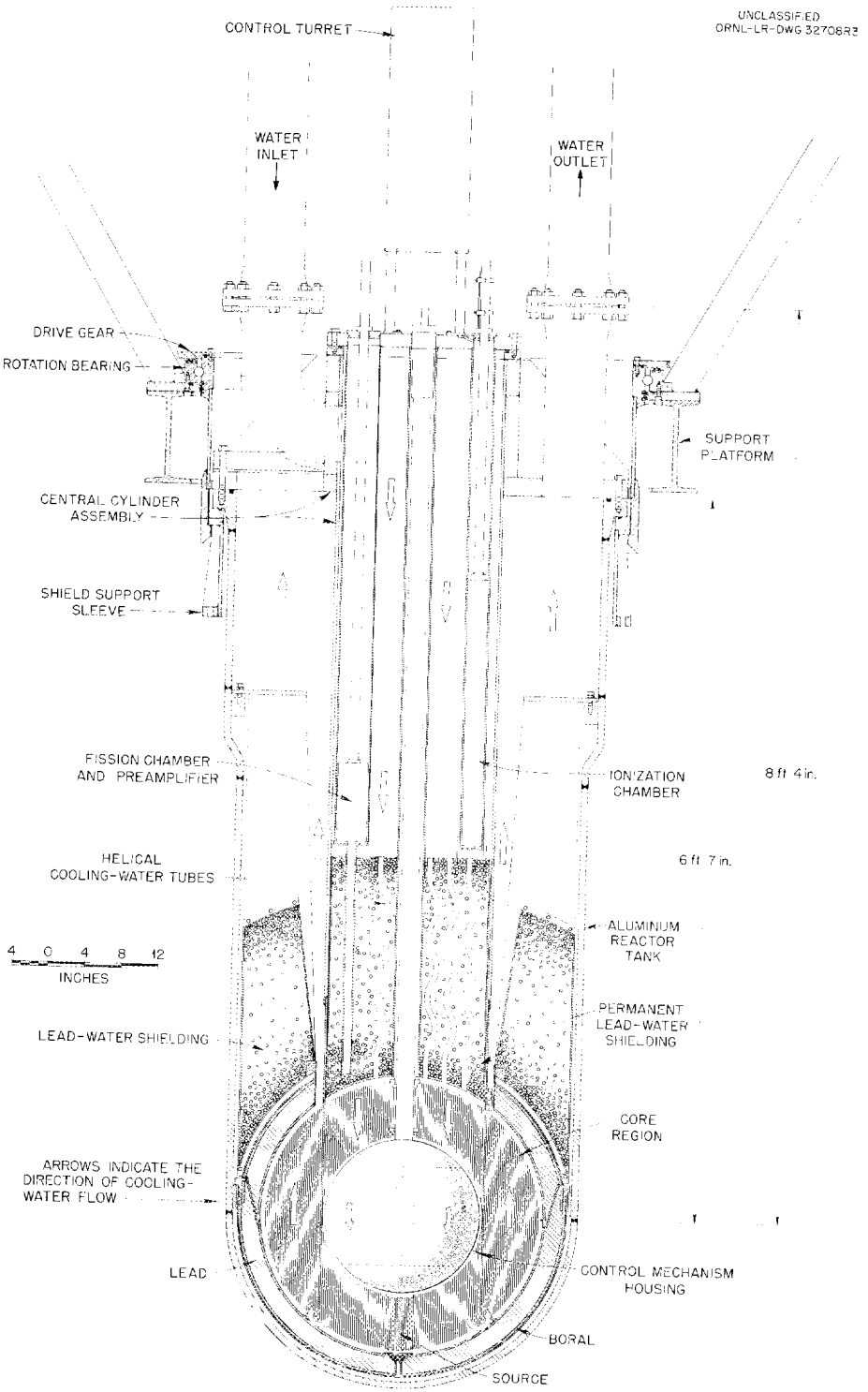

Fig. 2.3.1. Tower Shielding Reactor II Design (Vertical Section).

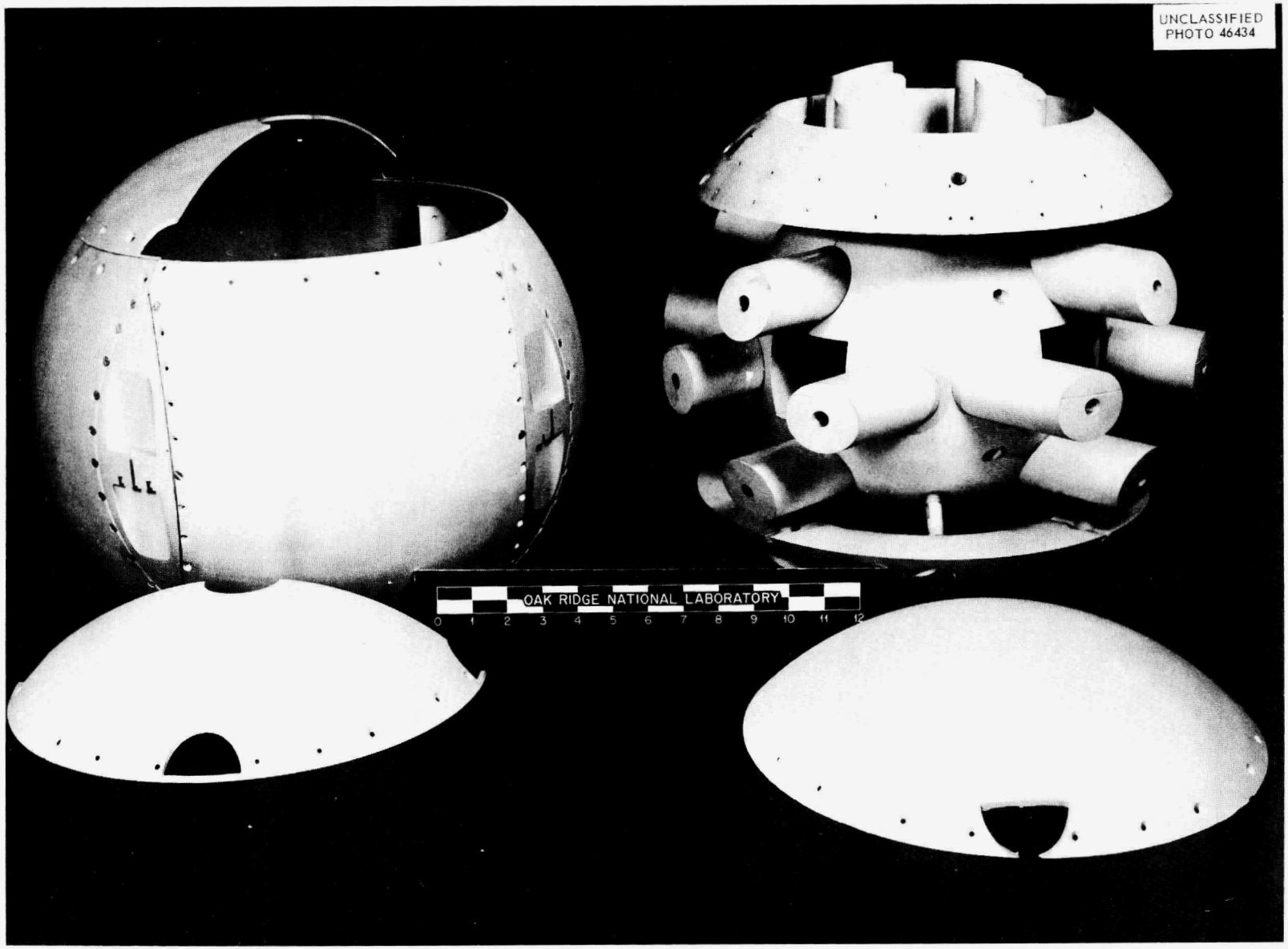

Fig. 2.3.2. Covers and Support Structure for TSR-II Control Mechanism.

UNCLASSIFIED
2-01-060-75

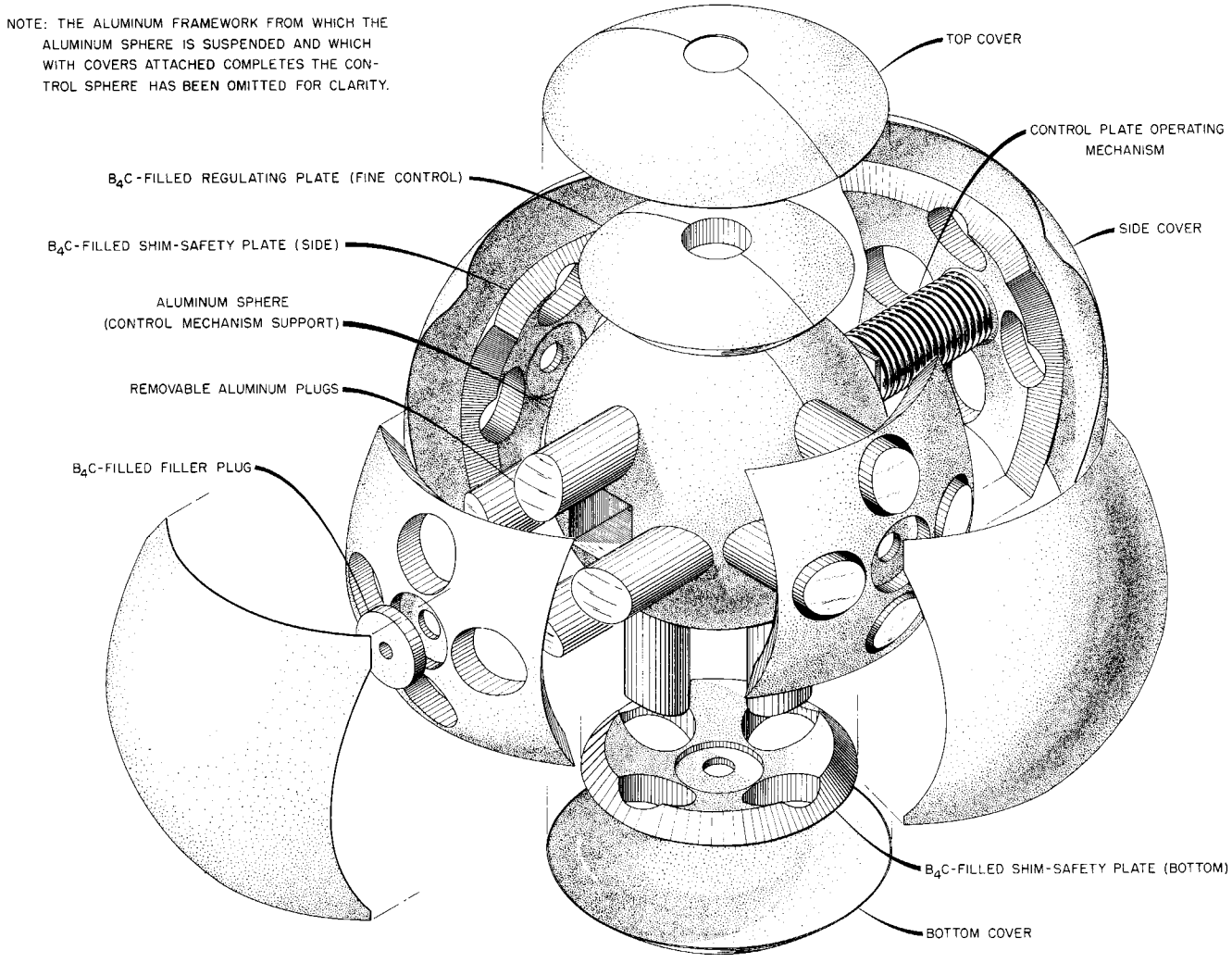

Fig. 2.3.3. Exploded View of TSR-II Control Mechanism and Housing.

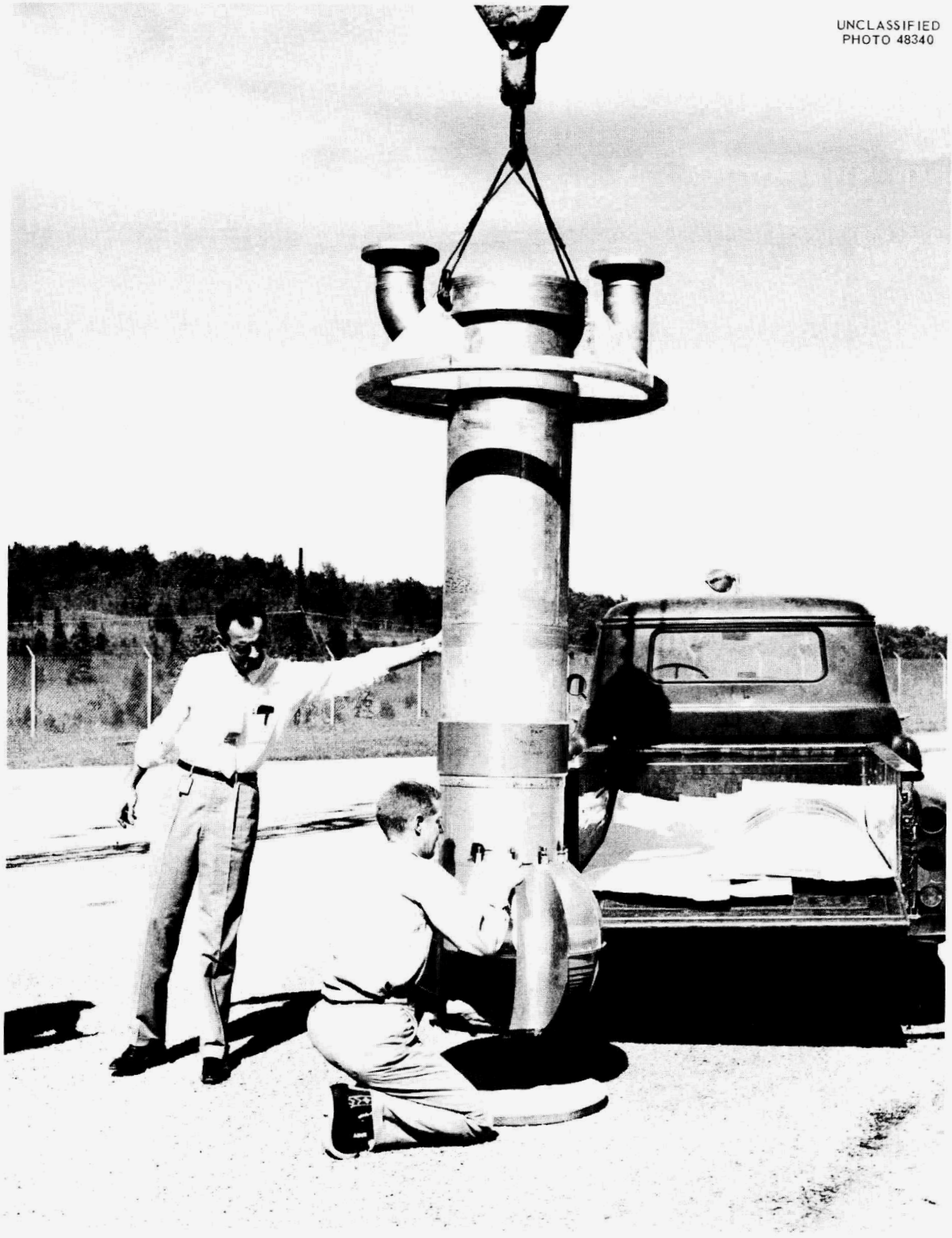

Fig. 2.3.4. Mounting of TSR-II Annular Elements on Central Cylinder.

Fig. 2.3.5. TSR-II Annular Elements Mounted on Central Cylinder. Upper section of elements covered with baffle plate.

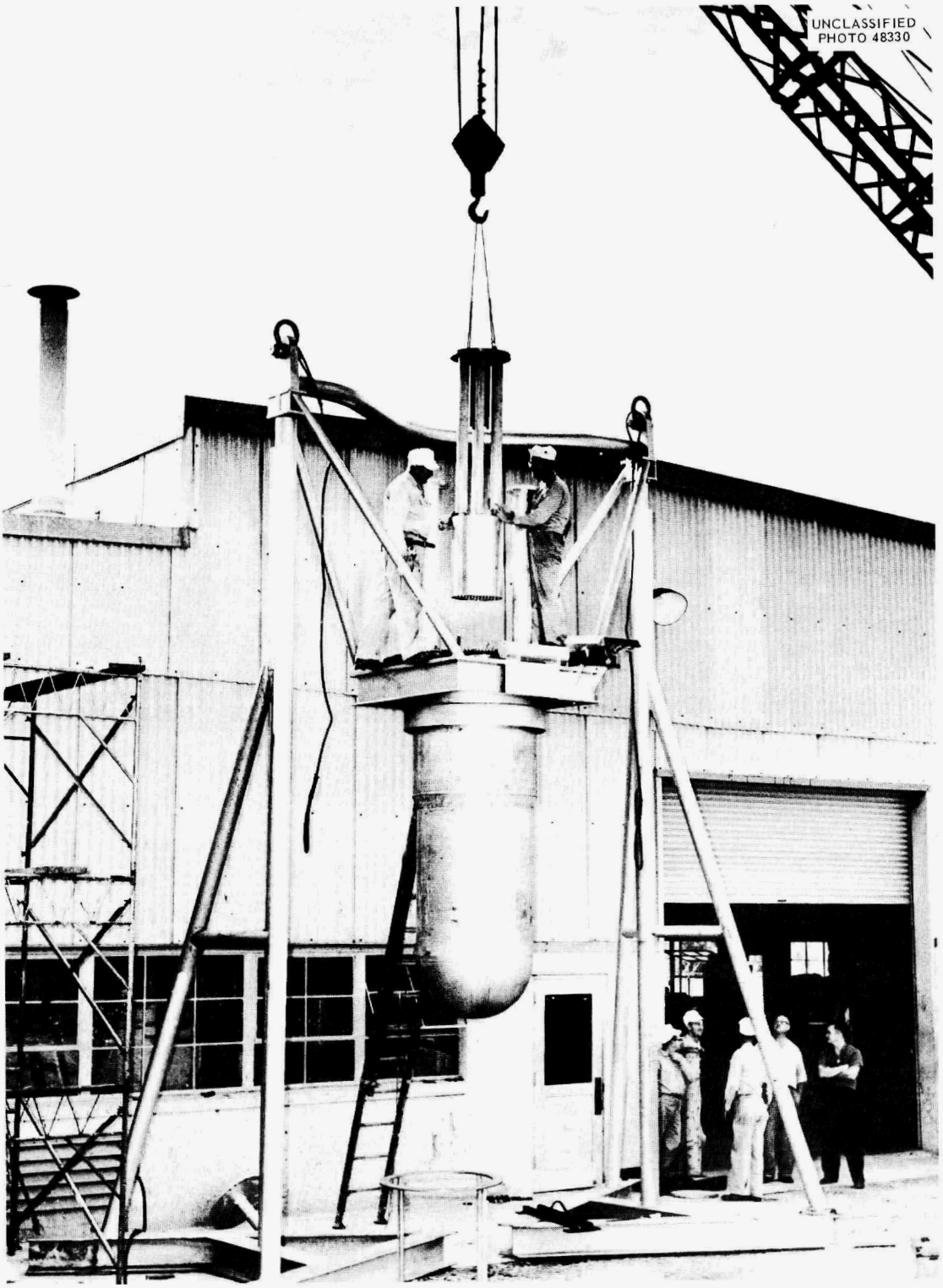

Fig. 2.3.6. Insertion of Ionization Chamber Guide Assembly into Central Cylinder of TSR-II.

Fig. 2.3.7. TSR-II Water-Cooling System.

The control panel for the reactor and water system is shown in Fig. 2.3.8. The graphic panel for the water system is to the left of center in the photograph.

Permission has been requested from[2] and granted by the AEC to operate the TSR-II at powers up to 100 kw so that its nuclear characteristics can be determined experimentally and the neutron and gamma-ray leakage spectra from the core can be measured. Following these tests, a report requesting permission to operate the TSR-II at its full 5-Mw design power will be prepared.

Critical Experiments

Two sets of critical experiments have been performed with the TSR-II fuel elements at the ORNL Critical Experiments Facility.[5] In the first set, only the fuel elements were used, with water as the moderator and the reflector; in the second set, the reactor core was completely assembled with the control mechanism interior to the core and the lead-boral shield outside the core. The control mechanism, which nearly fills the internal reflector, was modified after each set of experiments.

In the first set of experiments it was discovered that the water-reflected fuel annulus was subcritical. In order to make the annulus critical, aluminum was used to displace some of the water in the internal region. It was then possible to obtain a rough estimate of control plate worth and to measure the temperature coefficient of reactivity.

[5]These experiments were performed by members of the Critical Experiments Facility group, in particular by D. F. Cronin, J. K. Fox, and L. W. Gilley.

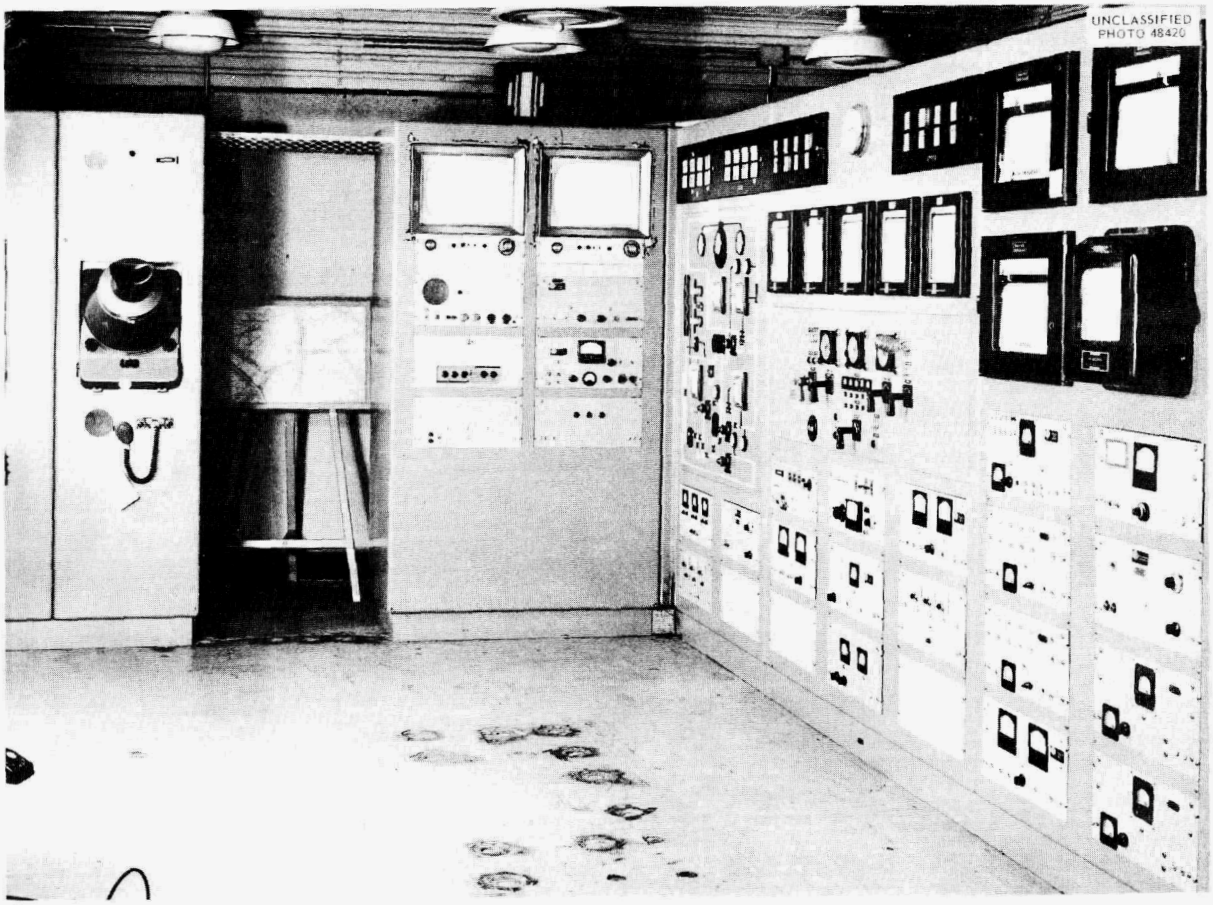

Fig. 2.3.8. TSR-II Control Panel for Reactor and Cooling System.

The experimentally determined temperature coefficient of reactivity for the water-reflected fuel elements is compared with the calculated value in Fig. 2.3.9. It was after this set of experiments that it was decided to redesign the control mechanism housing as shown in Fig. 2.3.3 so that reactivity could be added to the reactor and any hazard that would arise from a sudden displacement of water in the internal region with air could be eliminated.

When the redesigned control system had been fabricated, a second set of critical experiments was performed with the complete core assembly. In these experiments it was discovered that the additional excess realized by displacing water in the internal region with aluminum was offset by the boron in the control rods and the lead-boral shield surrounding the fuel annulus. Therefore, the reactor was again subcritical.

In order to obtain sufficient excess reactivity to perform some calibration experiments, fuel-bearing plates were placed on the outside of the 17-in.-dia aluminum sphere housing the control mechanism. This was so successful that the 17-in.-dia aluminum shell was refabricated from uranium-loaded aluminum as discussed above. (This new shell was not available for the critical experiments, however.)

The critical experiments with the assembled core included the calibration of the regulating rod by the inhour method and measurements of the shim-safety-rod worth by the rod-drop technique. The results of the rod-drop measurements, which were quite consistent for a number of measurements and for different chamber locations, showed that full insertion of all of the rods gave a reactivity reduction of 4.25 dollars. A comparison of the shim-rod worth vs the regulating-rod worth over a limited range of the shim-rod travel indicates that the shapes of the curves are similar. Based on the experimentally determined information, the reactivity worth of all shim-safety rods is compared with the calculated worth in Fig. 2.3.10. The same experimental curve can be used to denote the regulating-rod worth, by reduction of reactivity values by a factor of 10.

The series of experiments with the shim-safety rods yielded the following additional information:

1. The reactivity controlled by the motion of boron-filled rods and that controlled by the motion of cadmium-filled rods were approximately equal. (Both are black to thermal neutrons.)

2. Displacement of water with the 20 aluminum plugs extending through the control rods added an excess of approximately 0.5% $\Delta k/k$. Air-filled plugs added very little more reactivity.

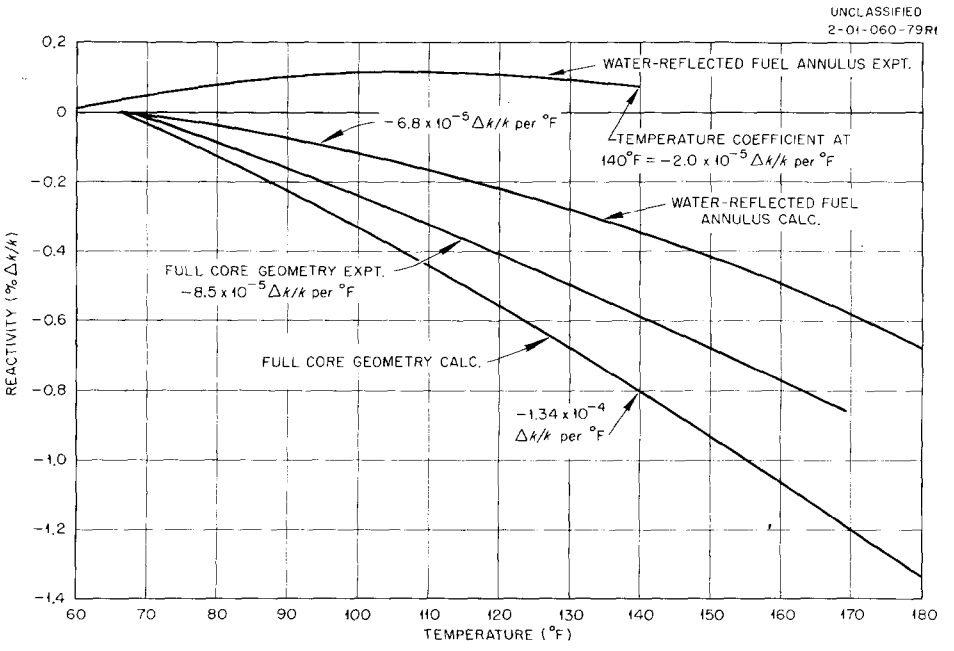

Fig. 2.3.9. Reactivity of the TSR-II Fuel Annulus with Different Reflector Materials as a Function of Bulk Water Temperature (Calculation and Experiment).

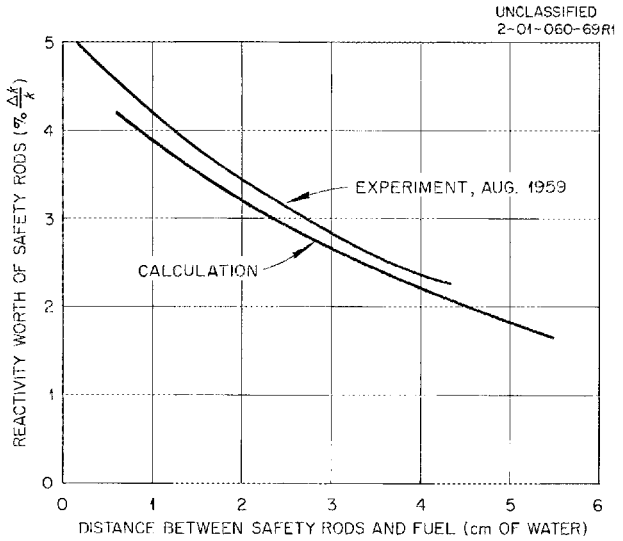

Fig. 2.3.10. Reactivity Worth of the TSR-II Safety Rods as a Function of Distance from the Fuel Region (Calculation and Experiment).

3. Removing the aluminum plugs and filling the holes in the rods with boron reduced the reactivity of the reactor by 0.15% $\Delta k/k$ but did not measurably change the reactivity controlled by motion of the control rods.

4. The worth of all the shim-safety rods in their fully withdrawn position was 2.25% $\Delta k/k$.

In one critical experiment it was found that the lead-boral shield reduces the reactivity by approximately 0.9% $\Delta k/k$.

The bulk temperature coefficient of reactivity was measured and an excess of 0.77% $\Delta k/k$ was required to compensate for a temperature rise from 67 to 160°F (see Fig. 2.3.9). From this experiment the temperature coefficient of reactivity at 140°F, which will be the mean core temperature at 5-Mw operation, was found to be -8.5×10^{-5} $\Delta k/k$. This is to be compared with a calculated value of -1.34×10^{-4} $\Delta k/k$ per °F.

Power Distribution and Heat Flux in the Fuel

The results of a Cornwash[6] calculation of the distribution of neutrons born in the core during 5-Mw operation have been presented previously.[1] This information has been used to determine the power distribution for each fuel plate. Results for several plates in a central fuel element are shown in Fig. 2.3.11, and results for plates in an annular fuel element are shown in Fig. 2.3.12. An integration over a fuel plate gave the total power generated in the plate. The total power generated in each fuel plate of a central element is shown in Fig. 2.3.13 and that in each plate of an annular element in Fig. 2.3.14. The maximum heat flux at 5 Mw is 41,200 $Btu \cdot hr^{-1} \cdot ft^{-2}$; the average heat flux is 26,000 $Btu \cdot hr^{-1} \cdot ft^{-2}$. (Since heat is removed from both sides of each fuel plate, the numerical value of the heat flux at a point on a surface is just half the value of the power generation.)

These calculations of the power generation were performed before it was decided to add fuel on the control-mechanism housing. This may change the source distribution on which the calculations were based. The distribution will be determined experimentally; if necessary, recalculations will be made.

Heat-Transfer and Flow-Distribution Studies

The development work required to properly distribute the cooling water flow in all fuel channels of the TSR-II was divided into separate studies, one for each of three fuel regions: upper central, lower central, and annular. Each problem was attacked in a different manner. (All three of the fuel regions can be seen in Fig. 2.3.1.)

Efforts were first directed toward obtaining the proper flow distribution in the annular fuel elements. The first step was to determine the minimum flow required to keep the water below the saturation temperature in each channel for different pressures in the core. From the results of these calculations, which are shown as dashed lines in Fig. 2.3.15, it became apparent that a flow of 1000 gpm would not be sufficient unless it could be shown that laminar cooling of the outer channels could be permitted. If laminar flow could be used and the pressure in the core maintained above 10 psig, a flow much lower than 1000 gpm could be used.

---

[6]The Cornwash code is the Corn Pone code (see Sec 6.8) modified so that the Goertzel-Selengut approximation and cross sections from the Eyewash code are used. The Eyewash code is described by J. D. Alexander and N. D. Given, *A Machine Multigroup Calculation: The Eyewash Program for Univac*, ORNL-1925 (1955).

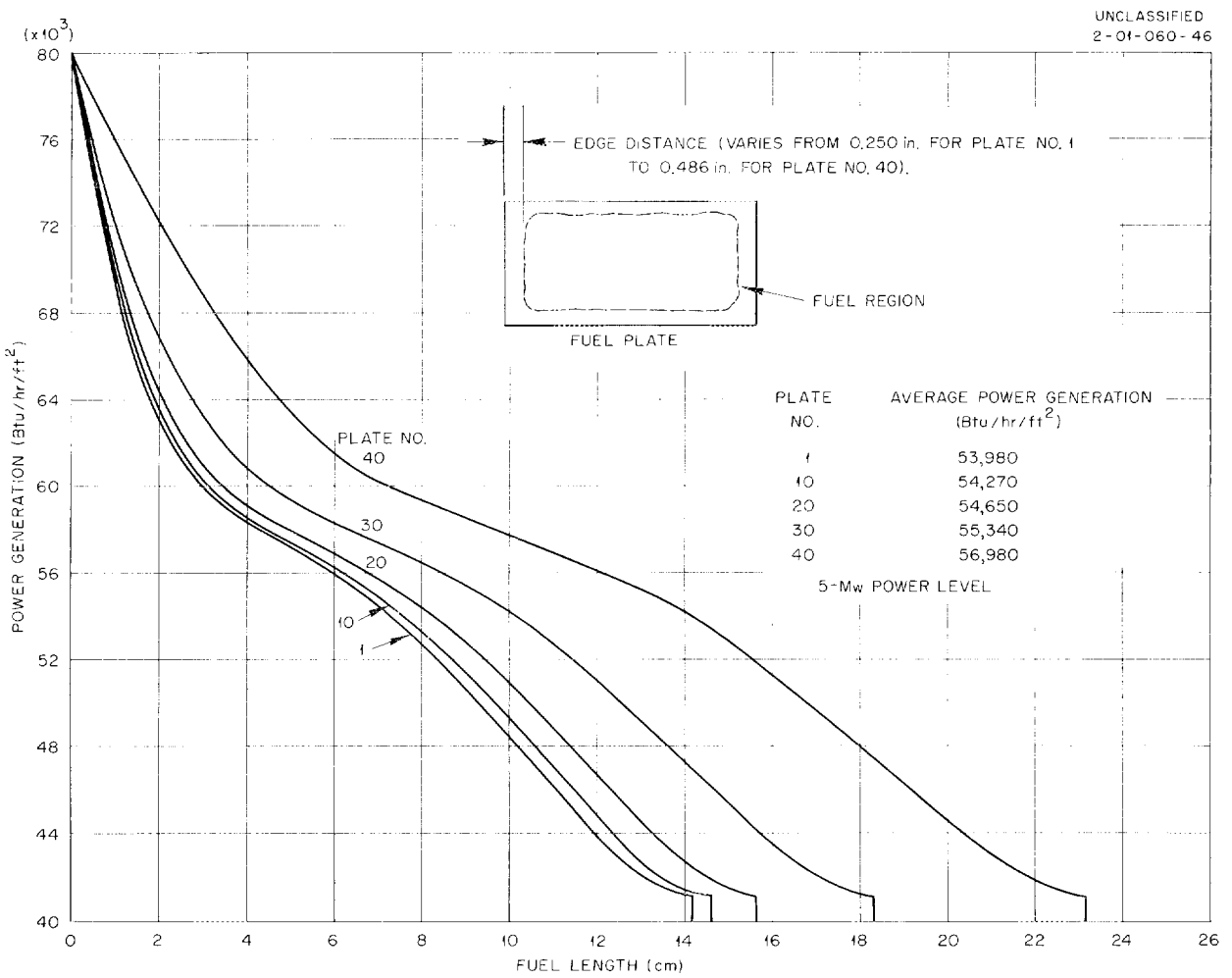

Fig. 2.3.11. Power Generation in the Fuel Plates of a TSR-II Central Element as a Function of Distance from the Inside Edge of the Fuel.

An experiment[7] performed to determine the friction factor vs Reynolds number for a typical flow channel in an annular element showed a smooth transition from laminar to turbulent flow; therefore, it will be possible to use transitional flow to cool the annular elements. Final calculations of the heat transfer from the annular fuel elements under a 30-psi head and optimized flow distribution indicate that, even with single-pass flow, less than 600 gpm is needed to keep the water from exceeding the saturation temperature (see Fig. 2.3.15). Since the proposed flow rate is 1000 gpm rather than 600 gpm, no allowance was made in the calculation for hot-channel factors. A complete summary of these calculations for laminar, transitional, and turbulent flow has been reported by Lewin.[8]

As an aid in the development of a baffle for the annular elements, a plastic model of an annular element was fabricated with flat rather than curved plates (Fig. 2.3.16). Flow measurements were made by injecting a dye into the inlet line and then photographing the dye as it moved through the cooling passages. The actual baffle plate is

[7] This experiment was performed by W. R. Gambill of the Engineering Research Group of the Reactor Projects Division.

[8] J. Lewin, *TSR-II Second Pass Heat Transfer*, ORNL CF-59-1-111 (1959).

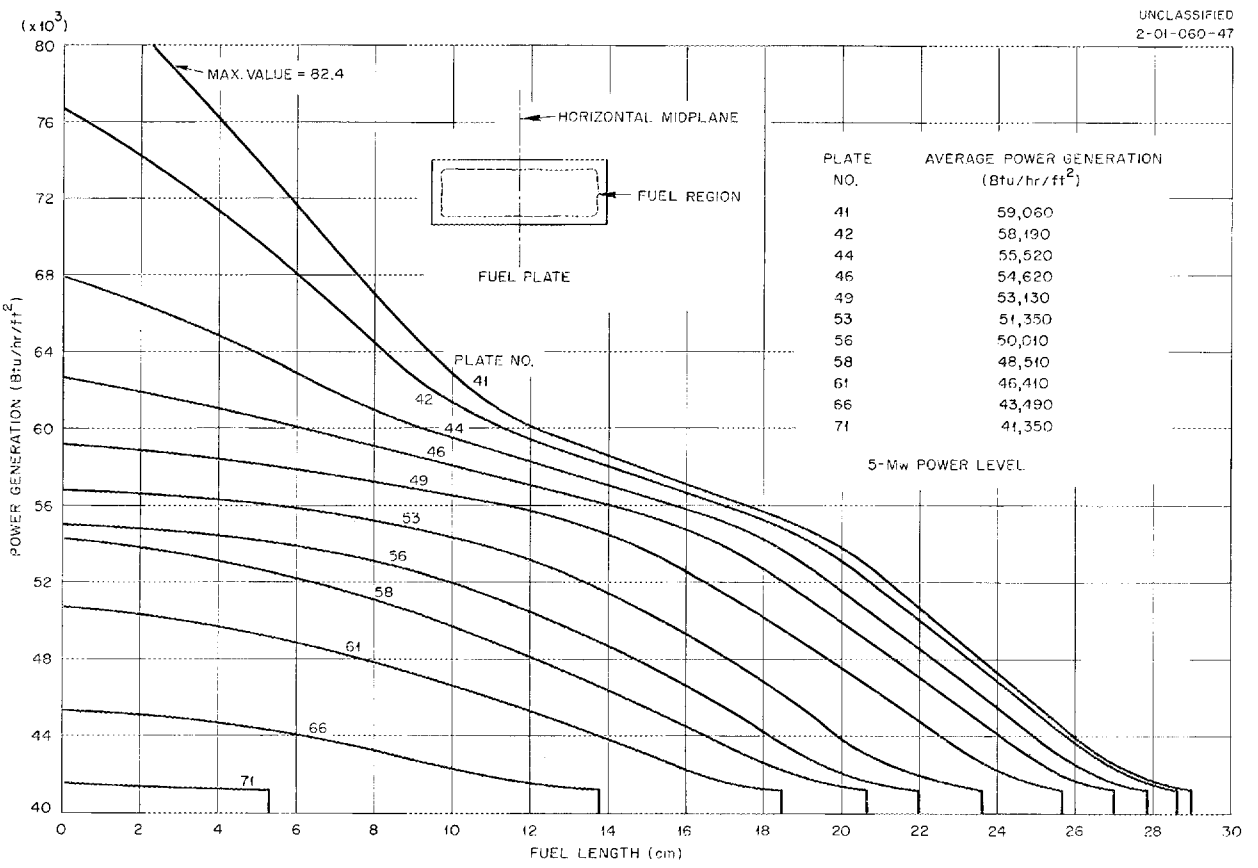

Fig. 2.3.12. Power Generation in the Fuel Plates of a TSR-II Annular Element as a Function of Distance from the Horizontal Midplane to the Edge of the Fuel.

a $\frac{1}{16}$-in.-thick aluminum shell that covers most of the upper half or exit end of each fuel element and has the hole pattern shown in Fig. 2.3.5. The baffle plate is mounted $\frac{1}{8}$ in. above the ends of the fuel plates so that there is communication between the coolant channels at the exit. This baffle design produced the flow distribution shown as a solid line in Fig. 2.3.15 for a total flow of 1000 gpm.

Another aluminum baffle plate is being developed to distribute the flow in the lower central elements. This baffle plate is hemispherical and is spaced $\frac{1}{8}$ in. above the lower central elements. It is perforated with a pattern of $\frac{1}{8}$ in. holes. The flow measurements in the fuel element channels have been made by injecting a salt solution into the water flowing through the central cylinder and measuring the time required for the salt solution to pass two probes which sense the change in resistivity of the water. Since each measurement, which is recorded by two pens on a strip chart, can be taken in milliseconds, a number of readings have been taken for each point and averaged.

The desired flow distribution in the lower central elements is nearly a straight line which runs from 2.0 fps for the channels with the smallest radius to 2.2 fps for the channel with the largest radius. At present, the average velocity reading for each point varies from the desired curve by as much as a factor of 2, but averages of several points in a channel and different distances into the channel give values much closer to the desired flow rate.

The pressure drop measured across the control-mechanism housing, the baffle plate, and the lower fuel elements, and around the end of the central cylinder is approximately 18 psi. Since

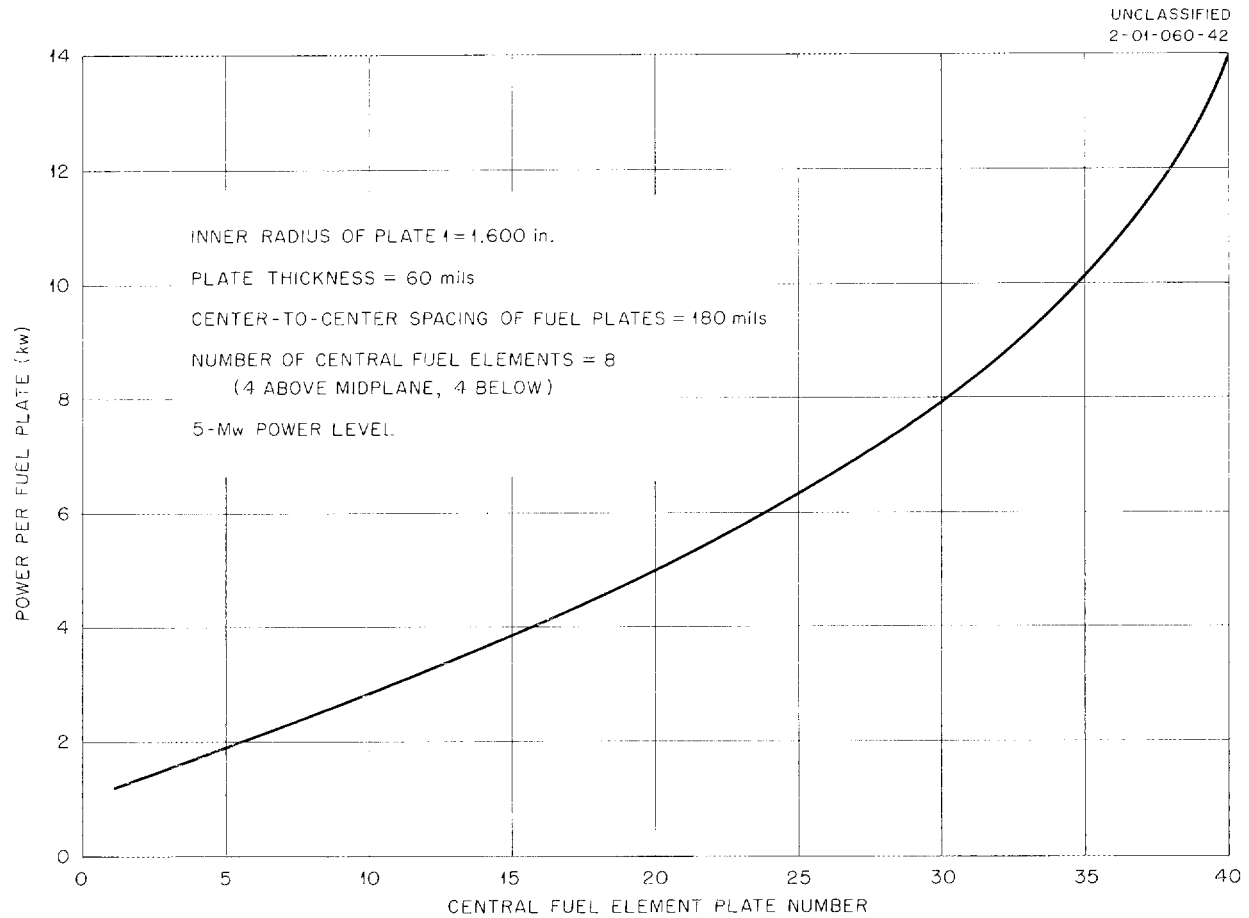

Fig. 2.3.13. Power Generation in the Fuel Plates of a TSR-II Central Fuel Element as a Function of the Fuel Plate Number.

this value is higher than was expected, more development work will be done to reduce it and to improve the flow distribution.

Very little has been done to obtain the proper flow distribution in the upper central fuel elements. The cooling water passes through the helical tubes in the lead and water shield (shown in Fig. 2.3.1) before it reaches the upper central fuel; therefore, it is distributed roughly evenly across the ends of the elements but with a high velocity below the tubes. The variation in velocity as measured was from +15 to −5 fps. A system of screens was fabricated to break up the flow before it enters the fuel element. It consisted of a 10-mesh base screen of 25-mil stainless steel wire upon which was tack-welded two layers of 120-mesh screen of 3.7-mil stainless steel wire. The finer screen was in ¾-in.-dia patches directly below the exit of each helical tube. The screen was mounted ¼ in. below the lead and water shield. The velocity variation was then +5 to −1 fps measured just where the top of the fuel elements would be placed. The pressure drop due to the screens was 0.3 psi and that through the helical tubes was 4.5 psi. Further development of the baffle screen has been suspended until velocity measurements can be made in the fuel elements. These experiments will be carried out in the same experimental setup used for the lower elements.

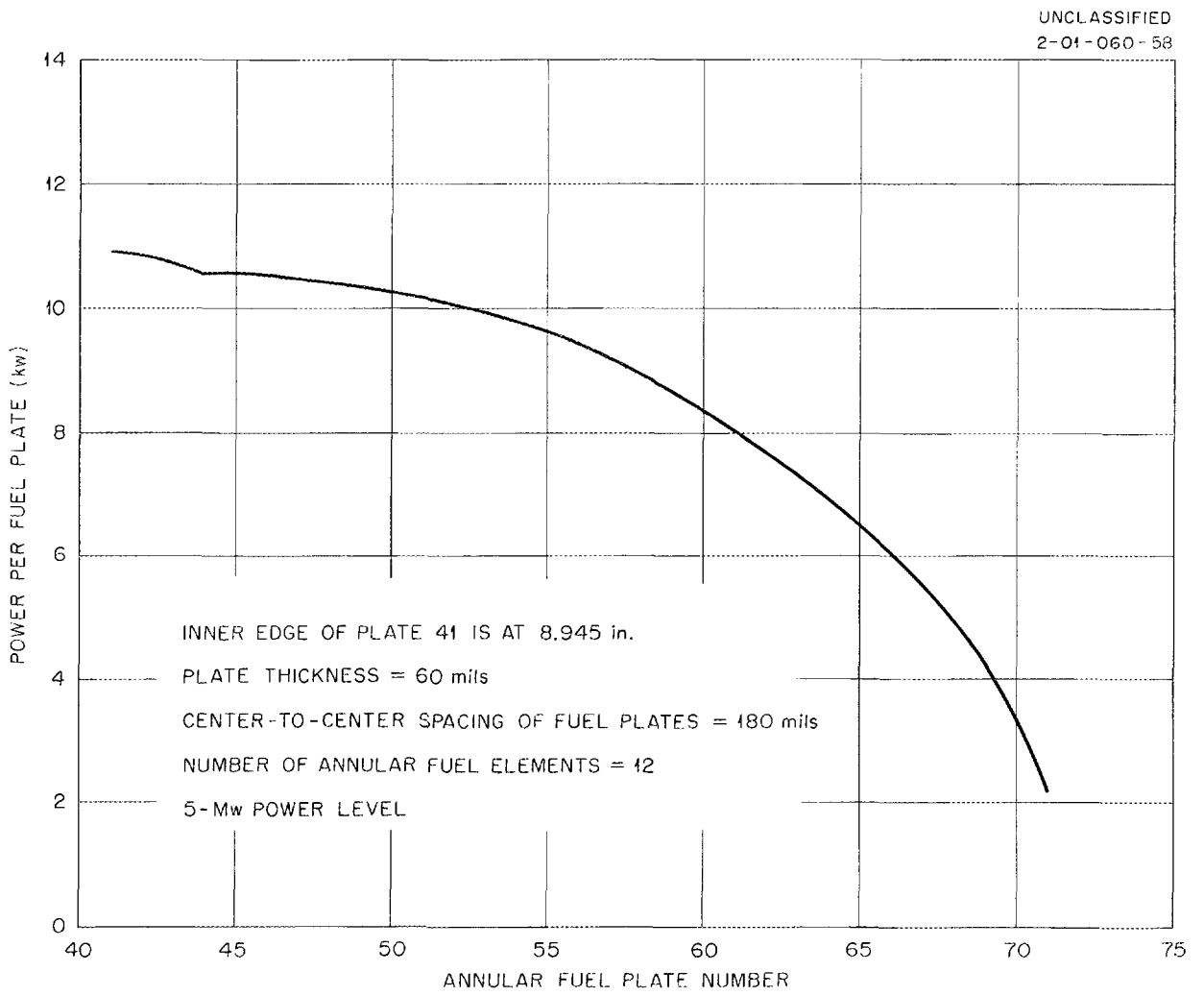

Fig. 2.3.14. Power Generation in the Fuel Plates of a TSR-II Annular Element as a Function of the Fuel Plate Number.

Safety System Development

Most of the safety instrumentation that will be used in the TSR-II is standard ORNL equipment.[9] Of the major components, only the control mechanism described previously[1] and the scram solenoid (previously referred to as an electrohydraulic transducer) which controls the water flow to the control mechanism are completely new. During the past year development work to increase the speed and reliability of the control mechanism has been continued, and the scram solenoid has been redesigned and tested.

The basic design of the control mechanism has not changed. The maximum spring force has been increased from 42 to 95 lb. Small ports have been placed in the drive nut (Fig. 2.3.17) so that the piston operates as a servomechanism and the force due to water pressure exactly counterbalances the spring force. The object of this change was to reduce wear and increase the life of the mechanism. The ports were sized to increase the water flow through the mechanism to aid in cooling the control-mechanism housing.

[9] The TSR-II control system was designed by members of the Reactor Controls Group of the Instrumentation and Controls Division, in particular by L. C. Oakes.

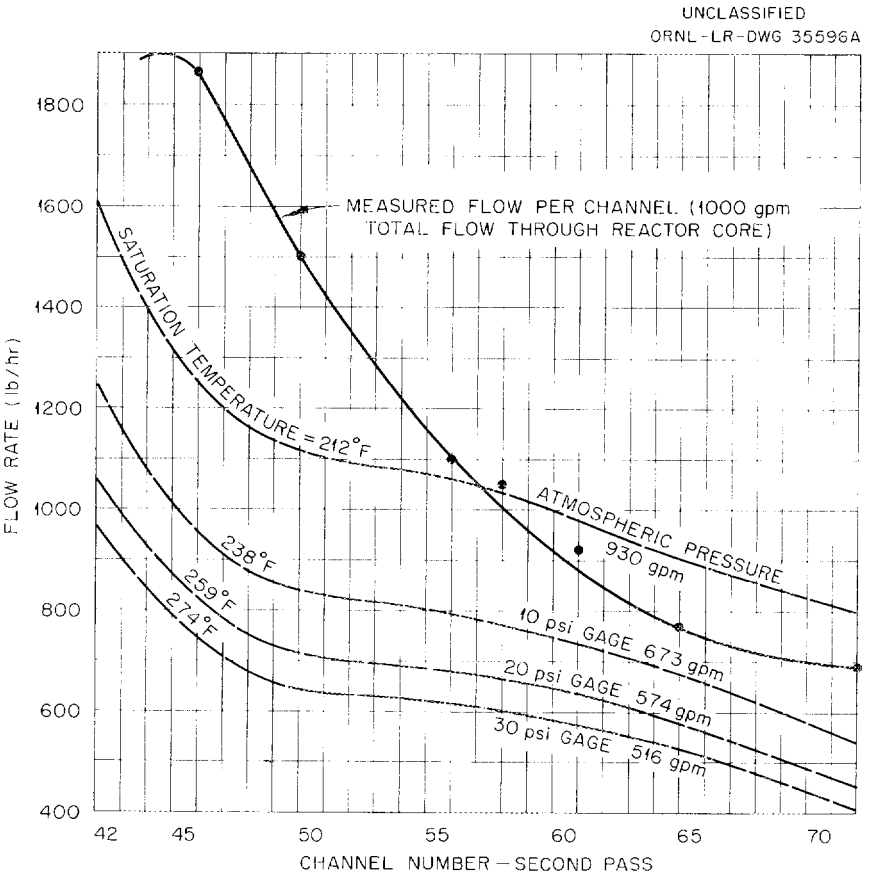

Fig. 2.3.15. Minimum Flow Required in Each Channel of TSR-II Annular Elements for Various Saturation Temperatures and a 5-Mw Total Reactor Heat Generation Rate.

With these changes[10] the release time of the mechanism used in conjunction with the scram solenoid was 22 msec and the total time for full insertion of the safety rods from initiation of a scram signal was 51 msec. The technique for measuring these times is described below.

The test assembly included a simulated sigma bus circuit, a standard magnet amplifier, a scram solenoid, and a control mechanism with connections between these components similar to those expected in the final reactor assembly. A differential-transformer type of linear motion transducer was mechanically connected to the control plate to translate the position of the plate into a 3000-cps differential voltage. This voltage was applied to an oscilloscope with a 200-msec sweep period initiated by the same change in sigma bus voltage that initiated the scram. The resulting plot of position vs time was calibrated in tenths of an inch between the limits of travel of the control plate. The plate was considered to have started moving when the slope of the curve left zero, and to have stopped when the slope returned to zero.

The delay time was measured by using the change of sigma bus potential that initiated the scram to simultaneously trigger the sweep of the oscilloscope. The length of sweep from the point it began to the first discontinuity was taken as an indication of the release time between initiation of a scram signal and the first perceptible motion of the control plate.

The scram solenoid used previously was designed to cut off the water flow to the mechanism.

[10] This work was performed by J. E. Marks of the Reactor Controls Group.

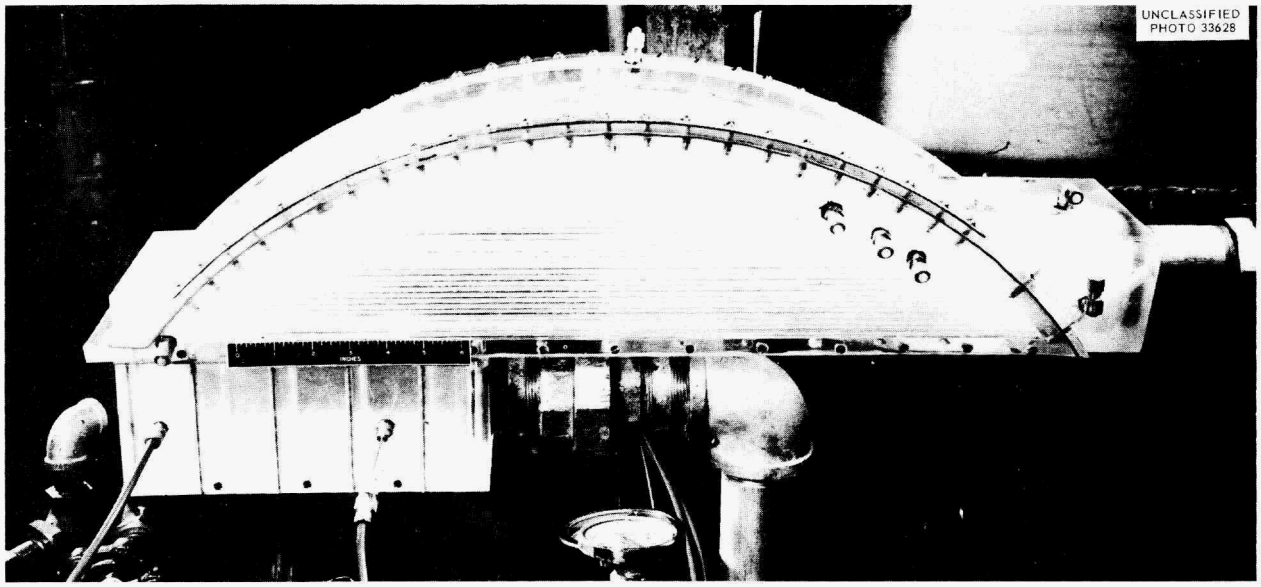

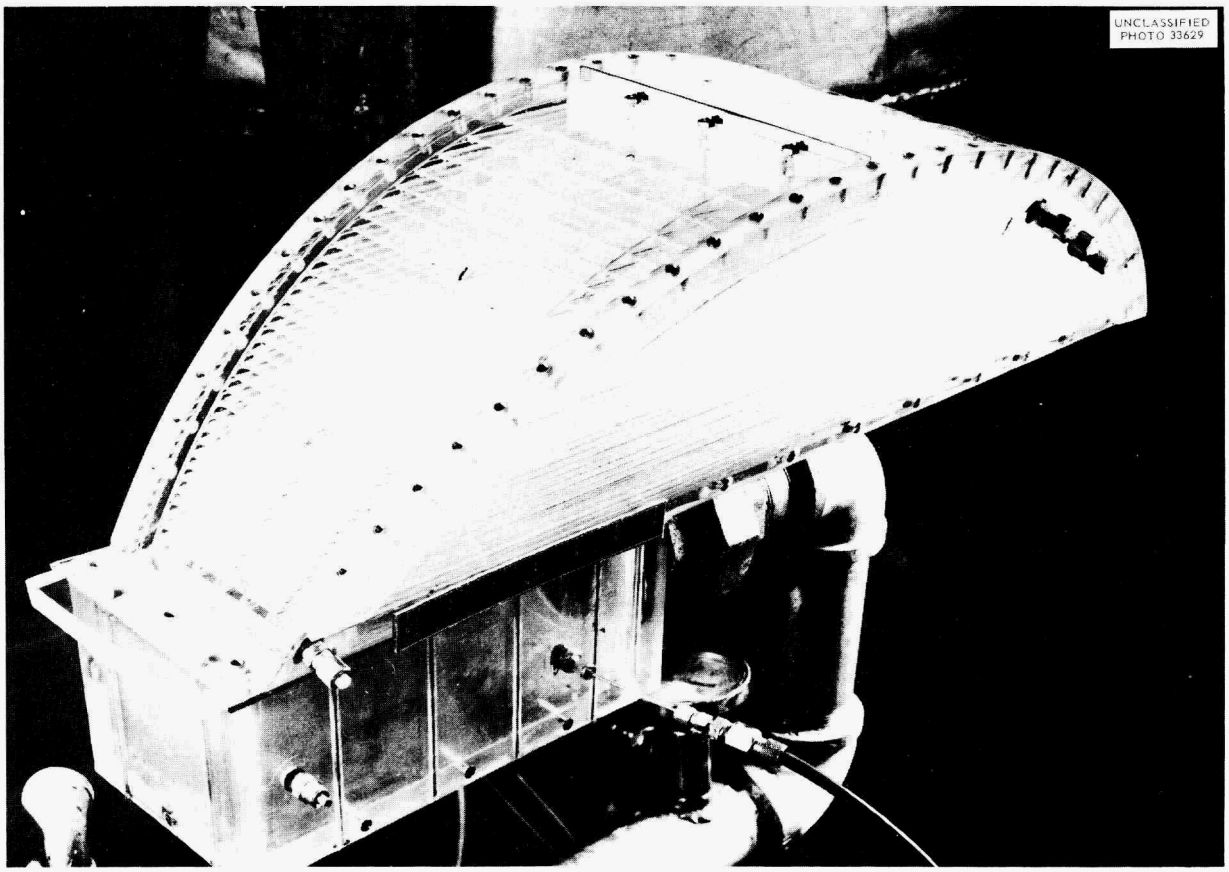

Fig. 2.3.16. Plastic Model of a TSR-II Annular Element for Baffle Plate Development.

UNCLASSIFIED
2-01-060-80R1

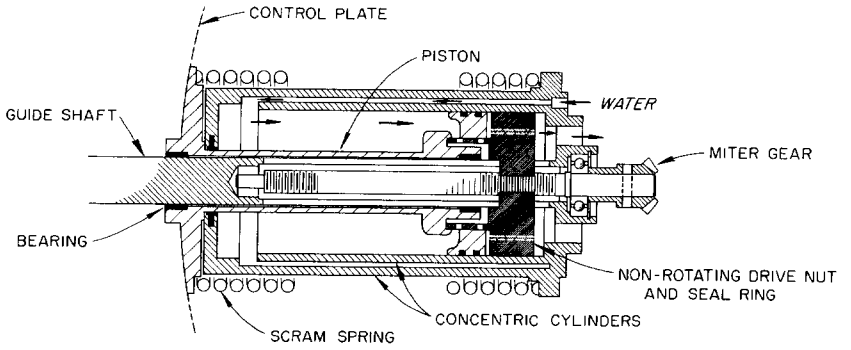

(*a*) Operating Position: Piston Under Command of Drive Nut.

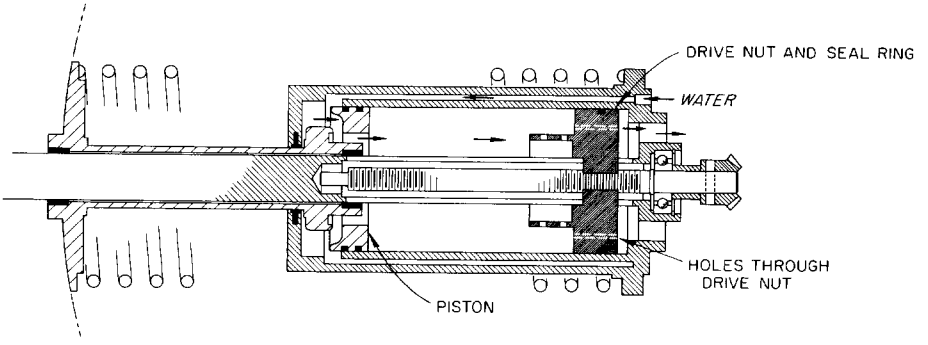

(*b*) Scrammed Position: Piston Independent of Drive Nut.

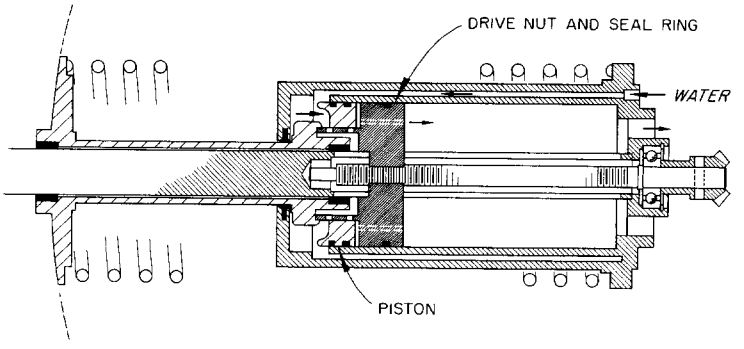

(*c*) Drive Nut Traversed Outward and Reassuming Command of Piston.

Fig. 2.3.17. Schematic of TSR-II Control Rod Drive in Three Positions.

Some misoperation was observed owing to collection of debris in the mechanism. A new solenoid, which would both cut off the flow of water to the mechanism and bypass it to the main coolant stream, was designed. The solenoid part of this mechanism operates in air, and the debris-accumulation problem does not exist.

Reactor-Core Kinetics Studies

The performance of the TSR-II safety system has been predicted on the basis of three analog computer tests simulating the reactor kinetics and heat transfer system.[11] Each test represents the limiting case for the type of accident considered. The configuration assumed for these tests included the reactor tank and the associated inlet and outlet pipes. It did not include the water coolant system external to the reactor tank, since the choice of the initial conditions for the tests precluded the need for an analysis of the external system.

In the first test, a simulated rod-drop test, it was found that for 5-Mw operations the safety system is capable of reversing a 14.5-msec period with a power excursion to a peak power of 1010 Mw without consideration of the advantage of the negative temperature coefficient.

The second simulated test was run to determine the effect of suddenly reducing the temperature of the inlet cooling water while the reactor is operating at a power of 5 Mw, and the third test was carried out to determine the effect of a sudden stoppage in the water flow.

Rod-Drop Test. – The TSR-II rod-drop test was performed to determine the minimum period for which the safety system could reverse an excursion in less than a three-decade power rise from the instant the instruments first detected the excursion. In the analog technique used,[12] the reactor simulator (computer) at time $t = 0$ is clamped in transient at a low level represented by a voltage of 0.1 to 0.5 v. This voltage is proportional to reactor power or flux and, by proper adjustment of the computer parameters, can be made to represent a specific nuclear power. At $t = 0$ the clamp is removed and the safety system is given the information that an excursion is in progress. The simulation allows for the safety-system delay, provides the corrective action, and shows the reactor behavior, heat transfer characteristics, and component temperature rises during the complete transient.

In the TSR-II, the initial power of 0.5 corresponds to a power of 5 Mw. A three-decade rise then would yield a peak power of 5000 Mw. Since the level safety of the TSR-II is intended to actuate a scram at 150% of the maximum power, the level safety was assumed to be 7.5 Mw. At 7.5 Mw, information requesting a scram was supplied to the safety actuator. A delay of 37 msec in the safety device was simulated, during which time the excursion continued unaltered. The corrective action was then initiated, after which the excursion was reversed and the simulated reactor was shut down. Since the test was for the safety system, the effect of the negative water-coolant temperature coefficient, which would only have improved the performance of the safety system, was not considered.

The power excursion curves obtained in this test are shown in Fig. 2.3.18 along with the safety-rod reactivity profile. The safety-rod profile shown as a solid line was obtained from measured release and scram time of the control mechanism before the final development. This value was used in rod-drop studies. The dotted line indicates the safety-rod profile as it is now. The associated reactor period is noted alongside each power excursion curve. From these data it can be seen that the TSR-II safety system is capable of reversing a power excursion caused by a 14.5-msec period with a maximum power rise of 2.02×10^2 above the initial power, that is, with a peak power of 1010 Mw.

The mean temperature increase of the fuel in the annular elements and the temperature rise of the water in the annular fuel region are shown in Fig. 2.3.19 for each of the power excursions plotted in Fig. 2.3.18.

"Cold-Water Slugging" Test. – Because of the negative coefficient of reactivity of the TSR-II, an analog simulator test was performed to investigate the effects of a sudden drop in the reactor-inlet cooling-water temperature. Figure 2.3.20 shows the effects on the reactor power and temperature of suddenly changing, within 0.5 sec,

---

[11] This work was performed by R. K. Adams of the Instrumentation and Controls Division.

[12] E. R. Mann and F. P. Green, *Reactor Safety System Response*, ORNL-2318, p 83 (1958).

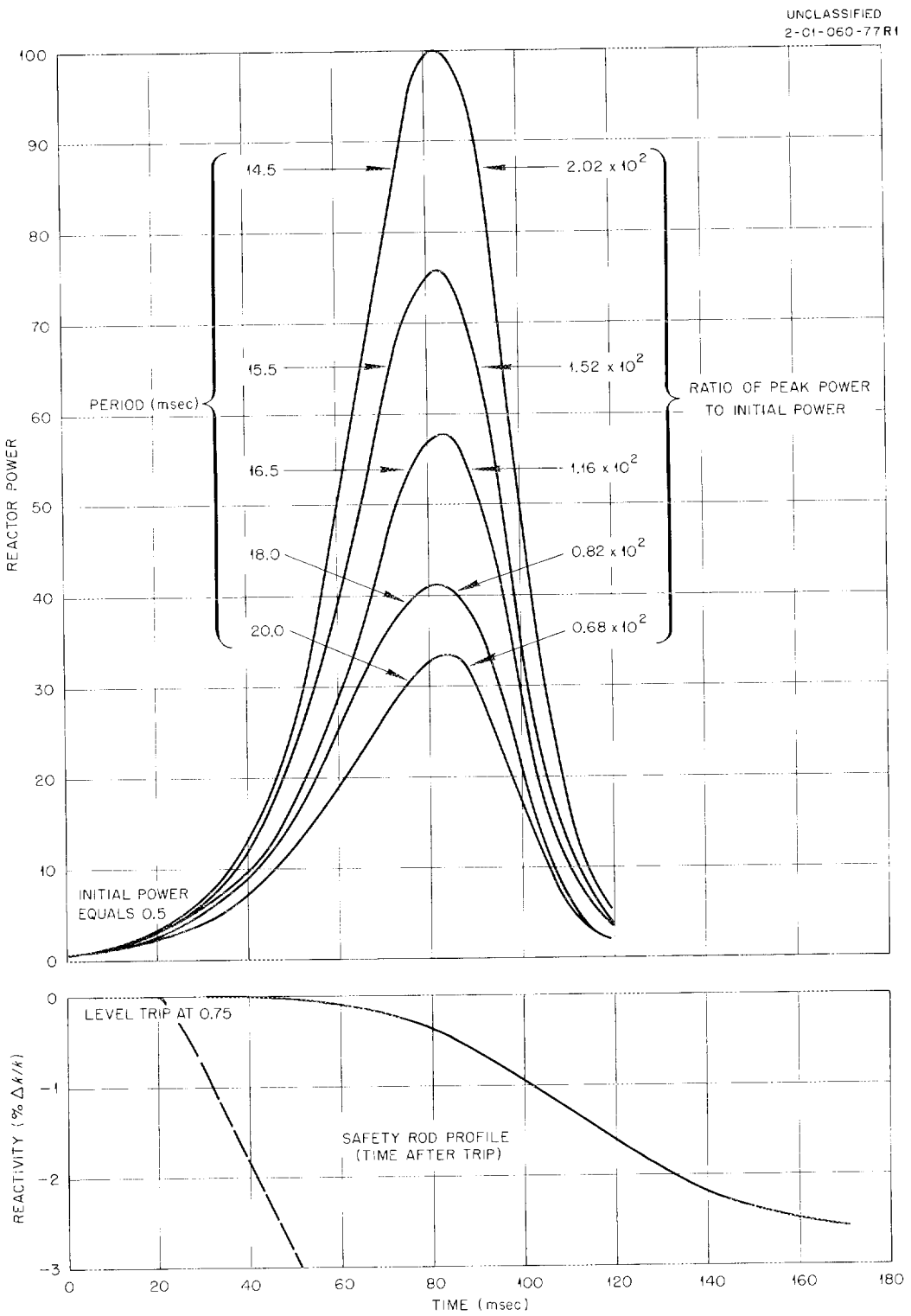

Fig. 2.3.18. Effectiveness of TSR-II Safety System in Limiting Power Excursions for Various Reactor Periods.

UNCLASSIFIED
2-01-060-78

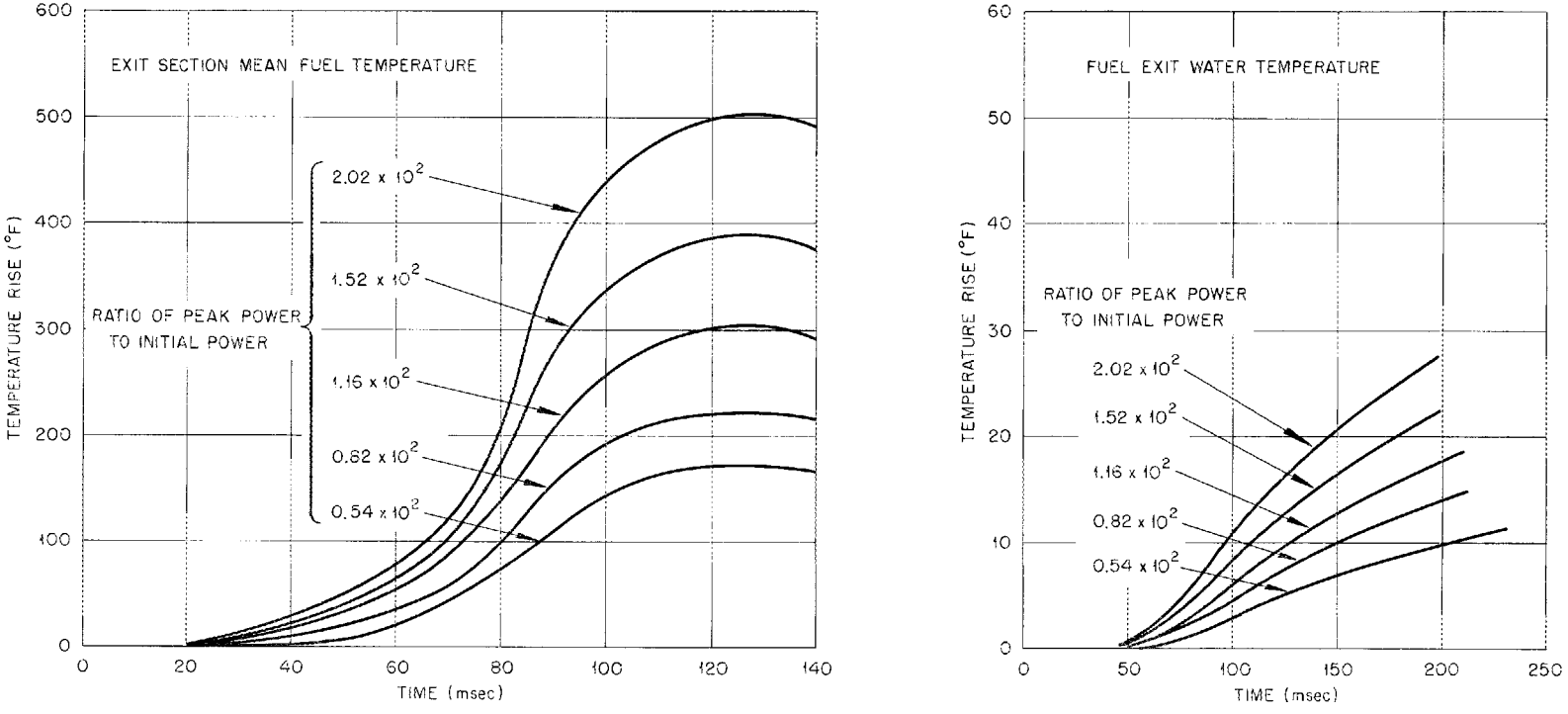

Fig. 2.3.19. Temperature Increase in TSR-II Annular Fuel Element Region for Various Power Excursions.

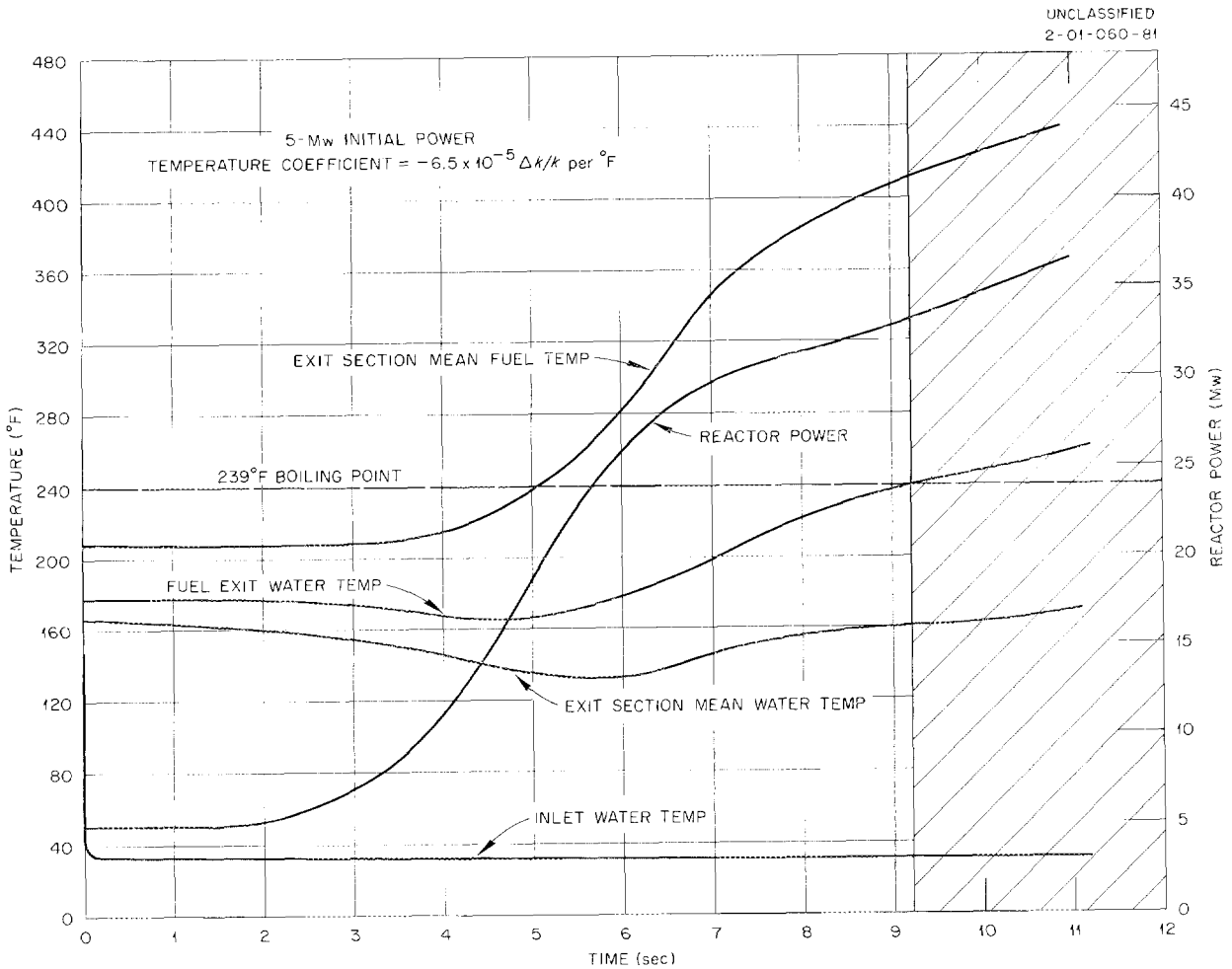

Fig. 2.3.20. Effect on TSR-II Power and Temperatures of Reducing the Inlet Water Temperature from 145.8 to 32°F (Temperature Coefficient = 6.5×10^{-5} $\Delta k/k$ per °F).

the inlet cooling-water temperature from 145.8 to 32°F while the reactor is operating at 5 Mw. Figure 2.3.20 is for an assumed coefficient of -6.5×10^{-5} $\Delta k/k$ per °F. Prompt gamma-ray heating was included in the simulation. No safety-rod action or control-rod action was permitted.

The simulation has no validity in the cross-hatched areas of the figure since no attempt was made to simulate boiling conditions within the reactor. An assumed pressure of 10 psig was used to calculate the boiling temperature of 239°F.

The "cold-water slugging" analysis was carried out without actuating the safety system. It should be noted that there is far more than adequate time for the system to shut the reactor down before the fuel temperature rises appreciably since the safety system can complete its action in less than 150 msec (Fig. 2.3.18). The use of the actual coefficient of -8.5×10^{-5} $\Delta k/k$ per °F would not significantly change the time scale on the figure.

Water-Flow Stoppage Test. – Mechanical conditions inherent in the design of the TSR-II cooling-water system prompted a test to determine

the effects of a sudden stoppage of the coolant-water flow. Figure 2.3.21 shows the results for an assumed temperature coefficient of -4.28×10^{-5} $\Delta k/k$ per °F. Prompt gamma-ray heating was again included in the simulation, and no safety-rod or control-rod action was permitted. The simulation included only the annular fuel region of the reactor, since this is where the highest temperatures are most likely to be. Again the simulation has no validity for the cross-hatched area in Fig. 2.3.21. As before, the test showed that the safety system could easily shut the reactor down before any appreciable change occurs in the temperature profile.

TSR-II Beam Shield

The first shielding experiments with the TSR-II will be "beam-differential" experiments designed

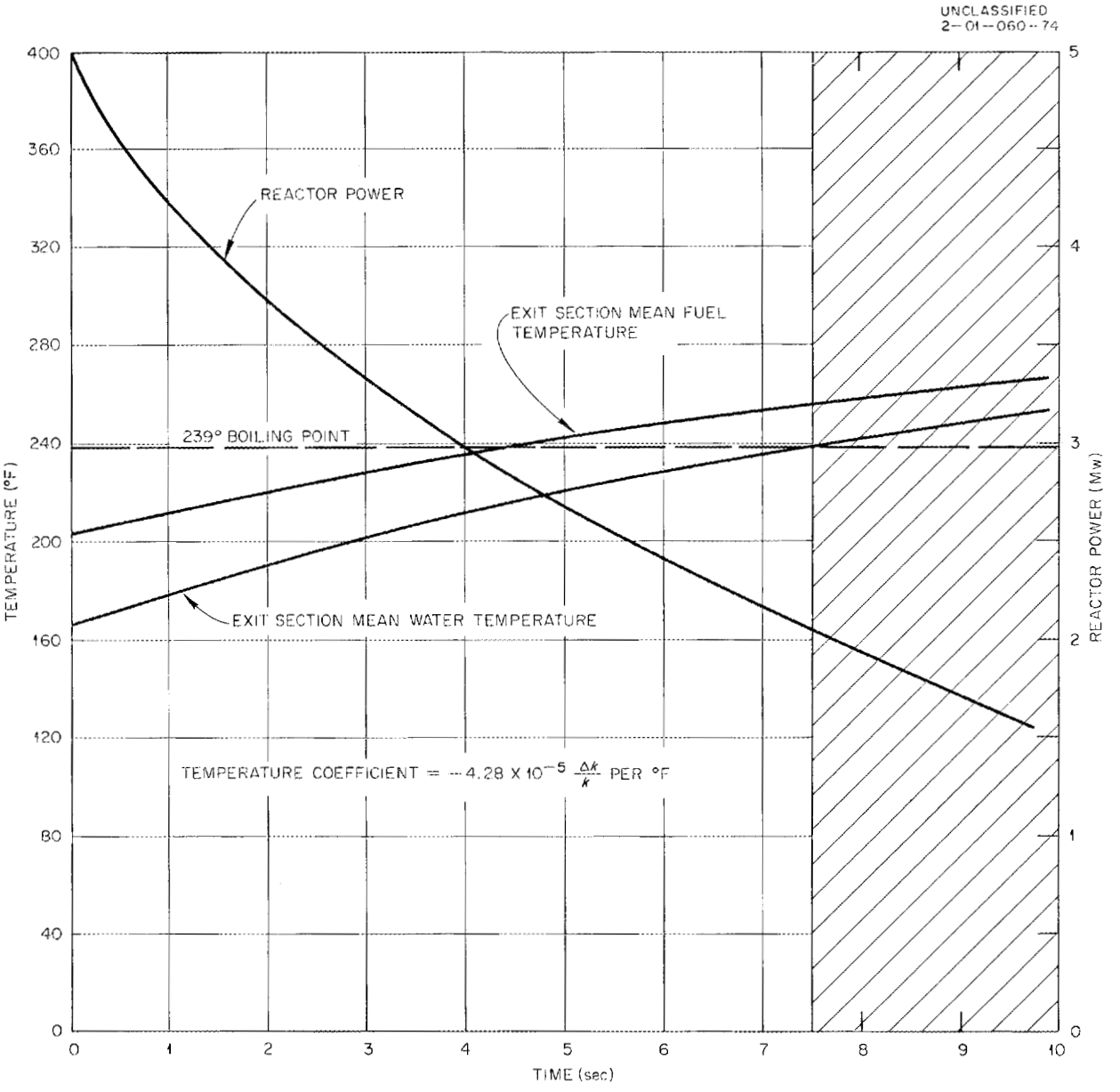

Fig. 2.3.21. Effect of Sudden Water-Flow Stoppage on TSR-II Power and Temperatures.

to supply information of a fundamental nature. In these experiments a collimated source of radiation (neutron or gamma rays) is used and the direction of the beam, as well as the energy spectrum, is varied. The detector is also to be equipped with collimation.

During the beam-differential experiments the TSR-II will be encased in a beam shield,[13] which is shown suspended from the reactor support platform in Fig. 2.3.22. Briefly, it consists of a lead-water gamma-ray shield followed by a water neutron shield. The lead is in the form of Raschig rings which have a packing fraction of 50%. The combined weight of the lead and water in the gamma-ray shield is 32,250 lb. The neutron shield outside the gamma-ray shield is 78.7 cm thick and weighs 38,500 lb. When structure weight is considered (9,097 lb), the total weight of the beam shield is approximately 40 tons. The radius from the outer surface of the shield to the center of the TSR-II is 172 cm.

Two beam holes spaced 180° apart extend through the shield. These beam openings are 15 in. in diameter at the outer periphery of the shield and are stepped down to a diameter of 10 in. halfway through the shield. They are designed so that both can be left open or so that one or both can be plugged with various materials. Therefore, by filling one beam hole with a lead and water plug having regions corresponding to the beam shield itself, a single beam of collimated neutrons and gamma rays can be used to sweep a horizontal or vertical plane. Other shielding materials can be used to provide a beam with a more useful spectrum.

[13] The design work to determine the dimensions of the beam shield was performed by L. Byrnes of GE-ANP, Cincinnati, Ohio.

When horizontal rotation of the beam is required, the beam shield will be supported from the reactor support platform. The shield and all components of the platform have been fabricated, and the rotating mechanism has been tested. All the components necessary to support the shield and reactor for vertical rotation of the beam have also been fabricated, and the rotating mechanism will be tested in the near future.

In order to effect collimation at the detector location, the detector will be housed in a spherical shield of lead and water, which is supported within a carbon steel structure and pierced by two collimators. The outer diameter of the shield is 127 in. A centrally located detector chamber, $14\frac{1}{8}$ in. in diameter, is surrounded by a mixture of lead and water much the same as the gamma-ray shield region in the reactor beam shield. The total weight of the detector shield is 30 tons.

One collimator opening through the detector shield is conical with an included angle of 15 deg and a $4\frac{3}{4}$-in. diameter on the inside. The second collimator opening is cylindrical and is $16\frac{1}{8}$ in. in diameter. Either collimator can be converted to a cylindrical 4.4-in.-dia opening by the use of plugs. These plugs have three separate compartments which can be filled independently. The openings can be further reduced to 3.3 in. in diameter by inserting Lucite liners in the plugs. Also, one or both openings can be completely plugged.

The entire shield can be rotated so that a collimator can point in any direction; however, the support structure immediately above the shield would limit the usefulness of data taken with a vertical collimator. The shield is now being fabricated.

UNCLASSIFIED
PHOTO 48339

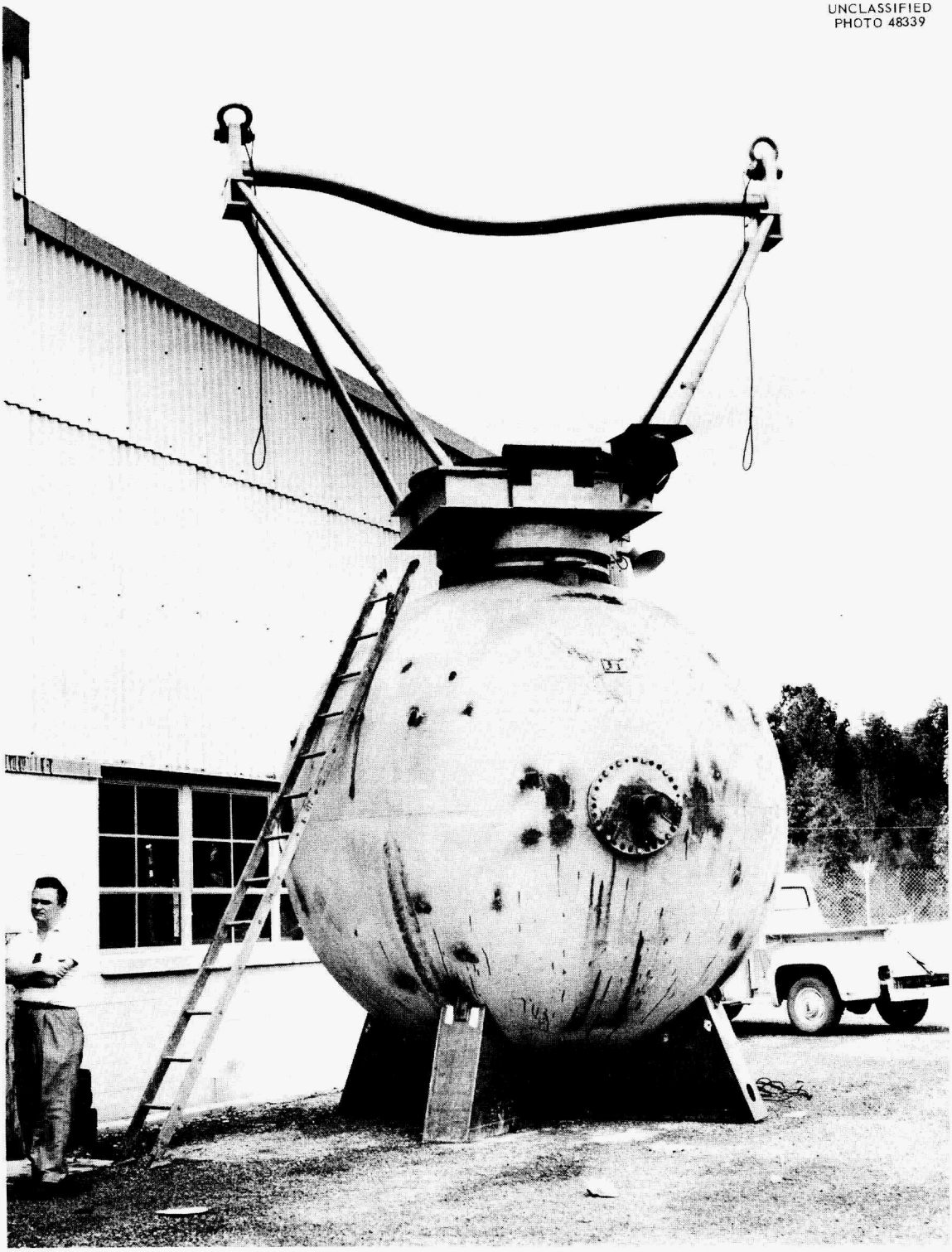

Fig. 2.3.22. TSR-II Beam Shield and Support for Vertical Rotation.

Part 3

CRITICAL EXPERIMENTS

3.1. MULTIPLICATION MEASUREMENTS WITH SLABS OF ENRICHED URANIUM

J. T. Mihalczo J. J. Lynn

A series of neutron multiplication measurements with arrays of $1 \times 8 \times 10$ in. slabs of 93.4% U^{235}-enriched uranium metal have been made to provide data from which safety criteria for the storage of these fissile units can be established. Each slab contains 22.9 kg of U^{235}. A maximum of 125 units was assembled, the arrays studied being cubic lattices of the units which were usually parallelepipedal in shape. Arrays were both unmoderated and Plexiglas-moderated and were surrounded in most cases by a 1-in.-thick Plexiglas reflector. The lattice densities (ratio of fissile unit volume to lattice cell volume) were between 0.023 and 0.06.

The number of fissile units required for each lattice to become critical can be estimated by linearly extrapolating the reciprocal multiplication curve for the lattice to zero. The results of these extrapolations for the various arrays are shown by the open circles on Figs. 3.1.1 and 3.1.2.

Another method can be used to estimate the number of fissile units required for criticality of a particular type of array provided that a good estimate of the number of units required for criticality at one lattice density is known. This method becomes apparent by a comparison of the plots in Figs. 3.1.1 and 3.1.2, which show the number of fissile units required for specific reciprocal multiplications in the various arrays as a function of the ratio of the fissile unit volume to lattice cell volume (lattice density). As the multiplication increases, the lines become more nearly parallel. This indicates that the slope of the line representing critical arrays is the same as the slope of the lines for higher multiplications. Hence, if the number of fissile units required for criticality at one lattice density is known and if the number of fissile units required for high multiplications at other lattice densities is known, a line representing the critical number of fissile units for other lattice densities can be drawn. This method may provide a better extrapolation of low multiplication experiments.

The extrapolation of the inverse multiplication curve for unmoderated arrays with a lattice density of 0.06 indicated that 145 ± 5 units would be required for criticality. The critical line for other lattice densities is then obtained by plotting this point on Fig. 3.1.1 and drawing a line that passes through the point and has the same slope as the line for the highest multiplication measured in the arrays. When the extrapolations of the inverse multiplication curves for other lattice densities are also plotted on Fig. 3.1.1, they fall close to the critical line.

The same procedure is used to determine the critical line for the moderated arrays (Fig. 3.1.2). In this case the extrapolation of the inverse multiplication curve indicated that 27 units would be required for criticality in a moderated array with a lattice density of 0.06.

Distributing Foamglas (containing 2% boron) throughout a moderated array increased the critical number of fissile units by a factor of 5, while Styrofoam had a small effect.

The details of these experiments are reported elsewhere.[1]

---

[1] J. T. Mihalczo and J. J. Lynn, *Multiplication Measurement with Highly Enriched Uranium Metal Slabs*, ORNL CF-59-7-87 (1959).

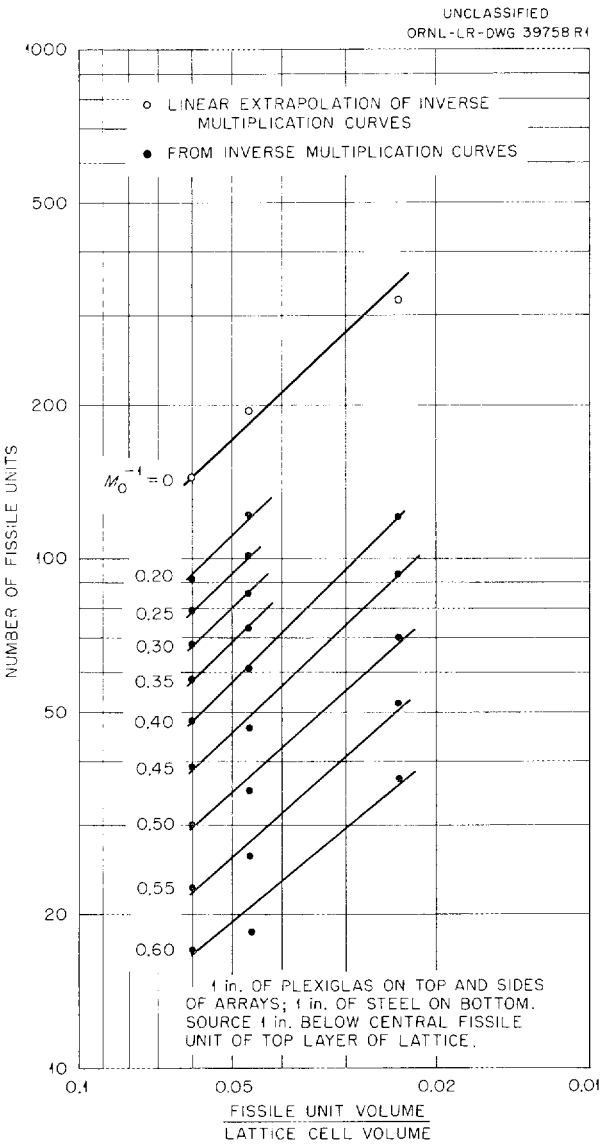

Fig. 3.1.1. Number of Unmoderated 93.4% U^{235}-Enriched Uranium Metal Slabs (1 × 8 × 10 in.) as a Function of the Ratio of Fissile Unit Volume to Lattice Cell Volume for Various Inverse Multiplications.

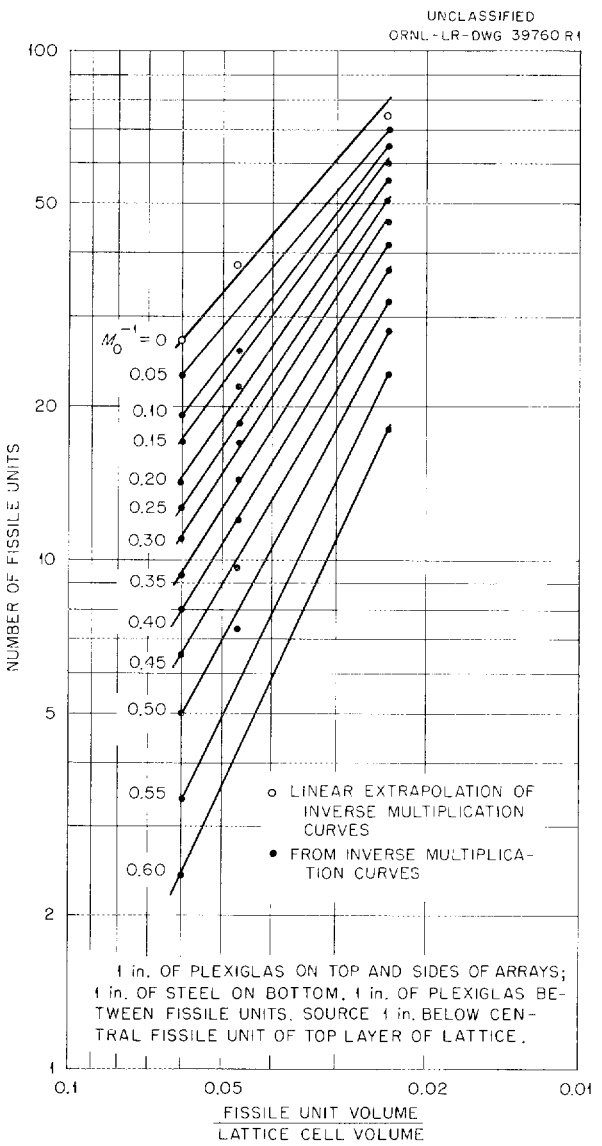

Fig. 3.1.2. Number of Plexiglas-Moderated 93.4% U^{235}-Enriched Uranium Metal Slabs (1 × 8 × 10 in.) as a Function of the Ratio of Fissile Unit Volume to Lattice Cell Volume for Various Inverse Multiplications.

3.2. RADIAL FLUX MEASUREMENTS IN A CYLINDRICAL ANNULAR CRITICAL ASSEMBLY OF $U^{235}O_2F_2$-H_2O

R. Gwin D. W. Magnuson

Radial flux measurements with bare gold foils have been made in a water-reflected cylindrical annular critical assembly. The assembly consisted of a 5.88-in.-dia water column located axially within a cylindrical annulus of uranyl fluoride solution highly enriched in the U^{235} isotope (~86 g of U^{235} per liter). The inside diameter of the annulus was 6.00 in., and the outside diameter was 15.00 in. At delayed criticality the height of the annulus was 9.3 in., when reflected with water to an equal height. The experimental vessels were made of $\frac{1}{16}$-in.-thick 2S aluminum, coated with Heresite, a plastic material, to prevent corrosion. The gold foil detectors were 0.002 in. thick and 0.500 in. in diameter.

Table 3.2.1 presents the relative activities determined, together with values from an unreflected assembly for both bare and cadmium-covered gold foils measured during a previous experiment.[1] Figure 3.2.1 presents a plot of the same data. Although no analysis of the data has been attempted, the information has been of interest for the design of the High Flux Isotope Reactor (HFIR).

[1] D. W. Magnuson and R. Gwin, *Neutron Phys. Ann. Prog. Rep. Sept. 1, 1958*, ORNL-2609, p 27.

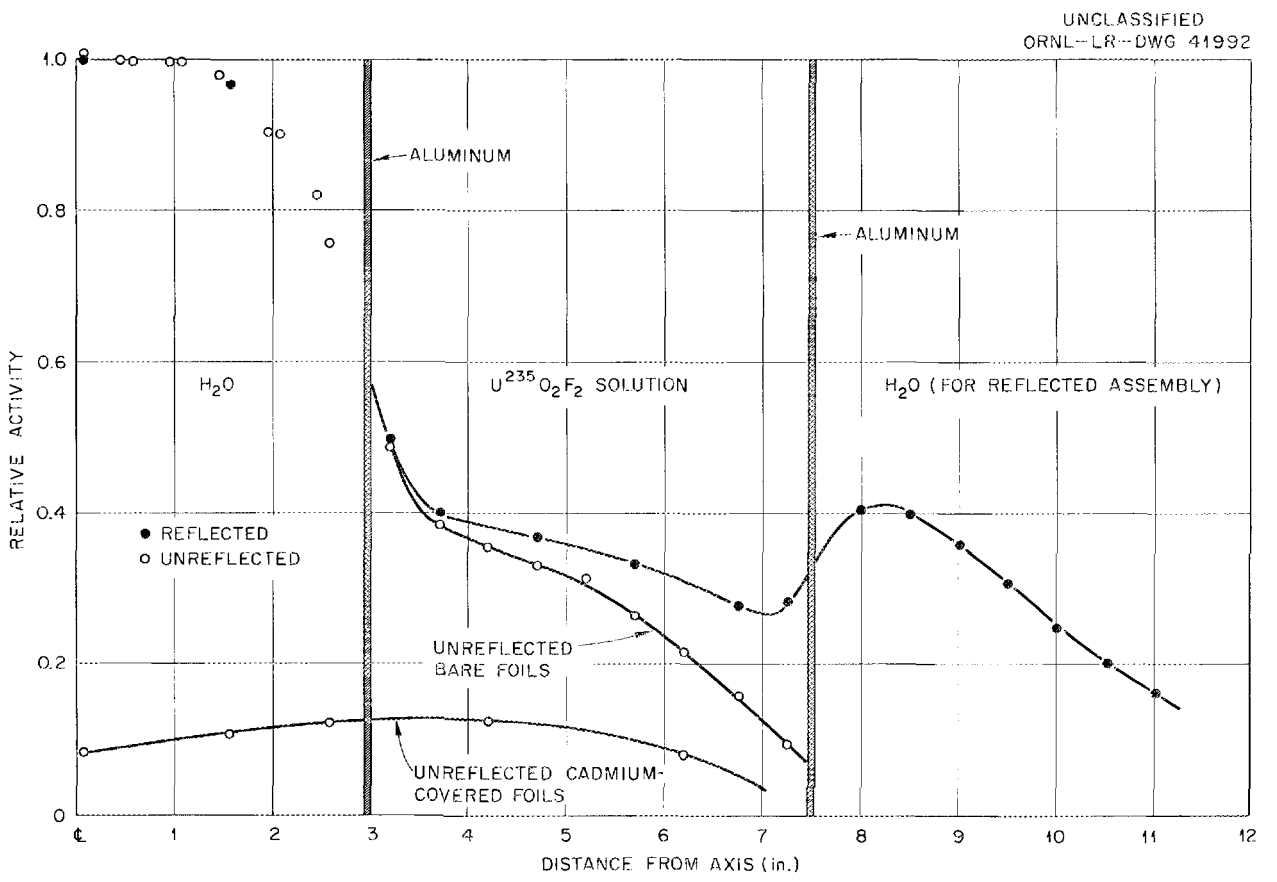

Fig. 3.2.1. Activities of Gold Foils Exposed Along a Radius in a Cylindrical Annular Critical Assembly of $U^{235}O_2F_2$-H_2O.

Table 3.2.1. Activities of Gold Foils* Exposed Along a Radius in a Cylindrical Annular Critical Assembly of $U^{235}O_2F_2$-H_2O

Distance from Axis (in.)	Relative Activity		
	Unreflected Assembly		Reflected Assembly, Bare Foils
	Bare Foils	Cd-Covered Foils	
$-2\frac{7}{16}$	0.822		
$-1\frac{15}{16}$	0.903		
$-1\frac{7}{16}$	0.981		
$-\frac{15}{16}$	0.998		
$-\frac{7}{16}$	1.000		
$+\frac{1}{16}$	1.008	0.083	1.000
$+\frac{9}{16}$	0.999		
$1\frac{1}{16}$	0.996		
$1\frac{9}{16}$	0.967	0.107	0.969
$2\frac{1}{16}$	0.901		
$2\frac{9}{16}$	0.757	0.122	
$3\frac{3}{16}$	0.488		0.498
$3\frac{11}{16}$	0.385		0.401
$4\frac{3}{16}$	0.355	0.125	
$4\frac{11}{16}$	0.331		0.369
$5\frac{3}{16}$	0.314		
$5\frac{11}{16}$	0.264		0.332
$6\frac{3}{16}$	0.216	0.080	
$6\frac{11}{16}$	0.159		0.279
$7\frac{3}{16}$	0.094		0.282
8			0.403
$8\frac{1}{2}$			0.400
9			0.360
$9\frac{1}{2}$			0.308
10			0.248
$10\frac{1}{2}$			0.202
11			0.163

*Foils 0.002 in. thick.

3.3. CRITICAL PARAMETERS OF SLIGHTLY ENRICHED ANNULAR CYLINDRICAL URANIUM METAL SLUGS

J. K. Fox L. W. Gilley

A study of some of the critical parameters for water-moderated and -reflected 0.94% U^{235}-enriched annular cylindrical uranium metal slugs is in progress. The slugs are unclad, nominally 6 in. long, 1.365 in. in outside diameter, and 0.485 in. in inside diameter. Thus far two arrays with regular lattices and a random array have been investigated. In all the experiments the arrays are constructed within a 9-ft-dia tank and reflected with a minimum of 6 in. of water.

For the experiments with regular geometries the slugs were placed in Tenite ($C_{12}H_{18}O_6$) tubes which were held in a triangular lattice by two ¼-in.-thick aluminum spacer plates, one near the top of the array and the other near the bottom. Alignment of the tubes was ensured by placing milled plastic strips horizontally through the assembly near the center or by using a third spacer plate made of ¼-in.-thick Plexiglas near the mid-plane. This resulted in a triangular lattice of uranium "rods" in an over-all hexagonal array, whose height could be varied by integral numbers of slugs. Results of check measurements throughout the array indicated that alignment between rods was maintained with a tolerance of ±0.1 in., part of which was due to variations in thickness of the Tenite tube walls.

Two lattice spacings were used: one in which the distance between rod centers was 2.00 in. and another in which the distance was 1.78 in. This corresponded to water-to-metal volume ratios of 1.70 and 1.14, respectively. The resulting critical parameters are given in Table 3.3.1. In most cases it was not possible to attain the condition of delayed criticality with an integral number of rods fully reflected; therefore the excess reactivity for the integral number of rods nearest to the critical number was determined.

The minimum critical number of rods for a specific assembly height and water-to-metal volume ratio was obtained by a process of "rounding" the hexagonal array by moving rods from the corners to the faces until the minimum condition was achieved. An indication of the effect of this rounding can be observed by comparison of the data given in Table 3.3.1 for an assembly height of 42 in. and a volume ratio of 1.70. In general, rearrangement of peripheral rods varied the reactivity by a few cents at most. As shown in the table, the approximate worth of a rod on the periphery is 2 cents.

Figure 3.3.1 shows the variation in the mass corresponding to the minimum critical number of rods as a function of critical assembly height for a water-to-metal volume ratio of 1.70. The curve indicates that the minimum critical mass for these slugs under the given conditions is greater than 5 tons of uranium.

For the experiments with the random array the slugs were contained in a 52-in.-dia stainless steel wire screen cylinder which was placed inside the 9-ft-dia tank. Random distribution of the slugs was obtained by dumping them into the cylinder from boxes at a height of about 5 ft above the cylinder. Each box contained 180 slugs. The resulting water-to-metal volume ratio, determined from six sets of measurements of assemblies of various heights, was 1.06 ± 0.05. This corresponds to an $H:U^{235}$ ratio = 156.

Since an insufficient number of slugs was available to make the random array critical, reciprocal multiplication measurements were taken. The measurements were checked by assembling the array three times. In each case the procedure consisted in positioning a neutron source having a strength of $\sim 10^7$ neutrons/sec on the vertical center line of the assembly approximately 1 ft above the bottom of the array and making successive additions of slugs while monitoring the neutron level after each addition with three BF_3 ionization chambers located directly below the center of the bottom of the tank. The first two loadings contained a maximum of 4410 slugs (11.6 tons of uranium) and had an average height of 34 in. The top of the array was somewhat rounded, the center being about 6 in. higher than the periphery. The third loading contained a maximum of 7174 slugs (18.8 tons of uranium), resulting in a nearly equilateral cylindrical array 53 in. high.

The reciprocal multiplication measurements for the random array are plotted in Fig. 3.3.2. Although there is some variation between the curves,

Table 3.3.1. Critical Parameters of 0.94% U^{235}-Enriched Annular Cylindrical Uranium Metal Slugs in Triangular Lattices

Slug dimensions: 1.365-in.-OD by 0.485-in.-ID by 6 in.
Slug density: 18.78 g/cc
Slug mass: 2384 g of U; 22.41 g of U^{235}

Spacing c to c (in.)	Water:Metal Volume Ratio	$H:U^{235}$ Ratio	Diameter of Rounded Array (in.)	Height of Array (in.)	Number of "Rods"	B^2, Buckling,[a] (cm^{-2})	Minimum Critical Mass U^{235} (kg)	Minimum Critical Mass Metal (tons)	Excess Reactivity, k_{ex} (cents)
						$\times 10^{-4}$			
2.00	1.70	252	34.4	48	266	28.04	47.8	5.58	1.4
2.00	1.70	252	34.4	48	271[b]				11.7
2.00	1.70	252	35.4	42	284[c]	28.20	44.5	5.22	1.0
2.00	1.70	285	35.4	42	285[c]				0.0
2.00	1.70	252	37.6	36	320	28.21	43.0	5.04	3.0
2.00	1.70	252	37.6	36	321[b]				3.5
2.00	1.70	252	37.6	36	322[b]				6.0
2.00	1.70	252	41.4	30	389	28.43	43.5	5.10	0.0
2.00	1.70	252	41.4	30	391[b]				2.2
1.78	1.14	169	45.4	48	589	19.34	105.4	12.40	2.0
1.78	1.14	169	48.5	42	673	19.10	105.4	12.40	0

[a]Values of the buckling were calculated from critical dimensions assuming an extrapolation distance of 7 cm.

[b]Added rod(s) centered on faces of preceding assembly.

[c]For the 284-rod array, the shape was roughly hexagonal, but five of the six corner positions were unfilled and three rods were centered on each face. For the 285-rod array all corner positions were filled, two rods were centered on each of four faces, and three rods were centered on each of two faces.

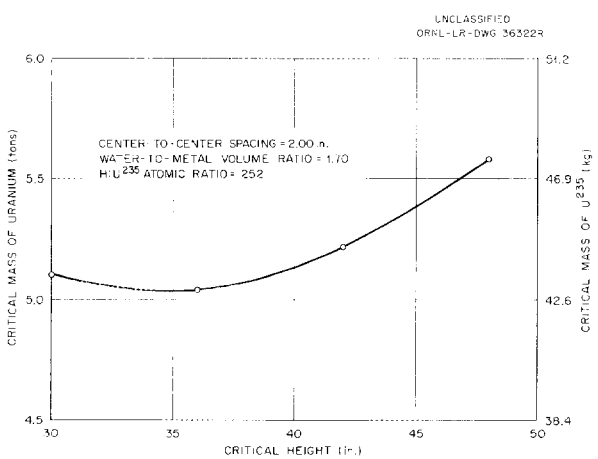

Fig. 3.3.1. Critical Mass of Triangular Lattices of 0.94% U^{235}-Enriched Uranium Metal "Rods" as a Function of Assembly Height.

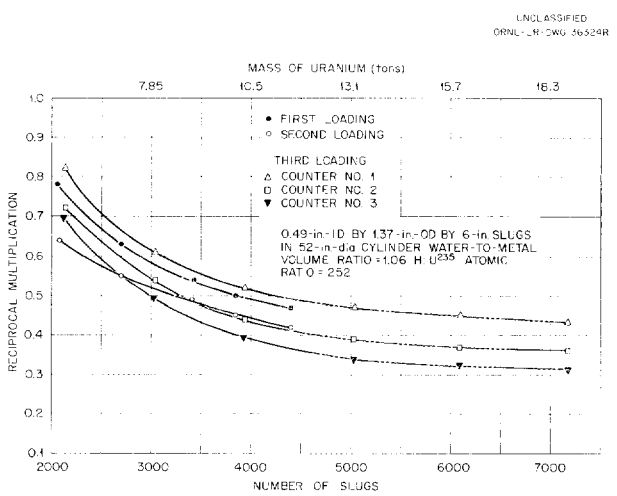

Fig. 3.3.2. Reciprocal Multiplication as a Function of the Number or Mass of 0.94% U^{235}-Enriched Uranium Metal Slugs in a Random Array.

the data for the three loadings are consistent in their general trends, showing an apparent source multiplication of about three. All the curves indicate that there would be little increase in the reciprocal multiplication with additional slugs. A comparison experiment showed that rounding the top of the 4410-slug array by placing a roughly hemispherical 16-in.-thick segment atop a 29-in.-high cylinder increased the neutron multiplication by about 2%.

3.4. THE POISONING EFFECT OF COPPER LATTICES IN AQUEOUS SOLUTIONS OF ENRICHED URANYL OXYFLUORIDE

J. K. Fox L. W. Gilley

The use of metallic copper in the design of some uranium processing plant equipment has established a need for information on the effects, from a nuclear safety standpoint, of copper placed in or near uranium solutions. Accordingly, a series of experiments to measure the poisoning effect of lattices of copper tubes and rods on an aqueous solution of uranyl fluoride was performed.

The solution used in these experiments was 93.2% U^{235}-enriched UO_2F_2 in water, at a concentration of 0.4693 g of U^{235} per cubic centimeter of solution, corresponding to an $H:U^{235}$ atomic ratio of 52.6. It was contained in a 10-in.-dia aluminum cylinder, which for most experiments was surrounded by a ¼-in.-thick copper shell, except for the top and bottom. With the exception of one case, the cylinder was reflected with water on the sides and bottom. In several experiments the copper tubes and rods were held in a stainless steel basket consisting of six ⅜-in.-dia by 6-ft-long rods equally spaced on a 9.5-in.-dia ring and attached to a perforated bottom plate. For most of the experiments, however, the copper was loaded directly into the containing vessel with edges in contact, forming a pseudo-triangular pattern. Using tubes having various diameters and wall thicknesses and placing small tubes inside larger tubes enabled the volume percentage of metal to be varied considerably.

The results of the experiments are given in Table 3.4.1, and typical curves showing the critical solution height as a function of the volume percentage of metal are plotted in Fig. 3.4.1. It can be seen that, for the case in which solution only was inside the cylinder, displacing a portion of the water reflector with the copper shell increased the critical solution height from 6.55 to 6.96 in. For the case in which the cylinder contained 27.7 vol % of copper, displacing a portion of the water reflector with the copper shell increased the solution critical height from 21.3 in. to 58.7 in. Inserting the stainless steel basket in the otherwise unpoisoned solution increased the critical height from 6.96 in. to 7.33 in., the copper

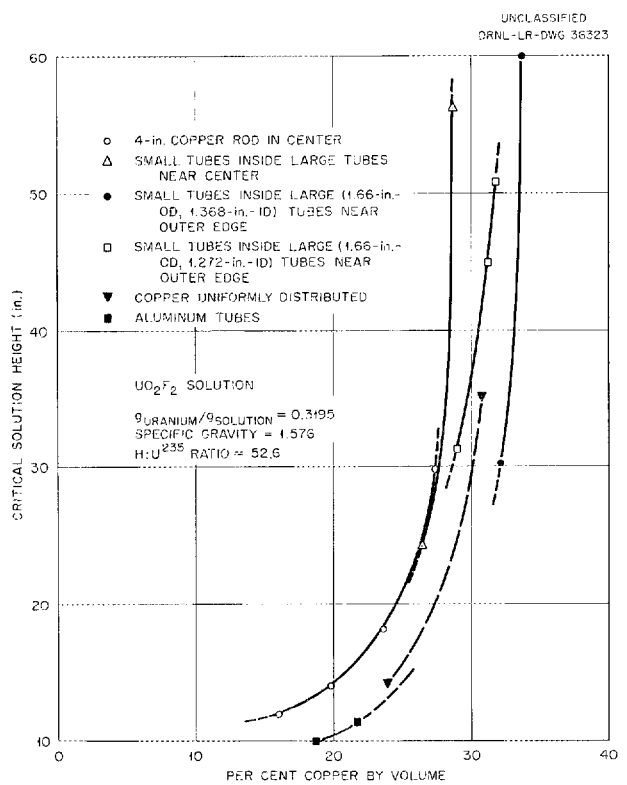

Fig. 3.4.1. Critical Height of a Reflected 10-in.-dia Aluminum Cylinder Containing a Copper-Poisoned Aqueous Solution of 93.2% U^{235}-Enriched UO_2F_2 as a Function of Copper Content.

Table 3.4.1. Critical Parameters of a 10-in.-dia Aluminum Cylinder Containing an Aqueous Solution of 93.2% U^{235}-Enriched UO_2F_2 Poisoned with Copper or Aluminum Tubes or Rods

Solution concentration: 0.3195 g of U per g of solution; 0.4693 g of U^{235} per cc of solution
$H:U^{235}$ atomic ratio: 52.6
Solution specific gravity: 1.576

Number of Tubes or Rods	Tube or Rod Dimensions (in.)		Metal Content (vol %)	Critical Conditions		Description of Assembly
	Inside Diameter	Outside Diameter		Solution Height (in.)	Mass (kg of U^{235})	
				H_2O Reflector Only		
				6.55	3.96	Contained solution only
				Copper Tubes and Rods; ¼-in.-thick Copper Shell Plus H_2O Reflector		
				6.96	4.21	Contained solution only
12 1	1.933 1.272	2.375 1.66	23.9	14.2	6.53	Tubes uniformly distributed
12 13	1.933 1.272	2.375 1.66	37.6	60.2 (NC)[a]		12 small tubes inside large tubes; one small tube outside
12 2 2 17 18	1.933 1.368 0.822 0.495	2.375 1.66 1.05 0.675 0.25	30.8	35.2	14.7	2.375- and 1.66-in. tubes uniformly distributed; smaller tubes successively placed in one another and uniformly distributed between large tubes
12 3 3 8 15	1.933 1.368 0.822 0.495	2.375 1.66 1.05 0.675 0.25	30.3	59.3 (NC)		Essentially same as preceding except one 2.375-in. tube near center filled with successively smaller tubes
26	1.272	1.66	29.5	31.3	13.3	Tubes uniformly distributed
26 2	1.272 0.736	1.66 1.05	30.7	60.4	25.3	Small tubes inside large tubes near center
26 3	1.272 0.736	1.66 1.05	31.2	45.0	18.7	Small tubes inside large tubes 120° apart on outer edge
26 4	1.272 0.736	1.66 1.05	31.8	50.8	20.9	Small tubes inside large tubes 90° apart on outer edge
26 4	1.272 0.736	1.66 1.05	31.8	50.5	20.8	Two small tubes inside large tubes; two small tubes outside; all on outer edge
26	1.368	1.66	23.0	14.5	6.75	Tubes uniformly distributed
26	1.368	1.66	23.0	58.4 (NC)		Tubes uniformly distributed; copper reflector only
26 6	1.368 0.736	1.66 1.05	27.4	24.2	10.8	Five small tubes inside large tubes near center; one small tube outside
26 10	1.368 0.736	1.66 1.05	28.7	56.2	24.2	Small tubes inside large tubes near center

Table 3.4.1 (continued)

Number of Tubes or Rods	Tube or Rod Dimensions (in.)		Metal Content (vol %)	Critical Conditions		Description of Assembly
	Inside Diameter	Outside Diameter		Solution Height (in.)	Mass (kg of U^{235})	
Copper Tubes and Rods; ¼-in.-thick Copper Shell Plus H_2O Reflector						
26 16	1.368 0.736	1.66 1.05	32.1	30.2	12.4	Small tubes inside large tubes near outer edge
26 19	1.368 0.736	1.66 1.05	33.7	60[b]	24.1	Small tubes inside large tubes around outer edge
Copper Tubes Contained in Stainless Steel Basket;[c] ¼-in.-thick Copper Shell Plus H_2O Reflector						
				7.33	4.69	Contained only stainless steel basket plus solution
60	0.822	1.05	25.6	22.2	9.98	Tubes uniformly distributed
60 10	0.822 0.495	1.05 0.675	27.7	58.7	25.7	Ten small tubes inside large tubes near center
Copper Tubes Contained in Stainless Steel Basket;[c] H_2O Reflector Only						
60	0.822	1.05	25.6	15.5	6.97	Tubes uniformly distributed
60 7	0.822 0.495	1.05 0.675	27.1	19.2	8.46	Seven small tubes inside large tubes near center
60 10	0.822 0.495	1.05 0.675	27.7	21.3	9.31	Ten small tubes inside large tubes near center
4-in.-OD Copper Rod Plus Tubes Held in Stainless Steel Basket;[c] ¼-in. Copper Plus H_2O Reflector						
1		4.0	16.0	11.9	6.39	Single rod in center
1 2	 1.933	4.0 2.375	19.8	14.0	6.79	Two tubes adjacent to copper rod on adjacent sides
1 4	 1.933	4.0 2.375	23.6	18.1	8.36	Small tubes placed around center rod
1 6	 1.933	4.0 2.375	27.4	29.8	15.6	Small tubes placed around center rod
1 6 2	 1.933 1.272	4.0 2.375 1.66	29.7	60 (NC)		Small tubes placed around center rod
Aluminum Tubes; ¼-in.-thick Copper Shell Plus H_2O Reflector						
7 9	2.062 1.590	2.375 1.875	18.7	9.88	4.86	Tubes uniformly distributed
7 12	2.062 1.590	2.375 1.875	21.7	11.3	5.35	Tubes uniformly distributed

[a]NC = not critical.

[b]This assembly was not critical, but the monitoring instruments indicated that removal of one small rod would have been more than sufficient to make the assembly critical.

[c]The calculations of critical volumes in these assemblies include the volume occupied by the basket; hence the volumes recorded are slightly high.

shell displacing part of the water reflector in both cases.

In some experiments the copper placement was varied in steps radially from the center. It was observed that the metal was more effective in positions near the center, a 4-in.-dia rod at the center having the greatest effect. It was also observed that for a given volume fraction the smaller-diameter tubes had a greater effect than the larger ones.

An indication of the relative effects of displacement of solution and poisoning by the copper was obtained by substituting aluminum tubes for copper in two experiments, since aluminum has a very low absorption cross section. Comparison of aluminum data with corresponding copper data where the tube sizes and distributions are similar indicates that displacement of solution is more important than the neutron absorption effect. This is clearly seen by comparison of the curves in Fig. 3.4.1.

3.5. CRITICAL PARAMETERS OF U^{235} AND U^{233} SOLUTIONS IN SIMPLE GEOMETRY

J. K. Fox
L. W. Gilley
R. Gwin
D. W. Magnuson

The measurement of the critical parameters of solutions of the fissionable uranium isotopes in simple geometry has been a continuing program for a number of years. The data presented in Tables 3.5.1 and 3.5.2 are an extension of previously reported experiments.[1,2]

For the U^{235} experiments performed in aluminum containers, an aqueous uranyl oxyfluoride solution enriched to 93.2% in U^{235} was used. The U^{235} solution in the stainless steel cylinders was an aqueous uranyl nitrate solution enriched to 92.8% in U^{235}. The nitrogen-to-uranium atomic ratio was about 3.8. An aqueous uranyl nitrate solution was also used for the U^{233} experiments. The uranium contained 97.4% U^{233} and the solution had a nitrogen-to-uranium atomic ratio of 2.4.

The value of the critical height (and hence volume and mass) reported herein for a 10-in.-dia water-reflected aluminum cylinder at an $H:U^{235}$ ratio of 49.5 is in disagreement with the previously reported value.[1] Since the present value is consistent with other data for the 10-in.-dia cylinder, whereas the earlier value is not, it is felt that there was an unaccounted-for error in the earlier experiment.

[1] J. K. Fox *et al.*, *Neutron Phys. Ann. Prog. Rep. Sept. 1, 1958*, ORNL-2609, p 42.

[2] J. K. Fox and L. W. Gilley, *Appl. Nuclear Phys. Ann. Prog. Rep. Sept. 1, 1957*, ORNL-2389, p 72.

Table 3.5.1. Critical Parameters of U^{235} Solutions in Simple Geometry

Solution Container and Diameter (cm)	Solution Concentration		Critical Values		
	U^{235} (g/cc)	$H:U^{235}$ Atomic Ratio	Height (cm)	Volume (liters)	Mass (kg of U^{235})
Totally Water Reflected					
Aluminum cylinders					
16.5	0.315	78.7	42.6	9.12	2.87
20.3	0.488	49.5	18.8	6.09	2.97
20.3	0.315	78.7	19.4	6.28	1.98
25.4	0.488	49.5	12.6	6.25	3.10
25.4	0.199	127	14.4	7.30	1.45
25.4*	0.488	49.5	16.5	8.35	4.08
Aluminum sphere					
55.9	0.0205	1270		91.2	1.87
No Reflector					
Stainless steel cylinders					
50.8	0.0259	1000	38.3	77.7	2.01
154.7	0.01613	1604	45.1	848	13.68
154.7	0.01422	1821	72.7	1,368	19.45
154.7	0.01359	1905	105.2	1,978	26.88
154.7	0.01307	1981	203.3	3,822	49.95
274	0.01324	1951	90.9	5,340	70.8
274	0.01292	2000	122.4	7,190	92.3
274	0.01261	2052	241.2	14,180	178.8

*This assembly was not reflected on top.

Table 3.5.2. Critical Parameters of Unreflected U^{233} Solutions in Simple Geometry

Solution Container	Solution Concentration		Critical Values		
	U^{233} (g/cc)	$H:U^{233}$ Atomic Ratio	Height (cm)	Volume (liters)	Mass (kg of U^{233})
154.7-cm-dia stainless steel cylinder	0.01412	1819	49.5	931	13.15
	0.01353	1900	59.2	1113	15.06
	0.01288	1966	77.7	1461	18.82
	0.01221	2106	139.0	2612	31.89

3.6. CRITICAL PARAMETERS FOR 20-in.-dia STAINLESS STEEL CYLINDERS CONTAINING AQUEOUS SOLUTIONS OF U^{235} POISONED WITH PYREX GLASS

J. K. Fox L. W. Gilley

The Nuclear Safety Group at the Y-12 Plant has suggested that Pyrex glass, nominally containing 4 wt % boron, might be a suitable poisoning material for ensuring nuclear safety in large vessels containing aqueous solutions of U^{235}-enriched uranium. An appropriate quantity of glass pipe contained in the storage vessels would prevent the achievement of criticality, even with optimum solution concentrations. Accordingly, a series of experiments has been performed to determine the volume per cent of glass necessary to assure subcritical conditions in both water-reflected and unreflected 20-in.-dia stainless steel cylinders containing aqueous solutions of U^{235}-enriched uranyl fluoride and uranyl nitrate.

Various diameters of Pyrex glass pipe were used, either in 3-ft lengths with their axes vertical to form lattices, or as short pieces (Raschig rings) randomly placed within the vessel to a height of 3 ft. For ease of handling, both the lattices and the randomly assembled arrays were contained in a stainless steel wire basket which fitted into the cylindrical experimental vessel. The results of all experiments are shown in Tables 3.6.1 and 3.6.2.

In a preliminary series of experiments, lattices of 1.5-in.-dia Pyrex pipe coated with a $\frac{1}{16}$-in. thickness of Unichrome, a polyvinyl chloride plastic, were used. The fuel solution was 93.2% U^{235}-enriched UO_2F_2 with an $H:U^{235}$ atomic ratio of 99.3, which is somewhat higher than the optimum ratio for minimum critical volumes. The resulting data are shown as Part A in Table 3.6.1. The volume fraction of glass plus coating required for poisoning was higher than that for the uncoated pipe used in subsequent experiments owing to the lesser poisoning effect of the Unichrome coating. Part A of Table 3.6.1 also shows the effect of replacing the UO_2F_2 solution with a $UO_2(NO_3)_2$ solution, which has a lower $H:U^{235}$ atomic ratio. The effect of substituting a cadmium-lined stainless steel cross for the pipe arrays in the UO_2F_2 solution was also determined.

Lattices of uncoated pipes of three different diameters were used with an 87.4% U^{235}-enriched $UO_2(NO_3)_2$ solution having an $H:U^{235}$ atomic ratio of 81.4. This concentration is very near that for minimum critical volume of nitrate solutions. Data from this solution are given in Part B of Table 3.6.1, and the critical height as a function of glass content is plotted in Fig. 3.6.1. The observed scatter in the data is believed to be due to an effect of the three diameters of pipe used. The curves indicate that for a system reflected with water on the sides and bottom, 15 vol % of glass, as 2-in.-dia pipe, would be sufficient to effectively poison a 20-in.-dia cylinder 3 ft long. For unreflected assemblies, 12 vol % would be required with 2-in.-dia pipes and 14 vol % required with 3-in.-dia pipes.

Parts C and D of Table 3.6.1 show the effect of two successive increases in the $H:U^{235}$ atomic ratio for 87.4% U^{235}-enriched $UO_2(NO_3)_2$ solutions. At an $H:U^{235}$ ratio of 141 the increased moderation increased the critical height of an unreflected cylinder containing 7.80 vol % of 2-in.-dia pipes from 16.7 in. to above 36 in., while the critical height of a reflected cylinder was increased from 9.75 in. to 12.5 in. For the same pipe assembly, a change in the $H:U^{235}$ ratio to 276 made the reflected 20-in.-dia cylinder subcritical.

The thickness of fuel above the top of the 36-in.-high Pyrex pipe assembly required for criticality is noted in the last column of Table 3.6.1. Comparison of these data with the clean critical height gives an indication of the neutron multiplication within the assembly. For example, the data in Part B show that an unreflected cylinder containing thirty-four 2-in.-dia pipes was not critical until the solution reached a height of 40.8 in., which was 4.8 in. above the top of the pipe assembly. This may be compared with a clean critical height for an unreflected system of ~5.5 in.

The results of experiments using Pyrex Raschig rings (1.469 in. OD by 1.28 in. ID by 1.56 in. long) in random arrays are presented in Table 3.6.2. Since a more homogeneous distribution of the boron poison resulted, the rings were more effective than any of the pipes used, a glass content of only 11 vol % being required to effectively poison the 20-in.-dia reflected cylinder. The data indicate that the effect of larger rings (2.375 in. OD by 2 in. ID by 2.375 in. long) is approximately the same as that of a pipe array occupying the same volume.

Table 3.6.1. Critical Parameters of Enriched Fuel Solutions Poisoned with Pyrex (~4 wt % Boron) Glass Pipe Lattices

Diameter of Pyrex Pipe (in.)	Number of Pipes	Center-to-Center Pipe Spacing (in.)	Glass Content (vol %)[a]	Reflector Condition[b]	Critical Values: Solution Height (in.)	Critical Values: Mass (kg of U^{235})	Remarks
A. Pipe Coated with 1/16-in. Unichrome; 93.2% U^{235}-Enriched UO_2F_2 Fuel Solution; $H:U^{235} = 99.3$							
1½	49	2.1	35.0	Reflected	c	c	No source neutron multiplication
1½	19	3.75	13.5	Bare	9.55	11.5	
1½	19	3.25	13.5	Bare	14.5	17.4	More free space on edges of this array than on above array
1½	19	3.25	13.5	Reflected	7.80	9.38	
1½	31	2.75	22.1	Bare	c	c	
1½	31	2.75	22.1	Reflected	16.3	17.6	
1½	31	2.75	22.1	Reflected	18.0	20.7	Fuel solution changed to solution in B below
				Bare	8.87	12.2	Cadmium cross substituted for Pyrex pipes[d]
B. Uncoated Pipe; 87.4% U^{235}-Enriched $UO_2(NO_3)_2$ Fuel Solution; $H:U^{235} = 81.4$							
1½	31	2.75	9.78	Reflected	12.7	16.9	
1½	31	2.75	9.78	Bare	26.6	35.6	
1½	53	2.13	16.7	Reflected	c	c	Critical when solution was 4.1 in. above top of pipe
2	34	2.68	13.95	Reflected	30.1	38.3	Closely packed
2	34	2.68	13.95	Bare	c	c	Critical when solution was 4.8 in. above top of pipe
2	19	3.00	7.80	Bare	16.7	22.9	
2	19	3.00	7.80	Reflected	9.75	13.3	Glass pipes arranged in an ~14-in.-dia central region of the cylinder
2	23	3.00	9.45	Reflected	11.6	15.5	
2	23	3.00	9.45	Bare	24.3	32.5	

Table 3.6.1 (continued)

Diameter of Pyrex Pipe (in.)	Number of Pipes	Center-to-Center Pipe Spacing (in.)	Glass Content (vol %)[a]	Reflector Condition[b]	Critical Values: Solution Height (in.)	Critical Values: Mass (kg of U^{235})	Remarks
B. Uncoated Pipe; 87.4% U^{235}-Enriched $UO_2(NO_3)_2$ Fuel Solution; $H:U^{235} = 81.4$							
2	28	2.68	11.5	Reflected	13.6	17.8	Closely packed except on edges
2	28	2.68	11.5	Bare	c	c	Critical when solution was 3.4 in. above top of pipe
3	16	3.78	11.34	Reflected	12.5	16.4	Closely packed
3	16	3.78	11.34	Bare	23.4	30.7	
			None	Reflected	4.98	7.33	Clean critical
			None	Bare	5.97	8.85	
C. Uncoated Pipe; 87.4% U^{235}-Enriched $UO_2(NO_3)_2$ Fuel Solution; $H:U^{235} = 141$							
2	19	3.0	7.80	Bare	c	c	Critical when solution was ~0.6 in. above top of pipe
2	19	3.0	7.80	Reflected	12.5	10.28	
			None	Reflected	5.19	4.62	Clean critical
			None	Bare	6.15	5.45	
D. Uncoated Pipe; 87.4% U^{235}-Enriched $UO_2(NO_3)_2$ Fuel Solution; $H:U^{235} = 276$							
2	19	3.0	7.80	Reflected	c	c	Critical when solution was 1.3 in. above top of pipe
			None	Reflected	5.41	2.53	Clean Critical
			None	Bare	6.60	3.11	

[a] Values include volume of the Unichrome coating when used.
[b] No top reflector in any of the experiments.
[c] Not critical when solution was at the level of the top of the pipe (36 in.).
[d] Glass replaced by 28-mil-thick cadmium-lined stainless steel cross 19.5 in. wide.

Table 3.6.2. Critical Parameters of Enriched Fuel Solutions Poisoned with Pyrex (~4 wt % Boron) Glass Raschig Rings in Random Arrays

Fuel solution: 87.4% U^{235}-enriched $UO_2(NO_3)_2$
$H:U^{235}$ atomic ratio: 81.4

Raschig Ring Dimensions			Glass Content (vol %)	Reflector Condition*	Critical Values		Remarks
Outside Diameter (in.)	Inside Diameter (in.)	Length (in.)			Solution Height (in.)	Mass (kg of U^{235})	
1.469	1.28	1.56	10.97	Reflected	Not critical		Critical when solution was 1.0 in. above top of rings
2.375	2.00	2.375	13.3	Reflected	19.6	25.1	
2.375	2.00	2.375	13.3	Bare	Not critical		Critical when solution was 4.0 in. above top of rings

*No top reflector in any of the experiments.

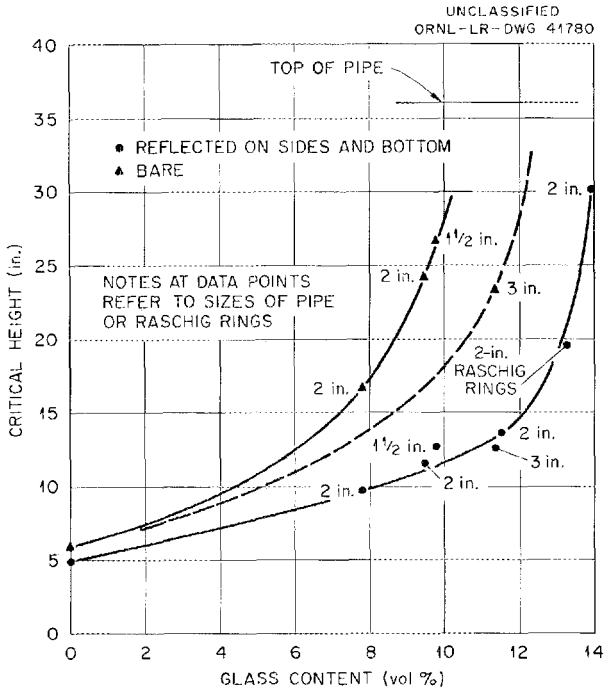

Fig. 3.6.1. Critical Heights, as a Function of the Pyrex Content, of Bare and Reflected 20-in.-dia Stainless Steel Cylinders Containing a Pyrex-Poisoned Aqueous Solution of 87.4% U^{235}-Enriched $UO_2(NO_3)_2$.

3.7. CRITICAL PARAMETERS OF UNREFLECTED ARRAYS OF INTERACTING CYLINDERS CONTAINING AQUEOUS SOLUTIONS OF U^{235}

J. K. Fox L. W. Gilley

A study of the critical parameters of aqueous solutions of 93.2% U^{235}-enriched uranyl fluoride in arrays of interacting cylinders was initiated several years ago. Experiments have been performed recently which extend these studies to include various unreflected arrays of aluminum cylinders containing solutions with $H:U^{235}$ atomic ratios of 297 and 309. (Previous work[1] with more than two cylinders was limited to an $H:U^{235}$ ratio of about 45.) The cylinders, which were coated on the inside with Heresite for protection against corrosion, had 6-, 8-, and 9.5-in. diameters and $\frac{1}{16}$-in.-thick walls. They were assembled in triangular, hexagonal, or line arrays that were isolated as far as possible from any reflecting material. In this respect, they differ from earlier unreflected experiments which were performed in a 9.5-ft-dia steel tank.

The results of measurements with 6- and 8-in.-dia cylinders for solutions with an $H:U^{235}$ atomic ratio of 309 are given in Table 3.7.1 and Fig. 3.7.1. Since single 6- or 8-in.-dia cylinders are not critical, the critical heights of arrays of these cylinders increase rapidly as the edge-to-edge spacings of the cylinders are increased. Because an isolated 8-in.-dia cylinder is more nearly critical than a 6-in.-dia cylinder, arrays of 8-in.-dia cylinders require wider spacings to approach an infinite critical height.

Interacting arrays of unreflected 9.5-in.-dia cylinders containing solutions with an $H:U^{235}$

[1] J. K. Fox, L. W. Gilley, and D. Callihan, *Critical Mass Studies, Part IX, Aqueous U^{235} Solutions*, ORNL-2367 (Feb. 5, 1958); see also J. K. Fox and L. W. Gilley, *Appl. Nuclear Phys. Ann. Prog. Rep. Sept. 10, 1956*, ORNL-2081, p 63.

Table 3.7.1. Critical Parameters of an Aqueous Solution of 93.2% U^{235}-Enriched Fluoride Contained in Unreflected 6- and 8-in.-dia Aluminum Cylinders in Hexagonal and Triangular (Equilateral) Arrays

Solution concentration: 0.0812 g of U per g of solution; 0.0836 g of U^{235} per cc of solution
$H:U^{235}$ atomic ratio: 309
Specific gravity: 1.105

Edge-to-Edge Cylinder Spacing (in.)	Cylinder Diameter (in.)	Critical Values		
		Height (in.)	Volume (liters)	Mass (kg of U^{235})
		Seven-Cylinder Hexagonal Array		
0.3	6	12.2	39.5	3.30
1.0	6	22.4	72.4	6.05
2.0	6	77*	~250	~21
1.0	8	11.3	65.1	5.44
3.0	8	17.8	103	8.62
6.0	8	35.4	205	17.1
7.0	8	46.9	271	22.6
		Three-Cylinder Triangular Array		
0.15	8	16.3	40.5	3.39
1.0	8	31.2	77.2	6.46
2.0	8	**		

*Extrapolated from fuel height of 63 in.

**Extrapolation indefinite (probably not critical at any height).

atomic ratio of 297 have been studied in a variety of configurations. The data are shown in Table 3.7.2. Figure 3.7.2 presents a plot of critical height as a function of edge-to-edge spacing for various in-line arrays of these cylinders. The graph demonstrates that the effect obtained by adding a cylinder decreases as the total number of cylinders in line increases, as expected. The addition of a sixth cylinder to an existing row of

Table 3.7.2. Critical Parameters of an Aqueous Solution of 93.2% U^{235}-Enriched Uranyl Fluoride Contained in Unreflected 9.5-in.-dia Cylinders in Line, Triangular, Square, and Hexagonal Arrays

Solution concentration: 0.0841 g of U per g of solution; 0.0868 g of U^{235} per cc of solution

$H:U^{235}$ atomic ratio: 297

Specific gravity: 1.109

Edge-to-Edge Cylinder Spacing (in.)	Critical Values		
	Height (in.)	Volume (liters)	Mass (kg of U^{235})
Two-Cylinder Line Array			
1.0	24.1	56.1	4.87
3.0	31.7	73.9	6.41
6.0	44.5	104	9.03
8.0	54.0	126	10.9
Three-Cylinder Line Array			
2.0	22.3	78.1	6.78
6.0	33.2	116	10.1
10.0	43.8	153	13.3
15.0	60.1	211	18.3
Four-Cylinder Line Array			
3.0	22.7	106	9.20
6.0	30.0	138	12.0
10.0	38.5	180	15.6
Five-Cylinder Line Array			
3.0	21.7	127	11.0
6.0	28.3	165	14.3
10.0	36.2	211	18.3
Six-Cylinder Line Array			
3.0	21.3	149	12.9
10.0	34.8	243	21.1
Three-Cylinder Triangular Array			
1.0	13.4	47.0	4.08
4.0	20.3	70.8	6.15
8.0	28.1	98.2	8.52
12.0	36.3	127	11.0
18.0	49.7	174	15.1
22.0	60.1	211	18.3
Four-Cylinder Square Array			
3.0	15.8	73.8	6.40
10.0	27.2	127	11.0
22.0	47.4	220	19.1
30.0	62.5	292	25.3
Seven-Cylinder Hexagonal Array			
3.0	12.1	98.6	8.56
10.0	20.1	164	14.2
22.0	32.9	268	23.3

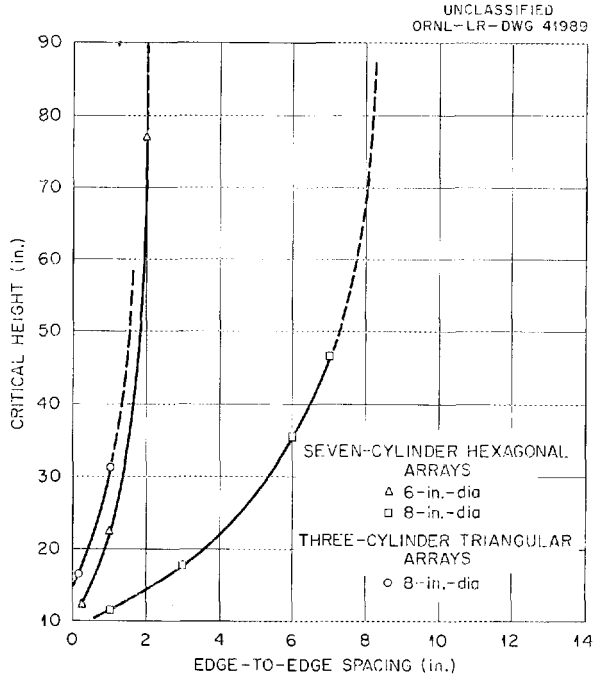

Fig. 3.7.1. Critical Solution Height as a Function of Edge-to-Edge Spacing of Unreflected Triangular and Hexagonal Arrays of 6- and 8-in.-dia Aluminum Cylinders Containing Aqueous Solutions of 93.2% U^{235}-Enriched Uranyl Fluoride ($H:U^{235}$ Atomic Ratio = 309).

five increased the over-all reactivity by approximately 26 cents. The effect of the addition appears to be insensitive to the edge-to-edge spacing.

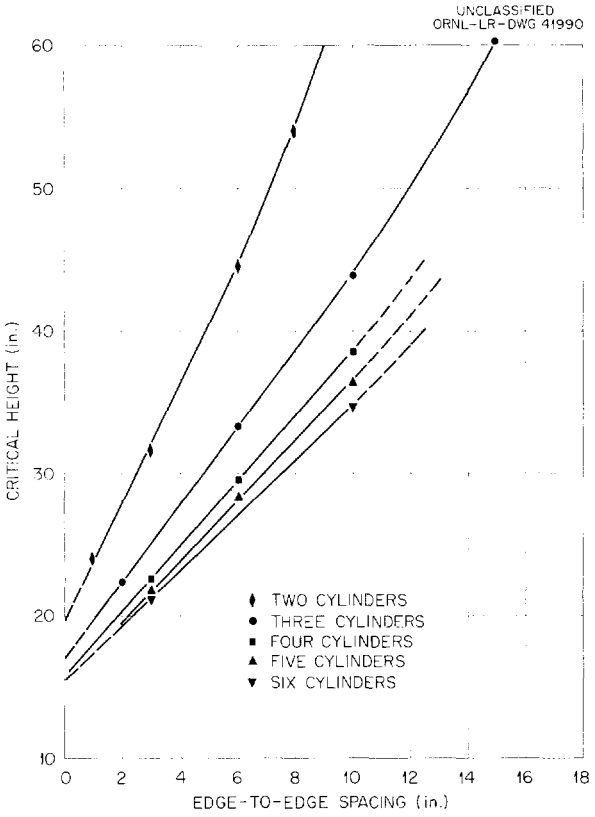

Fig. 3.7.2. Critical Solution Height as a Function of Edge-to-Edge Spacing of Unreflected Straight-Line Arrays of 9.5-in.-dia Aluminum Cylinders Containing Aqueous Solutions of 93.2% U^{235}-Enriched Uranyl Fluoride ($H:U^{235}$ Atomic Ratio = 297).

Figure 3.7.3 shows the variation in critical height as a function of the cylinder edge-to-edge spacing for the triangular, square, and hexagonal arrays of 9.5-in.-dia cylinders. In this figure, as opposed to the data in Fig. 3.7.1 for smaller cylinders, the variation is linear out to a spacing of about 20 in.

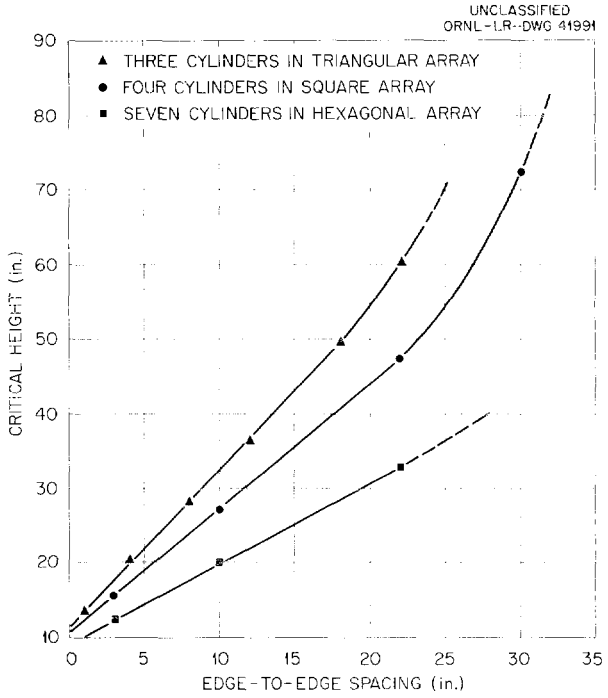

Fig. 3.7.3. Critical Solution Height as a Function of Edge-to-Edge Spacing of Unreflected Triangular, Hexagonal, and Square Arrays of 9.5-in.-dia Aluminum Cylinders Containing Aqueous Solutions of 93.2% U^{235}-Enriched Uranyl Fluoride ($H:U^{235}$ Atomic Ratio = 297).

3.8. HOMOGENEOUS CRITICAL ASSEMBLIES OF 2% U^{235}-ENRICHED UF_4 IN PARAFFIN

J. T. Mihalczo J. J. Lynn

Critical experiments with a homogeneous mixture of 2% U^{235}-enriched UF_4 and paraffin with an $H:U^{235}$ atomic ratio of 404 have been initiated to extend the data previously reported.[1,2] This fuel mixture contains 84.8 wt % UF_4 and has a uranium density of 2.2 g/cc.

Both cylindrical and parallelepipedal geometries have been assembled, some of which were surrounded with an effectively infinite reflector of paraffin and Plexiglas. The minimum critical volumes and minimum critical masses have been established and are shown in Figs. 3.8.1 and 3.8.2, along with the results of the previous experiments[2] with mixtures having $H:U^{235}$ atomic ratios of 195 and 294.

Since the last report[1] sufficient fuel with an $H:U^{235}$ atomic ratio of 195 was obtained to make unreflected assemblies critical. The results are included in the figures.

[1] J. J. Lynn, J. T. Mihalczo, and W. C. Connelly, *Neutron Phys. Ann. Prog. Rep. Sept. 1, 1958*, ORNL-2609, p 40.

[2] J. T. Mihalczo *et al.*, *Preliminary Report on 2% U^{235}-Enriched UF_4-$C_{25}H_{52}$ Critical Assemblies*, ORNL CF-59-4-120 (1959).

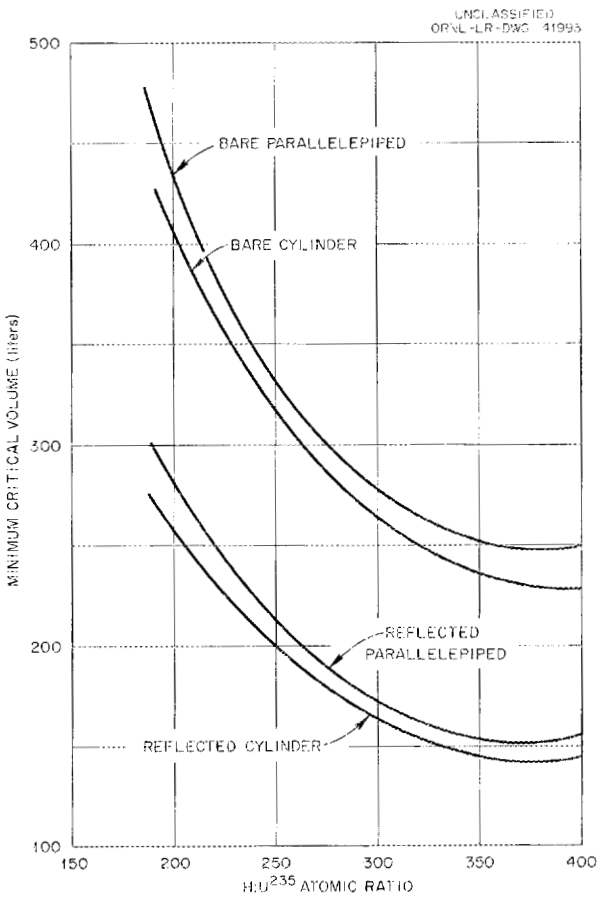

Fig. 3.8.1. Critical Volume of 2% U^{235}-Enriched UF_4-$C_{25}H_{52}$ as a Function of the $H:U^{235}$ Atomic Ratio.

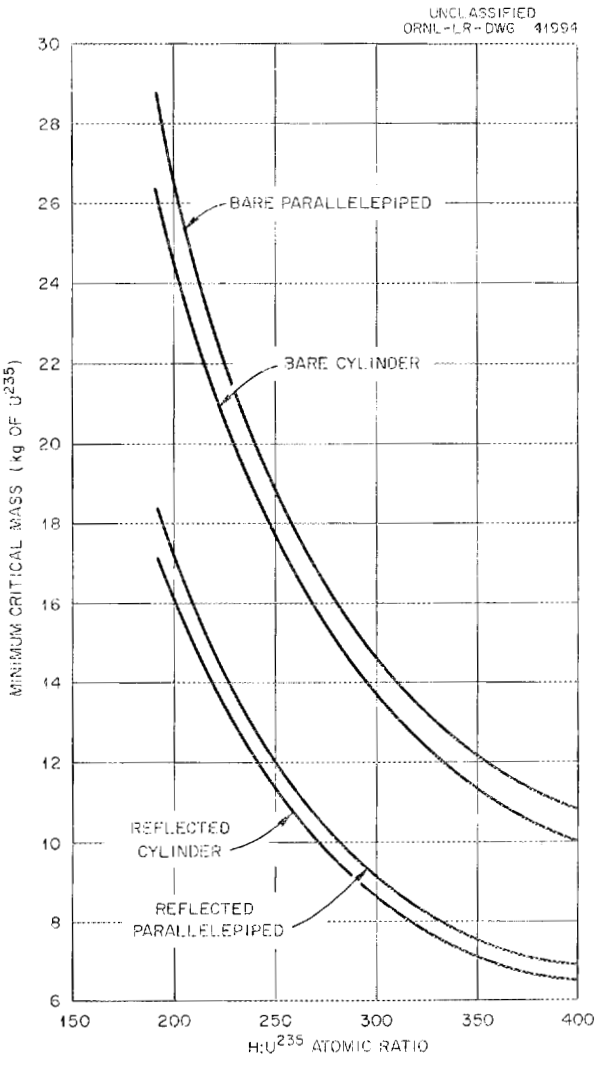

Fig. 3.8.2. Critical Mass of 2% U^{235}-Enriched UF_4-$C_{25}H_{52}$ as a Function of the $H:U^{235}$ Atomic Ratio.

3.9. DETERMINATION OF THE INFINITE MEDIUM MULTIPLICATION FACTOR FOR 2% U^{235}-ENRICHED UF_4 IN PARAFFIN

J. T. Mihalczo

The infinite medium multiplication factor for a mixture of 2% U^{235}-enriched UF_4 and paraffin with an $H:U^{235}$ atomic ratio of 195 has been determined. A series of critical experiments with this material was previously reported.[1] The material is a homogeneous mixture which contains 92 wt % UF_4 and 8 wt % paraffin and has a density of 4.5 g/cc. The average UF_4 particle size is 0.020 in.

The experiments consisted in making known changes in the buckling of critical systems and measuring the resulting stable periods. The interpretation was based on the critical equation

$$k_\infty P(B) = 1 \quad , \tag{1}$$

the static relation

$$k_{\text{eff}} = (1 - \beta)\, k_\infty\, K_p(B) + \frac{\beta}{\epsilon}\, k_\infty\, K_d(B) \quad , \tag{2}$$

and the kinetic relation

$$\Delta k = \frac{l}{T} + \frac{k_\infty}{\epsilon}\, K_d(B) \sum_i \frac{\beta_i}{1 + \lambda_i T} \quad , \tag{3}$$

where

$P(B)$ = nonleakage probability for all neutrons from fission,

$K_p(B)$ = nonleakage probability for prompt neutrons from fission,

$K_d(B)$ = average nonleakage probability for delayed neutrons.

For $T \sim 100$ sec the term l/T in (3) can be ignored.

For an incremental change in the buckling, (2) can be written as

$$\Delta k = (1 - \beta)\, k_\infty \sum \frac{\partial^m K_p(B)}{(\partial B^2)^m} \frac{(\Delta B^2)^m}{m!} + \beta\, \frac{k_\infty}{\epsilon} \sum \frac{\partial^m K_d(B)}{(\partial B^2)^m} \frac{(\Delta B^2)^m}{m!} \quad . \tag{4}$$

From (3) and (4)

$$K_d(B) \sum \frac{\beta_i}{1 + \lambda_i T} = \epsilon(1 - \beta) \sum \frac{\partial^m K_p}{(\partial B^2)^m} \frac{(\Delta B^2)^m}{m!} + \beta \sum \frac{\partial^m K_d(B)}{(\partial B^2)^m} \frac{(\Delta B^2)^m}{m!} \quad . \tag{5}$$

The nonleakage probability was obtained from both one- and two-group models by the usual expressions:

$$K_{d[p]}(B) = \frac{1}{(1 + M^2_{d[p]} B^2)} \quad , \tag{6}$$

$$K_{d[p]}(B) = \frac{1}{(1 + \tau_{d[p]} B^2)(1 + L^2 B^2)} \quad , \tag{7}$$

where

L = thermal diffusion length,

M_p^2, M_d^2 = migration area for prompt and delayed neutrons, respectively,

τ_p, τ_d = age to thermal for prompt and delayed neutrons, respectively.

Expressions for M_p^2 and τ_p can be obtained by combining (5) and (6) or (5) and (7) if β, L^2, B^2, ΔB^2, $\Delta\rho$, ϵ, and τ_d are known. The thermal diffusion area L^2 is computed from thermal cross sections[2] and is 1.8 cm^2. The buckling B^2 is a measured quantity obtained from the critical size of the assemblies and the measured extrapolation distance. The change in buckling ΔB^2 is known from the perturbations made on the systems. The change in reactivity $\Delta\rho$ is determined from the analysis of the stable periods produced by the perturbations. In determining $\Delta\rho$ from the inhour equation, fast fission in the U^{238} is accounted for. The fast fission factor ϵ is measured by using both depleted and enriched uranium foils and also by using depleted and enriched fission chambers. The neutron age to 0.8 ev for prompt fission neutrons and delayed neutrons of several initial

[1] J. T. Mihalczo *et al.*, *Preliminary Report on 2% U^{235}-Enriched UF_4-$C_{25}H_{52}$ Critical Assemblies*, ORNL CF-59-4-120 (1959).

[2] D. J. Hughes and R. B. Schwartz, *Neutron Cross Sections*, 2d ed., BNL-325 (July 1, 1958).

energies was determined by a Monte Carlo moments method calculation on the Oracle.[3] The results are shown in Table 3.9.1. The average delayed neutron age, τ_d, used in the analysis of the experiments was 25.6 ± 2.5 cm^2. The resulting values of M_p^2 and τ_p were then used to determine K_p.

Table 3.9.1. Neutron Age to 0.8 ev for a UF_4-CH_2 Mixture with an H:U^{235} Atomic Ratio of 195*

Source Energy (kev)	Neutron Age to 0.8 ev (cm^2)
Prompt neutron spectrum	47.20**
460	24.98
450	25.00
420	24.86
405	23.87
250	21.50

*Calculations by J. G. Sullivan, Neutron Physics Division.

**Inelastic scattering of prompt neutrons was neglected.

The relation for the infinite medium multiplication factor obtained from (1) and (2) is

$$k_\infty = \frac{1}{(1-\beta)\,K_p(B) + \frac{\beta}{\epsilon}\,K_d(B)} \,. \qquad (8)$$

The parameters for the various assemblies are given in Table 3.9.2, along with the values of k_∞, which are to be compared with a k_∞ value of 1.216 ± 0.013 determined from a Physical Constants Test Reactor experiment at Hanford.[4]

[3] R. R. Coveyou, *Appl. Nuclear Phys. Ann. Prog. Rep. Sept. 10, 1956*, ORNL-2081, p 144.

[4] V. I. Neeley, *Trans. Am. Nuclear Soc.* 2, 67 (1959).

Table 3.9.2. Parameters of 2% U^{235}-Enriched UF_4 in Paraffin

	71.5 × 71.5 cm Assembly*		81.7 × 86.7 cm Assembly*	
	One-Group Model	Two-Group Model	One-Group Model	Two-Group Model
M_p^2 (cm^2)	45.0 ± 3.5		46.1 ± 3.6	
τ_p (cm^2)		43.3 ± 3.5		44.4 ± 3.6
k_∞	1.195 ± 0.015	1.197 ± 0.015	1.200 ± 0.016	1.202 ± 0.016
B^2 (cm^{-2})	0.004332		0.004355	
ϵ	1.0407 ± 0.002		1.0398 ± 0.002	
Critical height (cm)	94.1		66.7	

*Base dimensions.

3.10. CRITICAL MASSES OF 93% U^{235}-ENRICHED URANIUM METAL "BUTTONS" AND "BRIQUETTES"

J. K. Fox L. W. Gilley

A series of experiments has been performed to provide data for the safe handling of uranium metal "buttons" and "briquettes" in processing plants. The buttons were each about 4 in. in diameter and $\frac{3}{4}$ to 1 in. thick, weighing from 4 to 6 kg. The briquettes consisted of metal shavings compressed into cylindrical shapes 4 in. in diameter and from 2 to 4 in. thick. One experiment was also performed with uranium metal pellets which were $\frac{1}{8}$-in.-dia rods approximately $\frac{1}{4}$ in. long.

In most of the experiments the uranium with water moderator was held in cylindrical graphite crucibles 7, 9, or 12 in. in diameter. The crucibles were approximately 1 in. thick and had heights that were about 50% greater than their diameters. Both reflected and unreflected cases were investigated. A few experiments were performed in a 6.7-in.-dia stainless steel beaker in order to obtain information on the relative reflecting properties of graphite and stainless steel. In some additional experiments the 7-in.-dia graphite crucible was placed in a firebrick annulus surrounded by copper cooling coils to simulate a remelt furnace.

In all cases the buttons and briquettes were stacked in the crucibles with a minimum of voids. It was discovered that the briquettes expanded appreciably with use owing to the absorption of water. This increased moderation reduced the critical mass by several per cent.

The loadings of the critical assemblies are shown in Table 3.10.1 and those of noncritical assemblies in Table 3.10.2. From these data the estimated critical mass for a fully reflected button assembly in the 7-in.-dia graphite crucible is 24 kg of metal, while the estimated critical mass for the buttons in the reflected 6.7-in.-dia stainless steel beaker is 27 kg. The difference is attributed to the difference in the reflecting properties of the two containers. The estimated critical masses for the fully reflected 9- and 12-in.-dia crucibles are 27 and 36 kg of metal, respectively, the difference being due to the difference in geometry. The critical masses of the unreflected button assemblies are less well defined than those for the reflected assemblies, since there was some reflector effect from the graphite containers and in some cases the moderator-water height was higher than the uranium. The estimated critical masses vary from about 42 kg of metal for the 7-in.-dia crucible to about 49 kg for the 12-in.-dia crucible. The minimum critical mass for a reflected button assembly is about 22 kg of U^{235}.

Excluding the experiments with the water-soaked briquettes, the lowest critical mass for a reflected briquette assembly occurred in a 12-in.-dia crucible; this was no doubt caused by the fact that the packing density of the briquettes was lower in the larger container. The estimated minimum critical mass for a fully reflected briquette assembly is approximately 23 kg of U^{235}.

Since only one experiment was performed with the metal "pellets," the results are inconclusive, but the data indicate that the pellets are less reactive than the buttons.

Table 3.10.1. Critical Loadings of 93% U^{235}-Enriched Uranium Metal Buttons and Briquettes

Container	Metal Loading (kg of U)	Average Fuel Height (in.)	Water Height (in.)		Remarks
			Moderator	Reflector	
			Uranium Metal Button		
7-in.-ID graphite crucible	47.3	8.0	7.1		No reflector; buttons not all submerged
	40.0	6.2	8.8		Assembly had 2.6-in. top reflector only
	23.9	4.5	7.0	7.0	
	26.0	4.8	6.1	6.1	
9-in.-ID graphite crucible	26.9	3.8	7.0	7.0	
	40.4	5.0	5.7		No reflector
	38.5	5.0	7.8		Assembly had 2.8-in. top reflector only
12-in.-ID graphite crucible	36.5	2.3	6.1	6.1	
	47.4	3.5	4.8		Assembly had 1.3-in. top reflector only
	44.0	3.5	5.3		Assembly had 1.8-in. top reflector only
7-in.-ID graphite crucible surrounded with fire-brick and Cu coils	38.0	6.5	7.5		Assembly had 1-in. top reflector only
	35.2	6.5	8.4		Assembly had 1.9-in. top reflector only
	27.0	5.0	6.6	6.6	
6.7-in.-dia stainless steel beaker	26.8	4.7	8.3	8.3	
	27.5	4.7	7.0	7.0	
			Uranium Metal Briquettes		
9-in.-ID graphite crucible	31.1	9.8	9.7	9.7	
	28.4	9.5	10.1	10.1	
	26.2*	8.3	9.1	9.1	
	22.7*	7.5	12.0	12.0	
12-in.-ID graphite crucible	37.2	7.8	8.3		
	34.9	7.0	9.1		Assembly had 2.1-in. top reflector only
	26.3	5.5	6.9	6.9	

*These runs were made after briquettes had expanded with use in water.

Table 3.10.2. Noncritical Loadings of 93% U^{235}-Enriched Uranium Metal Buttons, Briquettes, and Pellets

Container	Metal Loading (kg of U)	Average Fuel Height (in.)	Water Height (in.)		Remarks
			Moderator	Reflector	
Uranium Metal Buttons					
7-in.-ID graphite crucible	23.0	4.0	9.5	9.5	
9-in.-ID graphite crucible	26.4	3.8	10.8	10.8	
12-in.-ID graphite crucible	35.3	2.3	10.0	10.0	Small neutron source multiplication observed
	41.0	3.5	9.6		Assembly had 6.1-in. top reflector only
	46.6	6.0	11.0	11.0	Fuel formed an 8-in.-ID by 12-in.-OD annulus
7-in.-ID graphite crucible surrounded with fire-brick and Cu coils	33.5	6.0	10.1		Assembly had 4.1-in. top reflector only; moderate neutron source multiplication observed
	25.0	4.5	9.5	9.5	Moderate neutron source multiplication observed
6.7-in.-dia stainless steel beaker	40.6	6.7	6.7	0.6	Bottom reflector; small neutron source multiplication observed
Uranium Metal Briquettes					
7-in.-ID graphite crucible	23.5	10.4	15.1	15.1	Small neutron source multiplication observed
9-in.-ID graphite crucible	25.4	8.3	14.3	14.3	
	43.8	13.8	13.8		Small neutron source multiplication observed
12-in.-ID graphite crucible	34.0	7.0	12.0		Assembly had 5.0-in. top reflector only; high neutron source multiplication observed
	23.5	4.5	12.1	12.1	
Uranium Metal Pellets					
6.7-in.-dia stainless steel beaker	21.8	3.4	8.5	8.5	Small neutron source multiplication observed

Part 4

FISSION PHYSICS

4.1. PRELIMINARY RESULTS FROM A DETERMINATION OF THE LOW-ENERGY PORTION OF THE GAMMA-RAY SPECTRUM EMITTED PROMPTLY AFTER FISSION OF U^{235} BY THERMAL NEUTRONS

T. A. Love F. C. Maienschein R. W. Peelle

The energy spectrum of gamma rays emitted promptly ($<5 \times 10^{-8}$ sec) after fission of U^{235} by thermal neutrons has previously been studied for energies above 400 kev, and the results obtained from a preliminary analysis of part of the data have been reported.[1] The final analysis has been carried forward and is complete except for corrections for the nonunique spectrometer response and for the variation of spectrometer efficiency with gamma-ray energy. At the lowest energies considered in these measurements ($\sim$350 kev), a peak in the spectrum was observed. In order to verify the reality of this peak and the possible existence of other peaks, an additional measurement of gamma rays in the 10- to 800-kev range was initiated. (A similar measurement, not on an absolute yield basis and without discrimination against neutron effects, has been reported elsewhere.[2])

Knowing the low-energy prompt-fission gamma-ray spectrum is important for reactor heating considerations, since the energy of these gamma rays can be deposited in a relatively thin layer of reactor material. For the study of this lower energy region it appeared feasible to employ a single-crystal spectrometer, since the peak-to-total ratios are not too small (for the crystal used the ratio was >0.5 for energies below $\sim$0.5 Mev). A time-of-flight technique, made possible because the high inherent efficiency of the single crystal allowed a sufficiently long flight path, was utilized to exclude pulses from neutron interaction effects in the scintillator. Without this extra discrimination, the neutron effects in the single crystal would have been appreciably greater than those which have been observed for a multiple-crystal spectrometer.[3]

The crystal used in the spectrometer was an NaI(Tl) scintillation crystal 1.75 in. in diameter by 1.0 in. thick, protected on the end by a thin cover. It examined the gamma rays from a four-plate fission chamber, containing approximately 14.0 mg of U^{235}, through a 342-cm flight path of helium contained within thin foils. A largely thermal neutron beam from the ORNL Graphite Reactor produced about 25,000 fission counts/sec in the fission chamber. Extensive shielding of lead and lithiated paraffin reduced the background to an unimportant level. Studies were made of the response of the spectrometer to numerous monoenergetic gamma-ray sources in order to ascertain the pulse-height spectral response in the presence of the shielding and collimator system. Gamma-ray and x-ray sources were also used repeatedly to determine the energy vs pulse-height calibrations for the spectrometer.

In order to discriminate against fission neutrons which might travel down the flight path and interact exoergically in the scintillator, the output of the gamma-ray spectrometer was examined at a time after a fission event corresponding to the flight time for a photon ($\sim 10^{-8}$ sec). The resolving time employed in the coincidence circuit used to establish time coincidence was $(7.0 \pm 0.1) \times 10^{-8}$ sec. Because of the jitter in time due to the poor electron statistics at the photocathode of the electron multiplier for the low-energy gamma rays studied, it was necessary to determine the "efficiency" of the coincidence circuit as a function of gamma-ray energy. This determination was made with a short flight path ($\sim$15 cm) and a variable time delay between the two signals. Representative preliminary values for the coincidence-circuit efficiency are given in Table 4.1.1.

For the very approximate calculations of absolute spectral yield reported below, the spectrometer efficiency was guessed on the basis of measurements for a similar crystal.[4] This approach is poor for continuous spectral distributions because

[1] R. W. Peelle, F. C. Maienschein, and T. A. Love, *Neutron Phys. Ann. Prog. Rep. Sept. 1, 1958*, ORNL-2609, p 45–46; F. C. Maienschein *et al.*, *Proc. U.N. Intern. Conf. Peaceful Uses Atomic Energy, 2nd, Geneva, 1958* 15, 366–72 (1959).

[2] V. K. Voitovetskii, B. A. Levin, and E. V. Marchenko, *J. Exptl. Theoret. Phys. (U.S.S.R.)* 5, 184–88 (1957).

[3] F. C. Maienschein, R. W. Peelle, and T. A. Love, *Appl. Nuclear Phys. Ann. Prog. Rep. Sept. 1, 1957*, ORNL-2389, p 103.

[4] W. E. Mott and R. B. Sutton, *Handbuch der Physik* (ed. by S. Flügge), vol XLV, p 128, Springer, Berlin, 1958.

Table 4.1.1. Coincidence Circuit Efficiency (Preliminary)

Gamma-Ray Energy Absorbed in the Scintillator (Mev)	Coincidence Circuit Efficiency*
0.01	0.77 ± 0.03
0.015	0.89 ± 0.02
0.025	0.97 ± 0.02
0.035	0.98 ± 0.01
0.050	1.00 ± 0.005
> 0.05	1.000

*Defined as the fraction of pulses from true prompt gamma rays which were accepted as such by the coincidence circuit, using a $(7.0 \pm 0.1) \times 10^{-8}$ sec resolving time.

no correction has been made for the Compton tails resulting from the spectrometer response to higher-energy gamma rays.

The calculated subtraction of chance background was demonstrated to be correct by delaying the signals from the gamma-ray detector by 0.96 μsec and noting the agreement of the observed spectrum due to random coincidences with the predicted spectrum.

The data points in Fig. 4.1.1 show coincidence count rates obtained by delaying the signal from the fission chamber channel. The peak at 1.5×10^{-7} sec corresponds to the prompt-fission gamma rays. Greater times correspond to delayed gamma rays or neutrons. The expected contribution due to gamma rays from short-lived isomers which would penetrate a 1.75-mm-thick lead filter between the fission chamber and flight path is shown by the dashed curve, which was normalized to the prompt peak at 1.5×10^{-7} sec. This contribution was obtained with a time analyzer and a flight path of only a few centimeters. It has been corrected for the resolving time used in the measurement. The expected neutron contribution, indicated by the dotted curve, corresponds to the known prompt-fission neutron spectrum converted to a time scale appropriate to a 342-cm flight path and smeared to account for jitter in the gamma-ray detector and the coincidence resolving time. Constant efficiency vs energy was assumed to obtain this curve, which is normalized arbitrarily. The dash-dot curve, which is the sum of the plotted isomer and fission-neutron effects, fits the shape of the observed delayed data.

Spectral data (with poor statistics) were obtained at a delay time of 3×10^{-7} sec, corresponding to the maximum fission-neutron effects in the crystal. These spectra showed the most prominent of the usual peaks[3] (at 0.06 and 0.21 Mev) due to interaction of neutrons and sodium iodide.

Pulse-height spectra obtained with a time delay corresponding to the gamma-ray peak of Fig. 4.1.1 are shown in Fig. 4.1.2. The results of three runs at different gains are given. A total of 14 runs

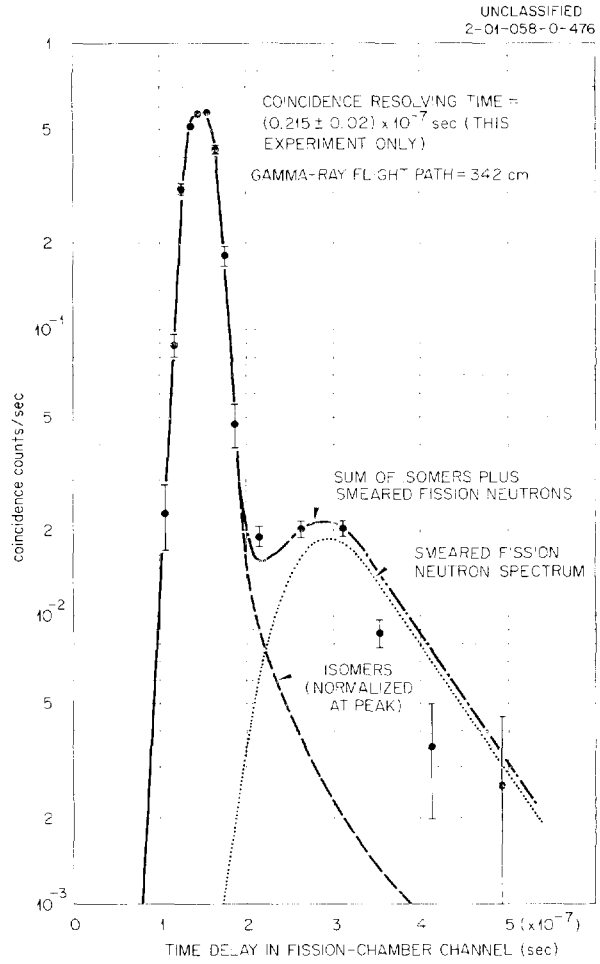

Fig. 4.1.1. Coincidence Count Rate as a Function of Time Delay (from an Arbitrary Zero) of the Fission Chamber Signal. Errors shown are statistical only. Gamma-ray channel set to accept pulses corresponding to energies in the range 0.035 Mev $\leq E \leq$ 0.99 Mev; 1.75-mm-thick lead absorber.

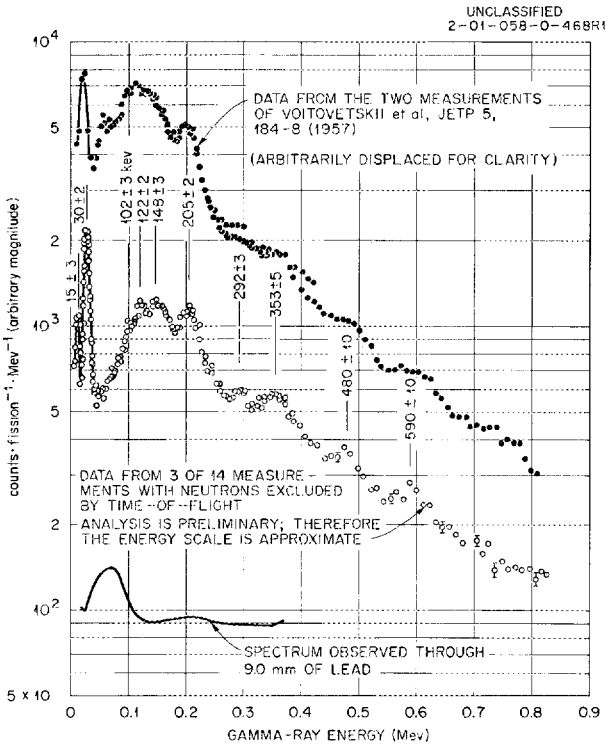

Fig. 4.1.2. Pulse-Height Spectra of Prompt Gamma Rays from the Thermal Fission of U^{235}. The top curve is the data of Voitovetskii *et al.*, the middle and lower curves are obtained with a coincidence resolving time of $(7.0 \pm 0.015) \times 10^{-8}$ sec and a 342-cm flight path. A 9.0-mm-thick lead disk was inserted in the flight path adjacent to the fission chamber to obtain the bottom curve.

was completed at these three gains. The energy scale is approximate with an error of 2% or 2 kev, whichever is greater, an error estimate which will be significantly reduced in the final data analysis. Energies of the apparent peaks in the spectrum are shown on the graph. The corresponding data of Voitovetskii[2] are also shown. He used a smaller crystal of sodium iodide and no time-of-flight discrimination against neutrons and therefore a much smaller detector-source separation distance. The curve at the bottom of Fig. 4.1.2 shows the results obtained with a 9.0-mm-thick lead sheet placed in the flight path. With this gamma-ray absorber present, any neutron-induced peaks should be greatly enhanced relatively. Similar data, not shown on the figure, were taken for a thicker piece of lead at the lowest gain, and the absorption effects of the lead were experimentally checked with monoenergetic sources of gamma rays and compared with good-geometry calculations. As shown by the lead data, any neutron peak at 60 kev is less than 10% as intense as the fission gamma rays, and at other energies the neutron-induced pulses are negligible. The very broad peak in the lead data at ~60 kev may include the effects of lead x rays.

The data of Fig. 4.1.3 represent the results of applying the approximate spectrometer efficiency values tabulated above to the spectral data of Fig. 4.1.2. The logarithmic energy scale makes more apparent the low-energy peaks due to the x rays emitted by the light and heavy fission fragments. The absolute intensities in this energy region are affected appreciably by the gamma-ray absorption in the fission chamber, but no correction has yet been made.

The new data substantiate the existence of a peak at ~350 kev as previously indicated by the

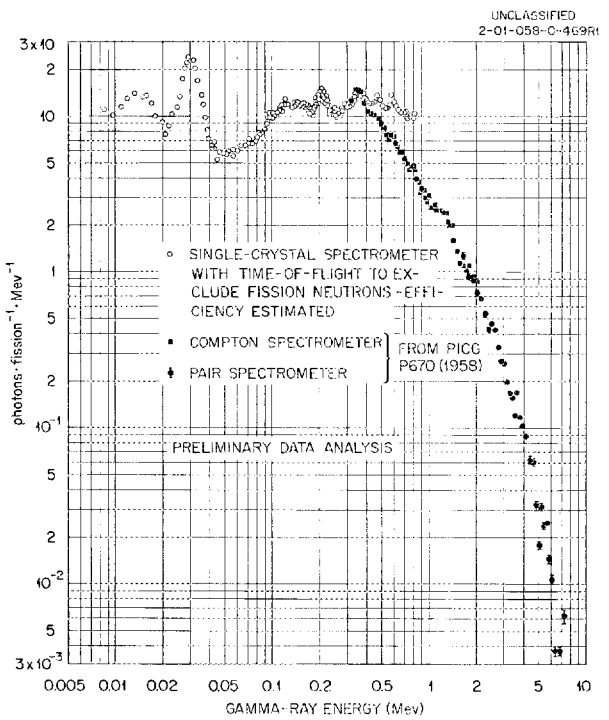

Fig. 4.1.3. Preliminary Spectrum of Gamma Rays of Energies from 10 to 800 kev Emitted Within ~10^{-7} sec After Fission of U^{235}. Assumed spectrometer efficiency and no correction for nonunique response of spectrometer. Previously obtained higher-energy data is also shown. The peaks due to the x rays from the light and heavy fission fragments show clearly at ~15 and ~30 kev.

Compton spectrometer, but the marked discrepancy in yield at energies above 0.4 Mev between these sets of data indicates the magnitude of the errors induced by the use of an assumed spectrometer efficiency and the lack of a correction for the nonunique response of the spectrometer. All of the above data must be regarded as preliminary.

A meaningful comparison of these data with the earlier results for higher energies must await a careful analysis of the data. However, the similarity of the spectral shape to that observed by Voitovetskii is striking and indicates that his separation of peaks into neutron and gamma-ray effects was correct. The peak in the data of Voitovetskii at 60 kev is due to neutrons, and that at ~75 kev is due to lead x rays. The more rapid fall-off with energy for his data would be expected, since he used a smaller crystal.

Fortunately it was possible in this experiment to measure at sufficiently low energies to separate clearly the x rays due to the light fragments (at ~15 kev) and those due to the heavy fragments (at ~30 kev). The yield of x rays from the lighter fragments is less, as would be expected, since internal conversion is less probable for the lower Z nuclei and since the K x-ray fluorescent yield is lower. The other more-or-less defined peaks with energies as shown in Fig. 4.1.2 are presumably superimposed on a continuum of gamma rays from the decay of a statistical ensemble of many of the nuclear levels formed in fission. The number of peaks separated in this measurement is probably limited by the finite resolution of the spectrometer.

It would be instructive to determine whether similar spectral structure is observed in fast fission or in the thermal fission of other nuclei. Studies with Cf^{252}, which are relatively easy because of the low backgrounds associated with spontaneous fission, would display the gamma rays from fission fragments in a higher mass region.

4.2. THE DETERMINATION OF η OF U^{233} BY DIRECT COMPARISON OF CRITICAL EXPERIMENTS IN LARGE SPHERES[1]

D. W. Magnuson R. Gwin

The method for the determination of η of U^{233} (the number of neutrons produced per neutron absorbed) which involves the direct comparison of critical assemblies of U^{233} and U^{235} in identical geometries has been described previously.[2] The experiments have now been extended to include measurements with five concentrations of aqueous $U^{233}O_2(NO_3)_2$ solutions and four concentrations of aqueous $U^{235}O_2(NO_3)_2$ solutions in a 69.2-cm-dia sphere, in which boric acid was used as a poison to enable variation in the uranium concentration. In addition, unpoisoned solutions of $U^{233}O_2(NO_3)_2$ and $U^{235}O_2(NO_3)_2$ have been made critical in a 122-cm-dia sphere.

In the critical equation used for the η comparisons, the neutron energy spectrum was assumed to consist of a Maxwellian flux, ϕ_M, and an epithermal flux, λ/E, where λ is the proportionality factor. The equation, which includes corrections for epithermal absorptions and fissions, is

$$k_{\text{eff}} = \frac{K(B)\left[\dfrac{\eta}{(1+L^2B^2)}\displaystyle\int_0^{0.2\text{ ev}} \phi_M \Sigma_{au}\, dE + \lambda\nu \int_{0.2\text{ ev}}^{10^6\text{ ev}} \frac{\Sigma_f}{E}\, dE\right]}{\displaystyle\int_0^{0.2\text{ ev}} \phi_M \Sigma_{at}\, dE + \lambda \int_{0.2\text{ ev}}^{10^6\text{ ev}} \frac{\Sigma_{at}}{E}\, dE},$$

[1] A more thorough analysis of these data, in which more recent cross-section values were used, will be reported elsewhere. This paper was presented at the Annual Meeting of the American Nuclear Society, Gatlinburg, Tenn., June 1959.

[2] D. W. Magnuson, *Neutron Phys. Ann. Prog. Rep. Sept. 1, 1958*, ORNL-2609, p 29.

where Σ_f is the macroscopic fission cross section, $K(B)$ the nonleakage probability of fission neutrons to thermal energies, B^2 the buckling, Σ_{at} the total macroscopic absorption cross section, Σ_{au} the macroscopic absorption cross section for the uranium isotope, L the diffusion length, and ν the number of neutrons produced per fission.

Values of λ were calculated by a neutron balance at the thermal cutoff from

$$\lambda = \frac{\int_0^{0.2\ \mathrm{ev}} \Sigma_{at} \phi_M \, dE}{\Sigma_s}$$

Experimental values of λ, evaluated from the fission-product gamma-ray activities of bare and cadmium-covered U^{233} and U^{235} foils introduced at the centers of the spheres, are in close agreement with the calculated values.

Flux traverses made with miniature fission chambers were used to obtain B^2, which represents the fission distribution in the sphere. The effective extrapolation distances δ were calculated from the values of B^2 and the volume average radii.

The infinite-dilution resonance integrals for U^{233} and U^{235} employed in the critical equation were those calculated by Kinney.[3] The Maxwellian-averaged cross sections are those of BNL-325,[4] and the f factors are from Harvey and Sanders.[5]

Table 4.2.1 summarizes the experimental and calculated data. The value of η of U^{233} determined from the data for the 122-cm-dia sphere should be the best value because of smaller neutron leakage and smaller resonance effects. This value is 2.295 ± 0.036.

---

[3] W. E. Kinney, unpublished Oracle calculations.

[4] D. J. Hughes and R. B. Schwartz, *Neutron Cross Sections*, 2d ed., BNL-325 (July 1, 1958).

[5] J. A. Harvey and J. E. Sanders, *Progr. in Nuclear Energy, Ser. I* 1, 1 (1956).

Table 4.2.1. Experimental and Calculated Data for Critical Spheres

Sphere Radius (cm)	Solution Concentration (g/liter)			λ	δ (cm)*	$K(B)^{(a)}$	$\eta^{(b,c)}$	$\eta^{233(d,c)}$
	U^{233}	U^{235}	Boron					
34.6		18.75	0.000	0.0434	1.9	0.8394	2.061 ± 0.036	
		21.92	0.0935	0.0483	1.9	0.8391	2.060 ± 0.036	
		24.94	0.187	0.0555	1.9	0.8418	2.066 ± 0.037	
		26.51	0.230	0.0602	1.9	0.8403	2.061 ± 0.038	
61.0		14.11	0.000	0.0368	1.0	0.9342	2.065 ± 0.019	
34.6	16.74		0.000	0.0417	1.9	0.8391	2.266 ± 0.046	2.277 ± 0.038
	17.45		0.0239	0.0423	1.9	0.8397	2.268 ± 0.047	2.279 ± 0.038
	18.10		0.0465	0.0428	1.9	0.8404	2.270 ± 0.047	2.281 ± 0.038
	18.74		0.0688	0.0433	1.9	0.8417	2.269 ± 0.047	2.285 ± 0.038
	19.36		0.0912	0.0439	1.9	0.8412	2.273 ± 0.047	2.283 ± 0.038
61.0	12.93		0.000	0.0343	1.0	0.9400	2.281 ± 0.027	2.295 ± 0.036

*A subsequent analysis has shown that better values of δ would be 2.2 and 2.4 cm instead of 1.9 and 1.0 cm.

(a) Values of η assumed for the $K(B)$ calculations are $\eta^{235} = 2.076$ and $\eta^{233} = 2.28$.

(b) Values of $K(B)$ used to determine η were calculated from the assumption that $K(B) = 1/(1 + \tau B^2)$, in which $\tau = 25$ cm^2; the numerical values are $K(B) = 0.8437$ for the 69.2-cm-dia sphere and 0.9397 for the 122-cm-dia sphere.

(c) Probable errors are based on fractional errors of 0.1 in τ, λ, $\int (\Sigma_f/E)\, dE$, and $\int (\Sigma_{au}/E)\, dE$; 0.01 in σ_{au} and η^{235}; and 0.005 in N_u (the uranium atom density in the solution).

(d) The values of $K(B)^{233}$ used to determine η^{233} were assumed to be equal to the average values of $K(B)^{235}$ calculated from the U^{233} experiments; the numerical values are $K(B)^{233} = 0.8401$ for the 69.2-cm-dia sphere and 0.9342 for the 122-cm-dia sphere.

4.3. CALCULATIONS OF η OF U^{235} AND U^{233} FROM CRITICAL EXPERIMENTS IN CYLINDRICAL GEOMETRY*

D. W. Magnuson R. Gwin

The critical experiments which were performed in 5- and 9-ft-dia stainless steel cylinders and which are described in Sec 3.5 of this report have been analyzed to determine the values of η, the fission neutron yield per neutron absorbed, for both U^{233} and U^{235}. For this analysis the method outlined in Sec 4.2 was used, the required nonleakage probabilities being calculated by the method described in Sec 5.2. For the nonleakage probability calculations, an age to thermal energy for delayed neutrons of 9 cm^2 was assumed. The errors include a 4% error in the delayed neutron yield, in addition to the experimental errors.

The nonleakage probabilities and η values are summarized in Table 4.3.1. Errors of 1% in the uranium cross sections and of 0.5% in the chemical analyses were included in the estimated errors for the η values. World consistent values of the cross sections were used to obtain these data.

*A more thorough analysis of these data, in which more recent cross-section values were used, will be reported elsewhere.

[1] J. A. Harvey, ORNL, private communication, July 15, 1959.

Table 4.3.1. Experimental and Calculated Data from Critical Experiments with Aqueous Solutions of $U^{235}O_2(NO_3)_2$ and $U^{233}O_2(NO_3)_2$ in Cylindrical Geometry

Cylinder Dimensions (in.)		Solution Concentration (g/liter)		Experimental Nonleakage Probability, $P(B)$	η	
Diameter	Height*	U^{233}	U^{235}		U^{233}	U^{235}
60.92	19.49	14.12		0.8865 ± 0.0077	2.290 ± 0.025	
	23.31	13.53		0.9093 ± 0.0059	2.283 ± 0.021	
	30.58	12.88		0.9341 ± 0.0040	2.281 ± 0.016	
	54.69	12.21		0.9602 ± 0.0022	2.284 ± 0.014	
60.92	17.75		16.13	0.8683 ± 0.0090		2.072 ± 0.025
	18.68		15.83	0.8790 ± 0.0082		2.052 ± 0.023
	28.64		14.22	0.9298 ± 0.0042		2.049 ± 0.014
	41.42		13.59	0.9517 ± 0.0027		2.055 ± 0.012
	80.03		13.07	0.9678 ± 0.0016		2.066 ± 0.012
107.7	35.8		13.24	0.9599 ± 0.0025		2.062 ± 0.014
	48.2		12.92	0.9730 ± 0.0016		2.057 ± 0.014
	94.9		12.61	0.9861 ± 0.0007		2.055 ± 0.014

*Critical volumes and masses for these data are included in Tables 3.5.1 and 3.5.2 of Sec 3.5 in this report.

4.4. MEASUREMENTS OF η OF U^{233} AND U^{235} BY A MANGANESE BATH TECHNIQUE

G. deSaussure
J. D. Kington
R. L. Macklin[1]
W. L. Lyon[2]

An increased emphasis on the investigation of the possibilities of breeding reactors operating in the thermal region, plus the recent publication of British measurements,[3,4] has emphasized the need for an accurate determination of the value of η of U^{233}. An experiment has been performed with the Bulk Shielding Reactor I (BSR-I) to measure this value with an accuracy of ±1% or better. In addition, a value of η of U^{235} has been determined.

The experiment consisted in measuring the intensity of a thermal-neutron beam and then measuring the total number of fission neutrons produced by the beam in a U^{233} or U^{235} sample. The ratio of the two measurements is, by definition, η. The neutron detector used for these measurements was a 1-m-dia sphere filled with an aqueous solution of manganese sulfate ($MnSO_4$). A large fraction of the neutrons was absorbed in the manganese, the activation of which was determined by measuring the 0.85-Mev gamma rays emitted in the decay of 2.56-hr Mn^{56}.

A diagram of the experimental arrangement[5] in the reactor pool is shown in Fig. 4.4.1. Fission neutrons emitted by the BSR-I were thermalized in a large tank of D_2O immediately adjacent to the reactor. Thermal neutrons from the D_2O tank

[1]Physics Division.

[2]Chemistry Division.

[3]C. J. Kenward, R. Richmond, and J. E. Sanders, *A Measurement of the Neutron Yield in Thermal Fission of U^{235}*, AERE-R/R-2212, revised (1958).

[4]From $\eta^{233}/\eta^{235} = 1.074 \pm 0.015$ of H. Rose, W. A. Cooper, and R. B. Tattersall, *Proc. U.N. Intern. Conf. Peaceful Uses Atomic Energy, 2nd, Geneva, 1958*, A/Conf 15/P/14, and $\eta^{235} = 2.02 \pm 0.03$ from ref 3.

[5]This equipment was designed by F. R. Duncan, Instrumentation and Controls Division.

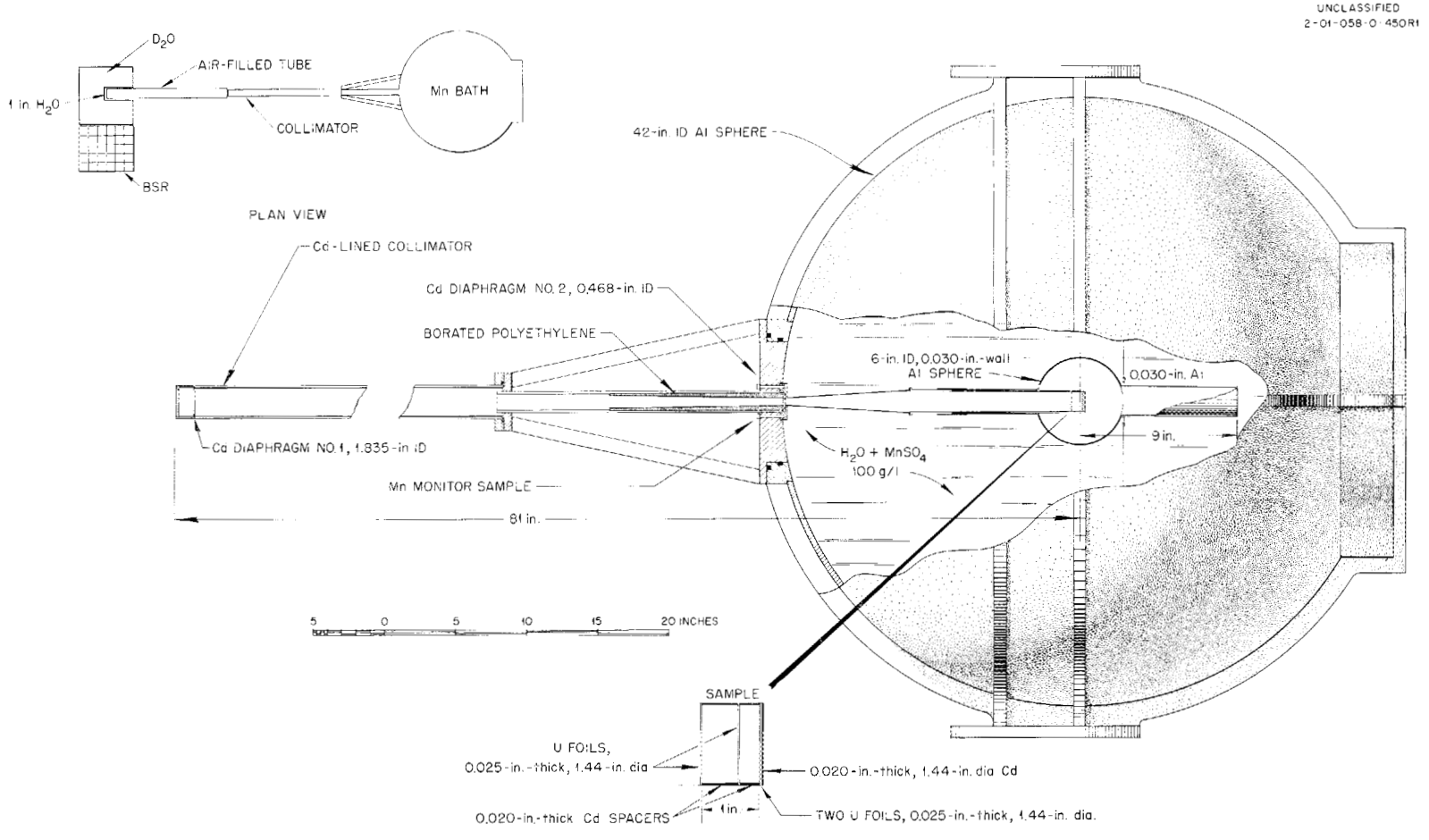

Fig. 4.4.1. Experimental Arrangement for the Measurement of η.

were then shaped into a beam by a long cadmium-lined, air-filled collimator containing two cadmium diaphragms. The beam terminated in the center of the sphere filled with the manganese sulfate solution. The target at this point consisted of four 1.44-in.-dia, 0.025-in.-thick foils of highly purified U^{233} or U^{235} followed by a 0.020-in.-thick cadmium foil. The fission neutrons produced in the target escaped into the manganese bath, which was large enough that the leakage of fission neutrons from the bath was less than 0.5%.

The four uranium foils were spaced so that multiplication in the target, an effect which is analogous to the fast effect in reactor fuel rods, would be minimized. The cadmium foil was included so that the sample could be reversed for cadmium difference measurements, which were taken to ensure that the value of η measured was an average over a thermal spectrum. Monitoring of the thermal-neutron beam was accomplished by a thin (20 mg/cm^2) manganese foil at the entrance to the sphere.

Activation measurements were made with a specially designed scintillation counter arrangement employing a 3-in.-dia by 3-in. NaI(Tl) crystal. The design of the counter permitted measurements of either the activated solution or the manganese foil monitor to be made with the same crystal-phototube combination and with accurately reproducible geometry.

For each measurement of η four irradiations were made: one with the fuel sample in place, another with the target reversed so that the beam was incident upon the cadmium foil, a third with the open beam (no sample), and the last with a cadmium disk in the target position. For each irradiation the BSR-I was operated at a power of 1 Mw.

Following each irradiation the manganese sulfate solution was stirred for 30 min. Then a 1-liter sample was weighed and its activity measured. In order to maintain a count rate of $\sim 10^3$ counts/sec, thus avoiding problems of pulse pileup in the counting equipment, samples taken after irradiation of the U^{233} target were diluted by a factor of 2.5. The ratio of solution activation to monitor activation was reproducible to within 0.3% from day to day. All measurements were repeated with several different crystal-phototube combinations to guard against unsuspected error.

The value of η was obtained by the relationship

$$\eta^* = \frac{R_U - R_{Cd+U}}{R - R_{Cd}} , \qquad (1)$$

where the R_i's are the ratio of the activity of an aliquot sample of the solution to the activity of the manganese foil monitor. Since, as noted, both activities were measured on the same detector, the ratio was independent of small day-to-day variations in detector efficiency, and because only the ratio between measurements was used, any constant activation of the manganese bath due to leakage of neutrons from the reactor was canceled. The asterisk in Eq. (1) indicates that some minor corrections had to be applied to the measured value to obtain the final result.

Table 4.4.1 summarizes the corrections which were applied. The largest correction was due to the fast effect in the target foil, even after this effect had been minimized by splitting the foil. A second correction was required because the sample was not totally absorbing for all neutrons below the cadmium cutoff energy, and another was necessary because some thermal neutrons were scattered out of the sample before being absorbed. Another correction is implicit in the probability that some fission neutrons, after slowing down in the manganese bath, will be captured in the sample and will produce further multiplication ("indirect" multiplication). Unavoidable isotopic and chemical impurities in the sample necessitate an additional correction, as well as the excess absorption of fission neutrons in the 340-ev resonance in manganese. Parasitic absorption of neutrons in structural materials involved a correction taking into account the differing absorptions of thermal and fission neutrons. Because of the finite radius of the sphere, some fission neutrons escaped without capture; others escaped through the collimator ("duct streaming"). The effects of (n,α) and (n,p) reactions in the detector bath were also considered, and finally a

Table 4.4.1. Corrections to the Measured Values of η^*

	Ratio of η^* to η	
	U^{233}	U^{235}
Fast multiplication	1.0347 ± 0.0030	1.0193 ± 0.0020
Transmission and energy dependence	0.9870 ± 0.0035	0.99 ± 0.01
Scattering from the fuel sample	0.9976 ± 0.0012	0.9976 ± 0.0012
Indirect multiplication	0.9871 ± 0.006	0.9861 ± 0.006
Impurities in the fuel sample	0.9995 ± 0.0005	0.9995 ± 0.0005
Excess resonance absorption in manganese	1.0052 ± 0.0005	
Absorption in structural materials	1.0057 ± 0.0040	
Leakage of fission neutrons	0.9976 ± 0.0015	
Duct streaming	0.9998 ± 0.0002	
(n,α) and (n,p) threshold reactions	0.9960 ± 0.0030	
Total effect: η/η^*	0.9906 ± 0.0090	1.0035 ± 0.013

correction was made to convert the thermal value of η to the value for a neutron velocity of 2200 m/sec.

Table 4.4.2 presents the preliminary results of this experiment and compares them with results of other experiments. The preliminary values of η of U^{233} and U^{235} are in excellent agreement with the world-weighted averages[6] but are inconsistent with the recent UK values.[3,4]

Since η^* can be measured in this experiment to $< \pm 0.2\%$, and since all the corrections are of the order of 1%, excellent accuracy can be achieved. It is anticipated that final evaluation of corrections will permit the determination of the absolute value of η to within ±0.015.

The method has also been used to determine the value of η of Pu^{239}, but since the corrections have not been made no value will be quoted.

[6]D. J. Hughes and R. B. Schwartz, *Neutron Cross Sections*, 2d ed., BNL-325 (July 1, 1958).

Table 4.4.2. Comparison of Various Values of η

Reported by	η	
	U^{233}	U^{235}
BNL-325[a]	2.29 ± 0.02	2.07 ± 0.015
United Kingdom[b]		2.02 ± 0.03
United Kingdom[c]	2.17 ± 0.03	
deSaussure *et al.* (present investigation)	2.30 ± 0.02	2.07 ± 0.02

[a]D. J. Hughes and R. B. Schwartz, *Neutron Cross Sections*, 2d ed., BNL-325 (July 1, 1958).

[b]C. J. Kenward, R. Richmond, and J. E. Sanders, *A Measurement of the Neutron Yield in Thermal Fission of U^{235}*, AERE-R/R-2212, revised (1958).

[c]From $\eta^{233}/\eta^{235} = 1.074 \pm 0.015$ of H. Rose, W. A. Cooper, and R. B. Tattersall, *Proc. U.N. Intern. Conf. Peaceful Uses Atomic Energy, 2nd, Geneva, 1958*, A/Conf. 15/P/14, and $\eta^{235} = 2.02 \pm 0.03$ from Kenward *et al.* (footnote *b*).

4.5. PRELIMINARY MEASUREMENT OF THE GROSS SPECTRUM OF GAMMA RAYS ASSOCIATED WITH THE INTERACTION OF THERMAL NEUTRONS AND U^{235}

F. C. Maienschein T. A. Love
R. W. Peelle

During the past several years extensive spectral measurements of gamma rays associated with the thermal fission of U^{235} have been carried out at the Laboratory.[1] From these measurements energy spectra for both prompt and fission product gamma rays have been obtained. It has been suggested by Goldstein[2] that a spectral measurement of the total gamma-ray production due to the absorption of thermal neutrons in U^{235} would be desirable for shielding calculations. A preliminary experiment has now been performed to measure the gross spectrum, and the results are reported below. Only the relative shape of the spectrum was obtained, since the fission rate was not determined and several sources of error which were recognized could not be corrected for. As explained later in the paper, an adequate refinement of the experiment would be difficult with the existing apparatus.

The pertinent features of the experimental arrangement are shown in Fig. 4.5.1. A three-crystal pair spectrometer[1] was used to examine the gamma radiation emitted by a disk of U^{235} positioned over the thermal column adjacent to the Bulk Shielding Reactor. The disk was approximately 0.700 in. in diameter and about 0.042 in. thick. The response of the pair spectrometer to monoenergetic gamma rays is shown in Fig. 1*b* of ref 1, and the neutron response was estimated to be small on the basis of investigations described elsewhere.[3] The magnitude of the radiation not associated with the interaction of thermal neutrons with U^{235}, that is, the background radiation, was determined by replacing the U^{235} disk with a U^{238} disk of approximately equal weight.

The experimental data obtained were not appreciably affected by the instrumentation errors such as analyzer nonlinearity, count losses, gain drifts, etc. Thermal-neutron interactions in the spectrometer walls and in the NaI(Tl) crystals used in the spectrometer were minimized by the extensive use of lithium shielding, and the short-time response of the spectrometer (about 10^{-7} sec) to fast capture or inelastic scattering of fission neutrons had already been shown to be small for this geometry.[3] Interactions due to partially moderated neutrons in the kev region were not eliminated as a source of appreciable background. Nor was a correction made for the nonunique response of the spectrometer. This latter correction would probably vary from about 10% at the high energies to about 20% at 2 Mev and to a factor of 2 at the lowest energy. No correction was made for the fact that the fission products were not quite saturated in the 9000-sec run. Examination of the fission product spectrum[1] indicates that this would have no appreciable effect on the spectral shape, however.

The spectral data obtained when the U^{235} disk was in position were combined into energy bins, and a subtraction was made for the background. (The background caused by random coincidences, which amounted to no more than 2.5% at any energy, was not subtracted.) The results, arbitrarily normalized to give the best over-all fit, are shown in Fig. 4.5.2. The background spectrum is also presented. Both sets of data were corrected for the *relative* spectrometer efficiency and thus represent the relative number of gamma rays as a function of energy. The errors shown are those due to counting statistics only. It may be noted that these errors become appreciable at the higher energies, since the background is about an order of magnitude larger than the foreground. An indication of the success of the background subtraction is given by the removal of the gamma-ray peak due to hydrogen capture, which is quite prominent in the background.

The solid curve in Fig. 4.5.2 was obtained by adding the prompt-fission and fission product gamma-ray spectra reported in ref 1. The statistical errors shown there vary from about 20% at 7 Mev to a negligible error at low energies. The

---

[1] F. C. Maienschein *et al.*, *Proc. U.N. Intern. Conf. Peaceful Uses Atomic Energy, 2nd, Geneva, 1958* 15, 366 (1958); see also sec 4.1 in this report.

[2] H. Goldstein, *Fundamental Aspects of Reactor Shielding*, p 63, Addison-Wesley, Reading, Mass., 1959.

[3] F. C. Maienschein, R. W. Peelle, and T. A. Love, *Energy Spectrum of Prompt Gamma Rays Accompanying the Fission of U^{235}*, ORNL-2389, p 99–110 (1957).

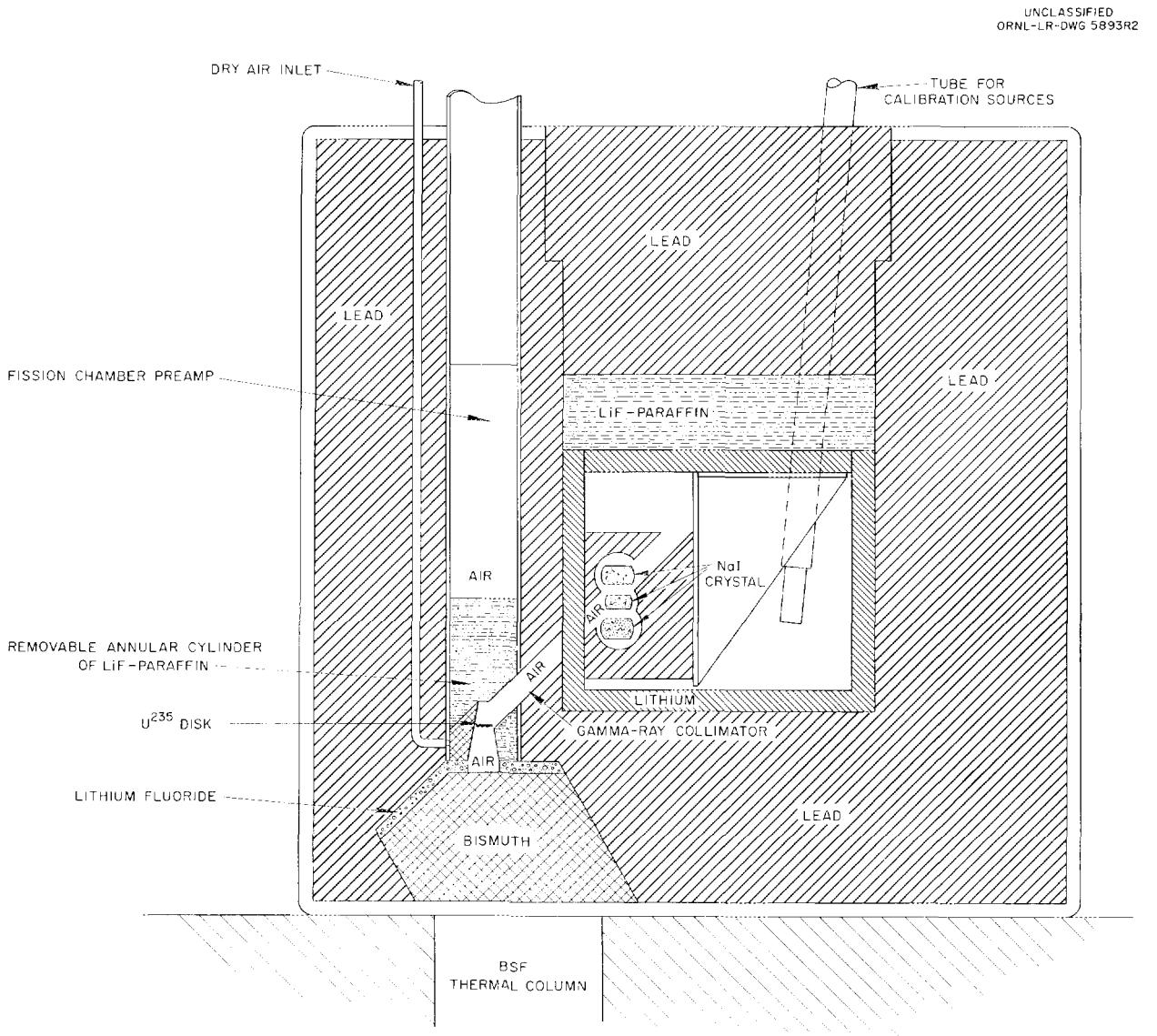

Fig. 4.5.1 Arrangement of Apparatus for Determination of Integral Gamma-Ray Spectrum Associated with the Interaction of Thermal Neutrons and U^{235}.

summation of these two spectra is completely consistent in shape with the results of the present experiment when the error due to the nonuniqueness of spectrometer response is considered. It is probable that the data of Motz,[4] also shown in Fig. 4.5.2, are consistent with the results of the present experiment, but this cannot be verified since no errors are available for the Motz experiment.

It is reassuring to observe the apparent agreement in spectral shapes between the two integral measurements of U^{235} gamma rays and the summation of the prompt-fission and fission product spectra. However, the errors in the integral measurements are so large that no meaningful conclusions can be drawn concerning the other sources of gamma radiation, primarily gamma rays resulting from neutron capture in

[4] J. W. Motz, *Phys. Rev.* 86, 753 (1952).

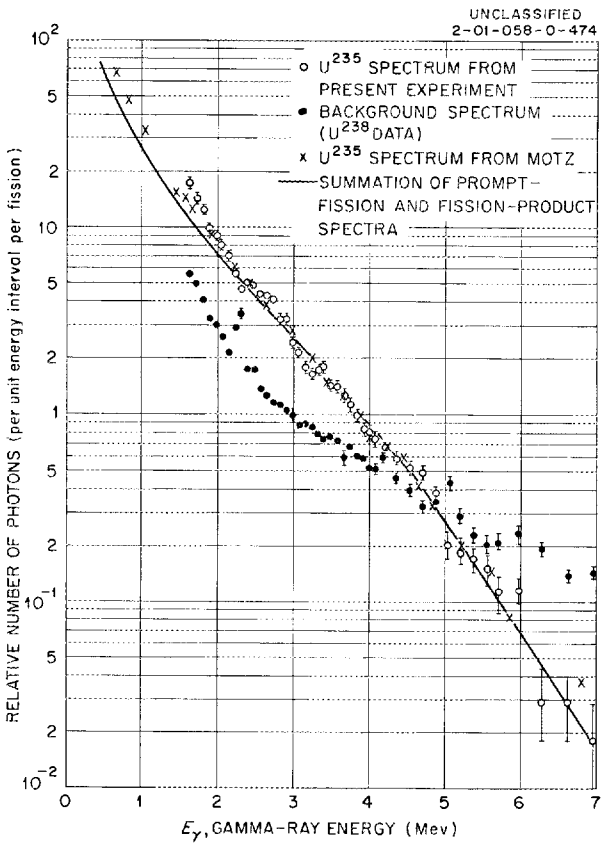

Fig. 4.5.2. Energy Spectra for Gamma Rays from the Interaction of Thermal Neutrons and U^{235}. All data *normalized* to give the best over-all fit.

U^{235} and very short-lived fission products ($T_{1/2} < .1$ sec). For this purpose a much more accurate measurement would be required, and the fission rate should be determined so that the energy yield could be checked on an absolute basis.

A measurement of adequate accuracy would be difficult with the existing apparatus, however. An accurate determination of the fission rate would be made difficult by the variation of the thermal-neutron flux in the region around the U^{235}. In addition, the presence of apparatus around the fission source may lead to the partial moderation of fission neutrons, thus increasing their probability of interaction in the sodium iodide crystals. Partially moderated prompt-fission neutrons would not have been detected in the prompt-fission gamma-ray experiment because of the time-coincidence requirement. Fully moderated (thermal) neutrons are excluded from the crystals by the lithium shield.

It further appears desirable to measure the gamma rays from the U^{235} at a backward angle with respect to the incident thermal-neutron beam, since the neutron beam is inevitably contaminated with gamma rays. The scattering of such gamma rays will be much worse at low energies, which were not studied in the present preliminary experiment.

Because of the considerations outlined above, it would appear that new experimental apparatus would have to be assembled if a meaningful measurement of the gamma rays due to the interaction of thermal neutrons with U^{235} were to be performed. The requirements for a well-collimated, high-intensity thermal-neutron beam with little contamination and low general background could not easily be met. The interfering effects considered in this section and the other sources of error would also need to be studied carefully. Some of the neutron-induced background problems might be alleviated by the use of a magnetic-deflection Compton spectrometer, but the extremely low efficiency of such devices would aggravate the need for an intense beam and the determination of the fission rate. It is not clear that the effort necessary for an accurate measurement would be warranted.

Part 5

EXPERIMENTAL REACTOR PHYSICS

5.1. AN INVESTIGATION OF THE SLOWING DOWN OF FISSION NEUTRONS IN WATER

T. V. Blosser D. K. Trubey

An experiment designed to measure the slowing down of U^{235} fission neutrons in water to indium resonance energy has been described previously.[1] This experiment is intended to resolve the long-existing discrepancy between the measured values of the age of fission neutrons in water and the many computed values, and to this end the major portion of the experiment is devoted to the determination of the importance of perturbing effects not examined in earlier measurements. These effects have been discussed in detail elsewhere;[1] they include (1) the effect of the water-graphite boundary inherent in the experimental arrangement on the flux within the noninfinite medium, (2) the effect of the foil detector employed on the flux detected, (3) the effect of the size of the source, and (4) the effect of the detector on the flux impinging on the source.

Because the neutron distribution from a fission source in water varies rapidly with distance, a large number of source–detector combinations must be utilized, and since the perturbing effects noted vary with each arrangement, a tremendous amount of data must be obtained. A large amount of information has already been collected and a partial analysis has been made. Although foil activities have been measured by both gamma-ray and beta-particle counting, only the gamma-ray data has been analyzed.

The arrangement for most of the experiments has been described previously.[1] The Lid Tank Shielding Facility (LTSF) has also been utilized for measurements at large source-to-detector separation distances. Data have been obtained to date for 1-, 2-, 4-, and 5-cm-dia by 0.004-in.-thick U^{235} source foils and 1.1- and 3.2-cm-dia by 0.005-in.-thick indium detector foils. The thickness of the cadmium covers on the indium foils has been varied from 20 to 140 mils. Very thin foils were prepared by an evaporation technique for use in the determination of the effect of the foil detector on the flux detected, and for a future measurement of the effect of source thickness. Useful films of indium as thin as 0.3 mg/cm^2 (0.016 mil) and of 93.22% U^{235}-enriched U as thin as 0.063 mg/cm^2 have been deposited on a 0.25-mil Mylar base. In the use of such thin indium films, the problems of slight variation in thickness over the evaporated sheet and statistical variation in weight determinations have largely been overcome by the following techniques: The relative thicknesses of the indium foils cut from one evaporated sheet were determined by activation analysis. With this information, an absolute thickness could be obtained for each foil by dissolving only a few of these foils and chemically analyzing the solutions. Thicknesses of the vacuum-deposited U^{235} foils are determined by alpha-particle counting and by counting of the natural gamma-ray activity of the U^{235}.

The effect of the water-graphite boundary has been evaluated by placing the source directly on the bottom of the thermal column tank, and then at varying distances from the bottom. It has been experimentally determined for the small sources used that the source position has no observable effect for large ($\geq$12–15 cm) source–detector separations. For small (<10 cm) separations a distance of 9.6 cm from the bottom of the tank to the source is more than sufficient to overcome any effect due to source position.

The effect of using cadmium covers on indium detectors has been investigated for a 2-cm-dia source and a 1-cm-dia detector, and the results are shown in Fig. 5.1.1, where saturated indium activity is plotted as a function of cadmium cover thickness for source-to-detector distances from 4.5 to 20.5 cm. A cadmium correction factor, F_{Cd}, derived from this data is plotted as a function of distance from the source for cadmium thicknesses of 40 and 140 mils in Fig. 5.1.2. The error shown is the standard error of the intercept in Fig. 5.1.1 as established by a least-squares straight-line fit, unless this was less than $\pm 1\frac{1}{2}\%$. (A more complete discussion of the cadmium cover effect may be found in Sec 8.9.)

The effect of the size of the source was studied by examining the source-strength distribution of the 2-cm-dia source used for most of the measurements. Concentric circular 2-mil-thick gold foils of various diameters were placed on each side of

[1] T. V. Blosser, D. K. Trubey, and E. P. Blizard, *Neutron Phys. Ann. Prog. Rep. Sept. 1, 1958*, ORNL-2609, p 55.

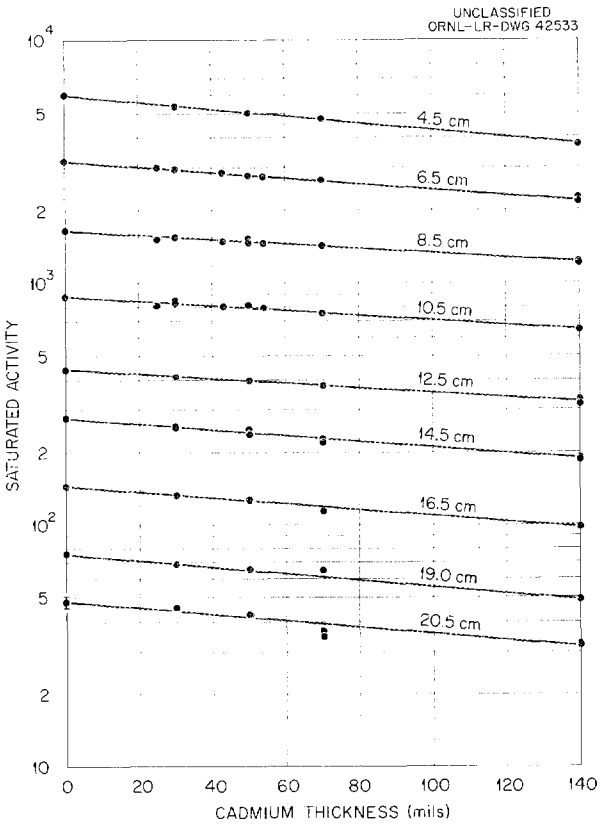

Fig. 5.1.1. Saturated Activity of a 5-mil-thick, 1.11-cm-dia Indium Foil as a Function of Cadmium Cover Thickness for Various Distances from a 1.95-cm-dia U^{235} Source.

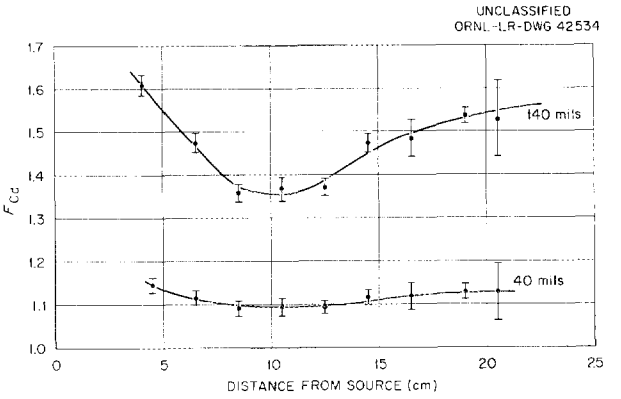

Fig. 5.1.2. Cadmium Correction Factor, F_{Cd}, as a Function of Distance from Source in Water. Five-mil-thick indium foils with 140- and 40-mil-thick covers.

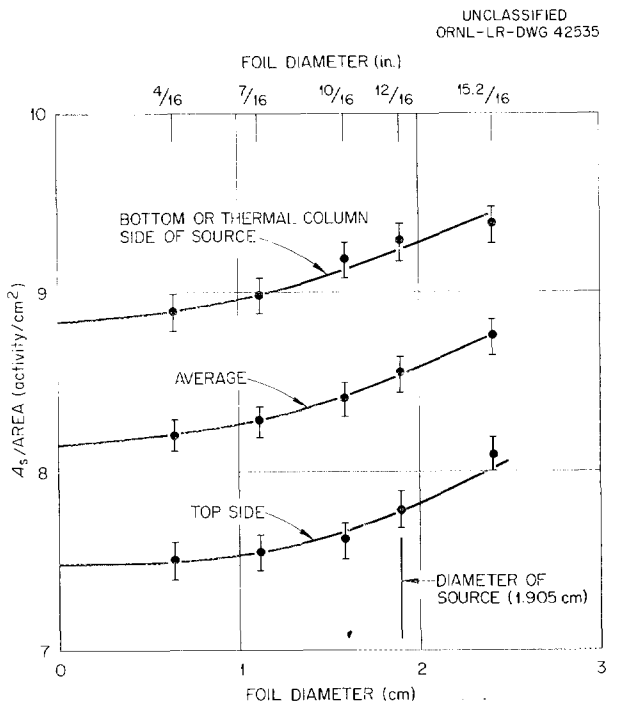

Fig. 5.1.3. Activity Per Unit Area of 2-mil-thick Gold Source Monitor Foil as a Function of Foil Diameter (Source is 0.75 in. in Diameter and 4 mils Thick).

the source. The activities of the foils, shown in Fig. 5.1.3, indicate that the variation of the source strength per unit area as a function of the diameter of the source is small. Since the geometric correction (described below) for a 2-cm-dia source is also very small (<2%), the source was assumed to have a constant strength. (The over-all average source strength is about 5% greater than that at the center.)

Analysis of experimental results requires a geometrical correction to reduce the data obtained from a disk-source–disk-detector configuration to the desired point-source–point-detector kernel. The ratio of the experimental detector response to the detector response in a point-source–point-detector geometry has been given[1] as:

$$A(R_0) = \frac{\int\int G(R)\, dS\, dS'}{G(R_0) \int\int dS\, dS'} ,$$

where

R_0 = separation distance of foils,

$G(R)$ = point-to-point kernel,

dS, dS' = differential source and detector areas, respectively.

In contrast to previous experiments, in which

$G(R)$ was approximated so that the transformation could be performed analytically, the present work employs an Oracle code for a numerical integration of the point-to-point kernel over the source and detector areas, beginning with an assumed $G(R)$ and using the calculated value of A to improve the assumption in successive iterations.

Various choices of the initial kernel may be made, including results of previous experiments, measured data, etc., but the initial kernel used in general has been determined by the type of transformation used by Hill and Roberts.[2] For circular disks:

$$G(R) \cong G_m(R) - \frac{a^2 + b^2}{4R} \frac{dG(R)}{dR} ,$$

where

a = source radius,

b = detector radius,

$G_m(R)$ = measured kernel.

Therefore,

$$A(R) = \frac{G_m(R)}{G(R)} \cong 1 + \frac{a^2 + b^2}{4R} \frac{dG(R)/dR}{G(R)} .$$

In the calculation it is assumed that

$$\frac{dG(R)/dR}{G(R)} = \frac{dG_m(R)/dR}{G_m(R)} ,$$

and that the kernel is a Gaussian over a distance of 1 cm. A smoothed set of data points at 1-cm intervals was taken to be $G_m(R)$. It was found that the Hill-Roberts expression yielded the correct kernel to within less than 1% for the source-detector combinations used. It is of interest to observe that results obtained by this code agreed within a few per cent with results obtained by the usual analytic transformation of LTSF data, and smoothed curves for the two sets of values agreed even more closely.

Sufficient data to deduce either an infinite-dilution age or a zero-cadmium age have not yet been obtained from the experiment. However, a preliminary 30-mil-cadmium, 5-mil-indium age has been computed, based on data obtained at 0.5, 1.0, 1.5, 2.5, 4.5, 6.5, and 8.5 cm from the source, with a 1.1-cm-dia, 4-mil-thick source and a 1.1-cm-dia, 5-mil-thick indium foil. These data plus the data from five other source-detector combinations were normalized at the overlapping portions to yield one composite kernel, which is plotted in Fig. 5.1.4. The data points shown are the

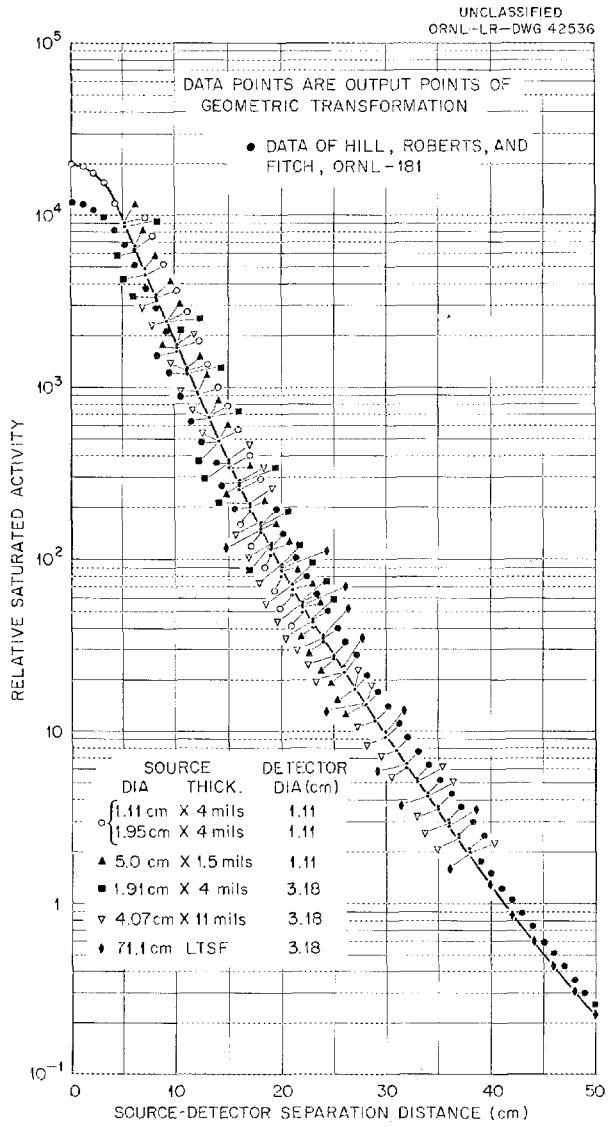

Fig. 5.1.4. Relative Saturated Activity of 5-mil-thick Indium Foils (30-mil-thick Cadmium Covers) as a Function of Source-to-Detector Separation Distance in Water.

[2] J. E. Hill, L. D. Roberts, and T. E. Fitch, *The Slowing Down Distribution from a Point Source of Fission Neutrons in Light Water*, ORNL-181 (1948).

results of the geometrical transformation codes. The resulting age ($\bar{R}^2/6$) of 26.7 cm^2 is in good agreement with the results of Lombard and Blanchard,[3] who report a value of 27.3 ± 0.9 cm^2, and Doerner and Martens,[4] who give 27.6 cm^2 as a preliminary value.

[3]D. B. Lombard and C. H. Blanchard, "Fission-to-Indium Age in Water," to be published in *Nuclear Sci. and Eng.*

[4]R. C. Doerner and F. H. Martens, *Trans. Am. Nuclear Soc.* 1(2), 30 (1958).

5.2. NONLEAKAGE PROBABILITIES IN CRITICAL EXPERIMENTS AND THEIR RELATION TO NEUTRON AGE[1]

R. Gwin D. W. Magnuson

This paper consists of a brief outline of the theory of unreflected reactors and a presentation of some critical and kinetic data obtained from experiments performed at the ORNL Critical Experiments Facility and analyzed by use of the theoretical model. The analysis yields the nonleakage probability for a given system as well as a value for the migration area for a critical infinite system of fissile material and water.

The formulation of the theory of unreflected reactors is given by Weinberg and Wigner.[2] It states that the nonleakage probability for a bare (unreflected) homogeneous reactor and the neutron age in water are related through the point-source slowing-down kernel, which is the function that gives the spatial distribution of neutrons of a specified energy which originate from a point fission source in an infinite medium.

The expressions for the neutron age and the nonleakage probability for finite unreflected systems in terms of the point slowing-down kernel, $g(r)$, are

$$\tau = \frac{\bar{r}^2}{6} = \frac{1}{6}\frac{\int_0^\infty g(r)\, r^2\, 4\pi r^2\, dr}{\int_0^\infty g(r)\, 4\pi r^2\, dr} ,$$

$$K(B) = \frac{\int_0^\infty g(r)\, \frac{\sin Br}{Br}\, 4\pi r^2\, dr}{\int_0^\infty g(r)\, 4\pi r^2\, dr} .$$

The nonleakage probability for a given theoretical formulation is the Fourier transform of the point slowing-down kernel. This statement is called the "second fundamental theorem of reactor theory."

If the reactor is large ($B^2 \ll 1$), then only the second moment, τ, enters in the expression for $K(B)$, that is, $K(B) = (1 - \tau B^2)$. The present work describes a method of deducing $K(B)$ directly from critical experiments on bare reactors. From $K(B)$, τ can be obtained.

[1]A more thorough analysis of these data, in which more recent cross-section values were used, will be reported elsewhere. This paper was presented at the Annual Meeting of the American Nuclear Society, Gatlinburg, Tenn., June 1959.

[2]A. M. Weinberg and E. P. Wigner, *The Physical Theory of Neutron Chain Reactors*, University of Chicago Press, Chicago, 1958.

The physical conditions required for the second fundamental theorem to hold are given by the first fundamental theorem. The persistent neutron flux in an unreflected critical reactor with an energy-independent extrapolation distance is separable in space and energy,

$$\phi(x,E) = \phi(E)\ \psi(x) \quad ,$$

and the spatial distribution is given by a solution of the wave equation

$$\nabla^2 \psi(x) + B^2 \psi(x) = 0 \quad .$$

This means that the neutron fluxes of all energies have the same spatial distribution. The use of the infinite-medium slowing-down kernel in the critical equation for finite systems is based on an analytic continuation of the solution of the wave equation through all space. Since the extrapolation distance is in reality somewhat energy dependent, the theorem can be expected to hold more accurately for large bare reactors, in which the extrapolation distance is less important than for small ones. The equations used in the analysis are:

$$\overline{\eta f}\ \frac{K(B)}{1 + L^2 B^2}\ F = k_{\text{eff}} \quad , \qquad F = p\epsilon \quad ,$$

$$\frac{K(B)}{1 + L^2 B^2} = P(B) \quad ,$$

$$\Delta k_{\text{eff}} = \overline{\eta f}\ F\ \frac{\partial P(B)}{\partial B^2}\ \Delta B^2 \quad .$$

Thus, $K(B)$ can be determined if all the other terms are known. However, from static critical experiments alone it is difficult to evaluate the nonleakage probability because of uncertainties in f and η.

An alternate, and more accurate, method of determining the nonleakage probability, similar in principle to the usual boron-poisoning method, is to change the buckling by a known amount. This can be done by increasing the height of a critical cylinder, observing the resulting stable period, and calculating the change in k_{eff} by the inhour equation. This change in k_{eff} can be combined with the expression for Δk_{eff} to yield the equation:

$$\frac{\partial P(B)}{\partial B^2} = P_d(B)\ \frac{\sum \dfrac{\beta_i}{1 + \lambda_i T}}{\Delta B^2} \quad ,$$

where β_i is the fraction of fission neutrons emitted in delayed group i, λ_i is the decay constant of the delayed-neutron precursor of group i, T is the stable reactor period, and $P_d(B)$ is the average nonleakage probability of delayed neutrons. If it is assumed that $P(B)$ can be represented by a group kernel of the form

$$P(B) = \frac{1}{\pi_i(1 + l_i^2 B^2)} \quad ,$$

then

$$\frac{\partial P(B)}{\partial B^2} = -P(B)\sum \frac{l_i^2}{1 + l_i^2 B^2} .$$

Note that the derivative of $P(B)$ with respect to B^2 is quite dependent upon the model when B^2 is large.

For large systems, and therefore for small values of B^2, the nonleakage probability can be obtained by the following method. In general,

$$P(B) = P(B_0) + \left.\frac{\partial P(B)}{\partial B^2}\right|_{B_0} \Delta B^2 + \left.\frac{\partial^2 P(B)}{\partial B^4}\right|_{B_0} \frac{(\Delta B^2)^2}{2!} + \ldots ,$$

and, for the infinite critical system,

$$1 = P(B_0) + \left.\frac{\partial P(B)}{\partial B^2}\right|_{B_0} (-B_0^2) + \left.\frac{\partial^2 P(B)}{\partial B^4}\right|_{B_0} \frac{B_0^4}{2!} + \ldots .$$

For B^2 sufficiently small, a one-group formulation can be used to represent $P(B)$:

$$\frac{\partial P(B)}{\partial B^2} = -M^2 P^2(B) = P_d(B)\frac{\sum \frac{\beta_i}{1 + \lambda_i T}}{\Delta B^2} = -N ,$$

and in this form the series can be summed, giving

$$P(B_0) = \frac{1}{2}\left(1 + \sqrt{1 - 4NB_0^2}\right) .$$

In the multigroup formulation, the error in $P(B)$ can be estimated from the series.

If the period resulting from a change in B^2 is measured at various values of B^2, an analysis of the following equation yields a value of the migration area at $B^2 = 0$:

$$S(B) = \frac{\sum \frac{\beta_i}{1 + \lambda_i T}}{-\Delta B^2} = \frac{P(B)}{P_d(B)} \sum \frac{l_i^2}{1 + l_i^2 B^2} .$$

Experimental data (included in Tables 3.5.1 and 3.5.2 of Sec 3.5) obtained from critical systems of U^{233} and U^{235} solutions contained in a 5-ft-dia cylinder have been analyzed in this manner and are displayed in Fig. 5.2.1. (Corresponding values of $P(B)$ are included in Table 4.3.1 of Sec 4.3.) The indicated limits of error on the points consist of both experimental errors and uncertainties in the extrapolation length. The latter error is the greater. The diagonal limits of error represent the sensitivity of both $S(B)$ and B^2 to variations in the extrapolation length. For the analysis of the data a constant extrapolation length of 3.0 ± 0.3 cm was assumed, with no uncertainty in the delayed-neutron fraction.

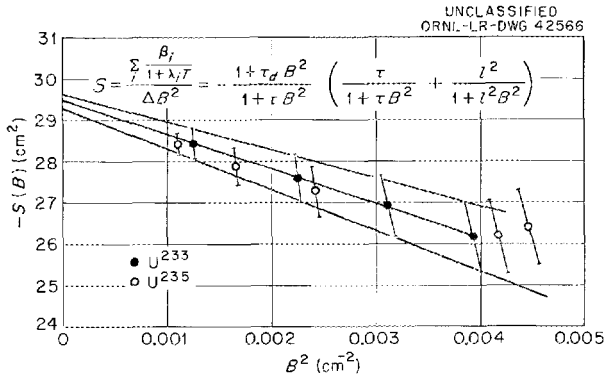

Fig. 5.2.1. Neutron Leakage Parameter, S, as a Function of Buckling, B^2.

Measurements of the extrapolation length made with U^{233} fission chambers, bare and cadmium-covered U^{235} fission chambers, and bare gold wires have all yielded values within the range assumed. It may be noted that the data for U^{233} and U^{235} solutions is virtually indistinguishable. The difference that would be expected owing to the differing values of L^2 for the two isotopes at a given B^2 is apparently smaller than the experimental reproducibility.

From these data the migration area in a critical system with zero buckling is 29.5 ± 0.3 cm^2, leading to a neutron age to thermal of 25.7 cm^2. An assumed error of 4% in the delayed neutron fraction produces an error of ±1.2 cm^2 in the migration area. The age to indium resonance is therefore 24.7 ± 1.2 cm^2.

This analysis will be presented in detail in a separate report.

5.3. MEASUREMENTS OF THE TRANSPORT MEAN FREE PATH OF THERMAL NEUTRONS IN BERYLLIUM AS A FUNCTION OF TEMPERATURE

G. deSaussure E. G. Silver

The variation of the transport mean free path of thermal neutrons in beryllium with temperature has been investigated for various temperatures higher than room temperature, and for one temperature below room temperature, by the pulsed-neutron technique. The theory of the method and a description of the experimental arrangement, as well as the results of earlier measurements of diffusion parameters in beryllium at room temperature, have been given previously.[1,2] Briefly, the method consists in irradiating the sample with a short burst of neutrons and then observing the decay of the neutron density.

In the experiments reported here, approximately cubical beryllium prisms of various sizes were assembled within a furnace[3] located at the target region of the 300-kv BSF particle accelerator.[4] The furnace, which has internal dimensions of about 22 × 22 × 22 in. and is lined with steel-covered boral, can be flushed with an inert gas (He) and attains a maximum temperature of 500°C.

After the beryllium assemblies reached equilibrium temperature within the furnace, they were

[1] G. deSaussure and E. G. Silver, *Neutron Phys. Ann. Prog. Rep. Sept. 1, 1958*, ORNL-2609, p 59.

[2] G. deSaussure and E. G. Silver, *Appl. Nuclear Phys. Ann. Prog. Rep. Sept. 1, 1957*, ORNL-2389, p 11.9

[3] The furnace was designed and assembled by F. R. Duncan of the Instrumentation and Controls Division.

[4] J. D. Kington, *Neutron Phys. Ann. Prog. Rep. Sept. 1, 1958*, ORNL-2609, p 61.

irradiated with short bursts of high-energy neutrons produced by the $T(d,n)He^4$ reaction, and the decay of the fundamental mode of the neutron density at the surface of the sample was observed.

Figure 5.3.1 shows the decay of the fundamental mode of the neutron density in a $20 \times 20\frac{1}{8} \times 20\frac{1}{8}$ in. beryllium assembly for various temperatures of the beryllium. The decay constant, λ, of the fundamental mode of the neutron population can be expressed as:

$$\lambda = \lambda_a + \frac{1}{3}\lambda_{tr}\bar{v}B^2(1 - CB^2) \ , \qquad (1)$$

where λ_a is the reciprocal of the mean lifetime, $\bar{v}$ the average neutron velocity, C the diffusion cooling constant, λ_{tr} the transport mean free path, and B^2 the buckling. In Fig. 5.3.2, the decay constant of the neutron density in three beryllium assemblies is plotted as a function of the beryllium temperature.

By replacing the average neutron velocity $\bar{v}$ in Eq. (1) with its value in a moderator at temperature T, the following expression is obtained:

$$\lambda_{tr} = \frac{3}{2}\left(\frac{\pi}{2}\frac{m}{k}\right)^{1/2} \frac{\lambda - \lambda_a}{B^2(1 - CB^2)T^{1/2}} \ , \qquad (2)$$

where m is the mass of the neutron, k the Boltzmann constant, and T the absolute temperature. Previously determined[1] values of λ_a $[(0.288 \pm 0.060) \times 10^3 \text{ sec}^{-1}]$ and C $(1.1 \pm 0.9 \text{ cm}^2)$ and the measured values of $\lambda(T)$ shown in Fig. 5.3.2 were used to compute the variation of λ_{tr} with temperature. The results are shown in Fig. 5.3.3, where they are compared with values calculated by Singwi and Kothari.[5] Agreement between the experiment and the calculation is excellent.

This work is being extended to further measurements below room temperature, and a refrigeration unit for this purpose is under construction. By measurement of the decay constant of small assemblies at various temperatures, the variation of the diffusion cooling constant C with temperature will be determined. This variation has been calculated by Singwi.[6] Similar measurements with BeO are also planned.

---

[5] K. S. Singwi and L. S. Kothari, *Proc. U.N. Intern. Conf. Peaceful Uses Atomic Energy, 2nd, Geneva, 1958*, Paper P/1638 (1958).

[6] K. S. Singwi, private communication.

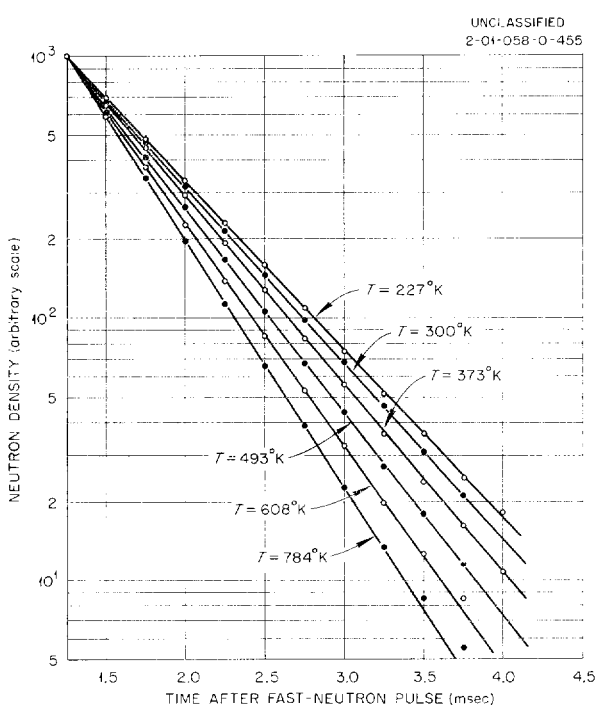

Fig. 5.3.1. Decay of the Neutron Density in a $20 \times 20\frac{1}{8} \times 20\frac{1}{8}$ in. Beryllium Assembly, for Various Temperatures of the Beryllium.

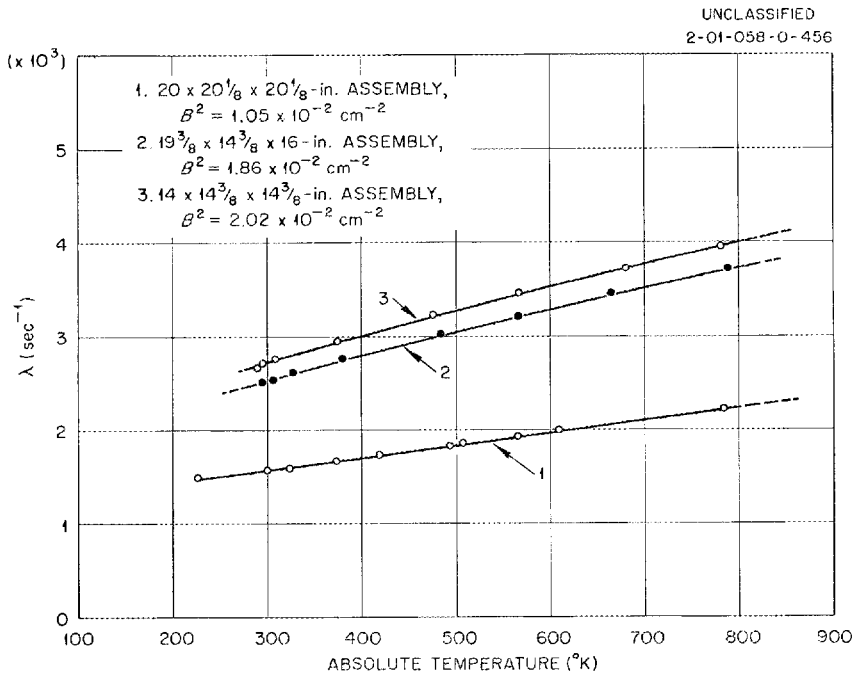

Fig. 5.3.2. Decay Constant λ of the Neutron Density in Three Beryllium Assemblies as a Function of Temperature.

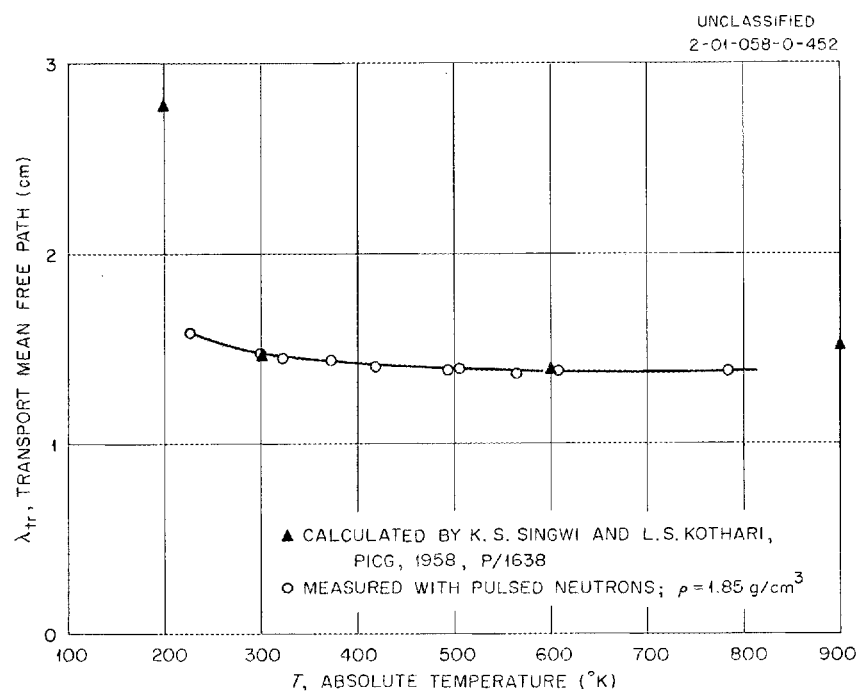

Fig. 5.3.3. Transport Mean Free Path of Thermal Neutrons in Beryllium at Various Temperatures.

Part 6

REACTOR THEORY

6.1. FAST MULTIPLICATION EFFECT OF BERYLLIUM

W. Häfele[1]

The beryllium $(n,2n)$ reaction produces neutrons which can be used to increase the available reactivity margin in a multiplying assembly. Especially in the neutron balance of thorium breeders can a reactivity margin of some per cent be helpful. This effect was therefore considered several times in the past. Mills and Smith,[2] using only integral measurements of the beryllium cross sections made with Ra-Be and Po-Be sources, estimated that the order of magnitude of the additional fast multiplication effect is 10%. Some years later Dillenburg, Jacob, and deToledo[3] considered this problem. Although they used the best cross-section information available at that time, the (n,α) values were wrong by a factor of about 2, and the $(n,2n)$ values that they used are not in very good agreement with present information. Their final results is a reactivity increase of about 6.8%. At the Second Geneva Conference a paper by Krasin *et al.*,[4] discussing this effect, was presented. They considered a critical assembly of enriched uranium (10%) and beryllium in which it was required that there be a neutron balance. But this way of determining the $(n,2n)$ effect is rather indirect, because all other contributing reactivity effects, (e.g., η, ϵ, p, f) have to be known exactly. They reported a reactivity increase of $(12 \pm 4)\%$. Another paper on this subject, by Benoist *et al.*,[5] was presented at the Second Geneva Conference. They were concerned with critical and subcritical experiments on U-BeO lattices and they carefully investigated the fast multiplication of beryllium. They used the latest cross-section data available at that time. For example, they used the correct (n,α) cross section and also calculated the spectrum carefully, taking into account one angular distribution of elastically scattered neutrons in the most important region of 2.9 Mev.

In order to obtain an upper and a lower limit for the effect, we use the latest cross-section information and recalculate the effect from first principles. For the $(n,2n)$ cross section we use the results as reported by Goldstein,[6,7] the results of Marion *et al.*,[8] and the results of Fischer.[9] For the (n,α) values we use the details of Stelson and Campbell.[10] The estimated upper and lower limit for the $(n,2n)$ cross section, and the (n,α) cross section we have used are plotted in Fig. 6.1.1. We also have

---

[1]On leave from Kernreaktor, Karlsruhe, Germany.

[2]C. B. Mills and N. M. Smith, Jr., *The Contribution of the* (n,2n) *Reaction to Beryllium-Moderated Reactor*, AECD-3973 (1951).

[3]D. Dillenburg, G. Jacob, and P. S. deToledo, *Proc. U.N. Intern. Conf. Peaceful Uses Atomic Energy, 2nd, Geneva, 1958*, P/2276.

[4]A. K. Krasin *et al.*, *Proc. U.N. Intern. Conf. Peaceful Uses Atomic Energy, 2nd, Geneva, 1958*, P/2146.

[5]P. Benoist *et al.*, *Proc. U.N. Intern. Conf. Peaceful Uses Atomic Energy, 2nd, Geneva, 1958*, P/1192.

[6]H. Goldstein, *A Review of the Cross Sections of Nonelastic Neutron Reactions of* Be^6, NDA-2-65 (1957).

[7]H. Goldstein and H. Mechanic, *Penetration of Neutrons from a Point Fission Source Through Beryllium and Beryllium Oxide*, NDA-2092-9 (1958).

[8]J. B. Marion, J. S. Levin, and L. Cranberg, University of Maryland Physics Dept., *Tech. Rep. No. 124* (1958).

[9]G. J. Fischer, *Phys. Rev.* 108, 99 (1957).

[10]P. H. Stelson and E. C. Campbell, *Phys. Rev.* 106, 1252 (1957).

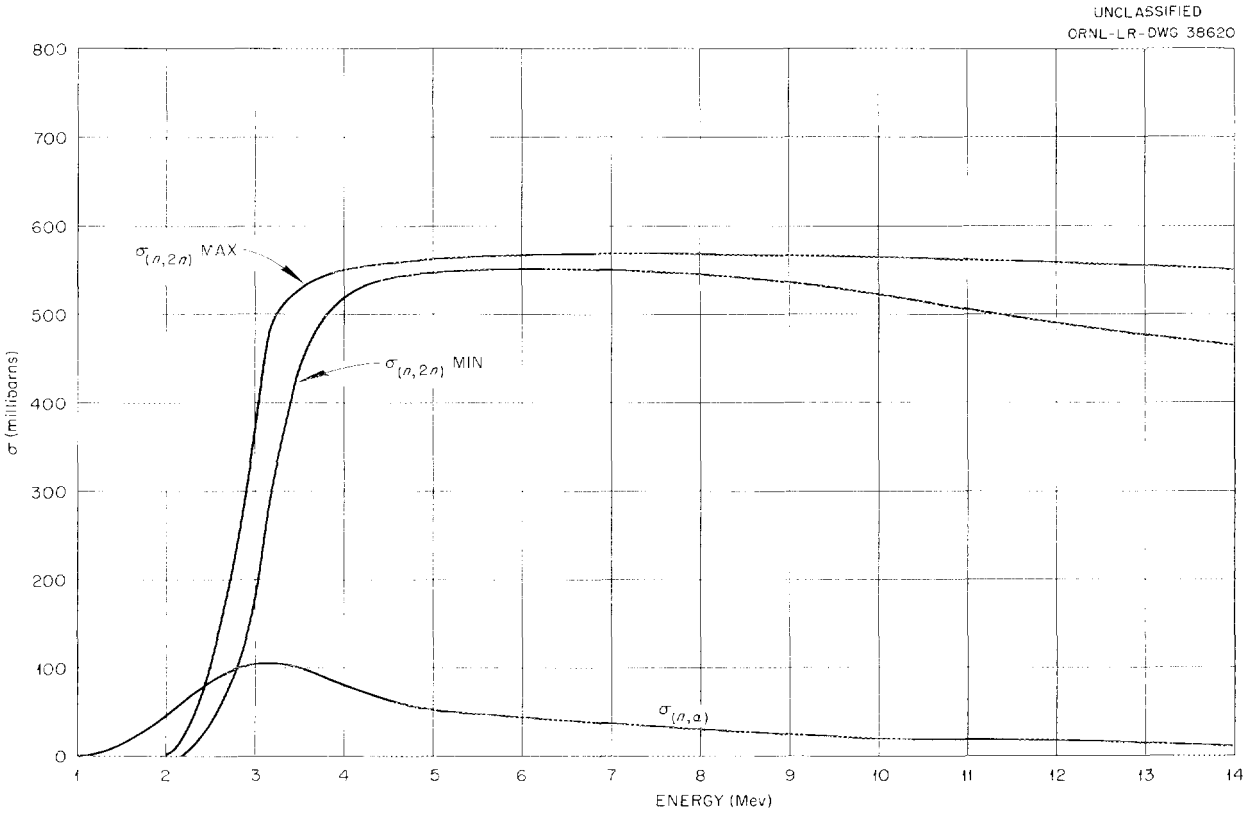

Fig. 6.1.1, Upper and Lower Estimates of the $(n,2n)$ Cross Section and the (n,α) Cross Section of Beryllium.

to employ angular distributions, and here we use BNL-400 values,[11] the distributions presented by Marion,[8] and the values of Fowler and Cohn.[12]

It is not difficult to show that the expression for the fast multiplication effect of beryllium must have the following form:

$$\epsilon\pm = 1 + p_{2n}^{\pm} - p_{\alpha} \ ,$$

where

$$p_{2n}^{\pm} = \int_{E_0}^{\infty} S \frac{\sigma_{2n}^{\pm}}{\sigma_T} dE \ ,$$

$$p_{\alpha} = \int_{E_0}^{\infty} S \frac{\sigma_{\alpha}}{\sigma_T} dE \ ,$$

$$S = \lim_{n \to \infty} \sum_{\nu=0}^{n} S_{\nu} \ .$$

[11] D. J. Hughes and R. S. Carter, *Neutron Cross Section: Angular Distributions*, BNL-400 (1956).

[12] J. L. Fowler and H. O. Cohn, *Phys. Ann. Prog. Rep. Mar. 10, 1959*, ORNL-2718, p 16.

The terms $\sigma_{2n}^{\pm}$ denote the upper and lower limits, respectively, of the $(n,2n)$ cross section, σ_α denotes the (n,α) cross section, and σ_T denotes the total cross section. In our calculations E_0 is 1 Mev and we have employed the relation

$$\sigma_n = \sigma_T \ , \qquad \text{for } E \leq E_0 \ .$$

Here σ_n is the elastic scattering cross section. As sources we use uniformly distributed fission neutrons and employ for the fission spectrum the ANL-5800 values.[13] The spectrum S_ν is the spectrum in an infinite beryllium moderator after the νth elastic collision, determined by the formula

$$S_\nu(E) = \int_E^{E/\alpha} S_{\nu-1}(\epsilon) \frac{\sigma_n(\epsilon)}{\sigma_T(\epsilon)} \frac{f(\epsilon)}{\epsilon(1-\alpha)} d\epsilon \ .$$

Here α is the relative maximum energy loss, and f is proportional to the probability of obtaining the angle of scattering which relates the energies ϵ and E. For isotropic scattering $f = 1$. All numerical integrations were carried out using Simpson's rule and 20 subintervals for each indicated interval of integration. The result is

$$\epsilon_{\mathrm{Be}}^{+} - 1 = p_{2n}^{+} - p_\alpha = 7.6 \times 10^{-2} \ ,$$

$$\epsilon_{\mathrm{Be}}^{-} - 1 = p_{2n}^{-} - p_\alpha = 5.1 \times 10^{-2} \ .$$

Attention has also been given to the poisoning effect of the daughter products of the (n,α) reaction.[5] We have the following decay scheme:

$$n + \mathrm{Be}_4^9 \longrightarrow \mathrm{He}_2^6 + \mathrm{He}_2^4 \ .$$

He_2^6 decays with a half life of 0.8 sec; the daughter is Li_3^6. The next reaction is

$$n + \mathrm{Li}_3^6 \longrightarrow \mathrm{He}_2^4 + \mathrm{H}_1^3 \ .$$

Tritium decays with a half life of 12.5 years; the daughter is He_2^3. The next reaction is

$$n + \mathrm{He}_2^3 \longrightarrow \mathrm{H}_1^3 + p \ .$$

This last cycle repeats. Thus we obtain the following reactivity losses due to poisoning (assuming a flux of 5×10^{13}):

$$\left(\frac{\delta k}{k}\right)_{\mathrm{Li}} = 4.97 \times 10^{-2} \quad \text{(at saturation; the half life of } \mathrm{Li}^6 \text{ at this flux level is 0.525 year)} \ ,$$

$$\left(\frac{\delta k}{k}\right)_{\mathrm{He}^3} = 1.12 \times 10^{-2} \quad \text{(after 5 years)} \ .$$

If we take into account the poisoning of the (n,α) daughter products we find that after some time the most probable over-all value of ϵ_{Be} is close to zero.

The results of this investigation have been issued as a separate report.[14]

---

[13] *Reactor Physics Constants*, ANL-5800 (1958).

[14] W. Häfele, *The Fast-Multiplication Effect in Beryllium in Reactors*, ORNL-2779 (1959).

6.2. ON THE THEORY OF THE DIFFUSION COOLING EFFECT IN HOMOGENEOUS AND HETEROGENEOUS ASSEMBLIES[1]

W. Häfele[2] L. Dresner

The flux distribution of a homogeneous pulsed-neutron assembly is governed by the following equation:

$$D\Delta\phi + R(\phi) - \Sigma_a\phi = \frac{1}{v}\frac{\partial\phi}{\partial t} , \tag{1}$$

where

$$R(\phi) = \int_0^\infty \Sigma(\epsilon' \to \epsilon)\phi(\epsilon')\, d\epsilon' - \Sigma_s(\epsilon)\phi(\epsilon) , \tag{2}$$

and

ϕ = space- and neutron-energy-dependent flux,

D = diffusion constant,

v = neutron velocity,

$\Sigma_a(\Sigma_s)$ = absorption (scattering) cross section,

$\Sigma(\epsilon' \to \epsilon)$ = energy-exchange kernel,

ϵ = ratio of neutron energy to moderator temperature.

We consider an expansion in terms of eigenfunctions with respect to both energy and space. Besides the usual space boundary conditions, we have the energy conditions

$$\phi(x,0) = 0 ,$$

$$\phi(x,\infty) = 0 ,$$

where x stands for all space variables. Let us consider the ansatz

$$\phi = e^{-\lambda t} \sum_{p,q} a_{p,q}\,\omega_p(\epsilon)\,\psi_q(x) , \tag{3}$$

where the ω_p's are the normalized eigenfunctions of the operator R with the eigenvalue $-2\mu\Sigma_0\sigma_p$, and the ψ_q's are the spatial eigenfunctions of the operator Δ with eigenvalues $-B_q^2$. We define the following quantities:

$$\alpha = \frac{\lambda - \Sigma_a v}{2\mu\Sigma_0\left(\frac{2T}{m}\right)^{1/2}} , \tag{4}$$

$$x_0^2 = \frac{D}{2\mu\Sigma_0} . \tag{5}$$

[1]A more extensive version of this paper has been submitted to *Nuclear Sci. and Eng.*

[2]On leave from Kernreaktor, Karlsruhe, Germany.

The absorption cross section obeys a $1/v$ law; the factor $2\mu\Sigma_0$ is used for convenience and introduces some simplification of notation in the heavy gas model. Here Σ_0 is the constant free-atom scattering cross section and μ is the reciprocal of the mass of a heavy gas atom in units of a neutron mass; T is the moderator temperature. Using the two symmetric matrix elements

$$V_{pk} = \int_0^\infty \omega_p(\epsilon)\, \epsilon^{-1/2}\, \omega_k^+(\epsilon)\, d\epsilon \ , \tag{6}$$

$$U_{pk} = \int_0^\infty \omega_p(\epsilon)\, x_0^2\, \omega_k^+(\epsilon)\, d\epsilon \ , \tag{7}$$

we obtain the equations

$$\sum_p a_{p,0}(\alpha V_{pk} - \sigma_p \delta_{pk} - B_0^2 U_{pk}) = 0 \ , \qquad k = 0,1,2,3, \ldots, \infty \ , \tag{8}$$

if we restrict ourselves to the lowest spatial mode. In these equations α is the eigenvalue, and in order to study the asymptotic time behavior we look for the lowest one. All off-diagonal elements in (8) are of the order α. If we examine the value of α only to order B_0^4, this fact can be used to establish the coefficient of the B_0^4 term exactly. We find that

$$\lambda = (\Sigma_a v) + \bar{v}\bar{D}\, B_0^2 (1 - CB_0^2) \ , \tag{9}$$

$$C = \frac{\bar{D}}{2\mu\Sigma_0} \sum_{k=1}^{\infty} \left(\frac{V_{0k}}{V_{00}} - \frac{U_{0k}}{U_{00}}\right)^2 \frac{1}{\sigma_k} \ . \tag{10}$$

All terms of the sum in (10) contribute with the same sign. The averages (denoted by the bar) are over a Maxwellian distribution. In the case of a heavy gas we have

$$L_p^{(1)}(\epsilon) = \sqrt{p+1} \sum_{\mu=0}^{p} (-1)^\mu \frac{p!}{\mu!(\mu+1)!(p-\mu)!}\, \epsilon^\mu \ , \tag{11}$$

$$\sigma_p = p \ ,$$

$$\omega_p^+ = L_p^{(1)}(\epsilon) \ ,$$

$$\omega_p = \epsilon e^{-\epsilon} L_p^{(1)}(\epsilon) \ .$$

Here $L_p^{(1)}$ is a normalized associated Laguerre polynomial of the first order. Thus

$$C = \frac{D}{2\mu\Sigma_0} \sum_{k=1}^{\infty} \frac{1}{k(k+1)} \left[\frac{(2k-1)!!}{(2k)!!}\right]^2 \ , \tag{12}$$

where $x!! = x(x-2)(x-4)\ldots(2 \text{ or } 1)$.

Equation (12) can be used to check the convergence of an expansion in Laguerre polynomials. The convergence is slow. If we define C_{k_0} as the partial sum (12) up to the index k_0 we have:

k_0	$C_{k_0}\left(\frac{D}{2\mu\Sigma_0}\right)^{-1}$	k_0	$C_{k_0}\left(\frac{D}{2\mu\Sigma_0}\right)^{-1}$
1	0.1250	9	0.1652
2	0.1484	10	0.1655
3	0.1566	11	0.1657
4	0.1603	12	0.1659
5	0.1623	13	0.1660
6	0.1635	14	0.1661
7	0.1643	15	0.1662
8	0.1649		

We propose in the case of a crystalline moderator, for example, an iteration process of the equation

$$R(\omega_p) = -2\mu\Sigma_0 \sigma_p \omega_p \quad ,$$

starting with the heavy gas eigenfunctions (11). Each iteration gives an improvement, which we use in (6) and (7) and which refers exclusively to crystal binding effects. That is, if we define

$$C(l_0) = \frac{\bar{D}}{2\mu\Sigma_0}\left\{\sum_{k=1}^{l_0}\left(\frac{V_{0k}}{V_{00}}-\frac{U_{0k}}{U_{00}}\right)^2\frac{1}{\sigma_k} + \sum_{k=l_0+1}^{\infty}\frac{1}{k(k+1)}\left|\frac{(2k-1)!!}{2k!!}\right|^2\right\} ,$$

the change produced by a stepwise increase of l_0 is due entirely to the introduction of crystalline effects in order l_0.

The procedure given here can be used also for heterogeneous assemblies. There we consider for the sake of simplicity only the one-dimensional case, although the two-dimensional case can also be treated.[3] This one-dimensional assembly consists of N_0 Wigner-Seitz cells and has no reflectors. The lumped absorbers have the width $2a$ and the distance d. The number of Wigner-Seitz cells is odd, that is, $N_0 = 2N + 1$. Since there are no reflectors, the over-all length of the finite reactor is $2l = N_0 d$. We have to consider in (1) in addition to the homogeneously distributed absorber the expression for the lumped absorber represented by δ-functions of finite absorption strength:

$$f_- = -\epsilon^{-1/2}\,\bar{p}\sum_{k=-N}^{+N}\delta(x-kd)\,d\phi\,(kd,\epsilon) \quad , \tag{13}$$

$$\bar{p} = \frac{2a(\Sigma_B v)}{2\mu\Sigma_0 d\left(\frac{2T}{m}\right)^{1/2}} \quad . \tag{14}$$

[3] K. Meetz, *Proc. U.N. Intern. Conf. Peaceful Uses Atomic Energy, 2nd, Geneva, 1958*, P/968.

We now apply the mathematics of plane heterogeneous structures as given by Meetz.[4] With respect to the energy expansion ω_p we restrict ourselves to the case that only two terms ω_0 and ω_1 are considered. After cumbersome calculations we find the following result:

$$\lambda = (\Sigma_a v)_{\text{hom}} + \bar{v}\bar{D}B_0^2 \frac{M}{Q}\left[1 - \left(\frac{V_{10}}{V_{00}} - \frac{U_{10}}{U_{00}}\right)^2 \frac{1}{\sigma_1} \frac{\bar{D}B_0^2\, M/Q}{2\mu\Sigma_0}\right] +$$

$$+ (\Sigma_B v)\frac{2a}{d}\frac{I}{Q}\left\{1 - \left(\frac{V_{10}}{V_{00}} - \frac{U_{10}}{U_{00}}\right)^2 \frac{1}{\sigma_1} \frac{(\Sigma_B v)\, 2a/d}{2\mu\Sigma_0\, \bar{v}}\left[y_2 S(y_2) - \frac{I}{Q}\right]\right\} +$$

$$+ 0[(U_{00}B_0^2)^{\mu} p^{\nu}] \ , \qquad (\mu + \nu) \geq 3 \ . \qquad (15)$$

The term y_2 is the root of the quadratic equation,

$$(U_{00}y - V_{00}\alpha)(U_{11}y + \sigma_1 - V_{11}\alpha) - (V_{10}\alpha - U_{10}y)^2 = 0 \ , \qquad (16)$$

which is not of order α, and $S(y)$ is defined as

$$S(y) = \frac{d}{2}\frac{1}{\sqrt{y}}\frac{\sin d\sqrt{y}}{\cos d\sqrt{y} - \cos\dfrac{\pi}{N_0}} \ ,$$

and M, Q, and I are auxiliary functions which refer to the heterogeneous structure. They are defined as follows:

$$M = 2\left(\frac{N_0}{\pi}\right)^2\left(1 - \cos\frac{\pi}{N_0}\right) \ ,$$

$$Q = \frac{2}{d^2 y_1}(1 - \cos d\sqrt{y_1}) \ ,$$

$$I = \frac{1}{d\sqrt{y_1}}\sin d\sqrt{y_1} \ ,$$

where y_1 is the other root of (16).

Since we considered only two terms, ω_0 and ω_1, we have in (15) only the expression

$$\left(\frac{V_{10}}{V_{00}} - \frac{U_{10}}{U_{00}}\right)^2$$

instead of (10). The first line of (15) is completely analogous to the homogeneous case, except that the corrected buckling $B_0^2\, M/Q$ instead of B_0^2 appears. An additional absorption effect with its own "cooling" effect appears in the second line.

The physical reason is obvious. Neutrons have to diffuse before they get absorbed in the lumps and the fast neutrons are absorbed faster. If we consider a process of homogenization ($N_0 \to \infty$, $d \to 0$,

[4] K. Meetz, *Z. Naturforsch.* 12a(9) (1957).

$N_0 d = 2l$ = finite), only the smoothed-out absorber $\Sigma_B v\ 2a/d$ is allowed to appear. Equation (15) describes this effect, for we have the following relations:

$$\frac{I}{Q} \leqq 1 \ ,$$

$$\frac{I}{Q} = 1 \text{ for the homogeneous assembly} \ ,$$

$$y_2 S(y_2) \leqq 1 + 0(\alpha^2) \ ,$$

$$y_2 S(y_2) = 1 + 0(\alpha^2) \text{ for the homogeneous assembly} \ .$$

It can also be shown that the absorption-diffusion effect is always a negative effect and disappears in the limit of homogenization.

It may be emphasized that (15) contains no approximations with respect to the heterogeneous structure, but only with respect to the expansion defining the energy spectrum. Furthermore, (15) is valid for all possible values of N_0. For example, the influence of one single foil for measuring purposes in the middle of the assembly can be evaluated. In this case $N_0 = 1$.

6.3. COMPARISON THEOREMS FOR THE ESTIMATION OF AVERAGE COLLISION PROBABILITIES

L. Dresner

The collision probability, P_V, of a uniform, isotropic volume source of neutrons in a convex solid V is a quantity of great importance in reactor physics. For example, it enters either directly, or through use of a well-known reciprocity theorem,[1] in calculations of the fast effect,[2] the resonance escape probability,[3] and the thermal utilization.[4] However, it has been explicitly calculated only for a few simple solids: the sphere, slab, and infinite right circular cylinder. These results are quoted (and tabulated) by Case, Placzek, and deHoffmann.[1] Chord-length distribution functions, from which P can be obtained, though often at the cost of considerable labor, have been given for the hemisphere, oblate spheroid, and oblate hemispheroid by Dirac, Fuchs, Peierls, and Preston.[5] Some values of P_V for these solids have been given in ref 1. The chord-length distribution function for a finite right circular cylinder has been given by Skyrme,[6] and discussed by Murray,[7] who also gives the chord-length distribution

[1] K. M. Case, G. Placzek, and F. deHoffmann, *Introduction to the Theory of Neutron Diffusion*, vol I, USGPO, Washington, D.C., 1953.

[2] A. M. Weinberg and E. P. Wigner, *The Physical Theory of Neutron Chain Reactors*, chap. XX, University of Chicago Press, Chicago, 1958.

[3] *Ibid.*, chap. XIX.

[4] A. Amouyal, P. Benoist, and J. Horowitz, *J. Nuclear Energy* 6, 79 (1957).

[5] P. A. M. Dirac *et al.*, *Approximate Rate of Neutron Multiplication for a Solid Arbitrary Shape and Uniform Density*, British Report MS-D-5, Part II (results quoted in ref 1) (n.d.).

[6] T. H. R. Skyrme, *Reduction in Neutron Density Caused by an Absorbing Disc*, British Report MS-91, Appendix (n.d.).

[7] F. H. Murray, *Fast Effects, Self Absorption, Fluctuation of Ion Chamber Readings, and the Statistical Distribution of Chord Lengths in Finite Bodies*, CP-G-2922 (1945).

function for the cube. In order to extend the usefulness of these results, and occasionally to avoid the labor of integration in cases where only the chord distribution is explicitly known, three comparison theorems are given with which the collision probability may be estimated.

Statement of the Comparison Theorems

In this section the collision probability will be defined precisely and the comparison theorems stated, and in the next section some illustrations will be given. Proofs will be given in the following section.

The collision probability is given by

$$P_V = \frac{1}{V} \int_V d^3 r \int_V d^3 r' \frac{e^{-|r-r'|}}{4\pi |r-r'|^2} , \tag{1}$$

where the unit of length has been chosen as the mean free path in the solid.

Theorem 1. – If a solid V^* is obtained from a convex solid V by Steiner symmetrization, $P_{V^*} \geqq P_V$.

Steiner symmetrization is defined with respect to some plane Q as follows:[8] (1) V^* is symmetric with respect to Q, (2) any straight line perpendicular to Q that intersects one of the solids V and V^* intersects the other also (*both intersections have the same length*), and (3) the intersection with V^* consists of just one line segment. It is known that Steiner symmetrization leaves the volume invariant.[8] It is also known that symmetrization in an appropriately chosen infinitude of planes reduces all finite solids to spheres; and symmetrization in an appropriate infinitude of planes, all containing the common axis, reduces all infinite right cylinders to right circular cylinders.[8] From this the following is evident.

Corollary. – Of all convex solids of given volume, the sphere has the maximum collision probability; and, of all right cylinders of given base area, the circular cylinder has the maximum collision probability.

Theorem 2. – If V is the volume common to (*a*) two perpendicular slabs, S_1 and S_2, (*b*) three mutually perpendicular slabs, S_1, S_2, and S_3, or (*c*) a convex right cylinder, C, and a slab, S, perpendicular to its axis, then

$$(a) \qquad P_{S_1} \quad \text{and} \quad P_{S_2} \geqq P_V \geqq P_{S_1} P_{S_2} ,$$

$$(b) \quad P_{S_1} \quad \text{and} \quad P_{S_2} \quad \text{and} \quad P_{S_3} \geqq P_V \geqq P_{S_1} P_{S_2} P_{S_3} ,$$

or

$$(c) \qquad P_C \quad \text{and} \quad P_S \geqq P_V \geqq P_C P_S .$$

Theorem 3, Part 1. – Consider a convex solid V and an arbitrary line L in space. Let the length along L be measured by a coordinate z. Let the intersection of V and a plane P perpendicular to L at z be denoted by $A(z)$. Let $P_C(z)$ be the collision probability of an infinite right cylinder with $A(z)$ as

[8] G. Pólya and G. Szegö, *Isoperimetric Inequalities in Mathematical Physics*, Princeton University Press, Princeton, N.J., 1951.

base and L as axis. Then

$$P_V \leqq \frac{1}{V} \int_a^b dz\, A(z)\, P_C(z) \quad ,$$

where a and b are the limits determined by the planes tangent to V and perpendicular to L.

Theorem 3, Part 2. – Consider a convex solid V and an arbitrary plane P in space. Let the position in P be measured by a coordinate two-vector ρ. Let the intersection of a normal L to P at ρ and V be a line segment of length $t(\rho)$. Let $P_S(\rho)$ be the collision probability of a slab of thickness $t(\rho)$. Then

$$P_V \leqq \frac{1}{V} \int_A d\rho\, t(\rho)\, P_S(\rho) \quad ,$$

where A is the projected area of V on P.

Theorem 4. – If $\bar{l} = 4V/S$, where V is the volume of a convex solid and S its surface, then

$$P_V \geqq 1 - \frac{1 - e^{-\bar{l}}}{\bar{l}} \quad .$$

Illustrations

Theorem 1 provides close overestimates for fairly symmetrical solids (e.g., equilateral cylinders, cubes, etc.). Theorem 2 provides fairly close underestimates if the P's involved are all fairly close to unity. Consider the example of a cube five mean free paths on a side. The probability P for the volume-equivalent sphere is 0.771; P obtained from theorem 2 (2) is 0.730; P obtained from theorem 4 is 0.711. Thus $0.730 \leqq P_{\text{cube}} \leqq 0.771$. Choosing the mean of these extremes to minimize the magnitude of the uncertainty gives $P_{\text{cube}} \simeq 0.75 \pm 0.02$. When the side of the cube is equal to one mean free path, P of the volume-equivalent sphere is 0.344; P obtained from theorem 2 (2) is 0.227; P obtained from theorem 4 is 0.270. Thus $0.270 \leqq P_{\text{cube}} \leqq 0.344$, the lower bound now being obtained from theorem 4. Using the mean of the extremes as an estimate now gives $P_{\text{cube}} \simeq 0.31 \pm 0.04$.

Theorem 1 is not very useful in the case of solids that are not highly symmetrical. Consider, for example, a cylindrical disk whose thickness is 0.5 of a mean free path, and whose radius is five mean free paths. The collision probability of a slab of the same thickness as the disk, which is an upper bound by theorem 2 (3), is 0.443. A lower bound of 0.399 is also obtained from theorem 2 (3). Thus $P \simeq 0.42 \pm 0.02$, while P for the volume-equivalent sphere is 0.681, a gross overestimate. The value of P obtained from theorem 4 is 0.343.

Furthermore, when the diameter of the disk is of the order of one mean free path, theorem 2 is not very useful, and is expected to grossly under- and overestimate P. For example, consider a disk whose thickness and radius are each 0.5 of a mean free path. An upper bound of 0.272 can be obtained from theorem 1; a lower bound of 0.213 can be obtained from theorem 4. Thus $P \simeq 0.24 \pm 0.03$. On the other hand, theorem 2 (3) gives 0.443 and 0.179, respectively, as upper and lower bounds.

Theorem 3 is particularly useful in obtaining upper bounds for quite unsymmetrical solids. Consider, for example, an oblate spheroid with a ratio of major to minor axis of 5, and a minor axis 0.342 of a mean free path in length. Using theorem 3, part 2, and theorem 4 we obtain $0.322 \leqq P \leqq 0.441$ or $P \cong 0.38 \pm 0.06$, whereas the value of P for the volume-equivalent sphere is 0.473. As a corollary of theorem 3, P_V should be less than that of a slab of a thickness equal to twice the minor axis of the oblate spheroid. In the case at hand, this latter collision probability is 0.517. This gross overestimate is not improved very much by a large increase in the eccentricity. For example, for an oblate spheroid with a ratio of major to minor axis of 30, and a minor axis one mean free path long, theorems 3 and 4 give $P \cong 0.49 \pm 0.04$, while the P for the thinnest circumscribing slab is 0.610.

Proofs of the Theorems

Theorem 1. – Let the plane of symmetrization be taken as the x,y plane for a Cartesian set of coordinate axes. Let us consider two cylinders whose axes are parallel to the z axis and whose base areas are $dx_1 dy_1$ at x_1,y_1 and $dx_2 dy_2$ at x_2,y_2. These cylinders intersect the solid V in two finite cylindrical volumes whose upper and lower ends are z_1',z_1'' and z_2',z_2'', respectively. It is enough to consider the contribution, ΔP, of this pair of cylinders to P. This is

$$\Delta P = \frac{dx_1\, dy_1\, dx_2\, dy_2}{V} \int_{z_1''}^{z_1'} dz_1 \int_{z_2''}^{z_2'} dz_2\, K\sqrt{(x_1 - x_2)^2 + (y_1 - y_2)^2 + (z_1 - z_2)^2}\ , \tag{2}$$

where K is an abbreviated notation for the integrand of Eq. (1). Let us choose a new origin of coordinates so that the segment $z_2'z_2''$ is symmetrically located with respect to the x,y plane. Thus the limits of integration of Eq. (2) can be taken as $-a + \zeta$, $+a + \zeta$ for z_1 and $-b$, $+b$ for z_2, where $2a$ is the length of the segment $z_1'z_1''$, $2b$ is the length of the segment $z_2'z_2''$, and ζ is the difference in z coordinates of the midpoints of these segments. It is easy to verify that P has an extremum at $\zeta = 0$ by a single differentiation with respect to ζ; a second differentiation shows that the extremum is a maximum if K is a monotonic decreasing function of its argument. The proof is completed by noting that Steiner symmetrization consists in shifting the midpoints of all segments into the (same) plane of symmetrization, that is, making $\zeta = 0$.

Theorem 2. – Let us begin by introducing the characteristic function, $f(\mathbf{r})$, of the solid V, which is defined to be unity in the interior of V and zero outside. Then

$$VP_V = \iint f(\mathbf{r})\, K(\mathbf{r} - \mathbf{r}')\, f(\mathbf{r}')\, d^3 r\, d^3 r'\ , \tag{3}$$

where the integrals are now over all space. (All integrals without explicitly specified limits are over all space.) Let us introduce the Fourier transforms

$$f(\mathbf{k}) = \int_V e^{i\mathbf{k}\cdot\mathbf{r}}\, d^3 r\ ; \qquad f(\mathbf{r}) = (2\pi)^{-3} \int e^{-i\mathbf{k}\cdot\mathbf{r}} f(\mathbf{k})\, d^3 k\ , \tag{4a}$$

$$K(\mathbf{k}) = \int K(\mathbf{r}) e^{i\mathbf{k}\cdot\mathbf{r}}\, d^3 r\ ; \qquad K(\mathbf{r}) = (2\pi)^{-3} \int K(\mathbf{k}) e^{-i\mathbf{k}\cdot\mathbf{r}}\, d^3 k\ . \tag{4b}$$

It follows from Eqs. (4*a*) and (4*b*) with the help of the identity,

$$(2\pi)^3\ \delta(\mathbf{k}) = \int e^{i\mathbf{k}\cdot\mathbf{r}}\, d^3 r \quad , \tag{5}$$

that

$$(2\pi)^3\, VP_V = \int f(\mathbf{k})\, f(-\mathbf{k})\, K(\mathbf{k})\, d^3 k \quad , \tag{6}$$

and

$$(2\pi)^3\, V = \int f(\mathbf{k})\, f(-\mathbf{k})\, d^3 k \quad . \tag{7}$$

Finally, it is shown in ref 1 that $K(\mathbf{k}) = (\arctan k)/k$.

Let us now consider V to be a rectangular parallelepiped of sides a_1, a_2, and a_3. Then

$$f(\mathbf{k}) = \prod_{i=1}^{3} \int_{-a_i/2}^{a_i/2} \exp(ik_i r_i)\, dr_i \equiv \prod_{i=1}^{3} f_i(k_i) \quad , \tag{8}$$

where r_i are the Cartesian coordinates of $\mathbf{r}$, and k_i are the Cartesian coordinates of $\mathbf{k}$. If a_2 and a_3 become very large, $f(\mathbf{k})$ is appreciable only when k_2, k_3 are near zero. Hence $k \cong k_1$, and

$$(2\pi)^3\, VP_V = \int f_1(k_1)\, f_1(-k_1)\, f_2(k_2)\, f_2(-k_2)\, f_3(k_3)\, f_3(-k_3)\, K(k_1)\, d^3 k \tag{9a}$$

$$= (2\pi) a_2 \cdot (2\pi) a_3 \cdot \int f_1(k_1)\, f_1(-k_1)\, K(k_1)\, dk_1 \quad . \tag{9b}$$

The second equality follows from the one-dimensional analog of Eq. (7). If a_2 and a_3 approach ∞, Eq. (9*b*) can be rewritten

$$(2\pi)\ a_1 P_{\text{slab}}(a_1) = \int f_1(k_1)\, f_1(-k_1)\, K(k_1)\, dk_1 \quad . \tag{10}$$

If a_3 only becomes very large, then

$$(2\pi)^3\, VP_V = (2\pi)\ a_3 \cdot \int f_1(k_1)\, f_1(-k_1)\, f_2(k_2)\, f_2(-k_2)\, K(k)\, dk_1\, dk_2 \quad , \tag{11}$$

where $k^2 = k_1^2 + k_2^2$. Since, with k so defined,

$$\frac{\arctan k}{k} \geqq \frac{\arctan k_1}{k_1} \cdot \frac{\arctan k_2}{k_2} \quad , \tag{12}$$

it immediately follows from Eqs. (10) and (11) that

$$P_V \geqq P_{\text{slab}}(a_1)\, P_{\text{slab}}(a_2) \quad . \tag{13}$$

This is the second inequality of part (1); the second inequality of parts (2) and (3) follow similarly.

The first inequality of part (1) can be proven by, for example, inserting the inequality

$$\frac{\arctan k_1}{k_1} \text{ or } \frac{\arctan k_2}{k_2} \geqq \frac{\arctan k}{k} \tag{14}$$

in Eq. (11). The first inequality of parts (2) and (3) follow similarly.

Theorem 3. – To prove this theorem we again employ the method of characteristic functions introduced above. For the first part of the theorem let us write the Fourier transform, $f(\mathbf{k})$, of the characteristic function as

$$f(\mathbf{k}) = \int_a^b e^{ik_3 z}\, dz \int_{A(z)} d\rho\, e^{i\mathbf{k}_\rho \cdot \rho} \;, \tag{15}$$

where ρ is the coordinate two-vector in plane P. Substituting Eq. (15) in Eq. (6) and rearranging the order of integration, we obtain

$$(2\pi)^3 VP_V = \int dk_3 \int_a^b e^{ik_3 z}\, dz \int_a^b e^{-ik_3 z'}\, dz' \int d\mathbf{k}_\rho \int_{A(z)} d\rho\, e^{i\mathbf{k}_\rho \cdot \rho} \int_{A(z')} d\rho'\, e^{-i\mathbf{k}_\rho \cdot \rho'}\, K(\mathbf{k}) \;. \tag{16}$$

If we insert $K(\mathbf{k}_\rho) \geqq K(\mathbf{k})$ on the right-hand side of Eq. (16) and then perform the k_3 and z' integrations in that order, we obtain

$$(2\pi)^3 VP_V \leqq (2\pi) \int_a^b dz \left[\int dk_\rho \int_{A(z)} d\rho\, e^{i\mathbf{k}_\rho \cdot \rho} \int_{A(z)} d\rho'\, e^{-i\mathbf{k}_\rho \cdot \rho'}\, K(\mathbf{k}_\rho) \right] \;. \tag{17}$$

If, in Eq. (16), we let $a \to -\infty$, $b \to +\infty$, we obtain, by reasoning similar to that employed in connection with Eqs. (9) and (10), that the bracketed term in Eq. (17) is just $(2\pi)^2 A(z) P_C(z)$. But then

$$VP_V \leqq \int_a^b dz\, A(z) P_C(z) \;, \tag{18}$$

which was to be proven. The second part of theorem (3) is proven in an exactly similar manner, except that we write $f(\mathbf{k})$ as

$$f(\mathbf{k}) = \int_A e^{i\mathbf{k}_\rho \cdot \rho}\, d\rho \int_{a(\rho)}^{b(\rho)} e^{ik_3 z}\, dz \;, \tag{19}$$

where $a(\rho)$ and $b(\rho)$ are the intersections of the normal L to P at ρ with V; interchange the order of integration so that those over k_ρ, ρ, and ρ' are last; and substitute $K(k_3) \geqq K(\mathbf{k})$ for $K(\mathbf{k})$.

Theorem 4. – According to Eq. (7), Sec 10.1 of ref 1,

$$P_V = 1 - \frac{1}{\bar{l}} \left[1 - \int f(l)\, e^{-l}\, dl \right] \;, \tag{20}$$

where $f(l)$ is the normalized distribution of chord lengths of the convex solid V. [$f(l)$ is defined in ref 1; there it is also shown that the mean of the distribution $f(l)$ is $\bar{l} = 4V/S$.] By theorem 184 of Hardy *et al.*[9] it can be shown that

$$\int f(l)\, e^{-l}\, dl \geqq e^{-\int f(l)\, l\, dl} = e^{-\bar{l}} \;. \tag{21}$$

Combining Eqs. (20) and (21) yields the desired result.

---

[9] G. H. Hardy, J. E. Littlewood, and G. Pólya, *Inequalities*, Cambridge University Press, London, 1934.

6.4. FIRST-FLIGHT NONESCAPE PROBABILITIES FOR NEUTRONS IN A SPHERE

E. Inönü

The second fundamental theorem of reactor theory gives a general expression for the nonescape probabilities for neutrons in a bare homogeneous reactor.[1] In order to verify the accuracy of this expression for small-sized reactors, a special case was considered previously.[2] First-flight nonescape probabilities for neutrons originating from either a persisting or a uniform distribution in an infinite slab were calculated using the fundamental theorem and the assumption that the "linear extrapolation" condition is satisfied at the boundary with a constant extrapolation length. Comparison with the accurate values obtained from transport theory showed that good agreement persists down to slab widths of the order of one mean free path (mfp). A similar comparison has now been carried out for a sphere.

In a sphere of radius a, the first-flight nonescape probability for an initial spherically symmetric flux $\psi(r)$ may be expressed as:

$$P = \frac{\int_0^a \phi(r)\, r^2\, dr}{\int_0^a \psi(r)\, r^2\, dr} , \tag{1}$$

where $\phi(r)$ represents the flux of neutrons which have made one collision. From transport theory, $\phi(r)$ may be exactly obtained as:

$$\phi(r) = \frac{1}{2r} \int_0^a \psi(r')\, r' \left[E_1(\Sigma|r' - r|) - E_1(\Sigma|r' + r|)\right] dr' , \tag{2}$$

where Σ is the macroscopic total cross section and the "scattering" (which may include emission) is assumed to be isotropic. However, by expanding the initial distribution in terms of the eigen solutions $\psi_n(r)$ of the wave equation for a sphere,

$$\psi(r) = \sum_n A_n \psi_n(r) = \sum_n A_n \frac{\sin B_n r}{r} , \tag{3}$$

where the eigenvalues B_n are determined, in correspondence to the slab case, by the boundary condition

$$[r\psi_n(r)]_a + d\left\{\frac{d}{dr}[r\psi_n(r)]\right\}_a = 0 , \tag{4}$$

and applying the second fundamental theorem to every mode, $\phi(r)$ may be expressed approximately as

$$\phi(r) = \sum_n A_n \kappa_n \frac{\sin B_n r}{r} , \tag{5}$$

where $\kappa_n = (\Sigma/B_n) \tan^{-1} (B_n/\Sigma)$ is the approximate nonescape probability for the nth mode.

---

[1] A. M. Weinberg and E. P. Wigner, *The Physical Theory of Neutron Chain Reactors*, chap. XII, University of Chicago Press, Chicago, 1958.

[2] E. Inönü, *Nuclear Sci. and Eng.* 5, 248–53 (1959).

In the case of a persisting distribution, the integral equation

$$\phi(r) = P\psi(r) \tag{6}$$

determines P. Pryce has shown[3] that quite accurate values of P can be obtained from this equation by a variational calculation using a simple trial function of the form $\psi_t(r) = r(1 - qr^2)$. Table 6.4.1 lists values of P computed by this method. The characteristic parameter is the product Σ_a which is here denoted as σ. The values for $\sigma = 0.1$, 0.5, 1.0, and 1.6 shown in the table are taken from Pryce's paper.

On the other hand, according to the fundamental theorem, the nonescape probability for the persisting distribution is given simply by

$$\kappa = \kappa_1 = \frac{\Sigma}{B_1} \tan^{-1} \frac{B_1}{\Sigma} ,$$

where B_1 is the first eigenvalue obtained from (4) with $d = 0.71/\Sigma$. The results for P and κ are shown in Fig. 6.4.1. The agreement appears quite good down to very small sizes, although it is not as satisfactory as it was for the slab[2] if one makes a comparison for the same value of σ; for example, for a sphere with a radius of 1 mfp, the fractional error in the nonescape probability is 5% as opposed to 1.5% for a slab of half-width = 1 mfp. However, if one compares the errors for identical values of P or κ, the agreement is better for the sphere.

Table 6.4.1 also gives values of κ_{ex} obtained by assuming that the flux vanishes at $r = a + d$. For small values of σ, they show considerably greater deviation from the accurate values. In the limit as $\sigma \to 0$, $P \to 0.78\sigma$ (ref 3), $\kappa \to \sigma$ and $\kappa_{ex} \to 0.305$. Frankel and Goldberg[4] have shown that the agreement of κ_{ex} with P can be very much improved by taking into account the dependence of the extrapolation length on σ (through P) according to transport theory. However, the interest here lies in testing the fundamental theorem with a simple extrapolation length which does not depend on the size.

---

[3] M. H. L. Pryce, *Critical Conditions in Neutron Multiplication*, MSP-2A (declassified 1947).

[4] S. Frankel and S. Goldberg, *The Mathematical Development of the End Point Method*, AECD-2056 (LADC-76) (1945).

Table 6.4.1. First-Flight Nonescape Probabilities for the Persisting Neutron Distribution in a Sphere

σ	P	κ	κ_{ex}	$\frac{\kappa - P}{P}$	$\frac{\kappa_{ex} - P}{P}$	$\frac{\kappa - P}{1 - P}$
0.1	0.075	0.091	0.340	0.21	3.53	0.017
0.5	0.309	0.342	0.463	0.11	0.50	0.048
1.0	0.503	0.528	0.584	0.050	0.16	0.050
1.6	0.650	0.664	0.689	0.021	0.060	0.040
4.0	0.878	0.880	0.882	0.0023	0.0046	0.016
10.0	0.9721	0.9726	0.9727	0.0005	0.0006	0.018

For an initial uniform distribution $\psi(r) = 1$, the first-flight nonescape probability is given exactly as

$$P = 1 - \frac{3}{4\sigma} + \frac{3}{8\sigma^3} - \frac{3}{2\sigma} E_3(2\sigma) - \frac{3}{\sigma^2} E_4(2\sigma) - \frac{3}{2\sigma^3} E_5(2\sigma) \ , \tag{7}$$

and approximately as

$$\kappa = 6 \sum_{n=1}^{\infty} \frac{\kappa_n}{(B_n a)^4} \left(1 + \frac{a}{d}\right)^2 \frac{\sin^2 B_n a}{1 - \dfrac{\sin 2B_n a}{2B_n a}} \ . \tag{8}$$

The functions $E_n(x)$ are the well-known functions[5] defined by

$$E_n(x) = \int_1^{\infty} \frac{e^{-ux}}{u^n} du \ .$$

The values calculated from (7) and (8) for $0.1 < \sigma < 10$, with $d = 0.71/\Sigma$, are listed in Table 6.4.2 and plotted in Fig. 6.4.2. A comparison with similar curves for the slab[2] shows that the agreement again is better for fixed P or κ but worse for fixed σ.

In the two limits of very small and very large sizes, (7) and (8) simplify[6] to:

$$P = 0.75\sigma \quad \text{and} \quad \kappa = 1.016\sigma \ , \qquad \text{for } \sigma \ll 1 \ , \tag{9}$$

$$P = 1 - \frac{0.75}{\sigma} \quad \text{and} \quad \kappa = 1 - \frac{3}{\sigma}\left(0.5 - \alpha + \alpha^2 \ln \frac{1+\alpha}{\alpha}\right) \ , \qquad \text{for } \sigma \gg 1 \ , \tag{10}$$

where $\alpha = d\Sigma$. It may be noted that in (9) κ is independent of α, while in (10) it is dependent on α. For $\alpha = 0.71$, $\kappa = 1 - (0.70/\sigma)$. Thus, with this choice of the extrapolation length, the fractional error in the escape probability remains finite even when the size is indefinitely increased, but will approach zero for $\alpha = 0.616$. This conclusion applies also to the infinite slab, where with the same choice of α agreement can be achieved between P and κ to first order in $1/\sigma$. A few values of κ obtained with $\alpha = 0.616$ are shown in Table 6.4.2 and plotted on Fig. 6.4.2. They agree a little better with the exact values.

---

[5] *Tables of Functions and Zeros of Functions*, NBS Applied Mathematics Series No. 37, USGPO, Washington, 1954.

[6] The method for carrying out these summations was suggested by W. Kofink.

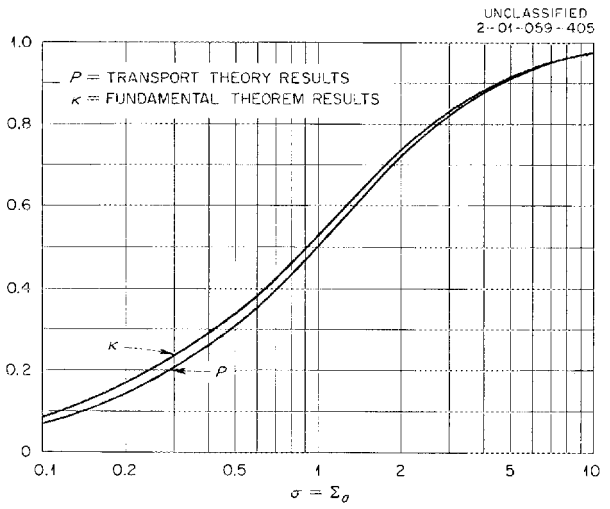

Fig. 6.4.1. First-Flight Nonescape Probabilities for the Persisting Neutron Distribution in a Sphere.

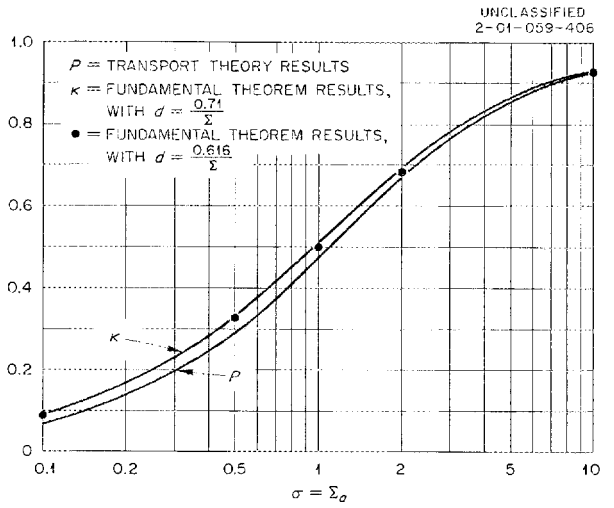

Fig. 6.4.2. First-Flight Nonescape Probabilities for a Uniform Neutron Distribution in a Sphere.

Table 6.4.2. First-Flight Nonescape Probabilities for a Uniform Neutron Distribution in a Sphere

σ	P	κ		$\frac{\kappa - P}{P}$		$\frac{\kappa - P}{1 - P}$	
		$a = 0.71$	$a = 0.616$	$a = 0.71$	$a = 0.616$	$a = 0.71$	$a = 0.616$
0.1	0.071	0.090	0.0895	0.27	0.26	0.66	0.64
0.2	0.135	0.167		0.24		0.37	
0.5	0.293	0.335	0.329	0.14	0.12	0.059	0.051
1.0	0.473	0.511	0.500	0.083	0.057	0.072	0.051
2.0	0.668	0.691	0.681	0.034	0.019	0.069	0.039
4.0	0.818	0.831		0.015		0.071	
5.0	0.853	0.863		0.012		0.068	
10.0	0.925	0.930	0.927	0.005	0.002	0.067	0.027

6.5. INFLUENCE OF THE GEOMETRIC SYMMETRIES OF A HETEROGENEOUS REACTOR ON THE FLUX DISTRIBUTION

L. Dresner

In an effort to understand the spatial variation of the thermal-neutron flux in heterogeneous reactors, Meetz[1,2] first employed a model of a reactor consisting of a finite, integral number of slab cells in the center of each of which was an infinitely thin plane fuel plate (which, however, had a finite absorption rate). The thermal neutrons were described in Meetz' model by one-group diffusion theory, with the slowing-down source given by Fermi age theory. One remarkable result of Meetz' detailed calculations was that at the positions of the fuel plates the spatial variation of the flux was the same as in a homogeneous reactor lying inside the same boundary. Later Meetz[3] generalized his study to a two-dimensional reactor with line sources, and again found the same result. Häfele[4] studied the flux spectrum as a function of space and neutron lethargy in Meetz' one-dimensional reactor model by using diffusion theory but not specifying the energy-exchange kernel, and again found that at the delta-function fuel plates the spatial variation of the flux was the same as in the homogeneous reactor lying inside the same boundary. Moreover, he found that at these points the space and lethargy dependences of the flux separated, and consequently the spectra at the fuel plates were all the same.

The results of Meetz and Häfele, as will be shown subsequently, are due exclusively to the very high degree of geometrical symmetry of the reactor configurations that they studied. Even in this respect, their assumptions are more restrictive than necessary; for example, in the one-dimensional slab model a sufficient geometrical requirement is that the reactor be composed of an integral number of identical slab cells, each of which is symmetric with respect to reflection in its midplane. The fuel need not necessarily be located in a central plate, nor for that matter, need the fuel and moderator even be in separate regions. The most general geometric configuration we have found which is sufficient to obtain results similar to those of Meetz and Häfele, and which we shall use throughout the remainder of this paper, is the following: The reactor is a rectangular parallelepiped constructed by stacking an integral number of identical, similarly oriented, rectangular parallelepipedal cells, each of which is symmetric with respect to reflection in its midplanes.

With regard to the properties of the reactor equation, the assumptions of Meetz and Häfele are likewise too restrictive; for example, the use of diffusion theory is unnecessary. Sufficient conditions for the considerations to follow may be summarized by saying that they must permit the use of the method

---

[1] K. Meetz, *Z. Naturforsch.* 12a(9) (1957).

[2] *Ibid.*, 12a(11) (1957).

[3] K. Meetz, *Proc. U.N. Intern. Conf. Peaceful Uses Atomic Energy, 2nd, Geneva, 1958*, P/968.

[4] W. Häfele, *Nukleonik* 1(6) (1959); a resume of this paper is given in *Trans. Am. Nuclear Soc.* 2(1) (1959).

of images.[5] In particular, the boundary condition we shall require for the flux is that it vanish at all energies on the reactor boundary.[6] Furthermore the reactor equation must be linear, but this hardly constitutes a significant restriction.

Under the afore-mentioned conditions it is then possible to prove the following theorem: There are eight separate networks of points each of which has the property that at each of the points (1) the space and energy dependences of the flux separate, (2) the space dependence is the same as in a homogeneous reactor lying inside the same boundary, (3) the spectrum is the same [an obvious corollary of (1)]. The eight networks are, respectively, the three sets of midpoints of the edges, the three sets of midpoints of the faces, the corners, and the midpoints of the cells.

Fourier Series Representations

Let us now consider a reactor medium consisting of a repeating pattern of identical, similarly oriented cells. Let each cell be a rectangular parallelepiped with edges given by the three orthogonal vectors $\mathbf{a}_i$. Let the cells be symmetric with respect to reflection in their midplanes. In this medium let us choose the origin at the corner of one reactor cell. Any physical property of the reactor medium, $f(\mathbf{r})$, for example, the fission cross section, is a periodic function of space which is left invariant by translation by any linear combination of the $\mathbf{a}_i$ with integral coefficients. Thus if we set

$$\mathbf{r} = \sum_{i=1}^{3} \mathbf{a}_i x_i \quad ,$$

we have

$$f(\mathbf{r}) = f(x_1, x_2, x_3) = \sum_{\beta_1=0}^{\infty} \sum_{\beta_2=0}^{\infty} \sum_{\beta_3=0}^{\infty} f(\beta_1, \beta_2, \beta_3) \prod_{i=1}^{3} \cos\,(2\pi\beta_i x_i) \quad . \tag{1}$$

Here the use of the cosines in the Fourier series guarantees the symmetry of $f(\mathbf{r})$ with respect to reflection of the cell in its midplanes.

Let the reactor we are considering be so located that its faces are given by $x_i = 0$ or N_i, where N_i is an integer. Let us suppose that we know a solution, $\phi(\mathbf{r})$, for the flux in the reactor interior. From $\phi(\mathbf{r})$ we can generate an infinite-medium solution which vanishes on the reactor boundary and is identical with $\phi(\mathbf{r})$ in the reactor interior by successive reflection with change of sign in the planes $x_i = \pm m_i N_i$, where $m_i = 0, 1, 2, 3, \ldots$. That this function will actually be a solution of the infinite-medium reactor equation depends on the fact that the latter equation is left invariant by these successive reflections. This last fact is a consequence of the reflection and translation symmetries of the infinite medium. Implicit in this whole procedure is the assumption that the reactor equation can be put in the form of a

---

[5] A. M. Weinberg and E. P. Wigner, *The Physical Theory of Neutron Chain Reactors*, p 349 ff., University of Chicago Press, Chicago, 1958.

[6] The author wishes to thank W. Häfele for bringing to his attention the work of Meetz, as well as his own work, and for many interesting and helpful discussions concerning the present paper. Thanks are also due to E. P. Wigner for his most valuable suggestions, and to E. Inönü for an illuminating conversation.

local equation, involving the flux and its space derivatives at only one point. This is to ensure that the finite- and infinite-medium reactor equations do not differ at all but only the boundary conditions.

The solutions generated by the above reflection method are all periodic with period $2N_i$ in the ith direction and are all odd around the planes $x_i = 0$. Thus they all have the form

$$\phi(\mathbf{r}) = \phi(x_1, x_2, x_3) = \sum_{\beta_1=0}^{\infty} \sum_{\beta_2=0}^{\infty} \sum_{\beta_3=0}^{\infty} \phi(\beta_1, \beta_2, \beta_3) \prod_{i=1}^{3} \left(\frac{2\pi\beta_i x_i}{2N_i} \right) \quad . \tag{2}$$

Furthermore, the converse is true; that is, any infinite-medium solution of the form (2) must necessarily be a solution of the finite reactor problem, since it vanishes on the actual reactor boundary.

Frequency Selection

If we interpret $f(\mathbf{r})$ as the total cross section, say, and multiply the Fourier series (1) and (2), we obtain terms in the Fourier series for the collision density of the type

$$\prod_{i=1}^{3} \sin \left(\frac{\pi\beta_i x_i}{N_i} \right) \cos (2\pi\beta_i' x_i) = \frac{1}{2} \prod_{i=1}^{3} \left\{ \sin \left[2\pi x_i \left(\beta_i' + \frac{\beta_i}{2N_i} \right) \right] + \sin \left[2\pi x_i \left(-\beta_i' + \frac{\beta_i}{2N_i} \right) \right] \right\} \quad . \tag{3}$$

Now the argument leading to (2) for the flux holds as well for the collision density; thus the frequencies appearing on the right-hand side of (3) must be among those appearing on the right-hand side of (2). Hence the condition

$$\left| \frac{\beta_i}{2N_i} \pm \beta_i' \right| = \frac{\beta_i''}{2N_i} \tag{4}$$

must hold, where β_i' is any nonnegative integer, and β_i and β_i'' are the same *set* of nonnegative integers except for a rearrangement of order. The absolute value signs are used in (4) because only positive frequencies appear in (2); if in (3) the last frequency is negative, its sign is changed and so is the sign of the coefficient of the term in which it appears. Equation (4) has $N_i + 1$ solutions given by

$$\beta_i = \left| 2N_i w_i + s_i \right| \quad , \tag{5a}$$

where

$$w_i = 0, \pm 1, \pm 2, \pm 3, \ldots \quad , \tag{5b}$$

and

$$s_i = 0, 1, 2, \ldots, N_i \quad . \tag{5c}$$

With the frequency selection (5), (2) can be rewritten as

$$\phi_{s_1, s_2, s_3}(x_1, x_2, x_3) = \sum_{w_1=-\infty}^{+\infty} \sum_{w_2=-\infty}^{+\infty} \sum_{w_3=-\infty}^{+\infty} \phi_{s_1, s_2, s_3}(w_1, w_2, w_3) \prod_{i=1}^{3} \sin \left[2\pi \left(w_i + \frac{s_i}{2N_i} \right) x_i \right] \quad , \tag{6}$$

where the expansion coefficients in (6) are related in a simple manner to those in (2).

Properties of Eigenfunctions. – An immediate but not surprising consequence of the frequency selection (5) is that the eigenfunctions (6) have a definite symmetry character with respect to reflection in the midplanes of the reactor. Even s_i corresponds to antisymmetry; odd s_i to symmetry.

The persisting- or ground-mode in a heterogeneous reactor must be given by $s_1 = s_2 = s_3 = 1$. To prove this we consider values of the eigenfunctions at the points $x_i = m_i + \epsilon_i \leq N_i$, $m_i = 0, 1, 2, \ldots, N_i$, and $\epsilon_i = 0$ or $\frac{1}{2}$. We need only consider odd values of s_i, since the ground-mode must be symmetric with respect to reflection in the midplanes of the reactor. At the points considered we have

$$\phi_{s_1,s_2,s_3}(m_1 + \epsilon_1, m_2 + \epsilon_2, m_3 + \epsilon_3)$$

$$= \prod_{i=1}^{3} \sin\left[\frac{\pi s_i}{N_i}(m_i + \epsilon_i)\right] \sum_{w_1=-\infty}^{+\infty} \sum_{w_2=-\infty}^{+\infty} \sum_{w_3=-\infty}^{+\infty} (-)^{\sum_{i=1}^{3} 2\epsilon_i w_i} \phi_{s_1,s_2,s_3}(w_1,w_2,w_3) \ . \qquad (7)$$

Only when all the s_i's are equal to 1 do the arguments of the sines never exceed π.

For a particular choice of the ϵ_i, the space dependence given by the sum of products in (6) reduces to a single product of three sines, multiplied by a sum over the w_i. The product of sines gives the space variation over the network $x_i = m_i + \epsilon_i$, $m_i = 0, 1, \ldots, N_i$, while the remaining factor gives the spectrum there [$\phi(w_1,w_2,w_3)$ is energy dependent in general]. Thus for each network of given ϵ_i, the separation of the space and energy dependences familiar in the homogeneous case reappears. Moreover, the space dependence at the points of each network is the same as in a homogeneous reactor lying inside the same boundary.[6]

6.6. THERMALIZATION OF PULSED NEUTRONS IN A NONMULTIPLYING MODERATING MEDIUM

S. N. Purohit

The time behavior of the thermal-neutron energy spectrum of neutrons from a monoenergetic pulsed source in beryllium assemblies with various geometric bucklings has been calculated using the heavy gas model. The neutron distribution, in the diffusion theory approximation, for the fundamental spatial mode due to a pulsed neutron source is given as:

$$\frac{1}{v}\frac{\partial\phi(E,t)}{\partial t} = -(\Sigma_a + \Sigma_s + DB^2)\,\phi(E,t) + \int_0^{E_T} \Sigma_s(E')\,\phi(E',t)\,F(E'\to E)\,dE' + S(E,t) \ . \qquad (1)$$

In this study a convenient source function $S(E,t)$ was arbitrarily chosen; the results given below are independent of $S(E,t)$, since the asymptotic behavior is being studied.

A multigroup formalism, over the thermal-neutron energy range from 0 to 10 kT, was used to generate the neutron distribution $\phi(E,t)$ by the use of an analog computer. The expression $\phi(E,t)$ was fitted by a sum of exponentials in the following manner:

$$\phi(E,t) = \phi_0(E)\,e^{-\lambda_0 t} + \phi_1(E)\,e^{-\lambda_1 t} \ , \qquad (2)$$

for $\lambda_1 > \lambda_0$. The resulting values of λ_0, assuming zero absorption, are shown in Table 6.6.1 for several bucklings. The value of λ_1 for zero

buckling is also given. For other bucklings λ_1 will be of the same order.

The total time required for the neutrons to reach thermal equilibrium in an infinite medium of beryllium, again assuming zero absorption, was estimated as ~100 μsec (plus 14 μsec slowing-down time for epithermal neutrons). Values of λ_0, λ_1, and λ_2 were obtained analytically for the case of an infinite medium of beryllium having zero absorption by using associated Laguerre polynomials in the expansion of the neutron energy distribution. The expansion was:

$$\phi(E,t) = \sum_i e^{-\lambda_i t} \phi_i(E) \qquad (3)$$

Table 6.6.1. Values of λ for Various Bucklings (Analog Computer Results)

B^2 (cm^{-2})	λ_0 (kc/sec)	λ_1 (kc/sec)
$\times 10^{-2}$		
0	0	47.5
2.94	3.641	
5.36	6.859	
7.18	8.390	

in which

$$\phi_i(E) = \sum_{n=\theta}^{\infty} a_n^i E e^{-E} L_n^{(1)}(E) \ , \qquad (4)$$

where $L_n^{(1)}(E)$ is the associated Laguerre polynomial of order one. The results obtained by using the first three polynomials in (4) are shown in Table 6.6.2.

The value of the thermalization time constant, λ_1^{-1}, obtained for beryllium by the use of the analog computer is 21.05 ± 1.0 μsec; the value calculated analytically by using the Laguerre polynomials is λ_1^{-1} = 18.63 μsec.

Table 6.6.2. Values of λ for an Infinite Medium of Beryllium (Analytical Calculation)

λ_i	λ_i ($\xi\Sigma_{s0}$)	λ_i (Be) (sec^{-1})
		$\times 10^3$
λ_0	0	0
λ_1	1.33 $\xi\Sigma_{s0}v_0$	53.6
λ_2	4.09 $\xi\Sigma_{s0}v_0$	165

6.7. MONTE CARLO NEUTRON ESCAPE PROBABILITY CODES

R. R. Coveyou W. E. Kinney J. G. Sullivan

In the course of an experiment to measure η of U^{233}, reported elsewhere in this report (Sec 4.3), it became necessary to know the escape probability of neutrons born in a thin disk. A Monte Carlo code, designated as Lump I, has been written to compute the escape probability.

Figure 6.7.1 shows the configuration adopted for the calculation. Thermal neutrons from an isotropic disk source of radius R_S pass through a collimator of radius R_C, located a distance c from the source, and strike a target disk of radius R_T at a distance d from the source. It is assumed that the radial distribution of thermal neutrons is maintained throughout the target disk but that the neutrons are attenuated in the axial direction as e^{-z/λ_t}, where λ_t is the mean free path for thermal neutrons.

In choosing the radial source distribution, x and y coordinates are chosen for the source disk, and x' and y' coordinates are chosen for the target disk. A test is then made to see if the line joining these coordinates could have passed through the collimator. The condition that the coordinates be accepted is

$$l(\bar{x}^2 + \bar{y}^2) - m(\bar{x}\bar{x}') + n(\bar{x}'^2 + \bar{y}'^2) \leq 1 \ ,$$

where

$$\bar{x} = x/R_S \ ,$$

$$\bar{y} = y/R_S \ ,$$

$$\bar{x}' = x'/R_D \ ,$$

$$\bar{y}' = y'/R_D \ ,$$

$$l = \frac{R_S^2}{R_C^2}\left(1 - \frac{c}{d}\right)^2 ,$$

$$m = -2\frac{c}{d}\left(1 - \frac{c}{d}\right)\frac{R_S R_D}{R_C^2} ,$$

$$n = \left(\frac{c}{d}\frac{R_D}{R_C}\right)^2 .$$

The axial distribution of fast-neutron sources within the target disk is chosen from e^{-z/λ_t}. After the source point for the fast neutron is selected, the direction of flight is chosen isotropically. The shorter distance to the boundary of the disk, δ, is then computed, and the escape probability is calculated from $e^{-\delta/\lambda_F}$, where λ_F is the mean free path for fast neutrons.

A sufficient number of histories are run so that the standard deviation of the escape probability lies below a specified convergence criterion. The time required to run a case is from 5 to 20 min on the Oracle and about one-fifth that time on the IBM-704.

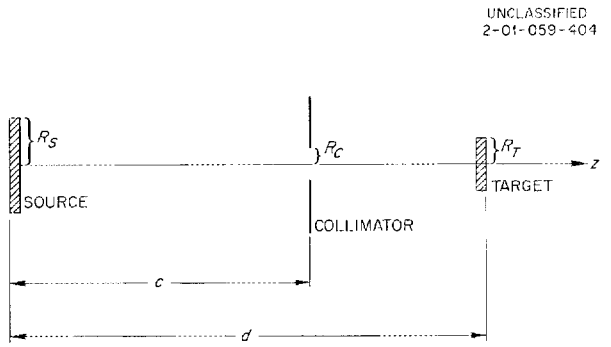

Fig. 6.7.1. Assumed Experimental Arrangement for Selecting the Radial Source Distribution in the Escape Probability Code.

Another code, identified as Lump II, has been written to compute the escape probability of uniformly distributed neutrons from a parallelepiped, a cylinder, a sphere, or an ellipsoid.

6.8. ADDITIONS TO CORN PONE – A MULTIGROUP, MULTIREGION REACTOR CODE

W. E. Kinney

Several additions have been made to Corn Pone, a P_1 multigroup, multiregion reactor code which has been described previously.[1] The number of neutrons absorbed, the number of fissions, and the number of neutrons produced in certain elements now may be computed and printed. A fixed or a variable transverse buckling may also be used. The thermal constants Σ_a and Σ_{tr}, as well as the number of space points in each region, may be inserted for each region as part of the input if desired.

A choice of initial source guess is also available. The choices are:

1. Flat source in fissionable regions,
2. Source of the form sin $(ax + \delta)$,
3. Source of the form sin $(ar + \delta)/r$,
4. Source of the form $e^{-(ax+\delta)}$,
5. Source from paper tape,
6. Source from the previous case.

The converged source may be punched on paper tape for use in a later case as an initial source guess. Vacuum regions may be treated at the origin and between each material region.

A report on Corn Pone has been prepared.[2]

[1] W. E. Kinney, R. R. Coveyou, and J. G. Sullivan, *Neutron Phys. Ann. Prog. Rep. Sept. 1, 1958*, ORNL-2609, p 84.

[2] R. R. Coveyou, W. E. Kinney, and J. G. Sullivan, *Corn Pone: A Multigroup, Multiregion Reactor Code*, ORNL-2789 (to be published).

6.9. NEUTRON REACTION RATE CODES

R. R. Coveyou W. E. Kinney

The O5R Code, a Monte Carlo reactor code described previously,[1] accounts for the motion of the nuclei comprising the medium in its treatment of the thermal region. Generally, the temperature of the medium will be greater than room temperature, at which most cross-section data are taken; but the cross sections, or equivalently, the reaction rates, may be computed for the higher temperatures from the room-temperature data. Codes have been written for the IBM-704 to perform the computation. The theory of the codes and the codes themselves are briefly described below.

Code Theory

The reaction rate for a neutron in a single-species medium is given by

$$R(V,T) = \left(\frac{M}{2\pi kT}\right)^{3/2} \int_{\mathbf{W}} \exp\left\{-\frac{MW^2}{2kT}\right\} R(|\mathbf{V}-\mathbf{W}|,0)\, d\mathbf{W} \ , \tag{1}$$

where

$R(V,T)$ = reaction rate for a neutron of velocity $\mathbf{V}$ in a medium at temperature T
$= V\sigma(V,T)$,
σ = cross section,
M = mass of the scattering nucleus,
W = velocity of the scattering nucleus,
k = Boltzmann's constant.

Now let

$$\tau = \frac{kT}{2M} \ . \tag{2}$$

Equation (1) then becomes

$$R(V,\tau) = \left(\frac{1}{4\pi\tau}\right)^{3/2} \int_{\mathbf{W}} \exp\left\{-\frac{W^2}{4\tau}\right\} R(|\mathbf{V}-\mathbf{W}|,0)\, d\mathbf{W} \ , \tag{3}$$

which is the solution of the age equation

$$\frac{\partial R(V,\tau)}{\partial \tau} = \nabla^2 R(V,\tau) = \frac{\partial^2 R(V,\tau)}{\partial V^2} + \frac{2}{V}\frac{\partial R(V,\tau)}{\partial V} \ . \tag{4}$$

Letting $S(V,\tau) = VR(V,\tau)$,

$$\frac{\partial S(V,\tau)}{\partial \tau} = \frac{\partial^2 S(V,\tau)}{\partial V^2} \ . \tag{5}$$

---

[1] R. R. Coveyou, J. G. Sullivan, and H. P. Carter, *Neutron Phys. Ann. Prog. Rep. Sept. 1, 1958*, ORNL-2609, p 87.

The boundary conditions are

$$S(0,\tau) = 0 \ , \qquad S(V_{max},\tau) = S(V_{max}) \ , \tag{6}$$

where V_{max} is some designated upper speed where the motion of the nuclei comprising the medium does not affect the reaction rate.

The difference equation approximating (5) to the fourth order in the velocity spacing, h, is

$$S\left(V,\tau + \frac{h^2}{6}\right) = \frac{1}{6}\left[S(V+h,\tau) + 4S(V,\tau) + S(V-h,\tau)\right] \ . \tag{7}$$

Thermal Prep I Code

Thermal Prep I uses the data from the master cross-section tape[2] to compute S for selected isotopes at equally spaced speed intervals between 0 and a specified V_{max}. Below a specified V_0, scattering cross sections are constant while fission and absorption cross sections are $1/v$. The results are put on a Thermal Prep data tape for use in later programs. The input consists of the isotope identification number, the number of cross sections to be treated (only total, scattering, and fission cross sections may be treated), V_0, V_{max}, and h, the speed interval.

Thermal Prep II Code

Thermal Prep II uses the Thermal Prep data tape to compute S for higher temperature from Eq. (7). The input specifies T_0, the reference temperature, and T, the new temperature. Both T_0 and T are in °K and $T > T_0$. All values of S at T_0 are raised to T and the results are added to the Thermal Prep data tape. Any temperature on the tape may be used as a reference temperature.

Reaction Rate Program

The Reaction Rate Program uses the Thermal Prep data tape to produce reaction rates at equally spaced energy points between specified lower and upper energies. The results are put on a reaction rate tape. The input specifies the isotope and cross section, the temperature (which must be on the Thermal Prep data tape), the lower energy, the upper energy, and the number of energy points <1200.

---

[2] J. G. Sullivan, *Neutron Phys. Ann. Prog. Rep. Sept. 1, 1958*, ORNL-2609, p 87.

6.10. RESONANCE ABSORPTION OF NEUTRONS IN A LUMP

K. Hasegawa[1]

Resonance absorption of neutrons in a lump has been calculated by two approximate methods: the narrow-resonance approximation and the wide-resonance approximation. Since actual resonance lines have finite widths, the slowing down of neutrons scattered by absorbing nuclei must be correctly considered to improve these approximations. In this paper a new resonance integral formula is proposed which tends to be equal to the result of the narrow (or of the wide) resonance approximation in the narrow (or the wide) resonance limit.

Resonance absorption of neutrons in a lump immersed in a strongly moderating infinite medium is considered. It is assumed that a resonance neutron is slowed down below the resonance region by one elastic collision with a moderating nucleus. The neutron flux inside the lump, $\phi(r,u)$, satisfies the equation

$$\phi(\mathbf{r},u) = P(\mathbf{r},u) + \int_0^u du' \, K_m(u-u') \, \Sigma_s(u') \int_V d\mathbf{r} \, \frac{\exp\left[-\Sigma_t(u)|\mathbf{r}-\mathbf{r}'|\right]}{4\pi|\mathbf{r}-\mathbf{r}'|^2} \, \phi(\mathbf{r},u') \ , \tag{1}$$

where the neutron flux outside the lump is normalized as unity. When it is assumed that the neutron flux is spatially flat inside the lump, Eq. (1) becomes, after spatial integrations,

$$\phi(u) = P(u) + \frac{[1-P(u)]}{\Sigma_t(u)} \int_0^u du' \, K_m(u-u') \, \Sigma_s(u') \phi(u') \ , \tag{2}$$

where $P(u)$ is the escape probability from the lump.

Equation (2) can be rewritten in another form:

$$X(u) = \frac{\Sigma_t(u)}{[1-P(u)]} \, P(u) + \int_0^u du' \, \psi_m(u-u') \, \frac{\Sigma_t(u)}{[1-P(u')]} \, P(u') - \int_0^u \psi_m(u-u') Q(u') X(u') \ , \tag{3}$$

where $\psi_m(u)$ is the Placzek function, and

$$X(u) = \frac{\Sigma_t(u)}{[1-P(u)]} \, \phi(u) \ , \tag{4}$$

$$Q(u) = P(u) + [1-P(u)] \, \frac{\Sigma_a(u)}{\Sigma_t(u)} \ . \tag{5}$$

Equation (3) is an extension of the equation derived by Weinberg and Wigner[2] and by Corngold[3] for a homogeneous system.

---

[1]Formerly on leave from Hitachi, Central Research Laboratory, Kokubunji, Tokyo, Japan; now deceased.

[2]A. M. Weinberg and E. P. Wigner, *Proceedings of the Brookhaven Conference on Resonance Absorption of Neutrons in Nuclear Reactions*, BNL-433 (C24) (1956); see also *Physical Theory of Neutron Chain Reactors*, University of Chicago Press, Chicago, Illinois (1958).

[3]N. Corngold, *Proc. Phys. Soc. (London)* **A70**, 793 (1957).

In the first approximation the Placzek function, $\psi_m(u)$, is replaced in Eq. (3) by its asymptotic form, $1/\xi$. Then the equation can be solved and the resonance integral, RI, becomes

$$RI = \frac{1}{N}\left\{\int_{u_1}^{u_2} du\, \Sigma_a(u)P(u) + \Sigma_{ps}\int_{u_1}^{u_2} du\, \frac{\Sigma_a(u)}{\Sigma_t(u)}\,[1 - P(u)]\right\} -$$

$$- \frac{1}{N}\frac{1}{\xi}\int_{u_1}^{u_2} du\, \frac{\Sigma_a(u)}{\Sigma_t(u)}\,[1 - P(u)]\int_{u_1}^{u_2} du'\,[\Sigma_{ps}\, Q(u') - \Sigma_s(u')P(u')] \times$$

$$\times \exp\left[-\frac{1}{\xi}\int_{u'}^{u} du''\, Q(u'')\right] . \quad (6)$$

The first term is the resonance integral of the narrow-resonance approximation, and the second term is the correction term (Σ_{ps} is the potential scattering cross section). It is interesting to note that the correction term vanishes in the narrow-resonance limit. Moreover, it can be shown that the formula given by Eq. (6) tends to be equal to that of the wide-resonance approximation in the wide-resonance limit.

When the rational approximation for $P(u)$ is used, the formula can be written in either of two forms:

$$RI = RI\,(\mathrm{NR}) - \sigma_{ps}\frac{\Gamma_\gamma}{\Gamma}\left(1 - b\frac{\Gamma_n}{\Gamma}\right)\cdot F \quad (7)$$

$$= RI\,(\mathrm{WR}) + \sigma_{ps}\frac{\Gamma_\gamma}{\Gamma}\left(1 - b\frac{\Gamma_n}{\Gamma}\right)\cdot G\ , \quad (8)$$

where F and G are positive quantities and vanish in the narrow- and the wide-resonance limits, respectively. Here $b = 1 + 1/(\Sigma_{ps}\,\bar{l})$, where $\bar{l}$ is the mean chord length of the lump. It is very interesting to note that RI (NR) [RI (WR)] overestimates when $b(\Gamma_n/\Gamma) < [>]1$. When

$$1 - b\frac{\Gamma_n}{\Gamma} = 0\ , \quad (9)$$

RI (NR) and RI (WR) become equal, and our correction term vanishes irrespective of the resonance width. Equation (9) is the extension of the equation given by Spinney[4] for the homogeneous mixtures of hydrogen and uranium. This work has been described in detail in another report.[5]

---

[4]K. T. Spinney, *Proceedings of the Brookhaven Conference on Resonance Absorption of Neutrons in Nuclear Reactions*, BNL-433 (C24) (1956); see also *J. Nuclear Energy* 6, 53 (1957).

[5]K. Hasegawa, *Theory of Resonance Absorption of Neutrons in a Lump*, ORNL-2705 (1959).

6.11. CALCULATION OF THE PROMPT NEUTRON GENERATION TIME FOR THE BSR-II

R. Perez-Belles[1]

An experimental method for determining the ratio of the prompt-neutron generation time of a reactor to its effective delayed-neutron fraction consists in pulsing neutrons into the reactor, which contains a known amount of negative reactivity, and observing the decay of the neutron density following the burst. The amount of negative reactivity in the reactor can be determined fairly well, in the range from zero to one dollar, by comparison with the worth of control rods calibrated by the customary inhour method. In connection with such an experiment (reported in Sec 2.2), a theoretical interpretation has been considered in terms of defining reactivity and neutron generation time for a reflected reactor.

The most simple yet reasonably correct theory which can be used to describe the experiment is the two-group treatment. After the neutron burst has entered the subcritical reactor under investigation, the mathematical description of the flux behavior is essentially an eigenvalue problem. In the case of a reflected reactor every spatial mode splits into $J + 1$ time modes, each associated with a different delayed neutron group.[2] The equations defining the modes are:

$$(D_{1c}\Delta - \Sigma_{1c})\phi_{1cn\alpha} + (1-\beta)\nu\Sigma_f\phi_{2cn\alpha} + \Sigma_j \tau_j^{-1} C_{jn\alpha} = \frac{\lambda_{n\alpha}}{V_1}\phi_{1cn\alpha}\,, \tag{1}$$

$$(D_{2c}\Delta - \Sigma_{2c})\phi_{2cn\alpha} + \Sigma_{1c}\phi_{1cn\alpha} = \frac{\lambda_{n\alpha}}{V_2}\phi_{2cn\alpha}\,, \tag{2}$$

$$\beta_j^1 \cdot \nu\Sigma_f\phi_{2cn\alpha} - \tau_j^{-1} C_{jn\alpha} = \lambda_{n\alpha} C_{jn\alpha}\,, \tag{3}$$

$$(D_{1r}\Delta - \Sigma_{1r})\phi_{1rn\alpha} = \frac{\lambda_{n\alpha}}{V_1}\phi_{1rn\alpha}\,, \tag{4}$$

$$(D_{2r}\Delta - \Sigma_{2r})\phi_{2rn\alpha} + \Sigma_{1r}\phi_{1rn\alpha} = \frac{\lambda_{n\alpha}}{V_2}\phi_{2rn\alpha}\,, \tag{5}$$

where the subindex 1 refers to the fast-neutron flux, 2 to the thermal-neutron flux, c to the core, and r to the reflector. The other symbols are defined as follows:

D = diffusion coefficient, cm,

V = neutron velocity, cm · sec^{-1},

l^* = neutron generation time, sec,

$\lambda_{n\alpha}$ = eigenvalue (nth, α mode),

Σ_f = macroscopic fission cross section, cm^{-1},

$\Sigma_{1c}, \Sigma_{2c}, \Sigma_{1r}, \Sigma_{2r}$ = macroscopic absorption cross sections,

---

[1]On assignment from Instituto Nacional de Industria, Madrid, Spain.

[2]M. Benedict, Massachusetts Institute of Technology, 1958.

ν = neutron multiplicity,

τ_j = period of the jth group of delayed neutrons,

$\phi_{n\alpha}$ = flux (nth, α mode),

$\phi^*_{n\alpha}$ = adjoint flux (nth, α mode),

$\rho_{n\alpha}$ = reactivity (nth, α mode),

β_{eff} = effective total fraction of delayed neutrons ($\beta_{\text{eff}} = \gamma\beta$),

γ = ratio of nonleakage probabilities for delayed and prompt neutrons.

When each of Eqs. (1) through (5) is multiplied by its respective adjoint flux, an integration is performed over the entire system, and the boundary conditions are applied, the result is:

$$\rho_{n\alpha} = \lambda_{n\alpha}\left[l^*_{n\alpha} + \Sigma_j \frac{\beta_j \tau_j}{1 + \tau_j \lambda_{n\alpha}}\right], \tag{6}$$

where

$$\rho = \frac{\text{rate of production} - \text{rate of losses by leakage and absorption}}{\text{rate of production}}$$

and

$$l^* = \frac{\text{total prompt-neutron population}}{\text{rate of production}}$$

$$= \frac{\displaystyle\int_{\text{core}} dr \left[\frac{\phi^*_{2c}\phi_{2c}}{V_2} + \frac{\phi^*_{1c}\phi_{1c}}{V_1}\right] + \int_{\text{reflector}} dr \left[\frac{\phi^*_{2r}\phi_{2r}}{V_2} + \frac{\phi^*_{1r}\phi_{1r}}{V_1}\right]}{\displaystyle\int_{\text{core}} dr\, \phi^*_{1c}\nu\Sigma_f\phi_{2c}} . \tag{7}$$

Here the subscripts n and α have been dropped for clarity.

Equation (6) is the inhour equation generalized to a reflected system and gives the reactivity in each mode as a function of the neutron generation time and the eigenvalue of the corresponding mode. In a pulsed experiment the fastest decay of the fundamental mode is selected (that is, $\lambda\tau_j >> 1$, where τ_j^{-1} is the largest decay constant of the delayed neutrons).

Equation (6) then reduces to

$$\lambda = \frac{\rho - \beta}{l^*} , \tag{8}$$

where again the subscripts have been dropped. When negative reactivities are inserted the result, from (8), is:

$$\lambda = \frac{\beta}{l^*}\left[1 + \rho^*\right] , \tag{9}$$

where ρ^* ($= \rho/\beta$) is expressed in dollars (ref 3).

[3] B. E. Simmons, *Nuclear Sci. and Eng.* **5**, 254 (1959).

Equation (9) may become the basis of a suitable method for measuring large negative reactivities, provided that the definition of l^* is independent of the amount of reactivity absorption inserted into the reactor. However, second-order variations in l^* produced by flux depression and the effect of non-$1/v$ absorbers on the neutron spectrum may arise for large reactivities.

In order to compute the generation time from (7) a theoretical fully reflected spherical reactor equivalent to the actual parallelepipedal reactor has been used in the computation of the two-group fluxes and their adjoints. A GNU code[4] computation of the flux-weighted two-group constants from a 32-group calculation has been used in a desk machine computation of the adjoint and real fluxes for the fundamental mode. The results are shown in Fig. 6.11.1. Numerical integration of (7) gives: $l^* = 21.3$ μsec. The experimental result (Sec 2.2) after introducing the known values of λ and ρ^* in (9) is $l^*/\beta_{eff} = 3.2 \pm 0.2$ msec. This figure, combined with a computed value of $\beta_{eff} = 0.00704 \pm 0.000035$, yields $l^* = 22.5 \pm 1.5$ μsec.

Two main sources of inaccuracies can be considered in the computation of l^*. The first one depends on the use of a two-group treatment which underestimates the peaking of the thermal-neutron flux in the

[4] C. L. Davis, J. M. Bookston, and B. E. Smith, *GNU II, Multigroup One-Dimension-Diffusion Program for the IBM-704*, GMR-101 (1957).

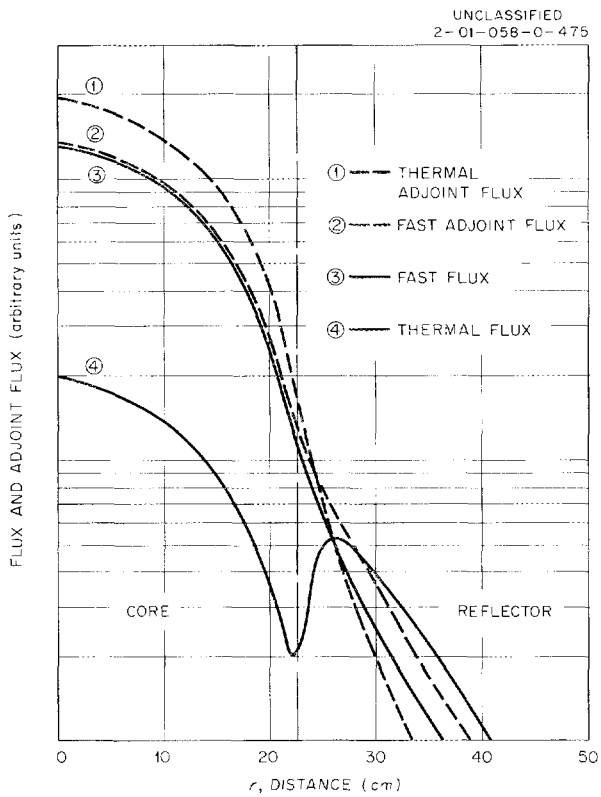

Fig. 6.11.1. Computed Real and Adjoint Flux Profiles for the BSR-II Spherical Model (Arbitrary Normalization).

reflector. The result is to lower the generation time. The second approximation arises from using the equivalent spherical reactor flux distribution as input in the generation-time calculation. However, the use of the adjoint fluxes as weighting functions and the process of integration tend to cancel details of fine structure in the flux distributions. It is therefore estimated that the theoretical result is good to within 10 to 15%.

The theoretical computation does not include the slowing-down time which was estimated to be negligible. The computation of l^* from (7) shows that the reflector contribution to the neutron lifetime accounts for about 20% of the total.

In order to theoretically interpret pulsed reactor experiments, computation of the adjoint fluxes is highly desirable. Calculations in this direction are being carried out by means of suitable changes in available numerical codes.

6.12. A CORN PONE CALCULATION OF THE ENERGY-DEPENDENT NEUTRON FLUX IN AN UNREFLECTED 69.2-cm-dia SPHERE

D. W. Magnuson R. Gwin W. E. Kinney

A series of calculations with the Corn Pone reactor code[1] has been initiated to compute the parameters of unreflected critical spheres. The results of these calculations should serve as a guide to the understanding of critical experiments, with particular emphasis on the use of the first fundamental theorem of reactor theory.[2]

A 69.2-cm-dia sphere was chosen for the calculational example because experimental data were available from a critical volume of this diameter and because there is enough neutron leakage from a critical aqueous U^{235} solution filling a sphere of this size for a variation in extrapolation length to be important.

The Corn Pone calculations yielded spatial distributions of steady-state source and neutron flux for each of several energy groups. In order for there to be any variation in the buckling, of course, the condition that the net inward current at the boundary of the sphere be zero must be applied. An examination of these data showed that the neutron spatial distribution did vary from one energy group to another. The fluxes and sources in the energy groups were then satisfactorily fitted to the equations

$$\phi(r) = A_\phi \frac{\sin B_\phi r}{r} ,$$

$$S(r) = A_S \frac{\sin B_S r}{r} .$$

The sources were calculated in the various groups because it was expected that the distribution of fast neutrons would be strongly affected by the spatial source of fission neutrons. Table 6.12.1 shows the results of this analysis. The variance in each derived B value is shown in the table as uncertainties in the extrapolated radius and the extrapolated length. The nonleakage probability would change about ½% for the variation of B^2 shown in the table.

Figure 6.12.1 shows the effective extrapolation length as a function of the energy group for the neutron source and flux. Table 6.12.2 lists the energy limits for the groups.

As the distance from the boundary increases, the stationary state fluxes in each group approach more closely the same spatial distribution. For example, omitting fluxes within 3.5 cm of the boundary reduces the difference in the B value for the fourth and thermal groups from 1.8% to 0.65%.

---

[1] R. R. Coveyou, W. E. Kinney, and J. G. Sullivan, *Corn Pone, A Multigroup, Multiregion Reactor Code*, ORNL-2789 (to be published); see also sec 6.8.

[2] A. M. Weinberg and E. P. Wigner, *The Physical Theory of Neutron Chain Reactors*, p 381, University of Chicago Press, Chicago, 1958.

Table 6.12.1. Calculated Values of Bucklings and Extrapolation Lengths for Various Energy Groups

Group	Neutron Distribution	B, Square Root of Buckling (cm^{-1})	$\bar{R}$ Extrapolated Radius (cm)	δ, Extrapolated Length (cm)
4	Source	0.085634	36.69 ± 0.03	2.08 ± 0.03
	Flux	0.084631	37.12 ± 0.03	2.52 ± 0.03
5	Source	0.085447	36.77 ± 0.02	2.17 ± 0.02
	Flux	0.084968	36.97 ± 0.02	2.37 ± 0.02
15	Source	0.085628	36.69 ± 0.02	2.09 ± 0.02
	Flux	0.085698	36.66 ± 0.03	2.06 ± 0.03
16	Source	0.085654	36.68 ± 0.02	2.08 ± 0.02
	Flux	0.085710	36.65 ± 0.03	2.05 ± 0.03
Thermal	Source	0.085733	36.64 ± 0.03	2.04 ± 0.03
	Flux	0.086152	36.47 ± 0.05	1.87 ± 0.05

Table 6.12.2. Energy-Group Limits

Group	Lower Energy (ev)	Group	Lower Energy (ev)	Group	Lower Energy (ev)
	1×10^8	11	3.372×10^1	22	1.523×10^{-1}
1	1×10^7	12	1.515×10^1	23	1.247×10^{-1}
2	6.065×10^6	13	1.016×10^1	24	1.021×10^{-1}
3	3.679×10^6	14	4.564×10^0	25	8.358×10^{-2}
4	2.231×10^6	15	1.375×10^0	26	6.843×10^{-2}
5	1.353×10^6	16	9.214×10^{-1}	27	5.603×10^{-2}
6	8.208×10^5	17	6.176×10^{-1}	28	4.587×10^{-2}
7	1.832×10^5	18	4.140×10^{-1}	29	3.756×10^{-2}
8	9.118×10^3	19	2.775×10^{-1}	30	3.075×10^{-2}
9	4.54×10^2	20	2.272×10^{-1}	31	2.518×10^{-2}
10	1.12×10^2	21	1.860×20^{-1}	32	Thermal

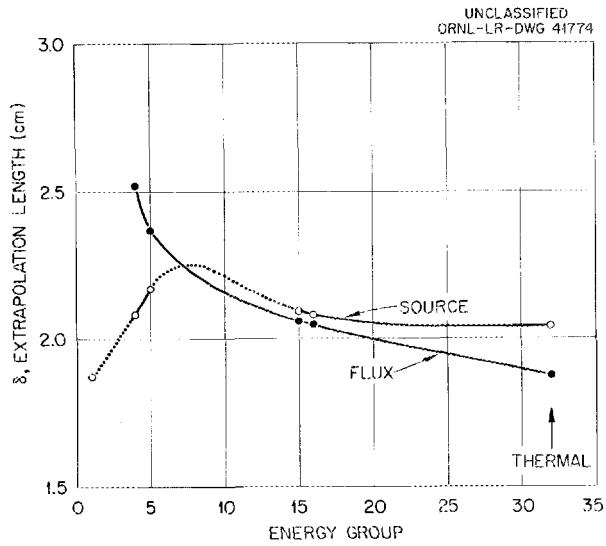

Fig. 6.12.1. Variation of the Extrapolated Length with the Energy Group in a 69.2-cm-dia Sphere Containing an Aqueous Solution of U^{235}: Computed Values.

6.13. REACTION CROSS SECTIONS USING THE STATISTICAL MODEL OF THE COMPOUND NUCLEUS

S. K. Penny

Hauser and Feshbach[1] used the statistical model to consider the total cross section for the inelastic scattering of neutrons. They further suggested that their formalism might be altered to include competition from other reactions and also to consider the possibility of charged particles as incident and emergent particles. These changes have now been written explicitly for the total reaction cross section for the case in which the statistical model applies to the compound nucleus only, and have been published elsewhere.[2]

[1] W. Hauser and H. Feshbach, *Phys. Rev.* 87, 366 (1952).

[2] S. K. Penny, *Reaction Cross Sections Using the Statistical Model of the Compound Nucleus*, ORNL CF-59-9-11 (1959).

6.14. EFFECTS OF CHEMICAL BINDING ON NEUTRON SCATTERING

F. S. Alsmiller

A knowledge of the neutron differential scattering cross section in both crystalline and fluid media is necessary for careful theoretical computations of thermal spectra, diffusion parameters,[1] etc., in these materials. Consequently, a study of the effects of chemical binding on low-energy neutron scattering is in progress.

Standard formulations, susceptible to computation, exist for simple Bravais lattices[2] (with Debye or other assumed frequency distributions) and ideal molecular gases, with symmetric molecules.[3] These models have recently been extended, to some degree, to include asymmetric molecules[4] and general lattices.[2] They were studied with the hope of applying them to calculations of the cross sections in ice, which may in turn help in understanding the cross sections of water.

However, H_2O and D_2O lattices are complicated by the fact that the hydrogen atoms do not appear to have well-defined equilibrium positions. Hence, the usual normal mode analysis does not treat the crystal dynamics correctly and is expected to be particularly invalid in computations of inelastic scattering. A suitable modification of the theory is being sought.

[1] Measurements of diffusion parameters in ice are planned by G. deSaussure and E. G. Silver as an extension to the work reported in sec 5.3.

[2] A. Sjolander, *Arkiv Fysik* 14, 315 (1958) (an extensive list of references is also supplied here).

[3] A. C. Zemach and R. J. Glauber, *Phys. Rev.* 101, 118 (1956).

[4] H. C. Volkin, *Phys. Rev.* 113, 866 (1959).

6.15. SLINKY: A MONTE CARLO CODE TO SOLVE MULTIGROUP, MULTIREGION DIFFUSION EQUATIONS

R. R. Coveyou D. J. Irving

An attempt has been made to develop an IBM-704 code to solve the equations of diffusion theory by the Monte Carlo method. The motivation for the research is to determine whether, for three-dimensional calculations, the Monte Carlo method possesses advantages over the straightforward (but very long) numerical integration of the equations. A tentative code, called SLINKY, is essentially complete and will be tested on various problems to establish its value.

Part 7

SHIELDING RESEARCH

7.1. PULSE-HEIGHT SPECTRA OF THERMAL-NEUTRON-CAPTURE GAMMA RAYS IN VARIOUS MATERIALS

F. J. Muckenthaler

Gamma rays resulting from neutron radiative capture, that is, those from the (n, γ) reaction, are often the most important source of gamma rays in a reactor shield, and an accurate knowledge of the spectra of capture gamma rays from various materials is required for the proper analysis of many shielding experiments. Accordingly, an experiment designed to measure the pulse-height spectra of gamma rays resulting from the capture of thermal neutrons in a variety of structural and shielding materials has been performed at the Tower Shielding Facility. Although a number of materials were studied, only the analyses for iron, aluminum, and lead have been completed, and the discussion below will be restricted to these three materials.

The experimental arrangement is shown in Fig. 7.1.1. The source and sample were placed near the center of a 4 × 4 × 3 ft tank containing oil. The samples, which were uniformly 8 in. square and ½ in. thick and had 2-in.-dia holes in their centers, were supported on a 6-in.-long lead cone which had a 2-in. maximum diameter at its upper end. A Po-Be neutron source was positioned at the lower end of the cone. The lead served to reduce the number of 4.43-Mev source gamma rays reaching the detector. The holes in the centers of the samples allowed them to fit around the lead so that the spectrum of gamma rays leaving the upper end of the lead was the same in each case.

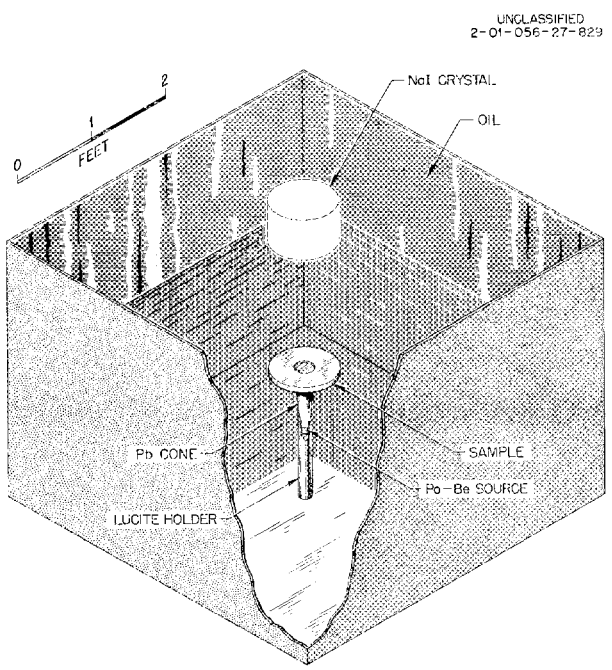

Fig. 7.1.1. Experimental Arrangement for Measurements of Spectra of Capture Gamma Rays from Various Materials.

Neutrons from the source were moderated to thermal energy by the oil bath and absorbed in the samples, resulting in the emission of capture gamma rays. The gamma rays were detected by a scintillation spectrometer employing a 3-in.-dia by 3-in. NaI(Tl) crystal, and pulses produced by the scintillation events within the crystal were fed into a 200-channel pulse-height analyzer.

An 18-in. thickness of oil was maintained between the irradiated sample and the crystal in order to eliminate neutron interactions in the crystal. The crystal was also surrounded by boron Plexiglas to minimize thermal-neutron activation.

The measurements with each sample consisted of two exposures, one with the bare sample and another with the sample covered with a $\frac{3}{16}$-in. thickness of boron Plexiglas. The boron reduced the number of thermal neutrons reaching the sample; therefore the difference between the pulse-height spectra for the two cases can be attributed to gamma rays from thermal-neutron captures in the sample. It is thus possible to eliminate essentially all the extraneous contribution to the gamma-ray spectrum, including that due to fast-neutron scattering in the sample. The difference spectra below 4.5 Mev are not too reliable, since they include a large contribution of 4.43-Mev gamma rays from the Po-Be source, as well as a contribution of carbon capture gamma rays from the oil bath, but a peak of strong intensity in this region of the capture gamma-ray spectrum of a sample in all probability would have been observed anyway. Background is included

in all the plotted data. The difference in background caused by the presence of the boron Plexiglas was found to be negligible.

The pulse-height spectrum for iron, shown in Fig. 7.1.2, displays prominent peaks at 9.24, 7.65, and 6.02 Mev. Preliminary analysis shows that the intensity of the gamma ray at 7.65 Mev is much stronger than that at either of the other two energies. Its presence is attributed mainly to Fe^{57}, since natural iron contains 91.6% of the isotope Fe^{56}, whose absorption cross section is also 92% of the total cross section for thermal neutrons. The measured value is also in good agreement with the 7.639-Mev value for the gamma ray from Fe^{57} obtained by Kinsey and Bartholomew.[1] The peak at 9.3 Mev represents the direct transition to the ground state of Fe^{55}. The peak at 6.02 Mev is really the combination of two gamma rays of energies of 6.015 and 5.944 Mev. Both of these gamma rays are believed by Kinsey and Bartholomew to come from the Fe^{57} isotope because of its relative abundance.

Figure 7.1.3, representing the pulse-height spectrum for 2S aluminum, shows only one prominent gamma-ray peak at 7.74 Mev. This is in good agreement with a previously observed value[2] of 7.73 Mev believed to represent a direct transition to the ground state of Al^{28}. A contribution in the lower energy region is possible through transitions from the many excited levels in Al^{28}. The nearness of these levels makes it very difficult to distinguish any particular gamma-ray energy, however.

Only one peak, at 7.39 Mev, has been observed for lead (Fig. 7.1.4). This agrees with the reported value of 7.40 Mev for Pb^{208}. No peak from Pb^{207} at 6.74 Mev is immediately evident in the data, since the ratio of the intensities of the gamma rays from Pb^{208} and Pb^{207} parallels the ratio of their thermal-neutron cross sections,[3] and the gamma ray from Pb^{207}, therefore, would be masked out by the 6.89-Mev first-escape peak from Pb^{208}.

An attempt is under way to determine the peak efficiency of the 3-in.-dia by 3-in. NaI(Tl) crystal for high-energy gamma rays by experimentally determining the number of neutron-capture gamma rays being emitted from the iron sample. To do this, it is necessary to know the total number of thermal neutrons being captured in the iron. Measurements of this thermal-neutron flux are being made with indium and gold foils, using the same source and sample geometry as in the capture gamma-ray measurements. The surface of the sample facing the source is mapped with a sheet of gold foil 5 mils thick, and small cadmium-covered gold foils are used to obtain a cadmium ratio. Measurements of the thermal-neutron flux on the upper surface of the sample were made with the indium foils, eight increments of sample being used so that the attenuation through the sample could be observed.

Figure 7.1.5 shows the uncorrected thermal-flux distribution through ½ in. of iron. A cadmium ratio through the iron varied from 7.7 on the surface nearest the source to 7.3 at the center and 7.1 at the other end of the sample. This difference would make only a slight change in the shape of the curve. No corrections have been applied for flux depression due to the presence of the foils.

[1] B. B. Kinsey and G. A. Bartholomew, *Phys. Rev.* 89, 375 (1953).

[2] B. B. Kinsey, G. A. Bartholomew, and W. H. Walker, *Phys. Rev.* 83, 519 (1951).

[3] B. P. Adyaserich, B. D. Grosher, A. N. Demidon, *Conference of the Academy of Science of the USSR on the Peaceful Uses of Atomic Energy*, vol 3, p 195 (1955).

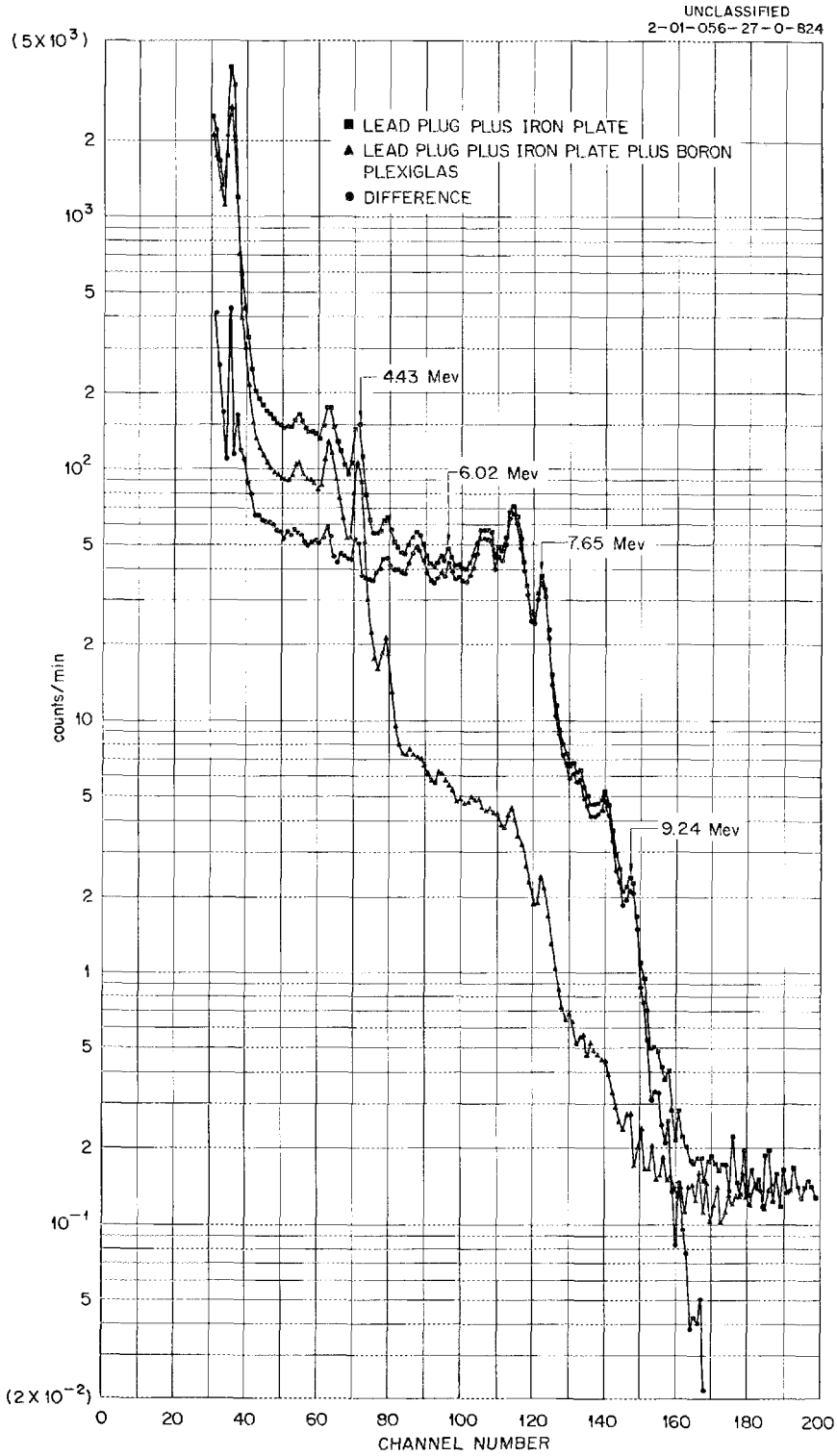

Fig. 7.1.2. Pulse-Height Spectra of Capture Gamma Rays from Iron.

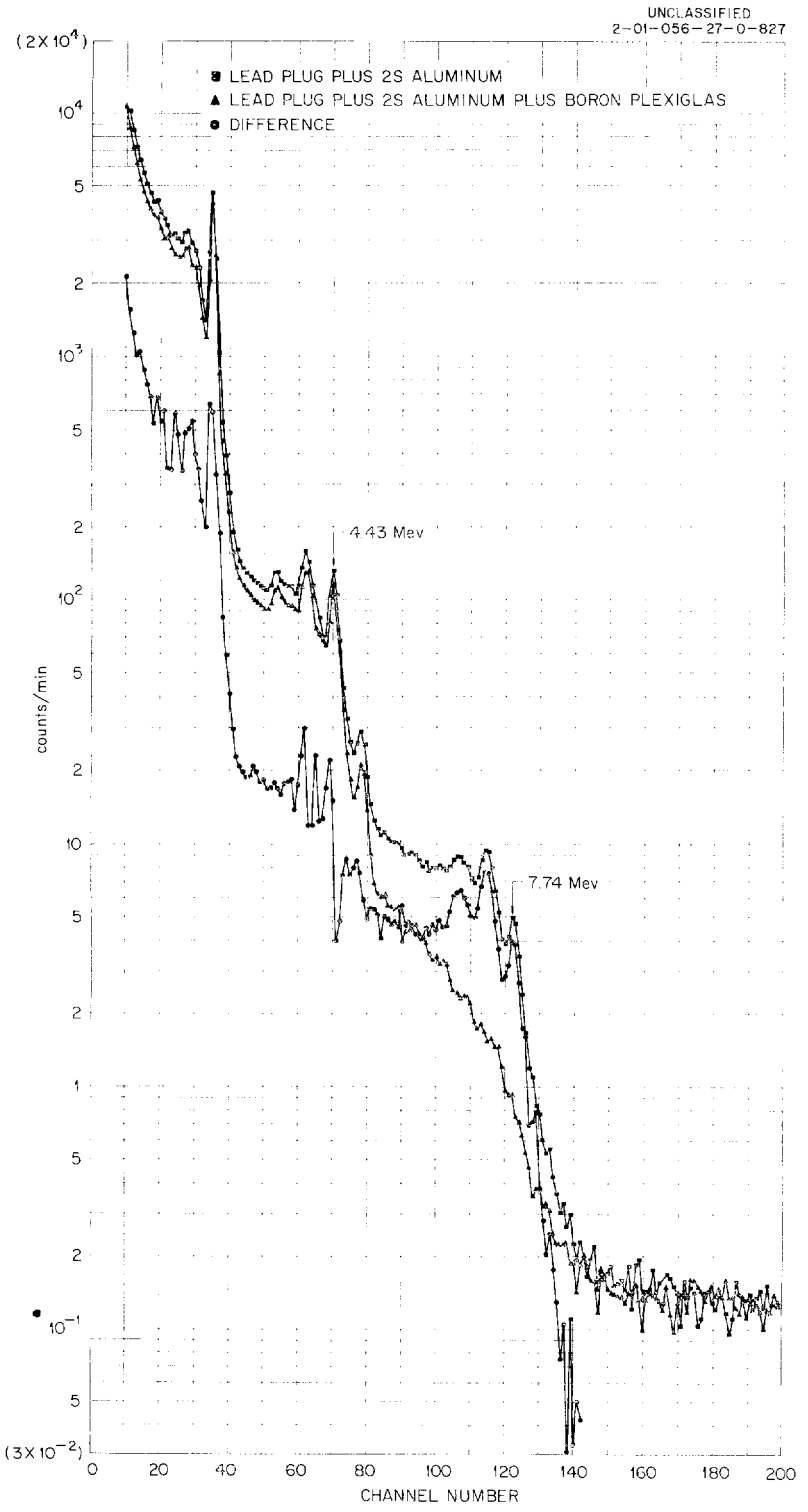

Fig. 7.1.3. Pulse-Height Spectra of Capture Gamma Rays from Aluminum.

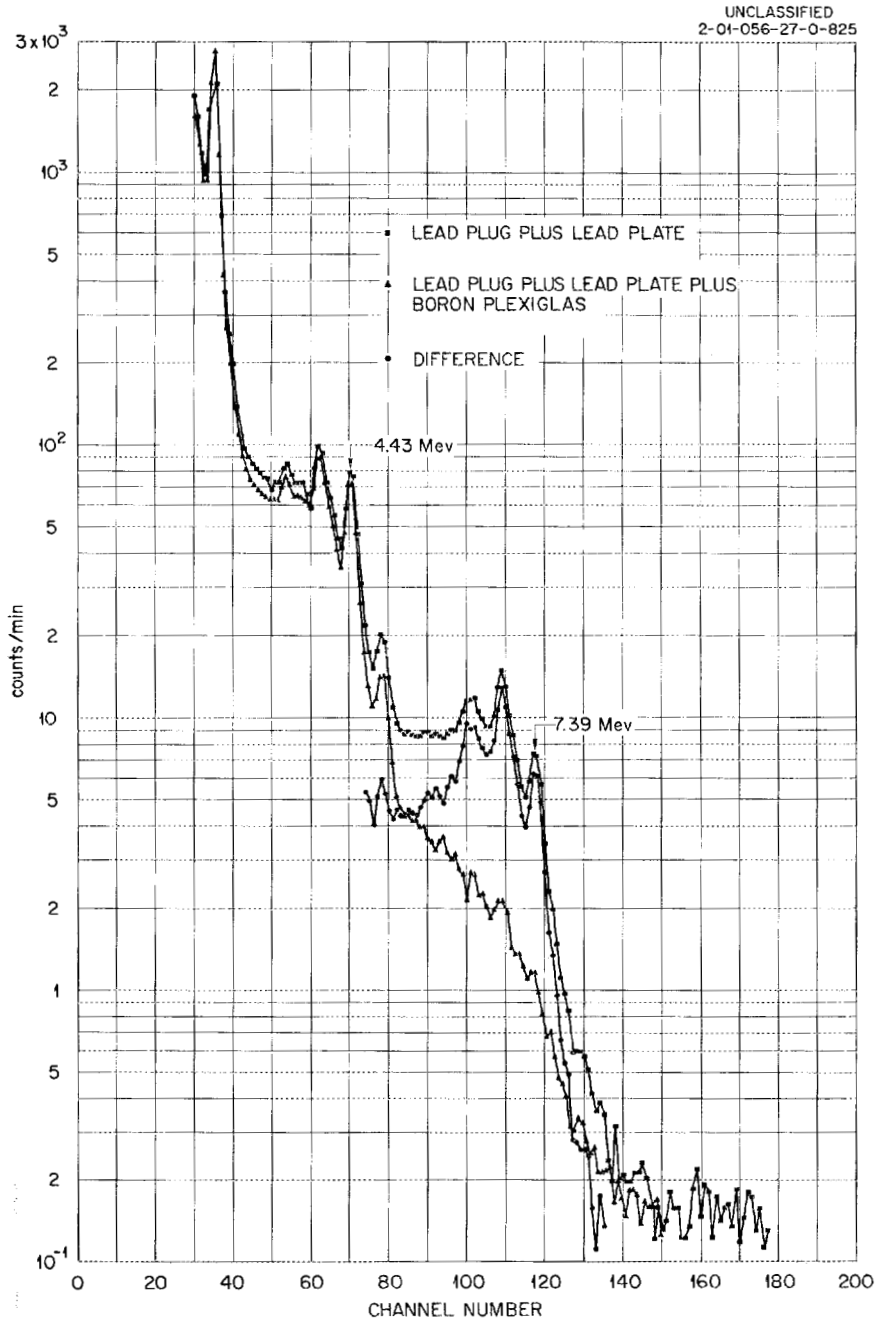

Fig. 7.1.4. Pulse-Height Spectra of Capture Gamma Rays from Lead.

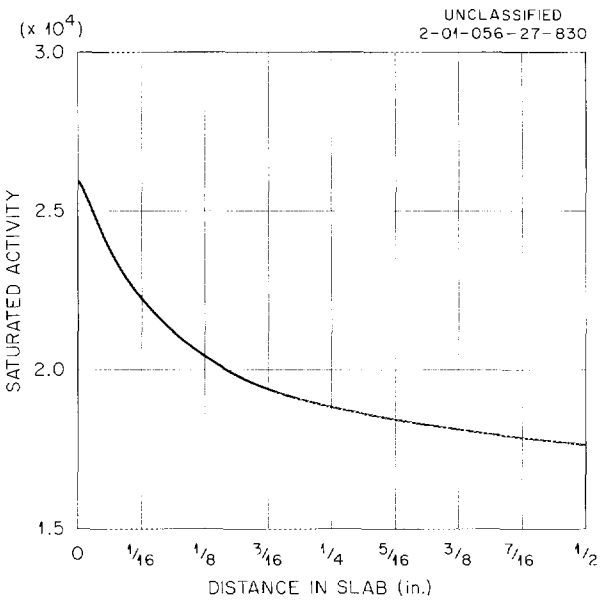

Fig. 7.1.5. Attenuation of Thermal-Neutron Flux Through ½ in. of Iron in Oil (Uncorrected for Cadmium Ratio).

7.2. PREDICTION OF THERMAL-NEUTRON FLUXES IN THE BSF FROM LTSF DATA

A. D. MacKellar

In order to obtain the maximum usefulness from shielding data collected at either the Lid Tank Shielding Facility (LTSF) or the Bulk Shielding Facility (BSF), the power of the experimental source must be accurately known. Furthermore, the data must be correctly converted by geometrical transformations from the experimental source to the reactor for which the shield is being designed. One method for checking the powers quoted for the LTSF source (a disk-shaped uranium plate) and the BSF reactor, as well as a method for checking on the validity of the geometrical transformations, is to perform a calculation predicting the neutron flux in the BSF on the basis of LTSF data transformed first to a point-to-point kernel and then to the geometry of the BSF reactor. A discrepancy between the predicted and the measured fluxes would indicate either that one of the quoted powers was in error or that the geometrical transformations were not properly derived.

A calculation[1] that compared the fast-neutron doses was performed in 1952. Since neither the power of the Bulk Shielding Reactor (BSR) nor the power of the LTSF source plate was accurately known at that time, it was not surprising that the calculated and experimental results were not in agreement. Re-estimates of both the power of the BSR[2] and the power of the LTSF source plate[3] have since become available, however, and a second calculation has been made in which the thermal-neutron fluxes at the two facilities have been compared.

[1] T. A. Welton and E. P. Blizard, *Reactor Sci. Technol.* 2(2), 73 (1952) (classified).

[2] E. B. Johnson, *Power Calibration for BSR Loading 33*, ORNL CF-57-11-30 (1957).

[3] D. R. Otis, *Lid Tank Shielding Facility at the Oak Ridge National Laboratory, Part II, Determination of the Fission Rate of the Source Plate*, ORNL-2350 (1959).

Before a conversion from LTSF data to BSF data could be made it was necessary to obtain information about the self-attenuation of neutrons inside the BSR. This was done by placing an all-aluminum mockup of one layer of fuel elements of the BSR adjacent to the source plate in the LTSF and taking thermal-neutron measurements in the water beyond the mockup. Three configurations were used: no mockup; a nine-plate mockup (one-half of a layer of elements); and an 18-plate mockup (a full layer of elements). The resulting data for a plane-disk source were converted to a point-source geometry by standard transformations for the three configurations measured. The data were then extrapolated to a reactor loading with a six-element thickness, which was the thickness of the loading for which BSR experimental data were available, and the thermal-neutron flux in the BSF was calculated from the following equation:

$$D(R) = \int_{\text{reactor vol}} P(R_1)\, G(R_1, R)\, dV \quad ,$$

where

$D(R)$ = flux in water at a distance R from the face of the reactor,

R_1 = distance from the face of the reactor to a point inside the reactor,

$P(R_1)$ = power distribution in the reactor,

$G(R_1, R)$ = attenuation kernel for a medium made up of an R_1 thickness of reactor material and an R thickness of water.

Since the power distribution through the BSF reactor was irregular, a single mathematical expression could not be obtained for the entire reactor. Therefore the reactor was divided into 304 volume elements, and the power in each volume element was computed. These calculations were based on mappings of the thermal-neutron fluxes in the reactor that were reported by Johnson.[2]

The results of the calculation are compared with experimental measurements in Fig. 7.2.1. At a distance of 25 cm from the reactor the predicted flux is too high by a factor of 1.21, while for a distance of 125 cm the predicted flux is too low by 1%. The agreement between the measured and calculated fluxes appears to be good for the larger distances, but there is a discrepancy of 15 to 25% for distances closer than 60 cm from the reactor. There is a possibility that the size of volume element used in the approximate integration over the reactor was too large to be accurate for these distances, or that extrapolation errors of the attenuation kernels were greater for closer distances. Also, the possibility of the source calibrations being in error is not completely discounted. This will be partially answered by a recalibration of the BSR now being planned.

The details of this calculation are presented elsewhere.[4]

[4] A. D. MacKellar, *Prediction of Thermal-Neutron Fluxes Near the Bulk Shielding Reactor from Lid Tank Shielding Facility Data*, ORNL CF-59-1-24 (to be published).

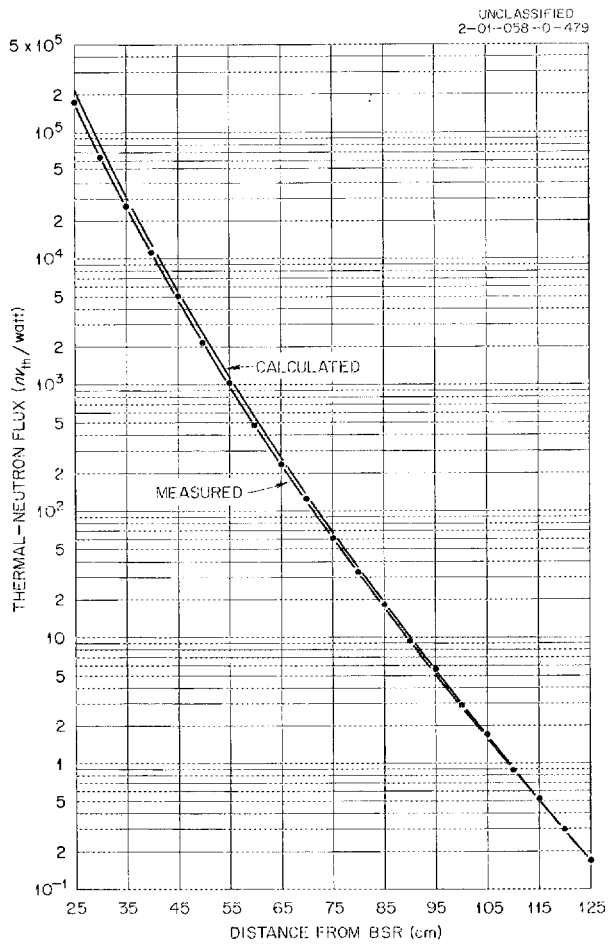

Fig. 7.2.1. Comparison of Predicted and Measured Thermal-Neutron Fluxes near the Bulk Shielding Reactor.

7.3. RADIATION ATTENUATION PROPERTIES OF BARYTES CONCRETE AND ITS COMPONENTS[1]

W. J. Grantham, Jr.[2]

Barytes concrete, because of its greater density and improved gamma-ray attenuation properties, is often chosen as a reactor shield material, particularly when the required aggegate is conveniently or locally available. It is of interest, therefore, to ascertain the relative importance in the shield of the various components of barytes concrete. This has been done in a recent series of experiments at the Lid Tank Shielding Facility which successively employed dry barytes aggregate, dry barytes aggregate and portland cement, and barytes concrete.

The barytes aggregate used in these experiments was locally mined at Sweetwater, Tennessee, and had previously been found to contain >92% $BaSO_4$. Its specific gravity, when water-saturated but surface-dry, was 4.04, with a moisture-absorption coefficient of 3.7% of the oven-dry weight. During the "dry" experiments the moisture content remained at 1.7%. The coarse aggregate had a fineness modulus of 6.06 and a maximum nominal size of 1 in.; the fine aggregate had a fineness modulus of 3.12 and a maximum size equal to the nominal size of a No. 4 U.S. Standard sieve opening. (Fineness modulus is defined as the sum of percentages in the sieve analysis divided by 100, when the sieve analysis is expressed as cumulative percentages coarser than each of the following sieves: Nos. 100, 50, 30, 16, 8, 4, $\frac{3}{8}$ in., $\frac{3}{4}$ in., and $1\frac{1}{2}$ in.)

Since the same materials were to be used in each series of measurements, proportioning criteria[3] were initially determined on the basis of a final water:cement ratio of 8 gal per 94-lb sack of cement (intended to achieve a 28-day strength of 3200 psi) and were maintained throughout all experiments. The combined fineness modulus of coarse and fine aggregates was established at 4.95, and the proportion of cement-to-aggregate at 1-to-8 by volume. (The specific gravity of portland cement was assumed to be 3.15.) For the final series of measurements, requiring barytes concrete, water was added to the dry mixture until the mix could be expelled from the mixing truck. The fresh concrete had a slump of 2 in. and an average density of 3.27 g/cm^3, which is very close to the computed density, allowing 2% for void volume, of 3.28 g/cm^3. The water requirement was such that the water:cement ratio was essentially 8 gal/sack, as intended, and measurements of five standard test cylinders after 28 days of curing indicated that the desired 3200-psi strength was achieved within a ±6% maximum deviation from the average. The water of hydration after a 28-day curing period was approximated[4] as 13% by weight, and the density at the time of the test was 3.30 g/cm^3.

Figure 7.3.1 shows the LTSF configuration adopted for the experimental measurements. The material under investigation, whether barytes aggregate, barytes aggregate plus cement, or barytes concrete, was contained in $61 \times 64\frac{1}{2} \times 8$ in. aluminum cans, which were incrementally placed between the Lid Tank source plate, operating at a nominal power of 5.18 w, and appropriate detectors placed in the auxiliary water tank following the samples. The instrumentation, conventional for LTSF measurements, consisted of three parallel-plate fission chambers, a $12\frac{1}{2}$-in. BF_3 proportional counter, two Hurst dosimeters, a 50-cc ion chamber, and an anthracene-crystal scintillation counter.

Measurements of fast-neutron dose rates, gamma-ray dose rates, and thermal-neutron fluxes were made for each increment of shielding material added to the configuration. Figures 7.3.2 and 7.3.3 display the measured fast-neutron dose rates and the gamma-ray dose rates, respectively, as a function of thickness of shield material. These curves were obtained by extrapolating to a zero water thickness the dose-rate data measured in water beyond the samples. The data clearly demonstrate the importance of the water in the concrete; the differences in the slopes of the curves, however, are believed to be due primarily to density differences, since the presence of the

[1] This paper is an abstract of a portion of a master's thesis that has been submitted to the Graduate Council of the University of Florida.

[2] University of Florida.

[3] W. J. Grantham, Jr., *Mix Design Criteria for Radiation Shielding Concrete*, master's thesis, University of Florida, 1959.

[4] R. Wilson and F. L. Martin, *Proc. Am. Concrete Inst.* 31 (1935).

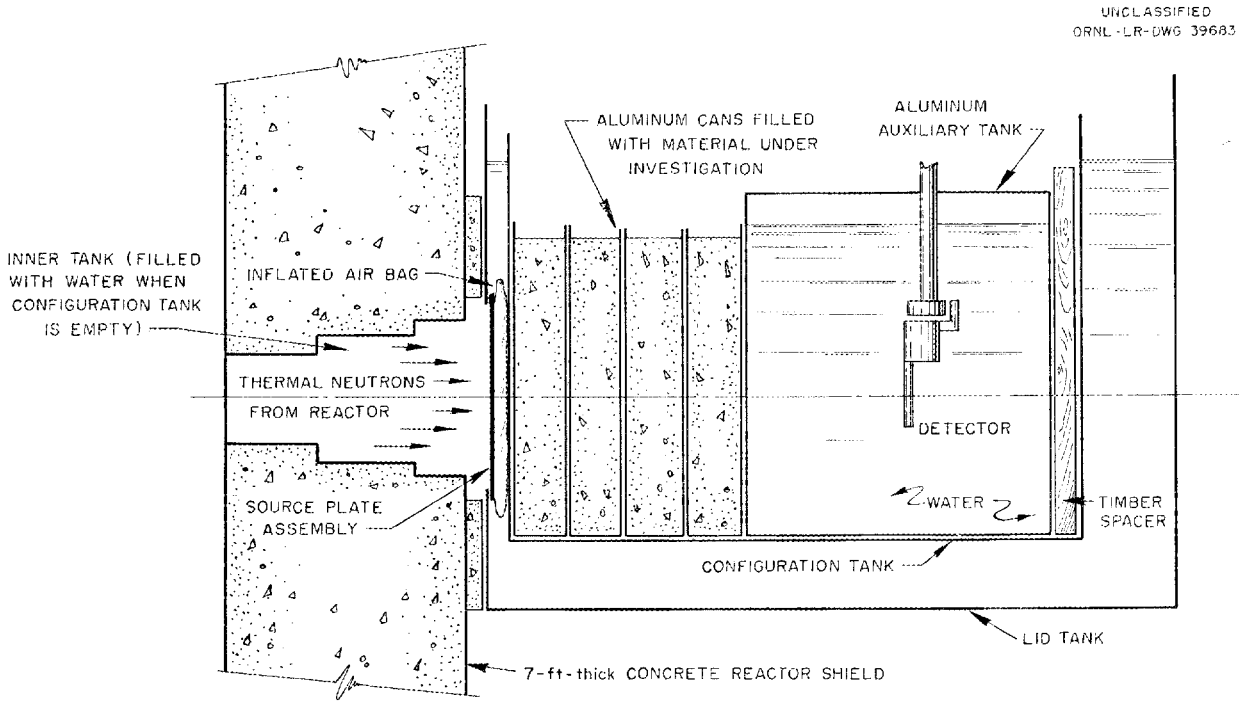

Fig. 7.3.1. LTSF Experimental Configuration for Measurements of Radiation Attenuation of Barytes Concrete.

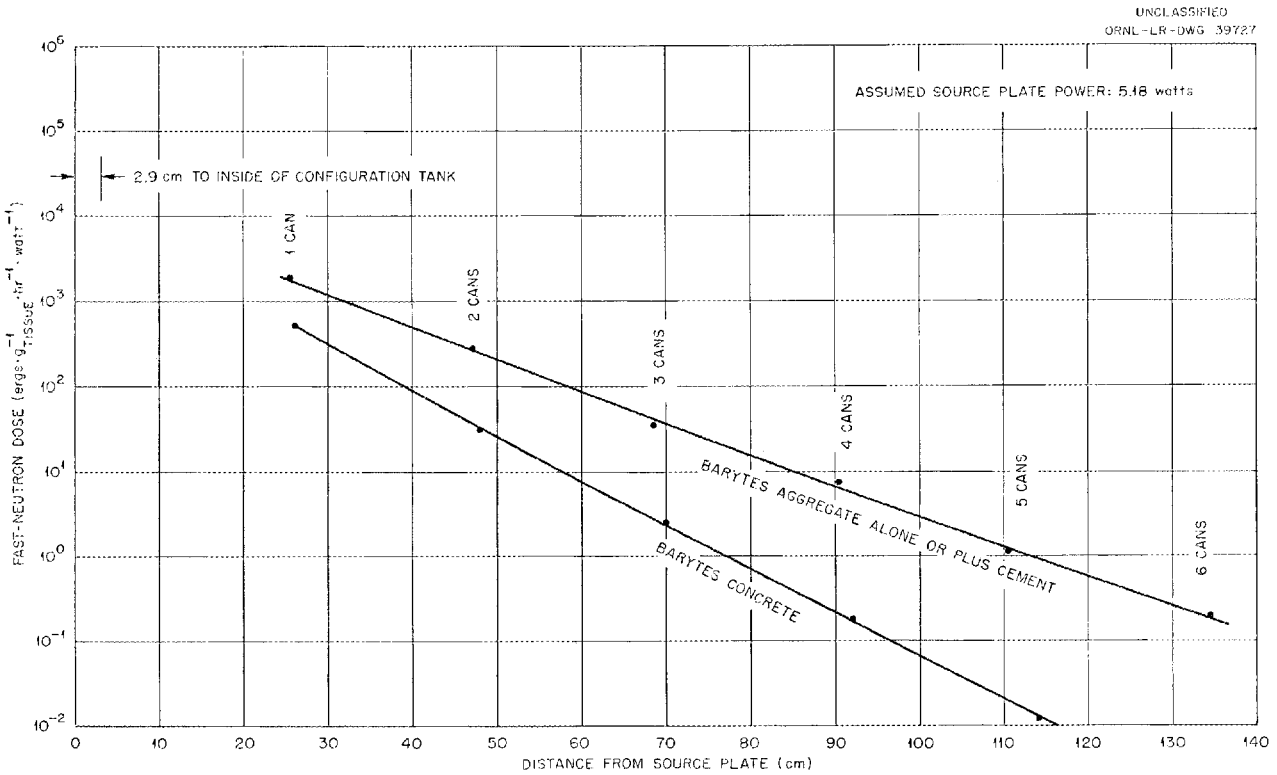

Fig. 7.3.2. Fast-Neutron Dose Rates Through Barytes Aggregate, Barytes Aggregate Plus Cement, and Barytes Concrete as a Function of Distance from LTSF Source Plate.

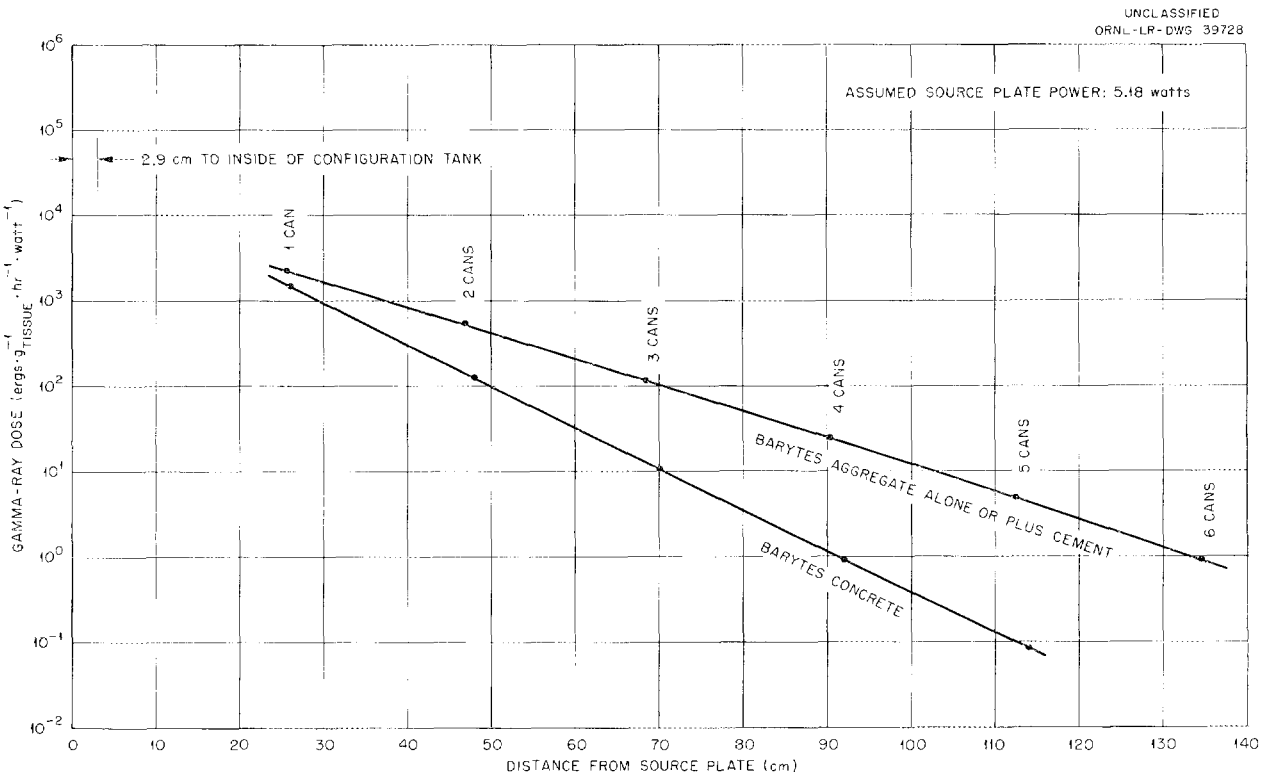

Fig. 7.3.3. Gamma-Ray Dose Rates Through Barytes Aggregate, Barytes Aggregate Plus Cement, and Barytes Concrete as a Function of Distance from LTSF Source Plate.

water permits more efficient compaction of the materials.

Fast-neutron removal cross sections and mass attenuation coefficients determined from the measured thermal-neutron flux data are shown in Table 7.3.1. Intermediate-energy (~1-Mev) neutron removal cross sections were also determined. In each of three cases the intermediate-energy removal cross sections were approximately 10% higher than the fast-neutron removal cross sections, indicating that buildup of intermediate-energy neutrons does not occur, even in the absence of water. In contrast, however, inspection of the fast-neutron dose-rate relaxation lengths in water beyond the barytes and barytes-plus-cement shields indicated that the emergent spectrum after an ~100-cm penetration was slightly softer than that from barytes concrete after the same penetration. This suggests the existence of small buildup in the barytes and barytes-plus-cement shields of the energy component between 200 kev, the threshold energy of the Hurst dosimeters used, and 1 Mev.

A calculated fast-neutron mass attenuation coefficient, based on a chemical analysis of the concrete used and removal cross sections for the individual elements, is shown as Table 7.3.2. The calculated value of $\Sigma_R/\rho = 0.0313$ cm^2/g is in excellent agreement with the value of 0.0301 cm^2/g determined by these experiments.

Table 7.3.1. Fast-Neutron Removal Cross Sections and Mass-Attenuation Coefficients for Barytes Concrete Components (6 Mev $\leq E_n \leq$ 8 Mev)

Material	$\bar{\rho}$, Average Density (g/cm^3)	Σ_R, Macroscopic Removal Cross Section (cm^{-1})	Σ_R/ρ, Mass Attenuation Coefficient (cm^2/g)
Barytes aggregate	2.68	0.0662	0.0247
Portland cement	2.67	0.0653	0.0245
Barytes concrete	3.30	0.0993	0.0301

Table 7.3.2. Calculated Mass-Attenuation Coefficient for Barytes Concrete, with Chemical Analysis and Mass Attenuation Coefficients of Constituents

Constituent	Content (wt %)*	Σ_R/ρ (cm^2/g)**	Weighted Σ_R/ρ (cm^2/g)
Ba	36.4	0.0124	0.0045
S	8.7	0.0275	0.0024
O	27.8	0.0372	0.0103
Si	4.2	0.0295	0.0012
Ca	4.1	0.024	0.0010
Al	0.2	0.0292	0.0001
Fe	8.4	0.0214	0.0018
Mg	0.3	0.030	0.0001
H_2O	9.9	0.100	0.0099
		Total	0.0313

*Normalized to 100 wt %; actual total from chemical analysis, 101 wt %.

**From G. T. Chapman and C. L. Storrs, *Effective Neutron Removal Cross Sections for Shielding*, ORNL-1843 (1955); see also E. P. Blizard, *Nuclear Engineering Handbook* (ed. by H. Etherington), p 7–60, McGraw-Hill, New York, 1958.

7.4. EFFECTIVE NEUTRON REMOVAL CROSS SECTION OF ZIRCONIUM

J. M. Miller

The effective neutron removal cross section, defined as the equivalent absorption cross section which most nearly describes the fast-neutron attenuation of a material added to a hydrogenous shield, has previously been measured for a wide variety of elements.[1] In an attempt to narrow the rather broad region between $Z = 29$ and $Z = 74$, for which no cross sections were recorded, a measurement of the effective removal cross section of zirconium ($Z = 40$) has recently been made at the Lid Tank Shielding Facility.

The zirconium used in the experiment is in the form of two slabs, each 54 × 49 × 2 in. The metal contains 1.8 wt % hafnium as the main impurity and has a density of 6.54 g/cm^3.

The dry sample was placed at the source-plate end of the usual steel configuration tank in the Lid Tank and was followed by an aluminum tank ($\frac{1}{8}$-in.-thick walls) containing light water. (The configuration tank has a $\frac{3}{8}$-in.-thick aluminum window in the side next to the source plate.) Thermal-neutron flux measurements were made on the axis of the source plate in the water beyond the material and are compared with measurements made with the zirconium removed in Fig. 7.4.1. Standard instrumentation, including a $12\frac{1}{2}$-in. BF_3 counter, a 3-in. fission chamber, and a $\frac{1}{2}$-in. fission chamber, was used.

The effective removal cross section of the zirconium was calculated from these measurements by use of a formula given by Blizard.[2] The resulting value was 2.36 ± 0.12 barns. The value of the mass attenuation coefficient of zirconium [$\Sigma_R/\rho = (1.56 \pm 0.08) \times 10^{-2}$ cm^2/g] calculated from these data is in excellent agreement with the predicted value deduced from published curves.[3]

[1] G. T. Chapman and C. L. Storrs, *Effective Neutron Removal Cross Sections for Shielding*, ORNL-1843 (1955).

[2] E. P. Blizard, *Procedure for Obtaining Effective Removal Cross Sections From Lid Tank Data*, ORNL CF-54-6-164 (1954).

[3] E. P. Blizard, *Proc. U. N. Intern. Conf. Peaceful Uses Atomic Energy, 2nd, Geneva, 1958*, P/2162.

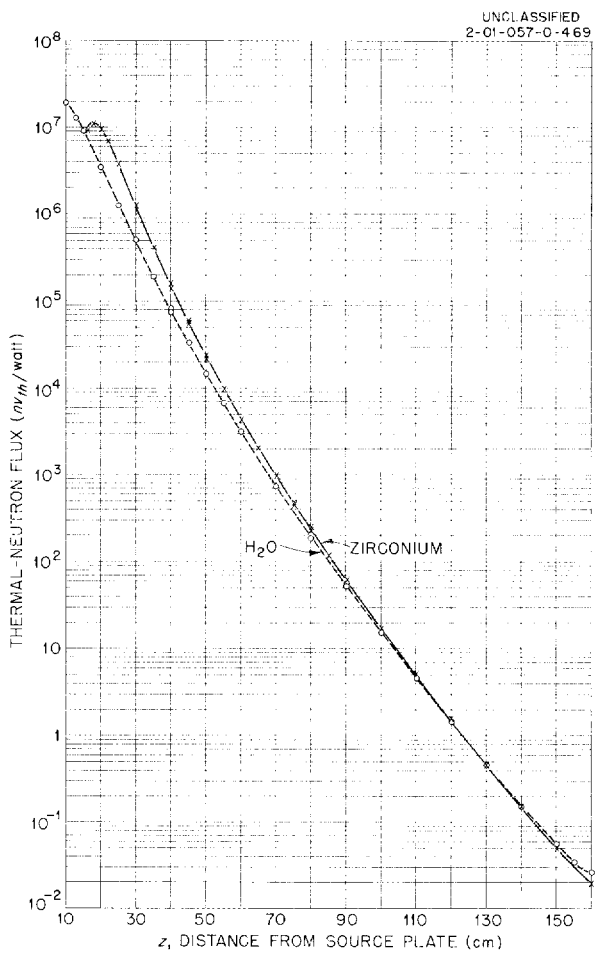

Fig. 7.4.1. Thermal-Neutron Flux Measurements in Water Beyond 4 in. of Zirconium.

7.5. RECHECKS AND EXTENSIONS OF THE 2π EXPERIMENTS AT THE TSF

D. R. Ward F. J. Muckenthaler S. C. Dominey[1]

A series of experiments[2] was carried out during the last quarter of 1956 at the Tower Shielding Facility by personnel of the General Electric Company to obtain data to aid in the design of a shield at their Idaho Shield Test Air Facility. The experiments, which were designed to investigate the effect of ground-scattered radiation, consisted in measurements of radiation in a cylindrical G-E crew compartment as a function of altitude for various shielding configurations encasing the Tower Shielding Reactor 64 ft away.

Since the results of the measurements at the highest altitudes were not always in agreement with the predictions made by a G-E analysis group,[2] G.E. requested that ORNL perform a second series of measurements to check and extend the original series. The extensions were added principally to aid in the calculation of secondary gamma-ray production and consisted in mapping the radiation escaping from the reactor shield as well as a series of gamma-ray spectral measurements inside several detector shields. The results of the second series of measurements, completed in late 1958, have been reported elsewhere in detail[3] and will only be summarized below. The analysis and conclusions concerning this work will be reported by G.E.

Altitude Traverses

All altitude runs were made with the TSR-I enclosed in the G-E reactor shield assembly No. 1, shown in Fig. 7.5.1. The lead-water 2π shield fitted over the lower half of the reactor shield and was detachable. The radiation detectors were contained in the G-E crew shield, which is also shown in Fig. 7.5.1. The end tanks of this compartment contained borated water at all times, while the side tanks were empty or filled with borated water according to the particular phase of the experiment. Fast-neutron and gamma-ray dose rates and thermal-neutron fluxes were measured as the reactor and detector compartment were raised simultaneously from near ground level to an altitude of 195 ft. Throughout the

[1] On assignment from Convair, Fort Worth, Texas.

[2] R. H. Clark *et al.*, *Test Data from the 2π-Solid-Angle-Cover Experiment*, APEX-439 (1958).

[3] S. C. Dominey, D. R. Ward, and F. J. Muckenthaler, *TSF Studies in Support of GE-ANP Program: Rechecks and Extensions of the 2π Shield Experiments*, ORNL CF-59-4-72 (1959).

UNCLASSIFIED
2-01-056-24-D-820

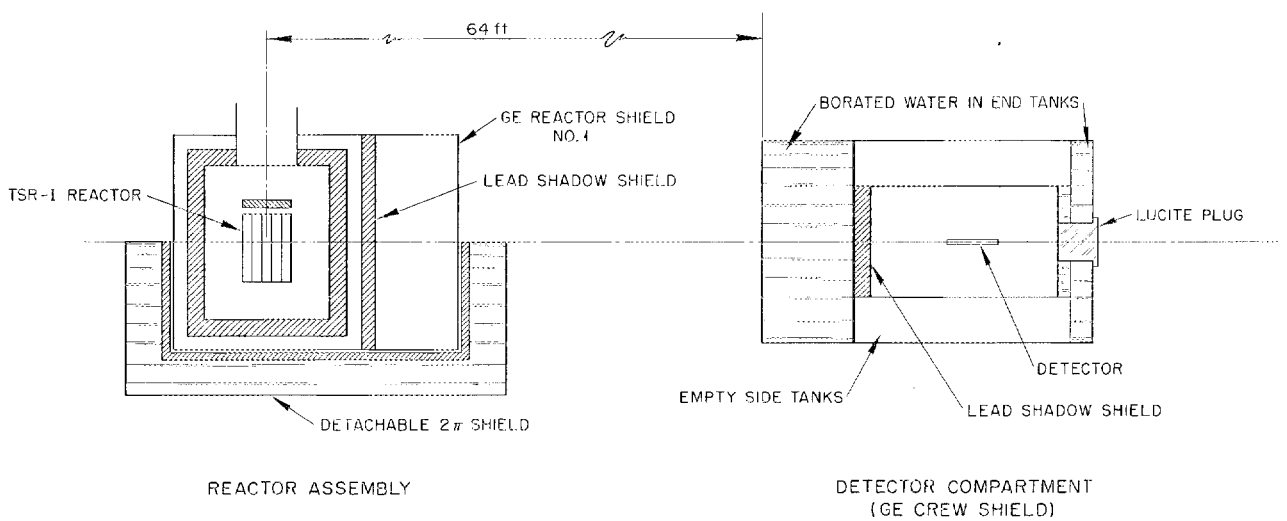

Fig. 7.5.1. Reactor and Crew Shield Arrangement Used in TSF 2π Experiments ($\theta = 0°$).

experiments a constant reactor–crew compartment separation distance of 64 ft was maintained, and the axes of the detector compartment and the reactor shield were held in the same horizontal plane. The reactor and shield assembly was rotatable, and measurements were made both in the relationship shown in Fig. 7.5.1, designated as $\theta = 0°$, and with the reactor–shield assembly rotated end for end ($\theta = 180°$) so that the lead shadow shield shown did not intercept the path of direct radiation to the detector.

Gamma-ray dose rates were measured with an ion chamber and with an anthracene crystal scintillation detector, both of which were calibrated against a Co^{60} source of known strength. Fast-neutron dose rates were measured with a Hurst-type dosimeter, while thermal-neutron fluxes were measured with a BF_3 counter. Neutron detectors were calibrated against a Po-Be neutron source.

Fast-neutron dose rates as a function of altitude are displayed in Fig. 7.5.2. This figure includes data points from the present measurements, curves drawn from the earlier G-E data, and values

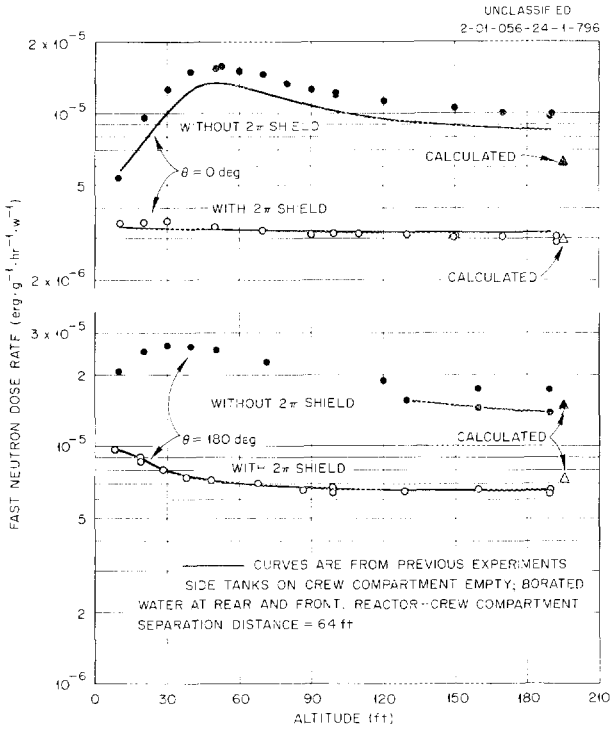

Fig. 7.5.2. Fast-Neutron Dose Rate in the G-E Crew Compartment 64 ft from the TSR-I as a Function of Altitude: With and Without a 2π Shield on the Reactor.

predicted by G.E. for an altitude of 195 ft. Corresponding curves for gamma-ray dose rates and thermal-neutron fluxes as functions of altitude, which are not included in this report, have similar shapes.

The fast-neutron dose rates for corresponding cases in the two sets of data are evidently in good agreement for the arrangement including the 2π shield and agree fairly well with the calculated dose rates. For the case without the 2π shield, the agreement for the two sets of data is within 15%, but the calculated value at 195 ft for $\theta = 180°$ lies between the two measurements, while the calculated value for $\theta = 0°$ is considerably lower than either measurement. Gamma-ray dose-rate measurements for the two sets of experiments agreed within 10%; however, the calculated dose rates at 195 ft were as much as a factor of 2 lower for $\theta = 0°$ and a factor of 2 higher for $\theta = 180°$. The thermal-neutron fluxes measured in the recent series agreed well with previous measurements when experimental conditions were duplicated.

Radiation Mapping

In order to provide a check on source-term calculations and to assist in the study of numerous secondary radiation effects, both gamma-ray and neutron intensities were measured with unshielded detectors at various positions around the reactor. For these measurements the reactor shield contained only plain water, and the 2π shield was detached. The experimental arrangement for measurements in a vertical plane through the center of the reactor is diagramed in Fig. 7.5.3. For measurements in other regions, the arrangement shown in Fig. 7.5.4 was utilized. The detectors were mounted on an aluminum truss, which could be held at angles varying from 30° above horizontal to 45° below horizontal, while the reactor itself was rotated on its vertical axis to accomplish a 360° mapping. Data from both arrangements were automatically plotted by a Variplotter machine, in which the abscissa motion was governed by the detector or reactor motion, and the ordinate motion was proportional to the detector output.

Figure 7.5.5 shows typical plots of fast-neutron and gamma-ray dose rates and thermal-neutron fluxes in the vertical plane through the reactor center. The drop in the thermal- and fast-neutron

UNCLASSIFIED
2-01-056-24-D-822

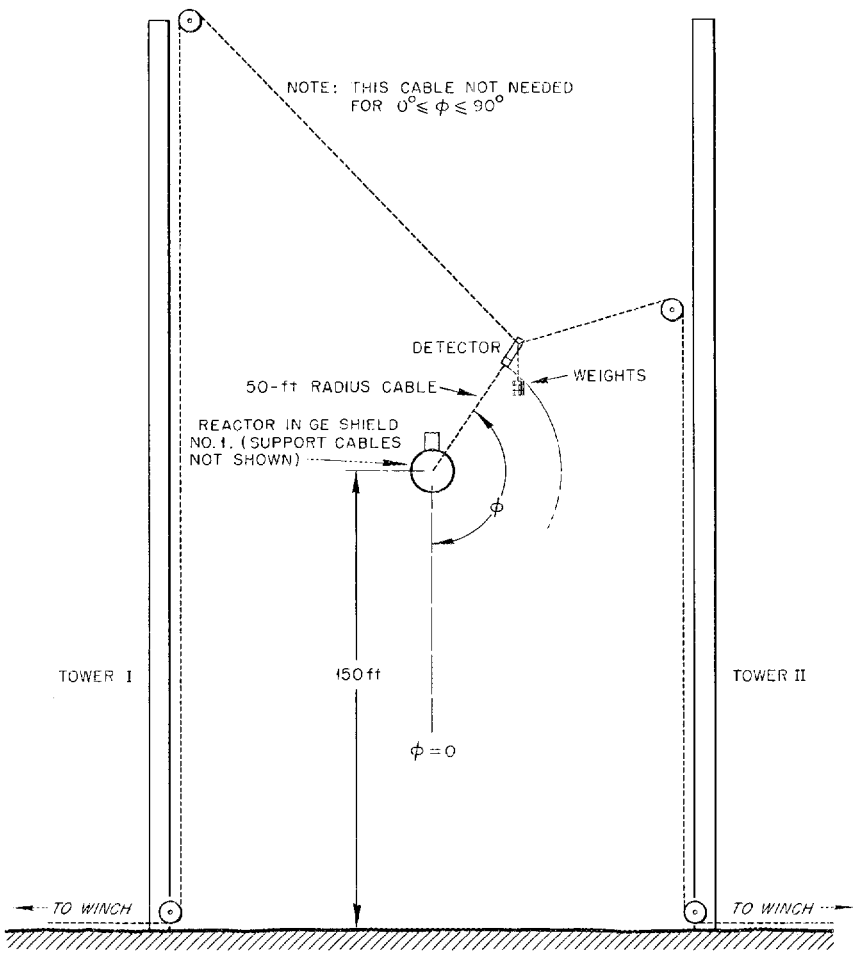

Fig. 7.5.3. Arrangement for Traversing Detector in Vertical Plane Around Center Line of G-E Reactor Shield.

curves as the detector approached 180° is due to the extra thickness of the water shield above the core. The gamma-ray peak at $\phi = 155°$ is due to a gap in the lead shielding at this point, while the peak at $\phi = \sim 30°$ is attributed to the rectangular parallelepipedal shape of the core. (For these measurements ϕ is defined as shown in Fig. 7.5.3.)

Typical plots of fast-neutron dose rates obtained with the arrangement shown in Fig. 7.5.4 are presented in Fig. 7.5.6; corresponding plots of thermal-neutron fluxes and gamma-ray dose rates are similar in shape. The fast-neutron and gamma-ray dose rates observed at the 100-ft station of Fig. 7.5.4 increased by as much as a factor of 7 as the reactor and shield were rotated and the lead shadow shield became ineffective. Under the same conditions, however, the thermal-neutron fluxes increased only about a factor of 2, since a large fraction of the thermal-neutron flux detected resulted from air-scattered neutrons rather than direct neutrons.

Gamma-Ray Spectral Measurements

A cylindrical tank which contains side and end compartments that can be filled with water was used to house the detector for the gamma-ray spectral measurements. These measurements are plotted in Fig. 7.5.7. Since only the scattered

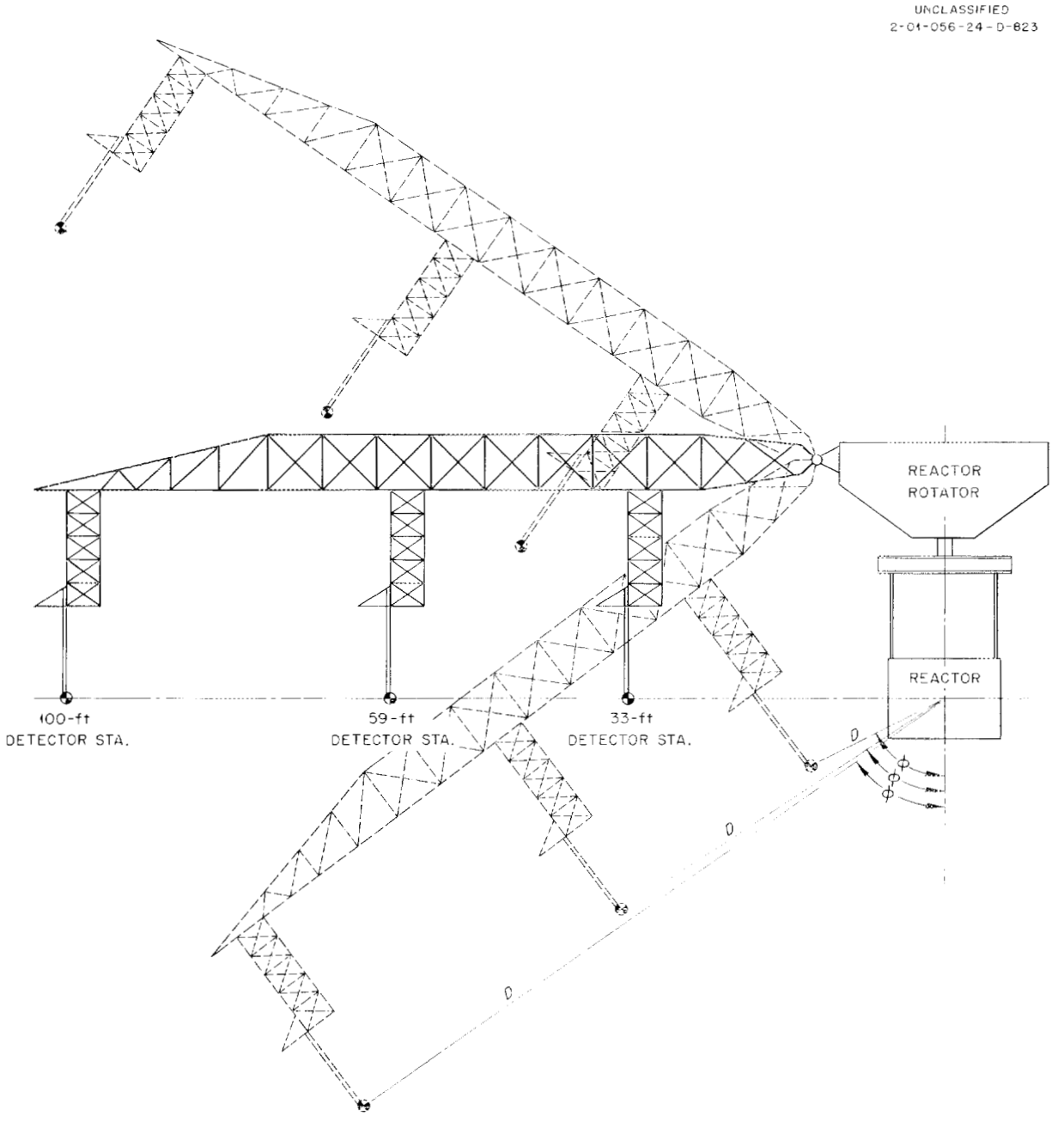

Fig. 7.5.4. Truss Positions for Various ϕ Angles in G-E 2π Experiments.

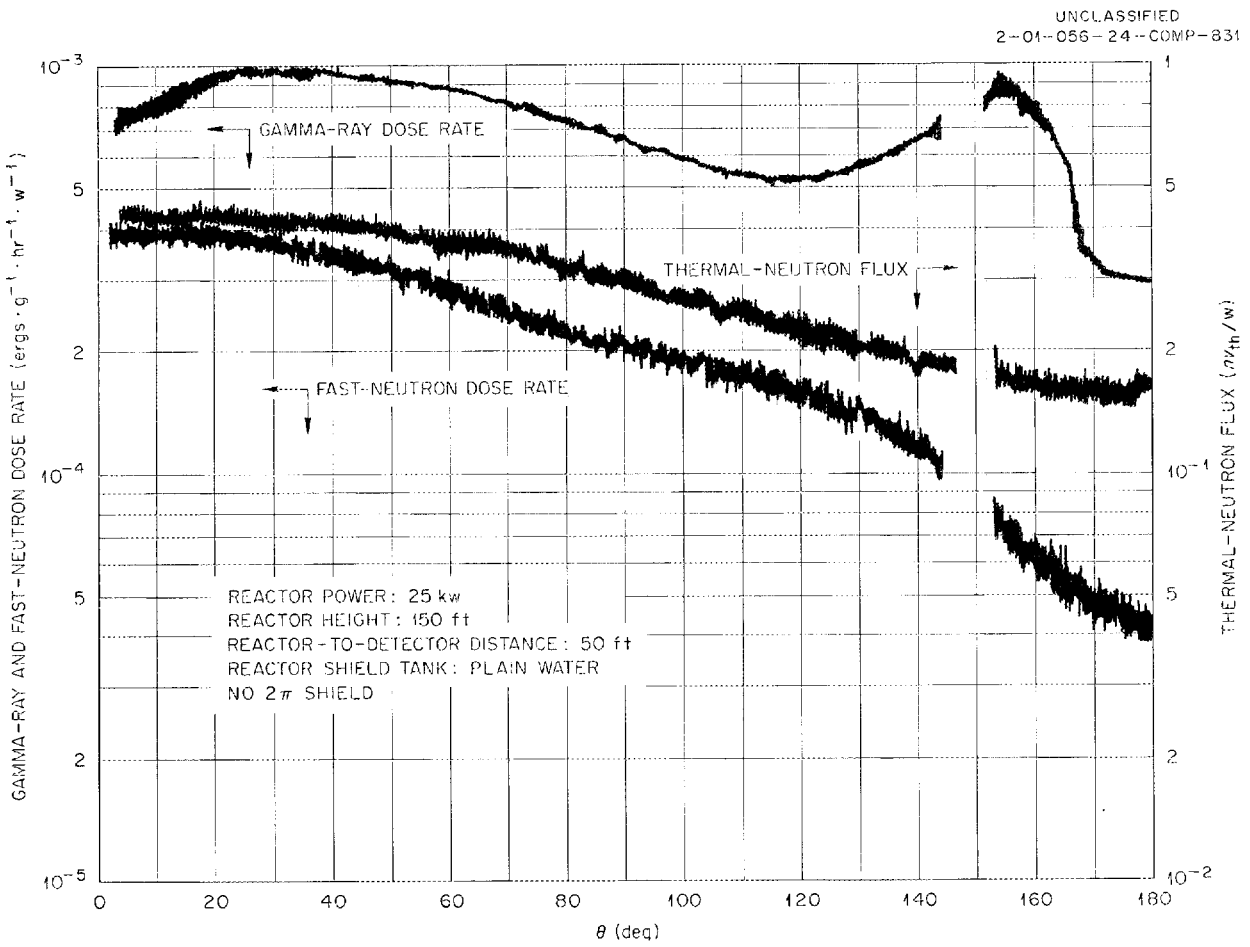

Fig. 7.5.5. Typical Plots of Radiation Measurements Around G-E Reactor Shield No. 1.

gamma rays were desired for these measurements, direct-beam radiation was greatly attenuated by a 5-in.-thick lead shadow shield located between the reactor and the detector.

Both end compartments of the detector tank were filled with borated water, and sufficient plain-water side shielding was employed to prevent neutrons from reaching the NaI(Tl) detector and causing neutron counts. A study of the gamma-ray spectrum of Fig. 7.5.7 shows the hydrogen capture peak at 2.23 Mev, as well as the peak resulting from nitrogen capture at 10.8 Mev, along with the first and second escape peaks at 10.3 and 9.8 Mev, respectively. The aluminum capture peak seen at 7.7 Mev is accompanied by escape peaks at 7.2 and 6.7 Mev, while the peak at 1.78 Mev represents the Al^{28} decay gamma rays.

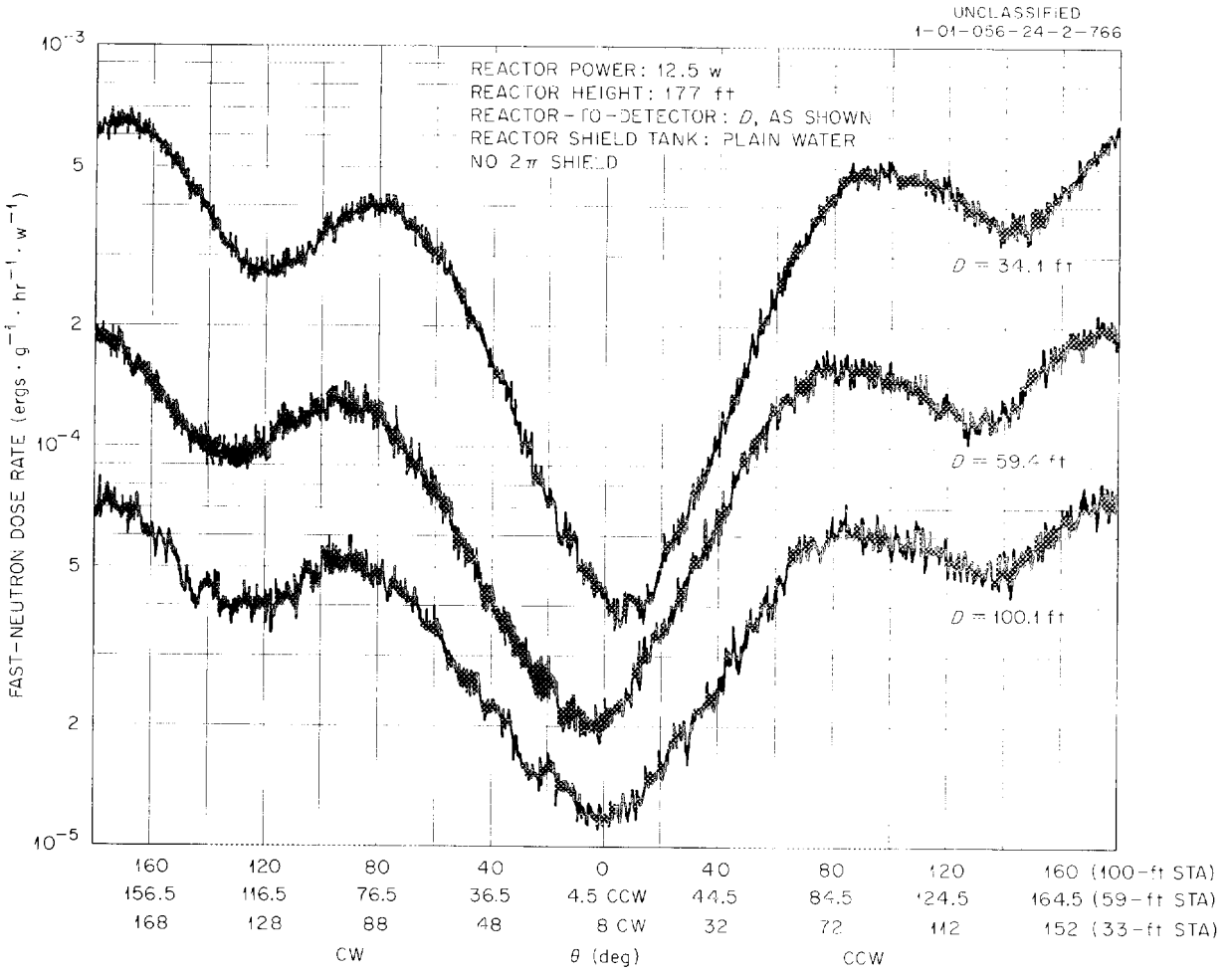

Fig. 7.5.6. Fast-Neutron Dose Rate at Various Distances from G-E Reactor Shield No. 1 as a Function of θ ($\theta = 90°$).

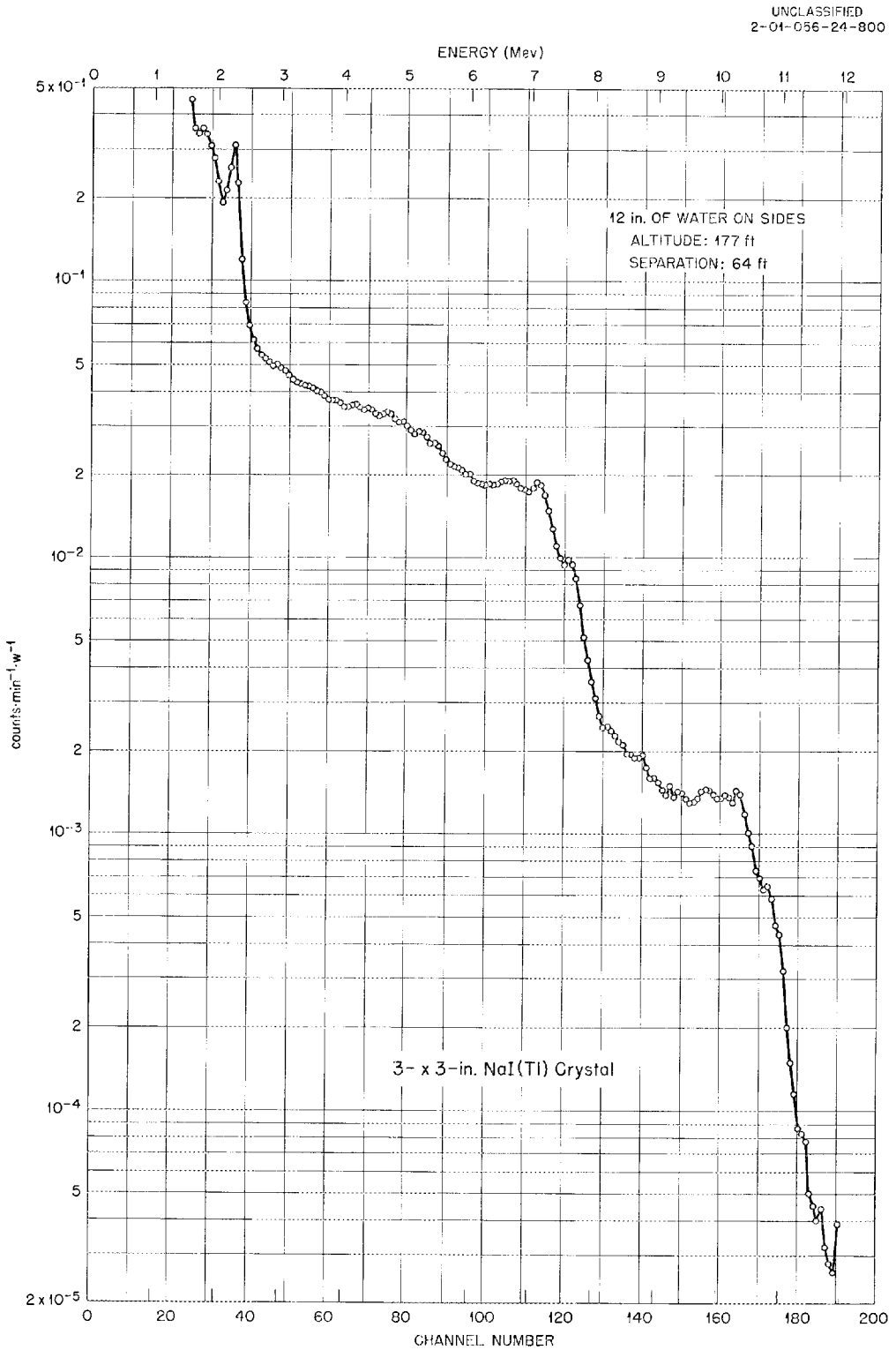

Fig. 7.5.7. Gamma-Ray Spectrum from 0 to 12 Mev in TSF Compartmentalized Tank (G-E 2π Experiments).

7.6. THE HIGH-ENERGY ACCELERATOR SHIELDING PROGRAM

C. D. Zerby H. W. Bertini

The high-energy accelerator shielding program has proceeded along the two lines previously determined.[1] The first is the development of calculational techniques for deep penetrations of particles through shields; the second is the development of a code to compute the inelastic differential cross sections for pions and nucleons incident upon complex nuclei. These cross sections are required by the penetration calculation.

For the penetration calculation it is desirable to use the Monte Carlo method. The reasons for this are twofold: first, this method permits variations in the geometry of the shield, and second, the complex chains of secondary radiation which can be important to the penetration are relatively easily handled.

In order to perform the deep penetration calculation by the Monte Carlo method, the establishment of a satisfactory statistical method was necessary. Of the methods which have been investigated, the one which shows the greatest promise is the "conditional" Monte Carlo method.[2]

The computation of the inelastic differential cross sections for complex nuclei is currently being coded for the IBM-704 computer. This intranuclear cascade calculation differs from published calculations[3] in several respects. The nucleus will be assigned a shape such that the inelastic cross section for single particles leaving the nucleus will be improved. The shape will be taken for convenience as a three-step well with nuclear densities determined from electron scattering experiments.[4] The depth of the well in each of the three regions will be determined from the binding energy of the last nucleon and the Fermi momentum.

In place of a zero-temperature Fermi momentum distribution, a distribution with a temperature of 15 Mev will be used and approximated by a Gaussian.[5] This should improve the high-energy portion of the spectrum of particles leaving the nucleus which is so important in the penetration problem.

With the addition of the Gaussian tail to the momentum distribution in the nucleus it is necessary to treat the collisions with these nucleons in a more exact manner than has been customary. It is hoped that some approximate methods of working out these kinematical problems can be achieved to simplify the calculation and reduce the running time.

For the production of mesons in the nucleus the isobar model[6] will be used in the region below 2 bev.

In addition to the above-mentioned penetration problem and nuclear cascade problem, an electron-photon cascade calculation is under consideration to determine the photon energy distribution and spatial distribution resulting from high-energy electrons incident on an arbitrarily chosen material. This information is of importance in connection with electron accelerators, since the stopped electron can give rise to photoneutrons through the secondary bremsstrahlung radiation.

---

[1] C. D. Zerby, *Neutron Phys. Ann. Prog. Rep. Sept. 1, 1958*, ORNL-2609, p 130.

[2] H. F. Trotter and J. W. Tukey, *Symposium on Monte Carlo Methods* (ed. by H. A. Meyer), Wiley, New York, 1956; see also paper by D. W. Drawbaugh, to be published in *J. Ind. and Appl. Math.*

[3] N. Metropolis *et al.*, *Phys. Rev.* 110, 185 (1958).

[4] R. Hofstadter, *Ann. Revs. Nuclear Sci.* 7, 231 (1957).

[5] E. M. Henle, *Phys. Rev.* 85, 204 (1952).

[6] R. M. Sternheimer and S. J. Lindenbaum, *Phys. Rev.* 109, 1723 (1958).

7.7. MONTE CARLO CODE FOR THE CALCULATION OF DEEP PENETRATIONS OF GAMMA RAYS: STATUS REPORT

S. K. Penny

The Monte Carlo code for deep penetrations[1] has been, in fact, several codes to investigate several methods, the most successful being the "conditional" Monte Carlo method. In initial investigations which were concerned with a one-velocity, isotropic scattering, isotropic point source situation, the Monte Carlo results for 20 mean free paths, with the ratio of scattering cross section to total cross section in the range from 0.1 to 0.5, were within 20% of the exact result.[2] When investigations were made with gamma rays, however, the Monte Carlo results fluctuated badly about the results given by the moments method.[3] It appears that more mathematical work needs to be done on the problem; however, the priority of other investigations necessitates suspension of the study for the time being.

[1] S. K. Penny, *Neutron Phys. Ann. Prog. Rep. Sept. 1, 1958*, ORNL-2609, p 118.

[2] K. M. Case, F. de Hoffman, and G. Placzek, *Introduction to the Theory of Neutron Diffusion*, Los Alamos Scientific Laboratory, Los Alamos, 1953.

[3] H. Goldstein and J. E. Wilkins, Jr., *Calculations of the Penetrations of Gamma Rays, Final Report*, NDA-15C-41 or NYO-3075 (1954).

7.8. NEUTRON YIELDS FROM (α,n) REACTIONS IN VARIOUS MATERIALS

F. S. Alsmiller G. M. Estabrook

A calculation of the neutron yields from (α,n) reactions in several materials has been initiated. The materials considered are the uranium isotopes with mass numbers from 232 to 236, Th^{228} and its daughters, and elements such as beryllium, boron, carbon, sodium, lithium, chlorine, calcium, and silicon which are often present as impurities in fabricated uranium. This calculation is being performed in support of a Chemical Technology Division investigation of hazards associated with fabrication of fuel elements from various U^{233} alloys and compounds.

If N_i is the density of the ith element or isotope undergoing an (α,n) reaction with cross section $\sigma_i(E_\alpha)$, the number, Q_n, of neutrons produced per cubic centimeter per second is given by

$$Q_n = \sum_i N_i Q_{ni} ,$$

$$Q_{ni} = Q_\alpha(E_0) \int_{E_0}^{0} \frac{\sigma_i(E_\alpha)}{dE_\alpha/dx} dE_\alpha , \qquad (1)$$

where $Q_\alpha(E_0)$ is the source strength of alpha particles per cubic centimeter per second at initial energy E_0, and $-dE_\alpha/dx$ is the average alpha energy loss per centimeter of path in the stopping material. The latter term is expressed as

$$-\frac{1}{N}\frac{dE_\alpha}{dx} = \epsilon_\alpha (\text{ev/cm}^2) , \qquad (2)$$

where N is the number of stopping atoms per cubic centimeter (or molecules per cubic centimeter in the case of compounds), and ϵ is the stopping cross section per atom (or molecule).[1] For a compound $(X_n Y_m)$, the relation

$$\epsilon_{mol}(X_n Y_m) = n\epsilon_{atom}(X) + m\epsilon_{atom}(Y)$$

is sufficiently accurate.

Experimental results for ϵ in some of the materials needed are given in ref 1; theoretical methods for computing ϵ in the materials not yet measured, including U^{233}, are under study.

In practice, the upper limit of the integral in Eq. (1) is taken variously as the threshold energy in endothermic reactions, or the lowest energy at which the cross sections are known.

Experimental values for the (α,n) cross sections of lithium, beryllium, boron, silicon, and C^{13} are available at present.

[1] W. Whaling, *Handbuch der Physik*, vol 34, p 213 (ed. by S. Flügge), Springer, Berlin, 1958.

Part 8

RADIATION DETECTOR STUDIES

8.1. THE MODEL IV GAMMA-RAY SPECTROMETER: STATUS REPORT

G. T. Chapman T. A. Love

The design of a new gamma-ray spectrometer system for use at the Bulk Shielding Facility (BSF) has previously been reported.[1] This spectrometer, called the model IV, consists of a "total absorption" NaI(Tl) crystal, housing for the crystal, a positioning device, and the necessary electronics.

All components of the spectrometer, including the lead-lithium eutectic alloy housing, have been received at the BSF, and the bridge crane and control mechanisms have been completed and installed. The assembly of all components is complete, with the exception of mounting the housing on the positioner.

Prior to the mounting of the housing, it was considered desirable to examine it for possible voids incurred during pouring and solidification of the lead-lithium alloy. The examination is being made by moving a 300-curie Co^{60} source over the outside surface of the housing at a given distance and observing the count rate produced in a large NaI(Tl) crystal mounted inside.

Because of the high intensity of the source, the mapping was performed in the water of the reactor pool of the BSF. The count-rate meter used to record the data was biased at an energy level only slightly below that of the 1.17-Mev gamma ray of the Co^{60}, and thus recorded only those gamma rays from the source which had suffered but a few scattering collisions in the forward direction. Constancy of the equipment gain was monitored by attaching a small Cs^{137} source to the NaI(Tl) crystal and frequently observing the spectrum of this source with a 256-channel pulse-height analyzer.

All the housing, with the exception of the end containing the collimator, has been checked with this method, and no evidence of unexpected voids has been found. Completion of the check must await the mounting of the housing on the positioner, which is in progress.

Concurrently with the assembly of the mechanical components of the model IV spectrometer, a number of theoretical and experimental investigations directed toward the selection of a suitable "total-absorption" crystal to be used as the gamma-ray detector have been continued and are detailed elsewhere in this report (Secs 8.3, 8.4, and 8.5).

[1] G. T. Chapman and T. A. Love, *Neutron Phys. Ann. Prog. Rep. Sept. 1, 1958*, ORNL-2609, p 133.

8.2. NONPROPORTIONALITY OF RESPONSE OF AN NaI(Tl) SCINTILLATION CRYSTAL TO GAMMA RAYS

R. W. Peelle T. A. Love

It is commonly observed that in the energy region above a few hundred kilovolts the integrated (charge) pulse from a photomultiplier tube is linearly related to the gamma-ray energy absorbed in an optically attached NaI(Tl) scintillator, or at least that within the precision of measurement possible, nonlinearity is not apparent. On the other hand, linearity through the low-energy region has not been well demonstrated, nor has exact proportionality in any energy region. Some authors have reported that the response to x rays and gamma rays is proportional,[1] while others have found a fairly linear response but a negative extrapolated intercept of about 15 to 30 kev at zero pulse height.[2] In all cases the results have depended heavily upon the behavior of the pulse-analysis equipment used, and usually errors have not been quoted.

The existence of these uncertainties is natural, because linearity measurements are quite difficult to perform with precision over a large dynamic range, and statements concerning proportionality depend upon the identification of the

[1] C. J. Taylor *et al.*, *Phys. Rev.* **84**, 1034 (1951); W. E. Mott and R. B. Sutton, *Handbuch der Physik*, ed. by S. Flügge, vol 45, p 86–173, see esp 99–102, Springer, Berlin, 1958.

[2] D. Engelkemeir, *Rev. Sci. Instr.* **27**, 589 (1956); see also Mott and Sutton, *op. cit.*

pulse height which corresponds to "zero" absorbed energy in the crystal. Both the "zero" and the linearity measurements depend upon results obtained by using precisely known pulses from an artificial source, but the experimenter has difficulty in showing that the analysis equipment reacts to these pulses in the same way that it does to the "natural" pulses from the NaI(Tl) phototube combination.

In an attempt to investigate the nonproportionality of one NaI(Tl) crystal, an experiment was performed which consisted in the measurement of "sum peaks" corresponding to the simultaneous detection of cascade gamma rays by a 3-in.-dia by 3-in. crystal.[3] Yttrium-88 and bismuth-207 sources were positioned very close to the crystal, and the apparent energy corresponding to each sum peak was compared with the known sum of the energies of the individual members of the cascade. This method allows a study of proportionality independent of the "zero" adjustment of the pulse-height analyzer and not sensitively dependent upon the linearity of the analysis system if a calibration energy close to the sum energy of the cascade is available. The calibration energy used in this experiment was the 1596 ± 2 kev transition in the decay of La^{140} (ref 4). (This work was carried out along with the study of the Y^{88} gamma-ray energies described in Sec 11.1; in fact, analysis of the data required the use of transition energies measured for Y^{88}.)

When the weak Y^{88} or Bi^{207} sources were placed adjacent to the crystal and on its axis, both gamma rays in a reasonable share of the cascades simultaneously lost all their energy in the crystal, yielding a sum photopeak which had an apparent energy (E_a). This apparent energy was determined by the usual sort of calibration, using gamma-ray photopeaks arising from total absorption in the crystal of the energy from individual photons. If the light production in NaI is proportional to the energy absorbed, and if the photomultiplier yields pulses proportional to the amount of light produced, then the apparent energy of the sum peak should be, within error, the sum of the energies of the two gamma rays which constitute the cascade. If not, then the excess is presumably a function of the individual energy components of the sum and perhaps of properties of the scintillation crystal used. (If the response is perfectly linear throughout the energy region which includes the possible components of the cascades, then the excess is independent of the energies of the components.) If the light production phenomena associated with each gamma ray in the absorbed cascade can be considered independent, then in a usual operation the observed excess represents the nonproportionality of the particular crystal being used.

The measured apparent excess energy (actually corresponds to excess light output) is defined as follows:

$$D(E_1,E_2) = E_a - E_1 - E_2 \ ,$$

with an error $\sigma(D)$, where

D = nonproportionality excess energy (kev),

$E_a \pm \sigma(E_a)$ = apparent sum energy determined by a calibration using single gamma rays, and its estimated standard error,

E_1,E_2 = known energies of the two cascade gamma rays simultaneously detected to produce each sum pulse.

Table 8.2.1 shows all the data obtained in this experiment, and Fig. 8.2.1 illustrates the data obtained for the Bi^{107} cascade. The results strongly indicate a lack of proportionality of response in the cases studied. If the response is assumed to be perfectly linear in the region of calibration (energies above 0.5 Mev), the observed excess is just equal to the negative of the energy-axis intercept of the linearly extrapolated curve of pulse-height vs energy which would have been observed by using a pulse-height analyzer having output strictly proportional

[3] The crystal was procured from the Harshaw Chemical Co. in a standard mounting.

[4] G. Scharff-Goldhaber, *Phys. Rev.* 59, 937A (1941); N. H. Lazar, G. Eichler, and G. D. O'Kelley, *Phys. Rev.* 101, 727 (1956).

to the pulse output of the photomultiplier. The 30 ± 6 kev excess is in qualitative agreement with the results of the other authors who have reported a nonproportional response.[2]

It is recognized that the results presented here are sufficiently incomplete that they may be considered merely suggestive, but the method employed avoids pitfalls present in other methods. In fact, it should probably be used to measure values of the apparent "excess energy" for a range of gamma-ray energies and for scintillators with a variety of properties.

Table 8.2.1. Summary of Measurements on Nonproportionality Excess of a 3-in.-dia by 3-in. NaI(Tl) Crystal

Emitter of Cascade	Energies of Cascade Gamma Rays*		E_a, Apparent Sum Energy (kev)	Nearest Calibration Energy (kev)	D, Nonproportionality Excess (kev)
	E_1 (kev)	E_2 (kev)			
Y^{88}	1840	899	2765.6 ± 5.5	2754 (Na^{24})	26.8 ± 6.2
Y^{88}	1840	899	2762.5 ± 3.7	2754 (Na^{24})	23.7 ± 4.2
Bi^{207}	1063.7	569.6	1677.0 ± 6.0	1596 (La^{140})	43.7 ± 6.0
					$\bar{D}$ = 30 ± 6**

*See sec 11.1.

**If D is assumed to be independent of E_1 and E_2 (light output truly linear with energy in the range of measurements), a weighted average of the three values obtained for this crystal is 30 ± 3 kev. A chi-square test indicates a probability of 2% that the three results are consistent. The quoted error of 6 kev is based on the scatter between the values. However, there is little reason to assume *precise* linearity of light output over this range of energies, since D is presumably a function of E_1 and E_2.

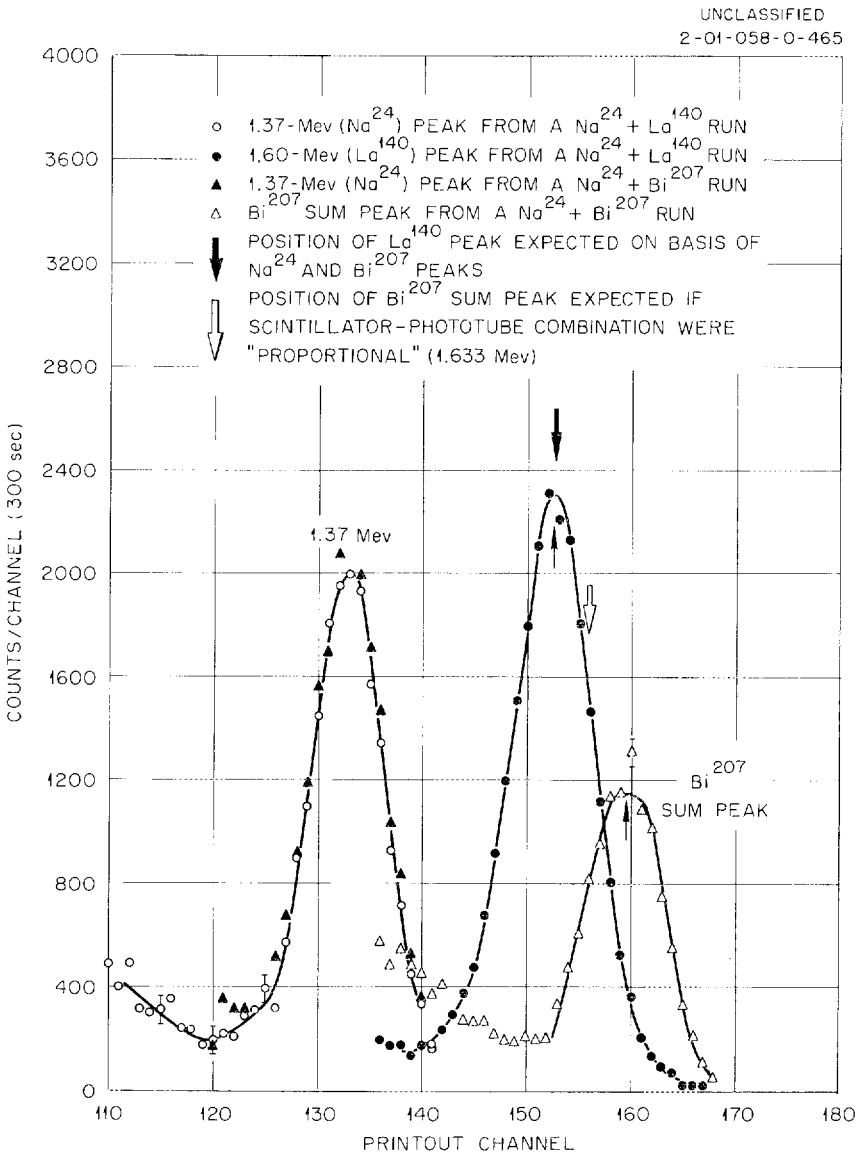

Fig. 8.2.1. Nonproportionality of Response of a 3-in.-dia by 3-in. NaI(Tl) Crystal for the Gamma-Ray Cascade in the Decay of Bi^{207}. The circled points were obtained using a combined source of La^{140} and Na^{24}, the others using combined sources of Bi^{207} and Na^{24}. Pulse-height distributions for interfering gamma rays are subtracted. The agreement between the two runs for the Na^{24} 1.368-Mev line shows that no significant drift occurred. Vertical arrows indicate that the peak from the 1.6-Mev gamma rays of La^{140} falls in the expected position. The sum peak for the Bi^{207} cascade falls almost four channels from the position it would have had if the response of the crystal-phototube combination had been proportional.

8.3. MONTE CARLO CODE FOR CALCULATIONS OF RESPONSE FUNCTIONS OF GAMMA-RAY SCINTILLATION DETECTORS

C. D. Zerby H. S. Moran

An important aspect of gamma-ray scintillation counter investigations is the interpretation of the response functions of the detector to obtain the original gamma-ray spectrum. In principle, if the response functions for a series of monoenergetic sources are known, then the response function resulting from a complex incident spectrum can be unfolded and the structure of that spectrum determined. For this reason, and to aid in determining the best detector geometry, a code using the Monte Carlo method to calculate the response functions of NaI and xylene scintillation detectors has been written for the IBM-704.

In order to encompass a maximum of variations in shape and dimensions, the code was written so that it could be used to calculate the response functions of the detector shown in Fig. 8.3.1. The dimensions of the detector are designated by letters which correspond to certain input numbers in the code. Since any of these dimensions may be set equal to zero, the code can be used for a right cylindrical detector by merely setting F, E, and D equal to zero. There is no restriction on the maximum value of any dimension.

Figure 8.3.2 shows the three alternative source types permitted in the calculation. The dimensions H, I, and J are arbitrary, and the source is restricted to a monoenergetic source of arbitrarily chosen energy in the range 0.005 to 10.0 Mev.

The calculation as it is presently coded does not take into account the losses from the detector resulting from secondary bremsstrahlung and annihilation radiation, although a later version now being coded includes these effects. The treatment of the primary incident radiation is as complete as possible, taking account of Compton scattering, pair production, and the photoelectric effect. The last two effects are treated as total absorption processes.

The particular Monte Carlo method used is designed for minimum statistical error in the so-called "Compton tail" of the spectrum. It employs a method of statistical estimation which, in essence, never allows the photon to become absorbed or to escape from the detector until its energy is degraded below 0.005 Mev. Because the photon is never lost, its statistical weight is adjusted at each collision point to account for the probability of surviving the collision and

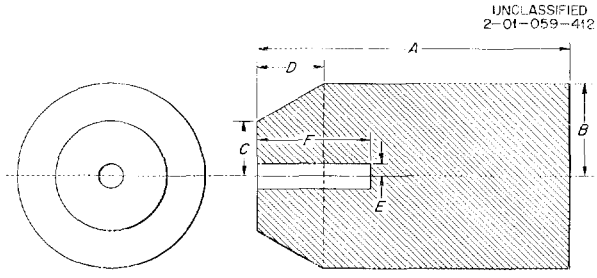

Fig. 8.3.1. Assumed Counter Geometry for Calculations of Scintillation Counter Gamma-Ray Response Functions.

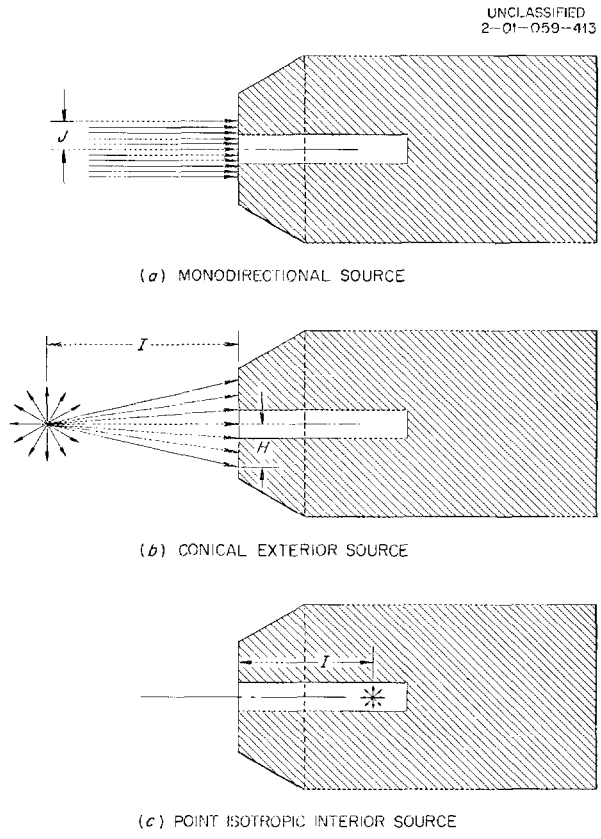

Fig. 8.3.2. Assumed Source-Counter Geometries for Calculations of Scintillation Counter Gamma-Ray Response Functions.

the probability that it will not escape during the flight following the collision.

The results obtained from the calculation include the intrinsic efficiency, the photofraction, and the shape of the "Compton tail" response function of an ideal detector-instrument combination. This means that no account has been taken of the so-called "broadening" of the spectrum during the Monte Carlo portion of the calculation. The broadened spectrum which should correspond to the actual response observed during an experiment is obtained by integrating the ideal response function $G(E)$ with a Gaussian weighting factor to obtain the broadened response function $F(E)$:

$$F(E) = \int_0^{E_0} G(E') \frac{1}{\sqrt{4\pi\sigma^2}} \exp - \frac{(E - E')^2}{2\sigma^2} dE' , \quad (1)$$

where E_0 is the source energy, $\sigma = A\sqrt{E'} + B$, and A and B are arbitrary constants. The results of the broadened function, as well as the ideal function, are obtained in histogram form.

Photofractions obtained from calculations with this code for the case of a right cylindrical NaI crystal are compared with published results for two calculations and one experiment in Table 8.3.1. No comparison of the intrinsic efficiency is given, since it is calculated analytically with the present code and is therefore as accurate as the existing cross sections will allow. As is usually the case, the calculations overestimate the photofraction. This is due, in part, to neglect of secondary radiation.

Calculations of response functions for NaI crystals of various geometries have been made in support of the program of investigation of total absorption spectrometers being pursued at the BSF. Results are published in Secs 8.4 and 8.5.

Table 8.3.1. Comparison of Experimental and Calculated Photofractions for a 4-in.-dia by 4-in.-long Cylindrical NaI Crystal with Monoenergetic Point Isotropic Source 30 in. from End of Crystal[a]

Author(s)	Photofraction	
	1.33-Mev Source	0.661-Mev Source
Kreger[b] (exp)	0.54	0.725
Miller *et al.*[c] (calc)	0.599	0.777
Berger and Doggett[d] (calc)	0.58	0.74
Present calculation	0.582	0.784

[a] That is, conical exterior source geometry; 0.625-in. beam radius at crystal face.

[b] W. E. Kreger, *Phys. Rev.* 96, 1554 (1954).

[c] W. F. Miller, J. Reynolds, and W. J. Snow, *Efficiencies and Photofractions for Gamma Radiation on Sodium Iodide (Thallium Activated) Crystals*, ANL-5902 (1958).

[d] M. J. Berger and J. Doggett, *Rev. Sci. Instr.* 27, 269 (1956).

8.4. MONTE CARLO CALCULATIONS OF GAMMA-RAY ENERGY-LOSS SPECTRA IN LARGE NaI(Tl) SCINTILLATORS

R. W. Peelle
C. D. Zerby
G. T. Chapman
H. S. Moran

It has long been recognized that large scintillation crystals (with dimensions approaching a few mean free paths for high-energy gamma rays) might be used as "total-absorption" gamma-ray spectrometers. Such scintillators are expected to have both high detection efficiency and sufficient uniqueness of response[1] that complicated or continuous spectra can be analyzed or unfolded. Thallium-activated sodium iodide, in which 3-Mev photons have a mean free path of about 3 in., is among the more promising of the available crystals.

Up to the present, however, it has not been possible to predict reasonably correct response functions for large crystals, and for various reasons experimenters with such crystals have been unable to produce results which can be employed as standards. The only calculation of pulse-height spectra for collimated beams of gamma rays that has been published[2] apparently considers only gamma rays incident on a plane face of the crystal. In order to provide more information on this subject, the Monte Carlo code recently written by Zerby and Moran (Sec 8.3) has been employed to compute the behavior of the expected pulse-height distributions from right cylindrical NaI(Tl) scintillators when irradiated with monoenergetic photons collimated along the crystal axis. The effect of wells (a re-entrant section of the crystal surface into which the gamma rays are directed) of various depths as well as the effects of variations in crystal size were investigated for several energies. Since the code does not take into account possible escape from the crystal of fast electrons, bremsstrahlung, or pair-annihilation quanta, results are not shown for photon energies greater than 2 Mev.

It was intended to study separately the effects of well depth, crystal length, and crystal diameter; so cases were studied in which only one of these parameters was varied, with the other dimensions chosen either to minimize escape of scattered radiation or to imitate the largest crystals presently used, although no parameters of the right cylindrical crystals studied were restricted to the dimensions currently available. For instance, most cases studied employed a well about 4 in. deep, probably deeper than is feasible for a practical crystal.

The figures discussed below display examples of spectra resulting from absorption of less than the full gamma-ray energy. Experimental results, of course, would show a photopeak centered on the incident photon energy. All cases were calculated for a 1-cm-dia pencil beam of gamma rays entering the crystal along its axis. The plots show the fraction of incident gamma rays per Mev energy interval which leave the indicated amount of energy within the crystal before escaping. The plotted errors are standard deviations estimated by means of the Monte Carlo code, and all results shown are proportional to the total efficiency of the crystal being studied. If P/T is the fraction of all interactions which are predicted to result in the absorption of the whole gamma-ray energy, $\epsilon = 1 - e^{-\mu t}$ the crystal intrinsic efficiency, and $T_i(E)$ the plotted tail spectrum function, then

$$\sum_i T_i(E)\Delta E_i = 1 - \frac{P}{T}\epsilon \ .$$

Thus when results from crystals of various thicknesses are compared, the tabulated efficiency becomes important. Table 8.4.1 shows the calculated integral parameters for all cases shown in the figures.

In one of the cases calculated the effect of piercing the surface of a crystal with a relatively shallow well was studied. Such wells, into which the incident gamma rays are collimated, are intended to minimize the escape from the crystals of photons Compton-scattered in the backward direction, and, more importantly, to increase the detection efficiency for annihilation radiation from high-energy gamma rays. The present limitations of the Monte Carlo code, as noted, permit only

[1] A scintillation spectrometer would have uniqueness of response if the pulse-height spectrum corresponding to a monoenergetic gamma-ray source is grouped in the neighborhood of a single pulse height.

[2] M. J. Berger and J. Doggett, *J. Research Natl. Bur. Standards* 56,355 (1956).

Table 8.4.1. Parameters for Monte Carlo Cases Plotted in Figs. 8.4.1–8.4.3

Case No.	Source Energy (Mev)	Crystal Parameters				Efficiency,** ϵ	Peak-to-Total Ratio
		Diameter (cm)	Over-All Length (cm)	Well Depth (cm)	Penetration Length* (cm)		
			Plotted in Fig. 8.4.1				
1	0.5	24	25		25	0.9997	0.958 ± 0.002
8	0.5	24	35	10	25	0.9997	0.9975 ± 0.0004
2	1.0	24	25		25	0.9949	0.921 ± 0.003
5	1.0	24	26.5	1.5	25	0.9949	0.950 ± 0.002
9	1.0	24	35	10	25	0.9949	0.964 ± 0.002
3	2.0	24	25		25	0.9774	0.861 ± 0.004
10	2.0	24	35	10	25	0.9774	0.893 ± 0.003
			Plotted in Fig. 8.4.2				
22	2.0	24	25	10	15	0.8970	0.807 ± 0.005
10	2.0	24	35	10	25	0.9774	0.861 ± 0.004
18	2.0	24	45	10	35	0.9950	0.922 ± 0.003
			Plotted in Fig. 8.4.3				
25	1.0	12	45	10	35	0.9994	0.847 ± 0.003
17	1.0	24	45	10	35	0.9994	0.947 ± 0.001
29	1.0	30	45	10	35	0.9994	0.988 ± 0.001

*The penetration length of a crystal is taken to be the length measured along the path of the gamma-ray beam.
**Interactions per photon.

calculation of the effect of the well on the backscattering. First-collision hand calculations of losses due to escape of annihilation radiation from a crystal without a well, however, indicate that at 2 Mev this contribution would have an area of 0.012 escape per incident photon, about 40% of that for Compton escape. At higher energies the pair effect becomes much more important, since about 7% of the incident 6-Mev gamma rays result in the escape of the 0.51-Mev annihilation photons.

Figure 8.4.1 demonstrates the effects due to the inclusion of 1.5-cm-dia wells of various depths in crystals uniformly 24 cm in diameter, but with lengths chosen so that the penetration length, the distance from the bottom of the well to the end of the crystal, was a constant. This choice makes cases for various crystals comparable at equal incident energies. In the figure the solid-line histograms show the behavior for gamma rays with energies of 0.5, 1.0, and 2.0 Mev irradiating a 25-cm-long crystal without a well. The dashed-line histograms show the behavior for the same energies collimated into a 10-cm-deep well in a crystal 35 cm long, while the crosses plotted with the 1-Mev data are for a well 1.5 cm deep in a crystal 26.5 cm long. Clearly, the well has a marked effect for the part of the spectrum about $\frac{1}{4}$ Mev below the full energy, and no discernible effect at lower energies. This is to be expected, since only the improvement in absorption of Compton-scattered radiation is considered. Simple hand calculations of this effect, considering only one scattering, predict contributions within

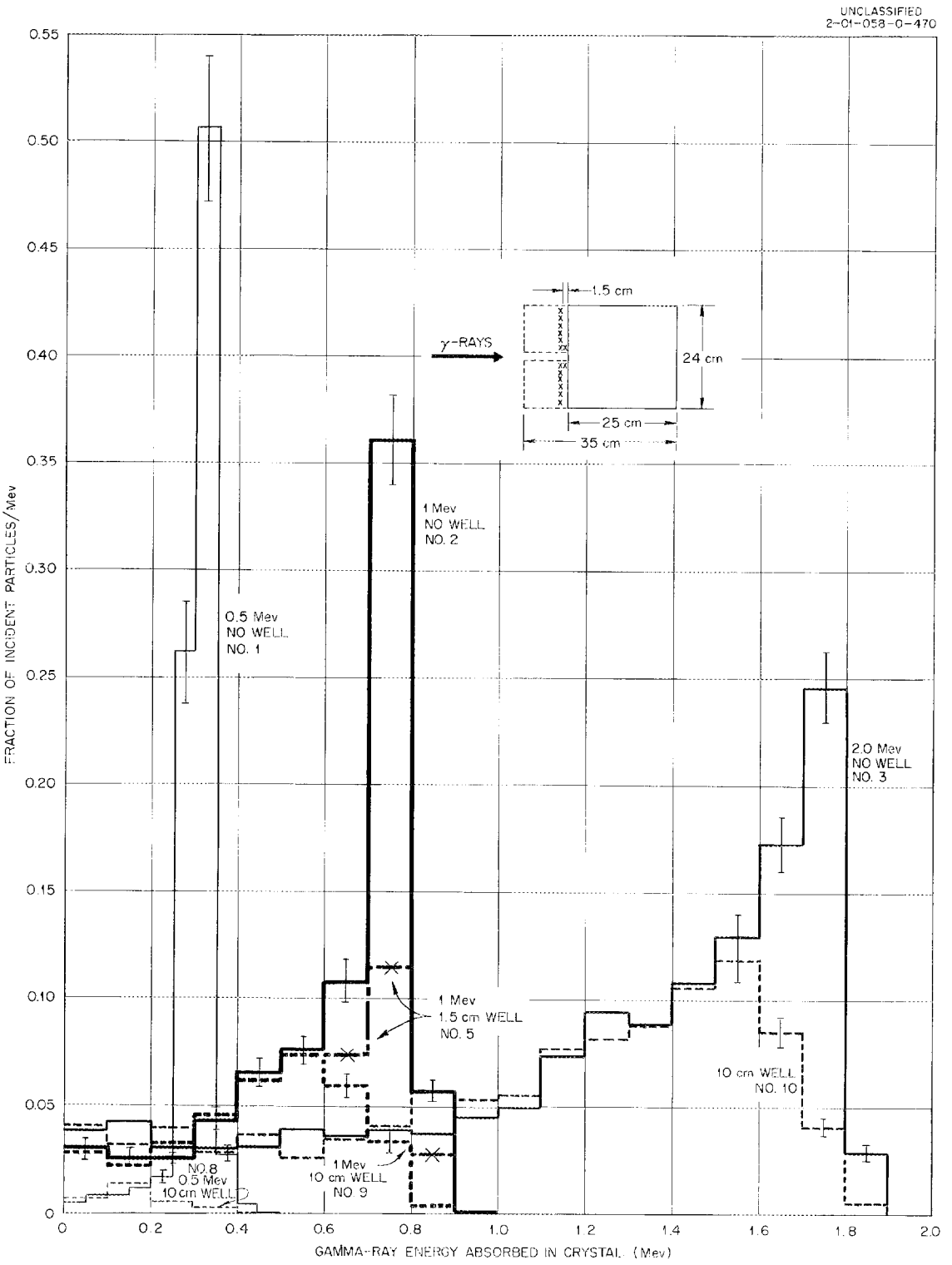

Fig. 8.4.1. Absorption of 0.5-, 1.0-, and 2.0-Mev Gamma Rays in a 24-cm-dia by 25-cm-long NaI(Tl) Crystal: Effect of Well on Predicted Tail Spectra.

50 to 70% of those shown. It may be noted that the shallow 1.5-cm-deep well effectively eliminates most of the backscatter escape at 1 Mev. At this energy no observable difference was noted between the 5- and 10-cm-deep wells.

Figure 8.4.2 shows the predicted effect of crystal length on the "Compton tail" spectra for 2-Mev gamma rays. The figure compares results for 24-cm-dia crystals 25, 35, and 45 cm long, each with a 10-cm-deep well. It may be observed that for absorbed energies above 1.2 Mev the crystal length makes no difference, suggesting that the losses at energies higher than 1.2 Mev are taking place through the side surface of the crystal. At low absorbed energies a marked effect of length is calculated, in agreement with the data shown by circles, which were obtained by an adaption of moments-method results[3] for slab penetration by plane monodirectional gamma rays.[4] The low-energy results of Fig. 8.4.2 are typical of the other cases studied both with respect to the degree of agreement with moments-method estimates and in the implication that the lowest-energy regions of the tail spectrum depend on penetration through the crystal and the escape of scattered photons from the end of the crystal.

Figure 8.4.3 demonstrates the effect of crystal diameter upon the predicted tail spectra for 2-Mev gamma rays. All crystals were 45 cm long with a 10-cm-deep well, so that both escape through the entire length of the crystal and backscatter escape are unlikely. Again, in confirmation of the data in Fig. 8.4.2, the lowest-energy points are independent of crystal diameter. The data indicate that escape of Compton-scattered radiation through the side surface of the crystal produces a peak in the tail of the spectrum at almost 0.5 Mev below the incident gamma-ray energy, as would be predicted on the basis of a single-interaction calculation. This result was also obtained in calculations considering 1- and

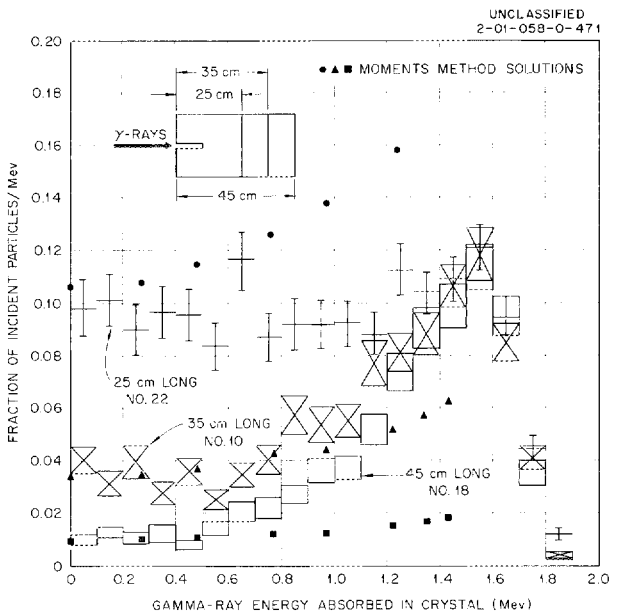

Fig. 8.4.2. Absorption of 2-Mev Gamma Rays in 24-cm-dia NaI(Tl) Crystals with 10-cm-deep Wells: Effect of Crystal Length on Predicted Tail Spectra.

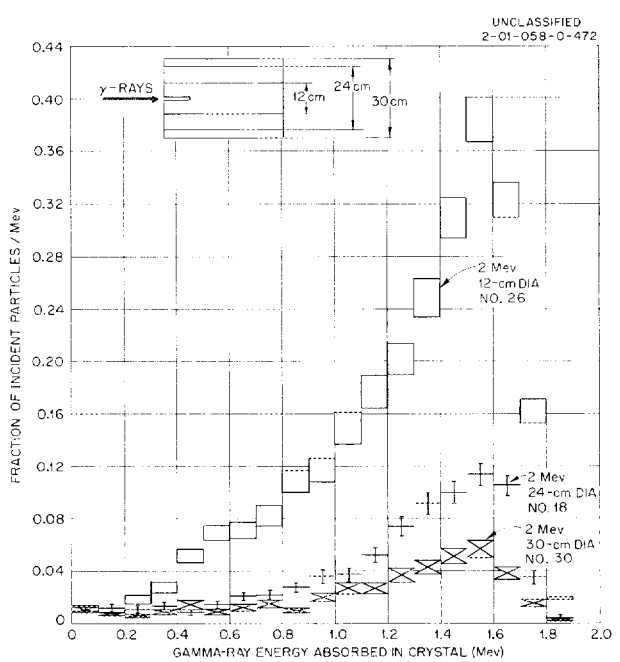

Fig. 8.4.3. Absorption of 2-Mev Gamma Rays in 45-cm-long NaI(Tl) Crystals with 10-cm-deep Wells: Effect of Crystal Diameter on Predicted Tail Spectra.

[3] H. Goldstein and J. E. Wilkins, Jr., *Calculations of the Penetration of Gamma Rays*, NYO-3075 (1954).

[4] The moments-method results of Fig. 8.4.2 were obtained by using the differential energy spectrum results of Goldstein and Wilkins for tin, which has very nearly the same cross section and ratio of scattering to absorption as does NaI. The points in the figure were obtained by employing the gross assumption that the current at the back boundary of the crystal is equal to the flux in the semiinfinite medium of Goldstein and Wilkins. This assumption is least presumptuous for the escape of photons with energies very close to that of the source. Such escapes correspond to the lowest absorbed energies in the tail spectra of Fig. 8.4.2. At higher absorbed energies the agreement is destroyed by the lack of validity of the assumptions.

4-Mev incident gamma rays. The effect of annihilation radiation produced by higher-energy gamma rays, not considered in these results, would add a sharper component to this region of the tail spectrum.

From the work reviewed herein, three conclusions concerning escape of Compton-scattered radiation from a scintillation crystal may be drawn: (1) Inclusion of a well in the crystal at the point of entry of a collimated beam of gamma rays will effectively eliminate the important peak in the tail spectrum due to backscatter escape. (2) For sufficiently large crystals, the magnitude of the low-energy end of the Compton tail spectrum can be estimated by using penetration-study results for slab geometry, since the magnitude of the tail in this region depends almost entirely on crystal thickness along the direction of the gamma-ray beam. (3) For sufficiently high source energies, the intensity of that part of the tail spectrum about 0.5 Mev below the photopeak is dependent on the diameter of the crystal.

8.5. COMPARISON OF EXPERIMENTAL GAMMA-RAY RESPONSES OF AN 8-in.-dia NaI(Tl) CRYSTAL WITH CALCULATED RESPONSES

G. T. Chapman T. A. Love R. W. Peelle

The advantages inherent in the use of a very large sodium iodide crystal as a scintillation detector in gamma-ray spectroscopy have encouraged continuation of the program of investigation of "big" crystals previously reported.[1] In brief, it is expected that the large crystals (~9-in. dia) will in effect be totally absorbing, and thus minimize the familiar low-energy tail caused by the escape of scattered gamma rays from smaller crystals. Previous work at the BSF has utilized a $9\frac{3}{4}$-in.-dia NaI(Tl) crystal which was essentially a right circular cylinder capped by a truncated right circular cone. The shape was dictated by the geometry of the ingot obtained in crystal growth. However, continued experiment with this crystal has led to the belief that such a geometry is detrimental to the gamma-ray response.

Recently one of the suppliers[2] of very large NaI(Tl) crystals was able to produce a relatively long, right-circular cylindrical crystal by optically coupling two smaller crystals together. The smaller crystals were each 8 in. in diameter and 4 in. long, producing, when coupled, a right-circular cylindrical crystal 8 in. in diameter and 8 in. long. The composite crystal is conventionally packaged with the customary aluminum oxide reflector, with an approximately $\frac{1}{2}$-in.-thick glass window at one end for photomultiplier placement. This crystal was obtained on a loan basis for tests at the BSF.

When tested with known-energy gamma rays, with an array of three 3-in.-dia photomultiplier tubes used to observe the light pulses in the crystal, the composite crystal responded as one uniform crystal. For gamma rays ranging up through the 2.76-Mev photon from the decay of Na^{24} there was no evidence of the double peaks which were characteristic of the conically ended crystal.[1] The resolution at the Cs^{137} gamma-ray energy of 0.662 Mev was 11.8%, and the ratio of the area under the peak to the total area under the distribution was about 0.75. Since the data were taken without a well in the crystal, there was a contribution to the tail of the distribution from the loss of gamma rays scattered back out of the crystal. This was demonstrated by collimating the Cs^{137} gamma ray through a $\frac{1}{2}$-in.-dia hole along the axis of an additional 4-in.-dia by 2-in.-thick crystal mounted on the end of the large crystal and observing the anticoincidence spectrum from the large crystal. This increased the peak-to-total ratio to 0.83.

As reported in Secs 8.3 and 8.4, a Monte Carlo code has been developed for calculations of the response functions of scintillation detectors to monoenergetic gamma rays. This code was used to calculate the response of an 8-in.-dia by 8-in.-long NaI crystal for five different gamma-ray

[1] G. T. Chapman and T. A. Love, *Neutron Phys. Ann. Prog. Rep. Sept. 1, 1958*, ORNL-2609, p 133.

[2] Harshaw Chemical Company, Cleveland, Ohio.

energies, and the results are compared with the experimental data for the composite crystal in Table 8.5.1. The conditions for the calculation, including crystal dimensions and collimation of gamma rays along the crystal axis, resembled the experimental conditions as closely as possible. The experimental data for the 0.662-Mev gamma ray from Cs^{137} are compared with calculated results in Fig. 8.5.1. Since the calculation gave only the peak-to-total ratio and the distribution in the tail, a Gaussian distribution with the same standard deviation as the experimental data was assumed for the total-absorption peak.

Although the experimental data give a smaller peak-to-total ratio (0.83) than the calculation (0.929), the shape of the calculated distribution resembles that of the experimental data. As shown in the figure, the anticoincidence data taken as noted above almost eliminated the escape peak found at ~0.45 Mev in the data from the composite crystal alone. This implies that the addition of a well in the end of the composite crystal would increase the peak-to-total ratio. It is probably impossible, however, to attain the calculated peak-to-total ratio in practice, because of unavoidable scattering effects in the materials surrounding the detector. For example, owing to the finite dimensions of the gamma-ray source and source container, it is estimated that as much as a 3% contribution to the distribution in the tail may be due to scattering within the source.

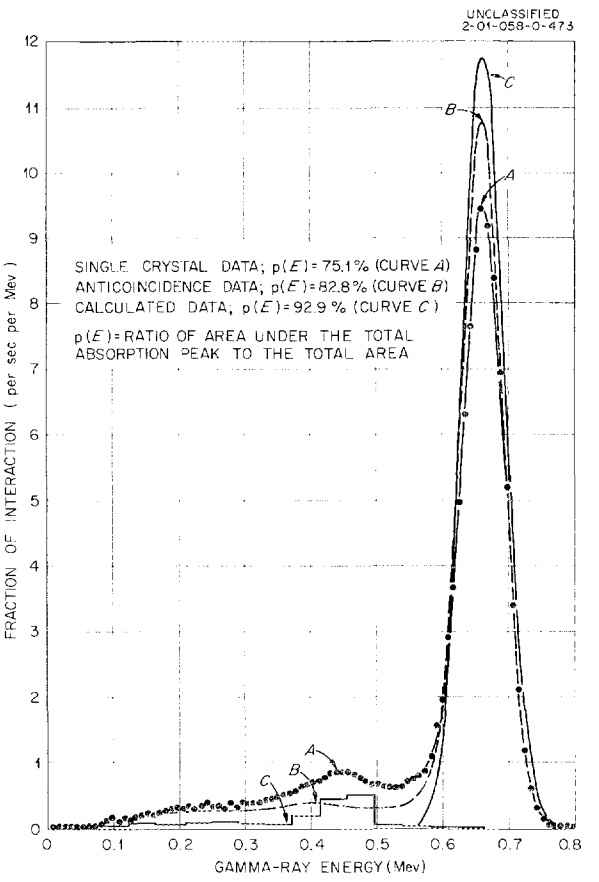

Fig. 8.5.1. Calculated and Experimental Responses of an 8-in.-dia by 8-in.-long NaI(Tl) Crystal to 0.662-Mev Gamma Rays from Cs^{137}.

Table 8.5.1. Comparison of Experimental and Calculated Results for the Response of an 8-in.-dia by 8-in.-long NaI(Tl) Crystal

Photon Energy (Mev)	Measured Resolution (%)	Measured Photofraction*, ** (%)	Calculated Photofraction* (%)
0.662	11.8	83	92.9
0.899	8.8	66	90.0
1.368	8.6	61	84.9
1.840	7.3	60	80.8
2.754	6.3	52	79.2

*Photofraction is defined as the ratio of the area under the total absorption peak to the total area under the pulse-height distribution curve.

**Values of the measured photofractions are reproducible to within 3%.

In addition, there may be as much as a 9% contribution from the effect of the collimator.[3] It is hoped, however, that more careful design of source and collimator will improve the peak-to-total ratios obtainable with large crystals.

[3] R. W. Carlson, D. J. McGoff, and J. L. Sapir, *Gamma-Ray Scattering and Penetration in a Lead Collimator*, KT-377 (1958).

Although the effects of the interface formed by coupling two crystals have not yet been studied to any extent, the over-all response of the composite crystal discussed has been much more satisfactory than that of the conically ended crystals, as is evident in the resolutions shown in Table 8.5.1, and it appears that large, usable, total-absorption crystals may be produced by this method.

8.6. RESPONSE OF END-WINDOW PHOTOMULTIPLIER TUBES AS A FUNCTION OF TEMPERATURE

R. B. Murray J. J. Manning

The effect of temperature on the response of a scintillation counter to incident radiation is of interest both from a practical and a fundamental point of view. As a practical matter, it is sometimes necessary to operate a scintillation counter in surroundings whose temperature is different from room temperature, or whose temperature may change in time. Of fundamental interest is the behavior of scintillation crystals, both activated and unactivated, as a function of temperature, especially in the region below room temperature. Since a photomultiplier tube is an integral part of any scintillation counter assembly, it is of interest to examine temperature-dependent effects in the gain and spectral sensitivity of photomultipliers.

Modern scintillation counting techniques employ end-window photomultipliers to a very large extent, so that studies of temperature-dependent effects may reasonably be focused on end-window tubes. In this type of photomultiplier, the photosensitive cathode is a semitransparent layer, usually of Cs-Sb composition, which is deposited on the interior of a flat glass (or quartz) window located at one end of the cylindrical bulb. This type of construction may be contrasted with early photomultiplier tubes, such as the RCA 1P28, in which the photocathode surface is deposited on a metallic backing located in the interior of the tube.

The effect of temperature on the gain of end-window photomultipliers has been studied near room temperature by several authors, with apparently conflicting results. Several experiments[1–5] have been reported in which the gain was found to decrease with increasing temperature; the results of Seliger and Ziegler,[6] however, indicated an increasing gain with increasing temperature.[7] At much lower temperatures (about −130°C and below) several workers[8] have noted an almost complete loss of sensitivity, although there apparently have been no detailed studies of very-low-temperature behavior.

It is thus of interest to examine in some detail the behavior of photomultiplier tubes at low temperatures, with attention to the influence of the wavelength of incident light. This paper reports a study of the response of various end-window photomultipliers to monochromatic light in the 4000- to 7000-Å interval as a function of temperature from 25 to −196°C.

[1] F. E. Kinard, *Nucleonics* 15(4), 92 (1957).

[2] L. A. Webb, *The Effect of Temperature Upon the Response of a Gamma-Ray Scintillation Spectrometer*, USNRDL-TR-48 (1955).

[3] W. P. Ball, R. Booth, and M. H. MacGregor, *Nuclear Instr.* 1, 71 (1957).

[4] T. R. Herold, W. A. Kropp, and J. S. Stutheit, *Temperature Coefficients of Scintillation Detectors*, DP-47 (1956).

[5] G. Laustriat and A. Coche, *J. phys. radium* 19, 927 (1958).

[6] H. H. Seliger and C. A. Ziegler, *IRE Trans. on Nuclear Sci.* NS-3, 62 (1956).

[7] These results need not be interpreted as necessarily in disagreement, however, as the wavelength of the exciting light in the various experiments was not the same.

[8] See, for example, R. B. Murray, *Nuclear Instr.* 2, 237 (1958); W. J. Van Sciver and L. Bogart, *IRE Trans. on Nuclear Sci.* NS-5, 90 (1958).

Apparatus and Method

The tubes which have been investigated to date were all of nominal 2-in. diameter and were contained at the center of a 4-ft-long glass tube which was embedded in Styrofoam for thermal insulation. The central 9 in. of the glass tube was surrounded by a coaxial jacket, through which was passed nitrogen gas which had been cooled by circulation in a liquid-nitrogen heat exchanger. Helium gas in the glass tube provided a heat exchange medium to cool the photomultiplier tube to the temperature of the glass jacket and ensured a uniform temperature along the body of the tube. By controlling the flow rate of cooling gas, the temperature was continuously variable down to the liquid-nitrogen point. The temperature was measured by a copper-constantan thermocouple bonded to the glass envelope of the photomultiplier. The resistor network for the photomultiplier was located far away from the cold region and was maintained at, or very near, room temperature. The cathode-anode voltage was typically ~800 v.

Monochromatic light was obtained from a Beckman quartz spectrophotometer and irradiated essentially the entire area of the photocathode. The photomultiplier anode current resulting from this illumination was measured with a d-c microammeter on the 0- to 1-μa scale.

The sequence of events in a typical experiment was as follows: At room temperature, for a particular wavelength of incident light, say 4000 Å, a spectrophotometer slit width was chosen which gave an anode current near full scale. This slit width was used for all subsequent low-temperature measurements at 4000 Å. A particular slit width was thus established at room temperature for each wavelength, the slit widths varying considerably over the 4000- to 7000-Å spectral region as a result of the strong wavelength dependence in both the emission spectrum of the spectrophotometer lamp and the sensitivity of the photomultiplier. The photomultiplier was then cooled to a selected temperature, and allowed time to come to equilibrium, and the anode current was measured at each wavelength. This process was repeated at various temperatures down to −195°C.

Results and Discussion

To date, one each of the following tubes has been studied: RCA 6342, RCA 5819, RCA 6655, RCA 6903, Du Mont K-1428 (modified 6292), and a modified RCA 6342. The last two are modifications of standard tubes in which a thin, semitransparent metallic backing was deposited over the semiconducting photocathode surface during manufacture.

The results of two experiments are shown in Figs. 8.6.1 and 8.6.2 for an RCA 5819 and a Du Mont K-1428, respectively. For purposes of clarity in presenting the data, the room-temperature current readings for the various wavelengths have been normalized to unity. The ordinates of Figs. 8.6.1 and 8.6.2 thus represent anode current in arbitrary units; as indicated previously, however, the scale is of the order of 1 μa.

In Fig. 8.6.1 it is seen that the temperature dependence of anode current is quite sensitive to the wavelength of incident light. In particular, in the region immediately below room temperature, the anode current increases with decreasing temperature for wavelengths less than about 5500 Å but decreases for longer wavelengths. In Fig. 8.6.2 increasing current occurs for wavelengths up to 5800 Å. Similar behavior has been observed in each of the photomultipliers studied; in all cases the slope of the curve changes sign in the wavelength region from ~5000 to 5800 Å.

At lower temperatures (~−70°C) the response of the RCA 5819 (Fig. 8.6.1) falls sharply with decreasing temperature for all wavelengths and continues to decrease down to the lowest temperature obtainable in the present experiment, −190 to −195°C. This behavior is characteristic of those photomultipliers studied which have not been modified by the addition of a conducting backing on the photocathode surface. In all cases, the response drops sharply in the region from −70 to −100°C and continues to decrease monotonically. This fall-off clearly does not occur in the Du Mont K-1428 (Fig. 8.6.2), and the behavior of the modified RCA 6342 (not shown) is quite similar to that of the K-1428.

The temperature-dependent effects illustrated in Figs. 8.6.1 and 8.6.2 can be discussed in terms of effects associated with the photocathode. Previous studies[9,10] have shown that the photocathode spectral sensitivity curve is temperature-dependent in such a manner that the long wavelength limi

[9] F. Boeschoten, J. M. W. Milatz, and C. Smit, *Physica* 20, 139 (1954).

[10] N. Schaetti and W. Baumgartner, *Helv. Phys. Acta* 24, 614 (1951).

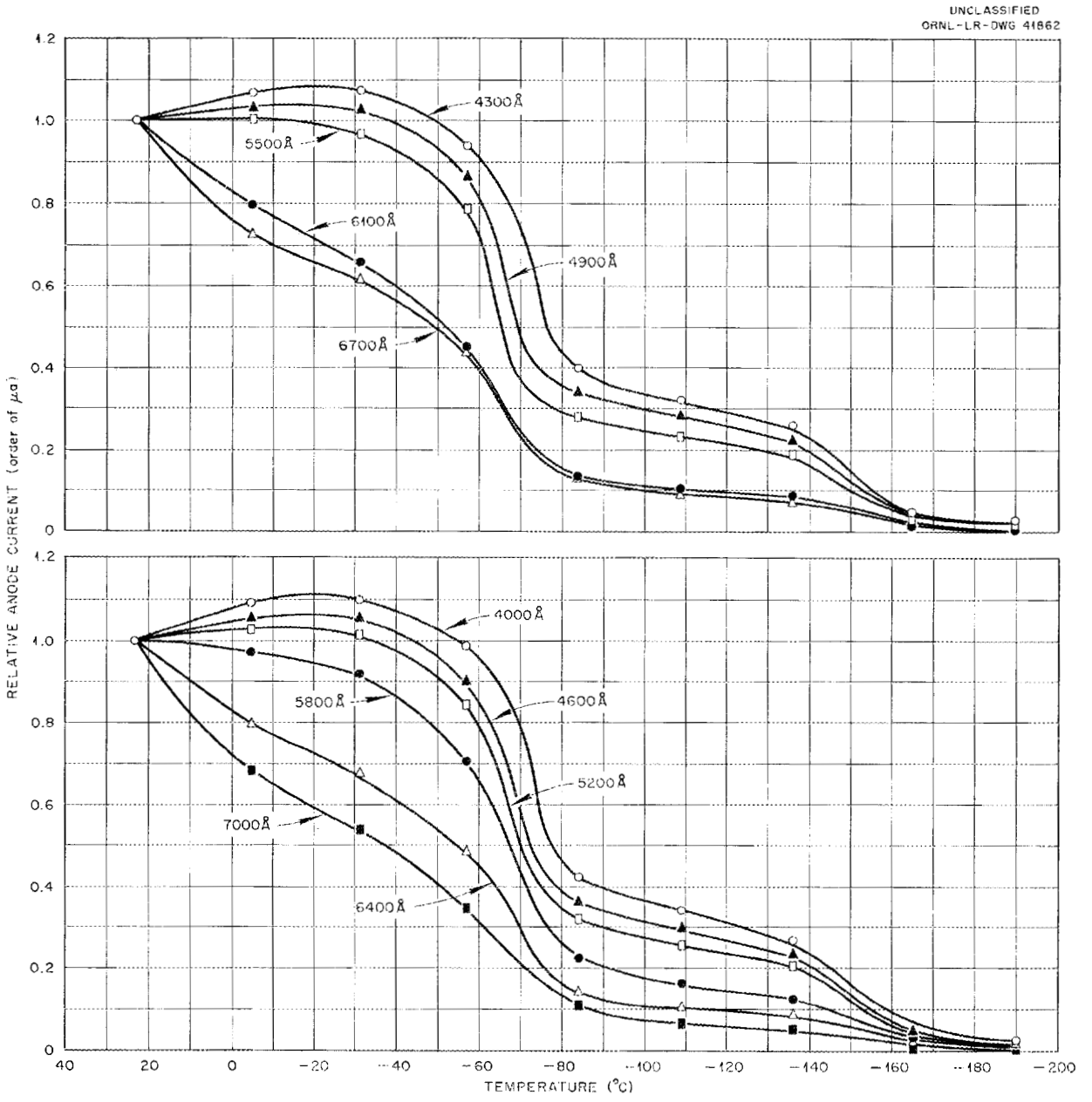

Fig. 8.6.1. Relative Anode Current as a Function of Temperature for Various Wavelengths of Monochromatic Light Incident on an RCA 5819 Photomultiplier Tube.

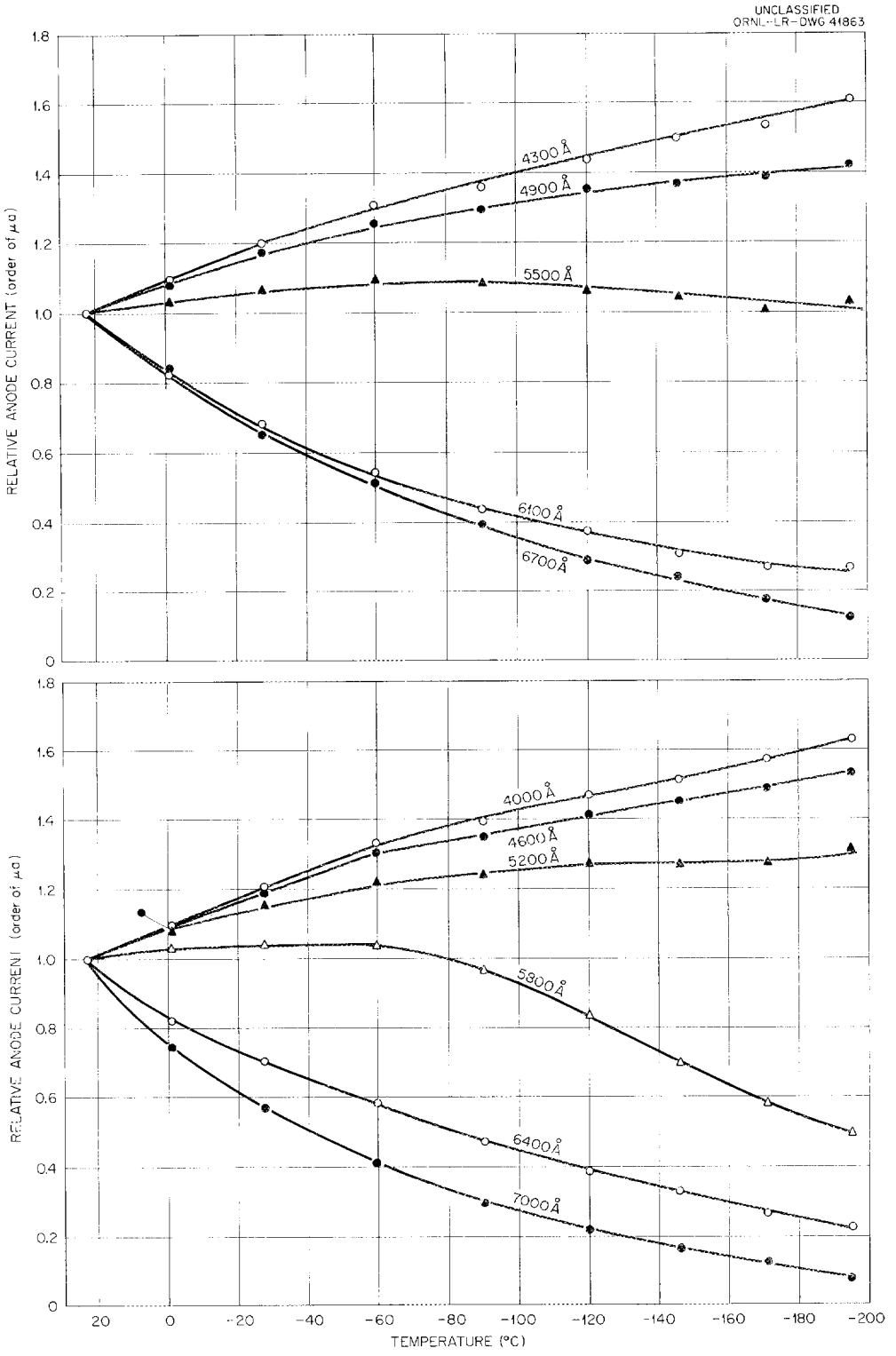

Fig. 8.6.2. Relative Anode Current as a Function of Temperature for Various Wavelengths of Monochromatic Light Incident on a Du Mont K-1428 Photomultiplier Tube. This tube has a conducting backing over the photocathode surface.

shifts toward the blue upon cooling, resulting, of course, in a decrease in sensitivity to monochromatic light in the red region of the spectrum. In particular, Boeschoten and co-workers[9] cooled a 1P-28 (Cs-Sb cathode) from room temperature to the liquid-air point and observed a decrease in sensitivity to red light (6500 Å) by a factor of 8, whereas the sensitivity to blue light (4000 to 4500 Å) increased 40%. The spectral sensitivity remained essentially unchanged in the 5500- to 6000-Å region. These results are quite consistent with those of Fig. 8.6.2. The shift in spectral sensitivity with temperature presumably arises from a temperature dependence of the photoelectric effect and has been discussed briefly by Boeschoten *et al.*[9] and in detail in a recent paper by Meesen.[11]

In addition to a shift in spectral sensitivity, it is known that the electrical resistance of Cs-Sb photocathodes is temperature dependent;[10-12] the resistance increases rapidly with decreasing temperature in a manner which is typical of the behavior of semiconductors. The decrease in anode current, for all wavelengths, at about −70 to −100°C, as in Fig. 8.6.1, is attributed to the rapid rise in cathode resistance with decreasing temperature. As the photocathode becomes more nearly an insulator, the electric field at its surface is distorted with a resultant loss in collection efficiency for electrons at the first dynode. It is clear from Figs. 8.6.1 and 8.6.2 that this effect is eliminated by the deposition of a thin metallic backing on the photocathode.

The effect of a temperature change on the secondary emission process in the dynode string has not been considered in the above discussion. The dynodes are, of course, cooled in the experiments reported here since the entire photomultiplier is surrounded by heat exchange gas and is allowed to achieve thermal equilibrium. In this regard it should be possible to eliminate the electron multiplication in the dynodes by connecting all dynodes together and operating the tube as a diode. It is hoped that this technique can be incorporated in future studies. It may be noted that the results of the present experiment (Fig. 8.6.1) are consistent with those of Schaetti and Baumgartner[10] in which the photocurrent was measured directly, without secondary multiplication.

[11] A. Meesen, *J. phys. radium* 20, 519 (1959).

[12] R. W. Engstrom *et al.*, *IRE Trans. on Nuclear Sci.* NS-5, 120 (1958).

8.7. SCINTILLATION PROPERTIES OF NONACTIVATED LITHIUM IODIDE

R. B. Murray H. G. Hanson[1] J. J. Manning

A study of the luminescence emission spectra of both activated and nonactivated lithium iodide scintillation crystals has been reported previously.[2] This investigation revealed a significant difference in the emission spectrum of a nonactivated lithium iodide crystal compared with that of europium-activated crystals. As part of a continuing program to investigate various aspects of the scintillation process in lithium iodide, further study has been made of some of the scintillation properties of a nonactivated crystal. This investigation, which is described herein, includes a study of the decay times and light intensity as a function of temperature, the relative response to gamma rays and the alpha-triton pair resulting from slow-neutron capture, and an identification of two observed scintillation components with the two bands in the emission spectrum. The crystal used in the present investigation was the same crystal used in the previous study of emission spectra.[2]

Crystal Preparation

The starting material was lithium metal enriched in Li^6 to 96% concentration, which was obtained from the ORNL Stable Isotopes Division. (Enriched Li^6 metal was chosen for convenience, in order to provide a high counting efficiency for neutrons.) The metal was reacted with distilled water, and an excess of hydriodic acid was added. The resulting solution was evaporated to yield

[1] Summer research participant from University of Minnesota, Duluth Branch.

[2] H. G. Hanson, J. J. Manning, and R. B. Murray, *Neutron Phys. Ann. Prog. Rep. Sept. 1, 1958*, ORNL-2609, p 138.

crystals of hydrated lithium iodide. Purification of these crystals was effected by repeated recrystallization and an organic extraction process. The purified crystals were dehydrated by slow heating in a vacuum. The resulting anhydrous lithium iodide was grown as a single crystal ($1\frac{1}{2}$ in. in diameter by 2 in. long) by the Bridgman-Stockbarger method. Crystal growth by this method constitutes a further purification step. The crystal was observed to be clear and colorless. Extreme care was taken throughout the preparation and growth of the crystal to avoid the use of vessels and apparatus normally used in handling europium-activated material. A semiquantitative spectrographic analysis of the crystal used in this study showed the presence of silicon in the concentration range 10^{-2} to 10^{-3}%, and calcium, copper, iron, magnesium, and tin in the concentration range 10^{-3} to 10^{-4}%.

It should be understood that the results presented here are properties of the crystal studied and are not *necessarily* characteristic of perfectly pure lithium iodide. The preparation of a perfectly pure crystal, on the other hand, is essentially impossible. The results given are considered meaningful in that they apply to nonactivated lithium iodide containing commonly found chemical impurities in trace amounts.

Experimental Methods and Results

In one phase of the experiment, a thin slice of crystal (about 2.5 cm in diameter and 3 mm thick) was placed in a low-temperature apparatus, which has been described previously.[3] The crystal temperature was continuously variable from room temperature to the liquid-nitrogen point.

The luminescent intensity as a function of temperature was recorded for alternate excitation of the crystal by slow neutrons and 0.661-Mev gamma rays from Cs^{137}. An RCA 6342 photomultiplier tube was used. Pulse-height spectra from both neutron and gamma-ray excitation were recorded on a 20-channel pulse-height analyzer. A clearly distinguishable slow-neutron peak in the pulse-height spectrum was observed at all temperatures; the full-energy peak in the gamma-ray spectrum was identifiable at −30°C and below.

[3] R. B. Murray, *Nuclear Instr.* 2, 237 (1958), Fig. 6.

The results of this experiment are given in Fig. 8.7.1. Analysis of the data reveals that the ratio of pulse heights (neutrons:gamma rays) is a temperature-independent quantity within an experimental uncertainty of $2\frac{1}{2}$%. The temperature independence of this ratio in nonactivated lithium iodide is distinctly different from the behavior of LiI(Eu), where the corresponding ratio increases by some 15% upon cooling from room temperature to the liquid-nitrogen point (see ref 3, Fig. 5).

In comparing the response of nonactivated lithium iodide to gamma rays and slow neutrons, a useful parameter is the gamma-ray equivalent energy at which the slow-neutron peak occurs. In the case of a well-activated LiI(Eu) crystal, the gamma-ray equivalent energy is typically 4.5 Mev or greater, which may be compared with the Q value of the $Li^6(n,\alpha)H^3$ reaction, 4.78 Mev. In the present experiment, the gamma-ray equivalent energy was determined at the liquid-nitrogen point, using 0.661-, 0.899-, and 1.11-Mev gamma rays as calibration points. An extrapolation of the straight

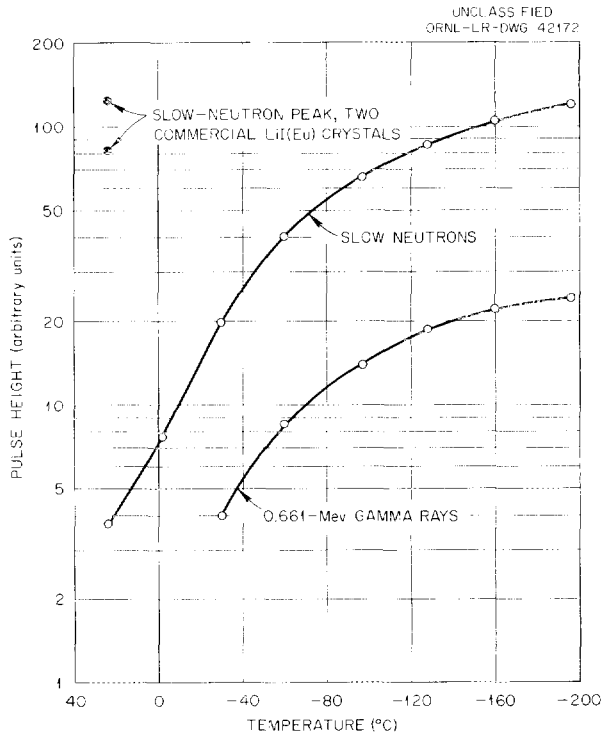

Fig. 8.7.1. Variation in Pulse Height as a Function of Temperature; Slow Neutrons and 0.661-Mev Gamma Rays Incident upon a Nonactivated Li^6I Crystal.

line connecting these points shows that the slow-neutron peak occurs at a gamma-ray equivalent energy of 3.45 Mev. This value should apply equally well at higher temperatures, since the results of Fig. 8.7.1 indicate a constant ratio of neutron-to-gamma-ray pulse heights.

The pulse heights corresponding to the slow-neutron peak in two commercially canned LiI(Eu) crystals at room temperature are also shown in Fig. 8.7.1. It is seen that the light output of the nonactivated crystal at the liquid-nitrogen point is comparable to that of activated crystals at room temperature.

The resolution of the nonactivated crystal may be described by the full width at half maximum of the slow-neutron peak in the pulse-height spectrum. In the present experiment, this quantity varied from about 45% at room temperature to 11% at the liquid-nitrogen point. In the case of LiI(Eu) at room temperature, the corresponding quantity might be 8 to 10% with a typical crystal, 6% with a good crystal.

A second phase of the present experiment was directed toward a study of the decay time of light pulses from nonactivated lithium iodide. For this purpose, the anode of the photomultiplier was connected with coaxial cable to the input of a Tektronix 53/54L preamplifier and type 545 oscilloscope, with a total rise time of 0.014 μsec. Current pulses from the photomultiplier anode were integrated on the cable capacitance; the RC time constant, which was fixed by this capacitance and the input resistance of the preamplifier, was measured as 63 μsec. The resulting voltage pulse was displayed on the oscilloscope screen, photographed, carefully projected onto graph paper, and corrected for the exponential decay corresponding to RC = 63 μsec. The curves so obtained were analyzed in a straightforward way to obtain the time dependence of the light pulses. Both neutron- and gamma-ray-induced pulses were studied, at temperatures from room temperature to $-196°$C.

This analysis showed that the decay law can be represented as the sum of two exponentially decaying functions, with decay times τ_1 and τ_2 of the order of 1 μsec and 4 μsec, respectively. The temperature dependence of τ_1 and τ_2 is shown in Fig. 8.7.2, in which each point is the average from the analysis of three or more pulses resulting from neutron excitation. The error flags are estimates of the uncertainty associated with each point, and were derived on the basis of internal consistency in data analysis and estimated uncertainties in the assignment of decay times to each set of data. The results in Fig. 8.7.2 indicate an increase in τ_1 with decreasing temperature. There is some indication of a decrease in τ_2 at low temperatures, although the uncertainties are such that the data might well describe a temperature-independent function. Data derived from analysis of pulses following gamma-ray excitation are not shown in Fig. 8.7.2, since the results are in quite good agreement with those presented for neutron excitation. Thus there is no observable difference, within the uncertainties of the present experiment, between the decay times associated with neutron and gamma-ray excitations.

It should be pointed out that a decay time longer than τ_2 would probably not be observed in the present experiment. Decay times shorter than τ_1, however, should have been observed.

The data from which the decay times were derived are capable of yielding further information, namely, information on the relative amplitudes of the two scintillation components. The assignment of two exponentially decaying components in the light intensity corresponds to the following form for intensity, I, as a function of time, t:

$$I = A_1 e^{-t/\tau_1} + A_2 e^{-t/\tau_2} \quad ,$$

where A_1 and A_2 are amplitude factors. For comparison with the previously observed luminescence emission spectrum, which corresponds to the time-integrated light intensity, the function of interest is

$$\int_0^\infty I \, dt = A_1\tau_1 + A_2\tau_2 \quad .$$

The term $A_1\tau_1$ now represents the integrated light intensity emitted by component 1; similarly for 2. The decay-time data indicate that the ratio $A_2\tau_2/A_1\tau_1$ decreases from about 1 at room temperature to about $\frac{1}{3}$ at the liquid-nitrogen point. For purposes of correlation, the luminescence emission spectrum of nonactivated lithium iodide is reproduced in Fig. 8.7.3. It is seen that two distinct bands occur in the emission spectrum, and that the relative intensity is temperature dependent. The relative intensities are apparently of the same order at higher temperatures, whereas

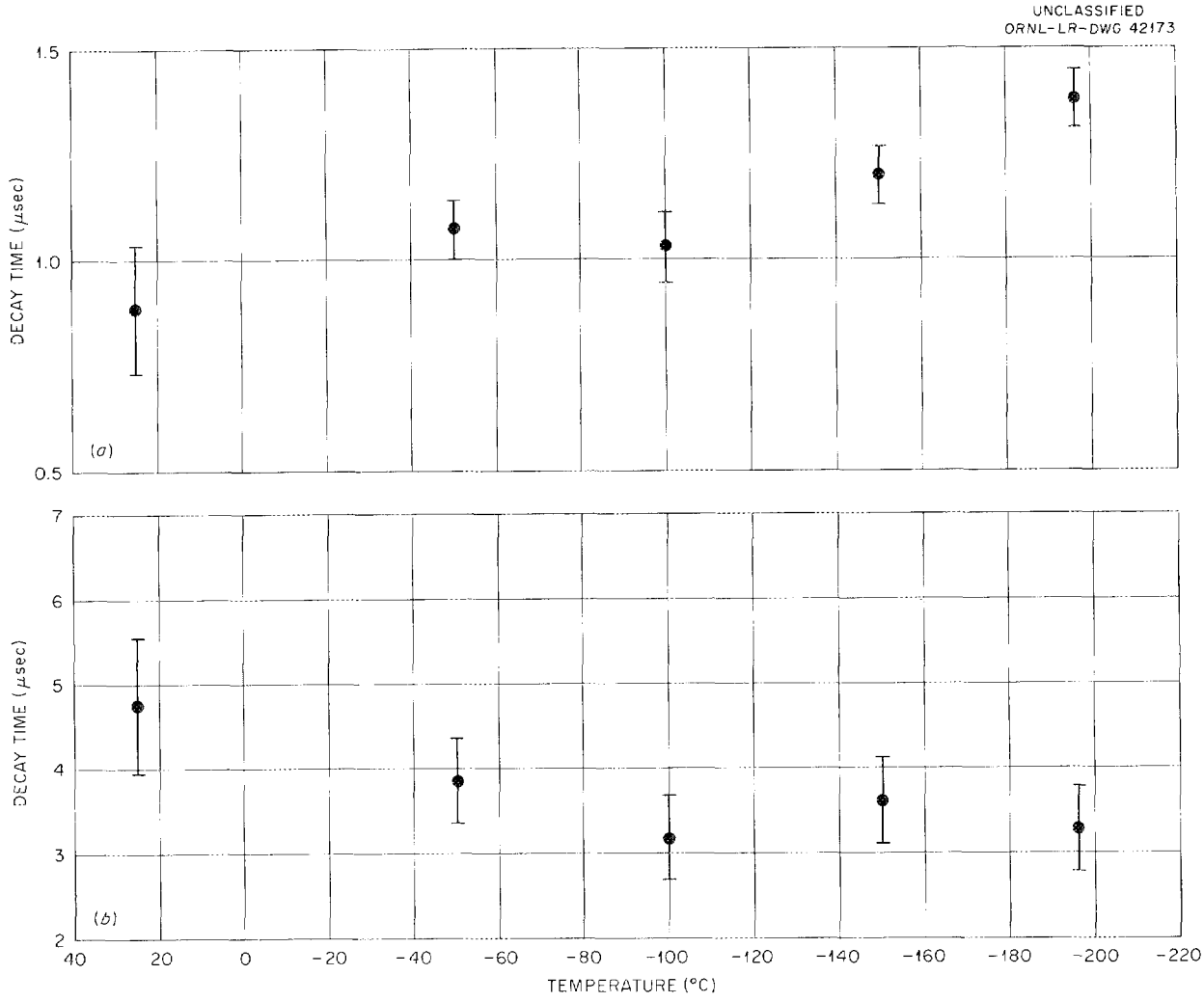

Fig. 8.7.2. Decay Time of Light Pulses as a Function of Temperature; Slow Neutrons Incident Upon a Nonactivited Li^6I Crystal: (*a*) Component τ_1; (*b*) Component τ_2.

the band centered near 4000 Å is considerably weaker than the 3700-Å band at −192°C. The foregoing facts suggest a correlation between the 4000-Å band and component τ_2, and the 3700-Å band and component τ_1.

In order to examine this point further, use was made of optical filters that could selectively absorb light in either the 3700-Å region or the 4000-Å region. The selected filter or filters were placed on the face of the photomultiplier tube, and the crystal was cooled directly to the liquid-nitrogen point. Scintillation pulses were recorded and analyzed as above, using slow-neutron excitation of the crystal. With a Corning glass filter, No. 7-60, the 3700-Å band is passed with about 60% transmission, whereas radiation of 4000 Å and longer is totally absorbed. In this case, analysis of the data revealed only one component whose decay time was 1.4 μsec (τ_1). With Corning filters Nos. 3-75 and 3-74, 4000-Å radiation is partially transmitted while radiation of 3700 Å and shorter is totally absorbed. In this case, the amplitude of the short-decay-time component was strongly attenuated, and the predominant component was that of 3.3-μsec decay time (τ_2). (Because of the inherent bandwidth, it is not possible to eliminate entirely the tail of the 3700-Å band.)

On the basis of the above results, it is concluded that component 1, with a decay time of the order of 1 μsec, is associated with light emitted

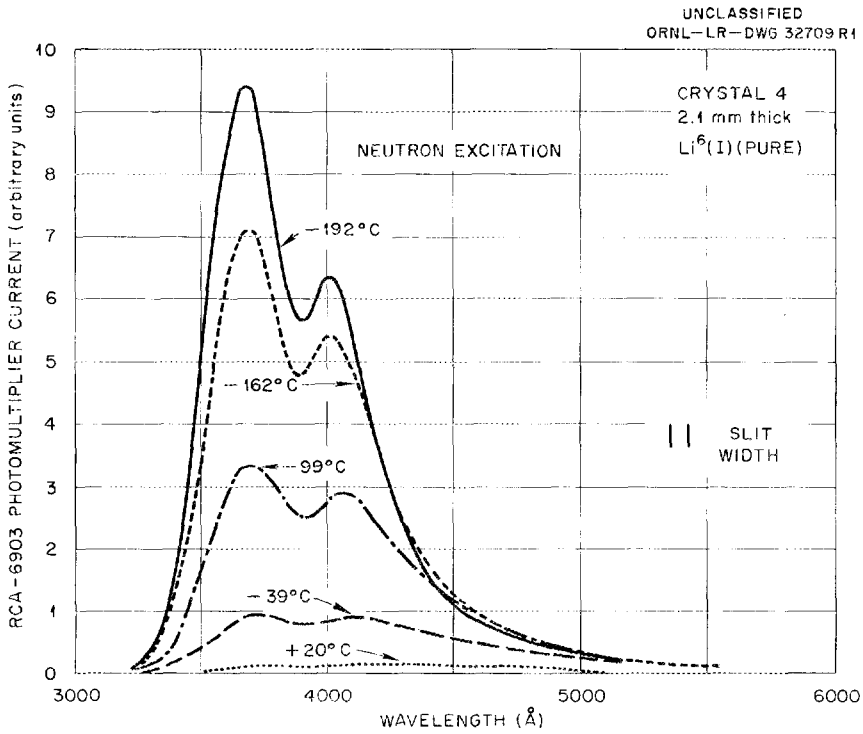

Fig. 8.7.3. Luminescence Spectrum of Nonactivated Li^6I Under Excitation by Slow Neutrons.

in the 3700-Å band, and that component 2, decay time ~4 μsec, is associated with light emitted in the 4000-Å band.

Conclusions

The experimental results discussed above lead to the following conclusions concerning the scintillation characteristics of nonactivated lithium iodide.

1. The luminescence intensity is a strong function of temperature, increasing by a factor of about 30 in going from room temperature to −196°C. At −196°C, the intensity is comparable to that obtained from LiI(Eu) at room temperature.

2. The shape of the intensity vs temperature curve is the same for excitation of the crystal by gamma rays and by the alpha-triton pair from slow-neutron capture. This behavior is different from that observed in LiI(Eu).

3. The gamma-ray equivalent energy of the slow-neutron peak in the pulse-height spectrum is 3.45 Mev.

4. Following excitation of the crystal by a charged particle, the light intensity decays in time as the sum of two exponential functions, with decay times $\tau_1 \cong 1$ μsec and $\tau_2 \cong 4$ μsec. The decay times are slowly varying functions of temperature. No difference is observed between decay times upon excitation of the crystal by gamma rays and by slow neutrons.

5. The 1-μsec component is associated with light emitted in a band centered near 3700 Å. The 4-μsec component is associated with light emitted in a band centered near 4000 Å.

From the practical point of view, nonactivated lithium iodide seems to offer no advantages over LiI(Eu) as a detector for either slow or fast neutrons. The decay time of the nonactivated crystal is no faster than that of LiI(Eu), and the light intensity is distinctly weaker except at very low temperatures. The width of the slow-neutron peak in the pulse-height spectrum is broader than that which can be obtained with a typical LiI(Eu) crystal at room temperature. Further, the gamma-ray equivalent energy of the slow-neutron peak in the nonactivated material is less than that of LiI(Eu), so that there is no advantage in gamma-ray discrimination. Finally, it does not seem

possible to discriminate between various charged particles by means of either the emission spectrum or the decay times.

From the standpoint of understanding the mechanism of the scintillation process, the data obtained to date are significant pieces of information but are by no means sufficient to permit the formulation of a model. It is hoped that further studies will lead to some understanding of the processes involved.

8.8. DETERMINATION OF EXPERIMENTAL FLUX DEPRESSION AND OTHER CORRECTIONS FOR GOLD FOILS EXPOSED IN WATER

W. Zobel

One of the methods for determining the thermal-neutron flux in a medium uses the activation induced in gold foils. Both bare and cadmium-covered foils are exposed in the medium, and the thermal-neutron flux at any specified position is calculated from the difference between the activations of a bare foil and a cadmium-covered foil at that position. This method is used frequently at the LTSF. Furthermore, since all thermal-neutron detectors at the LTSF are normalized to the gold foils,[1] a knowledge of the corrections to be applied to foil measurements is quite important.

The gold foils commonly used at the LTSF are 1 cm square and 0.002 in. thick. The cadmium covers on these foils are 0.020 in. thick. It was felt that all applicable corrections could be contained in one factor, the ratio of the flux measured with infinitely thin foils to the flux measured with 0.002-in.-thick foils having the same shape and area. In order to determine the values of this factor experimentally, several 1-cm-square foils of varying thickness were exposed at the same position in the LTSF so that an extrapolation to zero thickness would be possible. The position chosen was such that the neutron flux should have been isotropic. The foil thickness was varied from 9.2×10^{-7} in. (45 $\mu g/cm^2$) to 0.010 in. (483 mg/cm^2). Foils thicker than the usual 0.002 in. were used because it would make the extrapolation more reliable and also because other facilities normally use thicker foils. The thicker foils may even become desirable at the LTSF.

The experimental curves for both the bare and the cadmium-covered foils, as well as the difference curve between the two, are presented in Fig. 8.8.1. The value for "zero" thickness was obtained by fitting the data for thicknesses less than 1.7 mg/cm^2 with straight lines, using the method of least squares. From these data the experimental ratio of the saturated activity per unit mass of a foil of "zero" thickness to that of a 0.002-in.-thick foil is 1.22 ± 0.16.

Various calculational methods have been proposed from which the flux depression factor can be estimated.[2–5] Using the prescription of Bothe[2] results in a factor of 1.09; that of Tittle,[3] 1.08; that of Skyrme,[4] 1.21; and that of Bengston,[5] 1.30. In all these calculations the self-shielding in the foil has been included.

In all those calculations that consider a foil of finite area, the foil is assumed to be circular. To check the validity of assigning an effective radius to the square foil for calculational purposes, circular foils 1.11 cm in diameter (0.968 cm^2 in area) were exposed. Within the accuracy of the measurements ($\pm 2\%$) these circular foils gave the same thermal-neutron flux as the 1-cm-square ones.

It is apparent from the measurements that best agreement is obtained with the value calculated according to Skyrme. On the basis of the present error assignment, however, none of the other calculational methods can be ruled out. Further work, aimed at reducing the error in the measurement, is contemplated.

---

[1] D. W. Cady, *The Lid Tank Shielding Facility at Oak Ridge National Laboratory; Part III: Instrumentation*, ORNL-2587 (1959).

[2] W. Bothe, *Z. Physik* 120, 437 (1943).

[3] C. W. Tittle, *Nucleonics* 8(6), 5 (1951); *Nucleonics* 9(1), 60 (1951).

[4] T. H. R. Skyrme, *Reduction in Neutron Density Caused by an Absorbing Disc*, MS-91.

[5] J. Bengston, *Neutron Self-Shielding of a Plane Absorbing Foil*, ORNL CF-56-3-170 (1956).

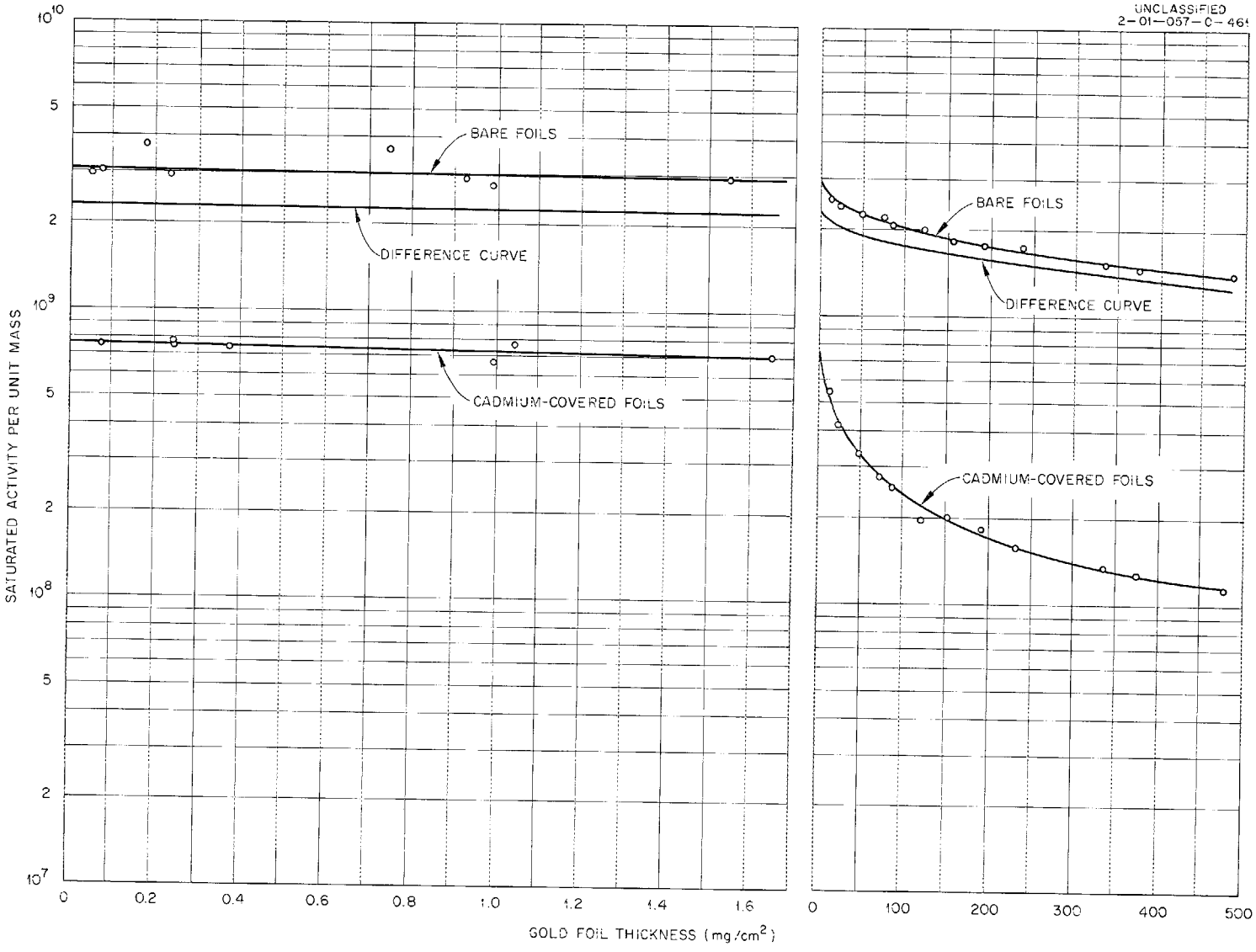

Fig. 8.8.1. Saturated Activities of Gold Foils Exposed in the LTSF.

8.9. CORRECTION FACTORS FOR FOIL-ACTIVATION MEASUREMENTS OF NEUTRON FLUXES IN WATER AND GRAPHITE

D. K. Trubey T. V. Blosser G. M. Estabrook

A standard technique employed in the measurement of low-energy neutron fluxes in various media is based upon the measurement of the activity induced in thin metal foils. A "resonance" detector, such as indium or gold, is particularly useful because it is essentially responsive to only one energy in the ev region (1.46 ev for indium, 4.9 ev for gold). At these energies the slowing-down of the neutron is largely completed but the energy has not been degraded to the point where chemical binding in the molecule is of importance. Experimental results based on the use of these detectors may thus logically be compared to various slowing-down calculations.

Unfortunately, the presence of the detecting foil within the flux to be measured creates a number of perturbations which cause the activation per unit mass of the foil to be not exactly proportional to the undisturbed neutron flux. These effects, in general, depend not only on the foil parameters but also on the characteristics of the medium in which the foil is activated and on the techniques of measuring the saturated activity of the foil. Difficulties involving beta-ray losses can be effectively eliminated if the gamma rays emitted by the activated foil are measured, and this technique has been adopted for the work reported herein.

The perturbations involving neutron effects can be separated into two categories: self-shielding and flux depression. Self-shielding arises from the attenuation of the neutron flux as it penetrates the foil, so that the interior of the foil has a lower saturated activity than the surface layers. Flux depression describes the decrease in the flux in the medium near the foil due to absorptions in the foil. Since the flux or track length of neutrons in a given small volume is partially due to neutrons on their second, third, and subsequent flights through the given volume, insertion of an absorber reduces the flux by diminishing the number of second, third, and subsequent flights. This effect is also called "self-shading" or "foil drain." A further complication may be introduced in the use of a relatively thick cadmium cover on the foil to remove undesired low-energy (thermal) neutrons.

The quantity of interest is, of course, the undisturbed flux at a specified point in the medium, given, in effect, by the saturated activity of a detector foil per unit mass as the foil mass approaches zero, that is, infinite dilution. In some cases (for example, see Sec 5.1), it is observed that the various perturbations vary as a function of the distance of the foil from the neutron source, apparently because of changes in the neutron angular distribution. This variation is considered at greater length below.

Resonance Detectors – Theory

Ideal Model. – For commonly used moderating media such as graphite or water, the average lethargy increment ξ, or the logarithmic energy loss, is considerably greater than the resonance lethargy width, so that the flux does not have contributions from second and subsequent flights. As a consequence, the flux-depression effect becomes negligible and the only perturbation to be considered is the self-shielding

effect. This effect, f, may be defined as the ratio of the absorption per unit thickness in a foil of thickness T (Fig. 8.9.1) to the absorption per unit thickness in a foil of thickness $t \to 0$. Thus, for a disk of infinite radius, in a $1/E$ flux,

$$f(T) = \frac{\frac{1}{T}\iint g(y)\left[1 - e^{-\Sigma(E)y}\right] dy \frac{dE}{E}}{\lim_{t\to 0}\iint \frac{g(y)}{t}\left[1 - e^{-\Sigma(E)y}\right] dy \frac{dE}{E}}, \tag{1}$$

where

$\Sigma(E)$ = macroscopic absorption cross section,

$g(y)$ = distribution of path lengths y for unit surface area

$= 2T^2/y^3$ for isotropic neutron flux.

Since the resonance width is narrow, the error will be small if the $1/E$ variation in the flux is neglected. Substituting the variable x, defined as $x = (E - E_0)/(\Gamma/2)$, where E_0 is the energy of the resonance peak and Γ is the total width of the resonance peak, and assuming (1) isotropic distribution, (2) the Breit-Wigner single-level formula for the absorption cross section, and (3) negligible scattering, gives

$$f(T) = \frac{\frac{1}{T}\int_t^\infty \int_{-\infty}^\infty \frac{2T^2}{y^3}\left\{1 - \exp - \left[\frac{\Sigma_0 y}{(1+x^2)}\right]\right\}\frac{\Gamma}{2E_0}\, dx\, dy}{\frac{1}{t}\int_t^\infty \int_{-\infty}^\infty \frac{2t^2}{y^3}\left[\frac{\Sigma_0 y}{(1+x^2)}\right]\frac{\Gamma}{2E_0}\, dx\, dy}, \tag{2}$$

UNCLASSIFIED
2-01-059-407

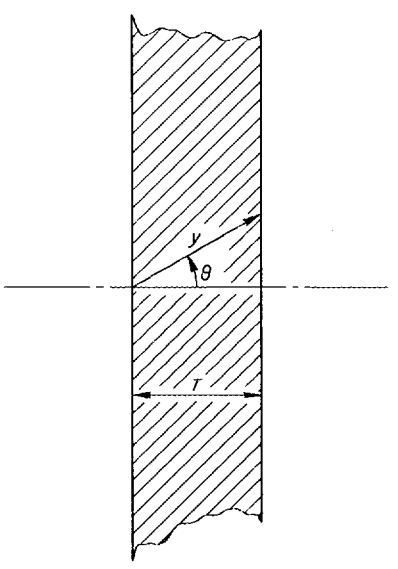

Fig. 8.9.1. Geometry for Self-Shielding Calculation.

where Σ_0 is the cross section at the peak of the resonance. If the path lengths are integrated first,

$$f(T) = \frac{\int_0^\infty \left\{\frac{1}{2} - E_3\left[\frac{\Sigma_0 T}{(1+x^2)}\right]\right\} dx}{\Sigma_0 T \int_0^\infty \frac{dx}{(1+x^2)}} = \frac{\int_0^\infty \left\{\frac{1}{2} - E_3\left[\frac{\Sigma_0 T}{(1+x^2)}\right]\right\} dx}{\Sigma_0 T \frac{\pi}{2}} , \tag{3}$$

where

$$E_n(z) = z^{n-1} \int_0^\infty \frac{e^{-y}\, dy}{y^n}$$

$$= \frac{1}{n-1}\left[e^{-z} - zE_{n-1}(z)\right] .$$

This is similar to the familiar one-velocity result,[1]

$$f(T) = \frac{\frac{1}{2} - E_3(\Sigma T)}{\Sigma T} .$$

Equation (3) may be numerically integrated as it stands since detailed values of $E_3(z)$ have been tabulated.[2] However, for present purposes it proves more convenient to integrate first over the energy. Von Dardel and Persson[3] give the following result:

$$(4\pi\Sigma_0)^{-1/2} \int_{-\infty}^{\infty} \left\{1 - \exp - \left[\frac{\Sigma_0}{(1+x^2)}\right]\right\} dx = \sqrt{\frac{\pi}{2}}\sqrt{\frac{\Sigma_0}{2}} \exp - \left(\frac{\Sigma_0}{2}\right)\left[I_0\left(\frac{\Sigma_0}{2}\right) + I_1\left(\frac{\Sigma_0}{2}\right)\right] ,$$

where $I_p(z)$ are the modified Bessel functions of the first kind, of order p.

Using this result in (2),

$$f(T) = \frac{\Sigma_0 T}{2} \int_{(\Sigma_0 T/2)}^{\infty} \frac{e^{-z}}{z^2}\left[I_0(z) + I_1(z)\right] dz , \tag{4}$$

where $z = (\Sigma_0 y)/2$.

This expression may be evaluated for very thick and very thin foils. For very thick foils,

$$I_0(z) \cong I_1(z) \cong \frac{e^z}{\sqrt{2\pi z}} .$$

Therefore,

$$f(T) \cong \frac{\Sigma_0 T}{2} \int_{(\Sigma_0 T/2)}^{\infty} \frac{2dz}{z^2\sqrt{2\pi z}} = \frac{\Sigma_0 T}{\sqrt{2\pi}} \frac{\frac{2}{3}}{\left(\frac{\Sigma_0 T}{2}\right)^{3/2}} = \frac{4}{3\sqrt{\pi}} \frac{1}{\sqrt{\Sigma_0 T}} . \tag{5}$$

---

[1] See, for example, *Argonne National Laboratory Reactor Physics Constants*, ANL-5800 (1958), p 487. In this report, as in many others, $f(T)$ is given as an expression involving $E_1(z)$ rather than $E_3(z)$.

[2] D. K. Trubey, *A Table of Three Exponential Integrals*, ORNL-2750 (1959).

[3] G. von Dardel and R. Persson, *Nature* 170, 1117 (1952).

It is important to note that (5) means that a resonance detector is never "black" or completely absorbing, but that, in an isotropic flux, the absorptions are proportional to the square root of the thickness. Therefore, a resonance absorber is not a "neutron-current detector." For very thin foils,

$$E_3(z) = \frac{1}{2} - z + \frac{z^2}{2}(0.9228 - \ln z) + \dots ,$$

and (3) can be shown to be

$$f(T) = 1 + \frac{\Sigma_0 T \ln \Sigma_0 T}{4} - 0.3274\, \Sigma_0 T + \dots . \tag{6}$$

These results, (5) and (6), were derived by Wilkins.[4] Intermediate values of $f(T)$ have been computed by a numerical integration of (4) and are plotted in Fig. 8.9.2. The result for a collimated beam is also plotted, giving an upper limit for the variation of $f(T)$ with angular distribution of the neutrons. The absorption for the collimated beam is considerably greater because the current per unit flux is higher.

Resonance Foils with Cadmium Covers. – The discussion has been concerned with the behavior of an ideal resonance detector. In order to isolate the resonance activation from the thermal activation, a filter, often a cadmium cover, must be applied to the resonance foil. The thickness of this cover must be sufficient to remove essentially all the neutrons of energies less than ~0.5 ev. A 40-mil-thick cover, recommended by Stoughton *et al.*[5] for a $1/v$ detector, will reduce the indium activation by 10 to 12%. Although previous experimenters have often used cadmium thicknesses much greater than 40 mils, the transmission data reported below indicate that a 20-mil cadmium thickness is sufficient in the use of indium foils in a nearly isotropic flux.

Many experimenters have fitted their cadmium transmission data with an exponential expression, and Tittle,[6] by combining results from several experiments, has shown a variation of the exponential slope with indium thickness. However, the results reported below, which have been fitted by an exponential and also by the $E_3(x)$ function, do not show this dependence. [The $E_3(x)$ function is the transmission function to be expected for an isotropic flux impinging on a totally absorbing one-velocity detector. Because of the square-root behavior of a resonance detector, the transmission function for a thick indium foil should be closer to the $E_{2.5}(x)$ function, but since the cadmium cover is relatively thin the difference is not evident.]

Angular Distribution. – To this point the assumption has been made that the angular distribution is isotropic. Since this is not always the case, reliance must be placed on experimental measurements, and only in the limit of infinite dilution ("zero" thickness) will the flux be measured.

It is of interest to examine the trend in the angular distribution of the flux from a point source in an infinite medium. If the quantity $\bar{\mu}$ is defined as the average cosine of the angle between a neutron

---

[4] J. E. Wilkins, *The Activation of Thick Foils*, CP-3581 (1946).

[5] R. W. Stoughton, J. Halperin, and M. Lietzke, *Effective Cadmium Cutoff Energies*, to be published in *Nuclear Sci. and Eng.*

[6] C. W. Tittle, *Nucleonics* 9(1), 60 (1951).

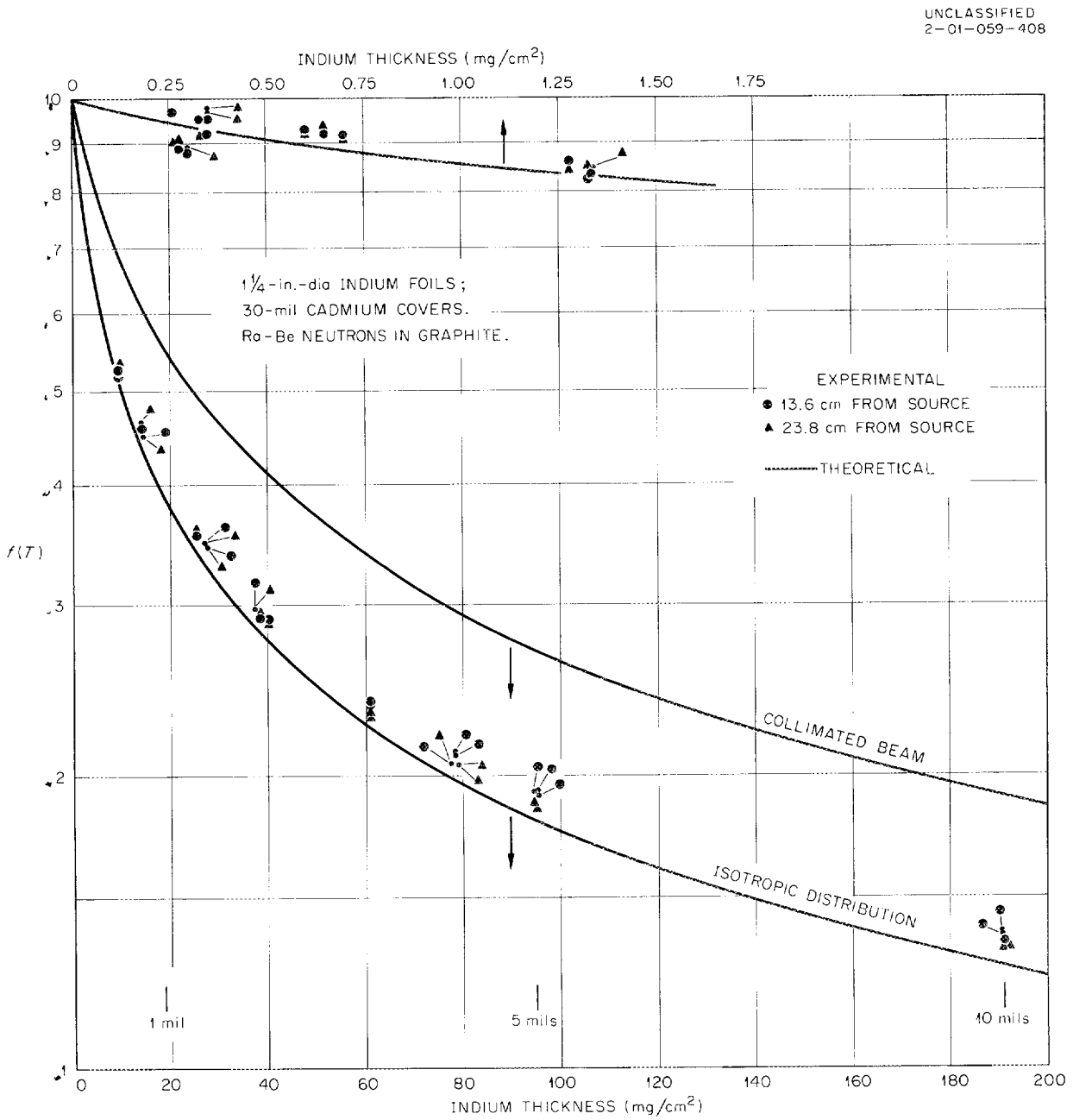

Fig. 8.9.2. Comparison of Experimental Values with Theoretical Calculations of the Self-Shielding Factor, $f(T)$, as a Function of Indium Foil Thickness for Both Isotropic Neutron Distribution and Collimated Beam.

velocity vector and the radial direction, $\bar{\mu} = 0$ for an isotropic distribution, and $\bar{\mu} = 1$ for a radial distribution. The quantity $\bar{\mu}$ is also the ratio of the net current **J** to the flux, that is, $|\mathbf{J}| = \bar{\mu}\phi$. If diffusion theory holds, **J** is also proportional to the gradient of the flux; that is, $\mathbf{J} = -D\nabla\phi$. Combining these relationships,

$$\bar{\mu} \propto \frac{\nabla\phi}{\phi} . \tag{7}$$

A plot of (7) based on preliminary measurements employing a 5-mil-thick indium detector in water and in graphite is shown in Fig. 8.9.3. As expected, $\bar{\mu}$ goes to zero at the origin, due to symmetry. Since the proportionality factor is not the same, the two curves are not directly comparable in magnitude; but it is readily evident that the shapes are not alike. The forward component of the neutron distribution apparently goes through a maximum in water relatively close to the source. This may be explained in terms of the neutron-transport mechanism. In water, fairly close to the source (and at a much greater distance in graphite), the transport is largely due to the first flight. The uncollided neutron

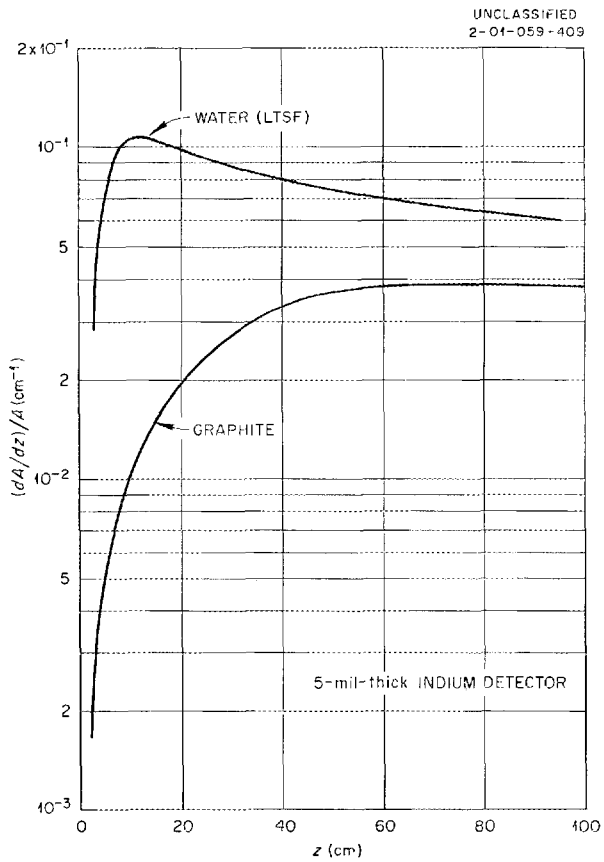

Fig. 8.9.3. Angular Distribution Index, the Instantaneous Rate of Variation of Indium Activity with Distance from the Source Divided by the Activity, as a Function of Distance from the Source.

spectrum hardens as a function of distance from the source; thus the slope of the first-collision distribution increases. That is, if the distribution is nearly exponential, $\bar{\mu}$ will behave like the reciprocal of the relaxation length. The resulting indium activation is complicated because it depends on an average of the distributions on the front of the foil and on the back. In addition, the angular distribution may be perturbed by the foil itself. For a precise measurement, therefore, such as the measurement of the age of neutrons in water, it is necessary to extrapolate to zero indium thickness and zero cadmium thickness at all space positions.

Resonance Detectors – Experimental

Data from a recent experiment intended to measure the age to indium resonance energy (described in Sec 5.1 of this report) has been analyzed in the light of the above conclusions. Other measurements were made with indium foils in the graphite of the ORNL standard pile, using an Ra-Be source. The foils, which varied in thickness from $\sim$0.12 mg/cm^2 to $\sim$190 mg/cm^2, were counted on both sides simultaneously with an NaI(Tl) scintillation counter. The resulting experimental measurements of the self-shielding factors $f(T)$ are included as points in Fig. 8.9.2. The values plotted are the saturated activity per unit thickness normalized by fitting the data for the thin foils to the theoretical function given by (6), using the method of least squares. The value of Σ_0 was taken to be 0.18 cm^2/mg, derived from the resonance parameters given in BNL-325.[7]

The fact that the simple curve given by (3), (4), and (5) fits so well over the entire range of data is remarkable, since no correction has been made for deviation from isotropy, for higher resonances, $1/v$ absorption, or Doppler broadening. All these corrections would tend to increase the measured $f(T)$. An estimate of the effect of Doppler broadening was made by numerically integrating (3) over the line shape, ψ (ref 8), for a thickness of 18 g/cm^2 (1 mil). For this case the quantity f increases by about 1%. Estimates of the corrections for absorption in higher resonances can be made by weighting the various f's by the resonance integrals. The results for 5- and 10-mil-thick foils increase the value of f by 7% and 8%, respectively.

Table 8.9.1 summarizes the results of cadmium transmission data obtained in graphite. Figure 8.9.4 displays the saturated activity per unit thickness for several thicknesses of indium foil as a function of cadmium-cover thickness. As previously noted, no indium-thickness effect is observed in these curves. The data were satisfactorily fitted by the method of least squares both to a straight line on the semilog plot and to the logarithm of the $E_3(x)$ function.

Since the cadmium is "thin" for 1.45-ev neutrons, the exponential fit is nearly as good as the $E_3(x)$ fit, and the probable error in the intercept of either curve includes the intercept of the other curve. At the scale of the figure, the curves lie one upon the other; therefore, only the exponential fit is drawn.

Computations were performed using the Oracle. The resulting constants a, where $a = \ln F_{Cd}/t$, when t is the cadmium thickness, a removal cross section Σ, defined by $F_{Cd} = 1/2E_3(\Sigma t)$, and a microscopic

[7] D. J. Hughes and R. B. Schwartz, *Neutron Cross Sections*, BNL-325, 2d ed. (1958).

[8] M. E. Rose *et al.*, *A Table of the Integral $\psi(x,t)$*, WAPD-SR-506 (October 1954).

Table 8.9.1. Summary of Cadmium Transmission Data for 1.25-in.-dia Cadmium-Covered Indium Foils in Graphite (Ra-Be Source)

Slot Number (ORNL Standard Pile)	Distance from Source (cm)	t, Average Foil Thickness (mils)	F_{Cd} (40-mil sample)		a (in.$^{-1}$)	Σ (in.$^{-1}$)	σ (barns)
			E_3 Fit	Exponential Fit			
1	13.6	5.2	1.131	1.125	2.94	1.64	14.0
2	23.8	5.2	1.135	1.128	3.01	1.69	14.4
3	34.0	5.2	1.132	1.126	2.97	1.66	14.1
4	44.1	5.2	1.141	1.134	3.14	1.77	15.1
6	64.4	5.2	1.144	1.137	3.21	1.80	15.3
1	13.6	~0.069	1.112	1.107	2.65	1.41	12.0
1	13.6	~0.037	1.126	1.121	2.85	1.59	13.5

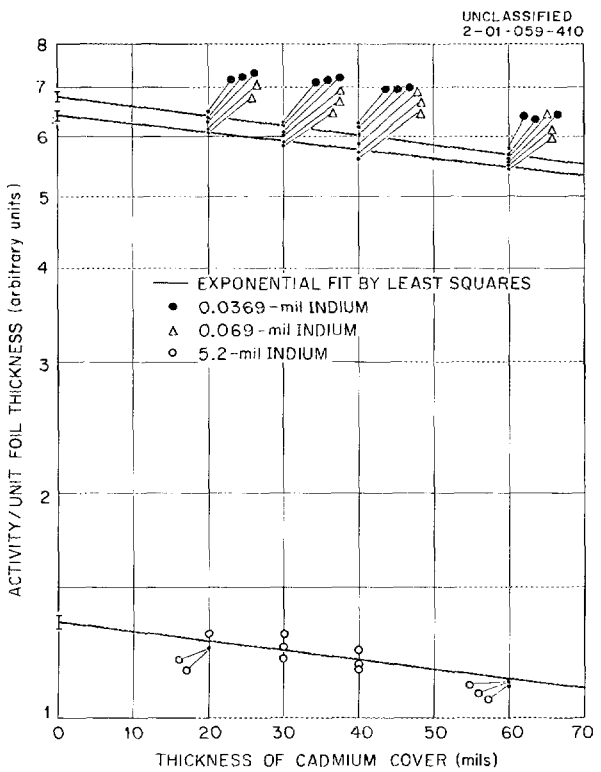

Fig. 8.9.4. Indium Activation as a Function of Cadmium Cover Thickness for Various Thicknesses of 1.25-in.-dia Indium Foils (Ra-Be Neutrons at 13.6 cm in Graphite).

cross section σ, derived from Σ, are shown in Table 8.9.1. The values of σ shown in the table are comparable with the value of 11 barns for the cadmium total cross section at 1.45 ev.

The value of the factor F_{Cd}, which agrees quite well with the published summary of Martin,[9] remains essentially constant with variation of position in graphite. This indicates that the angular distribution over the regions measured in these experiments was very nearly isotropic. This, however, was not the case for the measurements in water. Figure 8.9.5 shows a plot of the factor F_{Cd} as a function of distance from the Lid Tank Shielding Facility source, for thicknesses of 40 and 140 mils. The 140-mil data is derived from an exponential extrapolation from 30-, 40-, 50-, and 70-mil data. The minimum in the curves in the vicinity of $z \approx 10$ cm is in agreement with the prediction of the angular distribution data shown in Fig. 8.9.3 (a similar plot is shown in Sec 5.1).

Thermal-Neutron Detectors – Theory

The preceding discussion has been primarily concerned with the use of foil detectors in the resonance regions. Indium foils are also useful as detectors of neutrons in the thermal energy region, if the resonance activity is subtracted, and it is of interest to consider the perturbations inherent in this use of foils. Published comparisons have usually indicated good agreement between theory and experiment, but because of the limits imposed by the assumptions requisite to development of the theory, it is possible that theoretical results may not always be applicable to experimental problems.

Within the assumptions of (1) one-velocity diffusion theory in the medium, (2) no scattering in an infinite-radius foil, and (3) the usual P_1 expansion of the neutron flux, the total foil perturbation f_t is

[9] D. H. Martin, *Nucleonics* 13(3), 52 (1955).

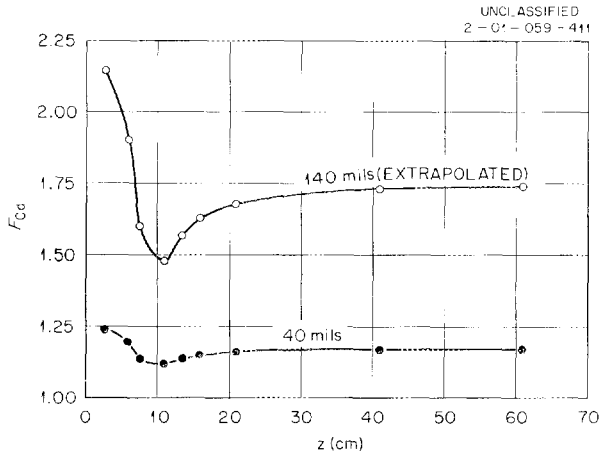

Fig. 8.9.5. Cadmium Correction Factor in LTSF as a Function of Distance from the Source.

given by

$$f_t(x) = \frac{\dfrac{1 - 2E_3(x)}{2x}}{1 + \dfrac{1 - 2E_3(x)}{4\Sigma_a L} - \dfrac{1 - 3E_4(x)}{2}} = f(x) \left[1 + \frac{\alpha_1(x)}{4\Sigma_a L} - \frac{\alpha_2(x)}{2}\right]^{-1} , \tag{8}$$

where

$\alpha_1(x) = 1 - 2E_3(x)$,

$\alpha_2(x) = 1 - 3E_4(x)$,

$f(x) = \dfrac{1 - 2E_3(x)}{2x}$,

Σ_a = macroscopic absorption cross section of the medium,

L = diffusion length in the medium.

The factor $f(x)$ is readily recognized as the self-shielding factor, and therefore the flux depression factor $F_f(x)$ is given by

$$F_f(x) \equiv \left[1 + \frac{\alpha_1(x)}{4\Sigma_a L} - \frac{\alpha_2(x)}{2}\right]^{-1} . \tag{9}$$

In the practical case, however, the assumption of an infinite-radius foil may not be valid. Bothe[10] has derived expressions for the flux depression caused by a sphere and has recommended that the radius be reduced by a factor of 2/3 if the expressions are used for a disk. His expressions are:

$$F_f(x) = \left[1 + \frac{\alpha_1(x)}{2}\left(\frac{R}{\lambda_s}\,\frac{3L}{2R + 3L} - 1\right)\right]^{-1} \qquad \text{for } R \gg \lambda_s \tag{10}$$

and

$$F_f(x) = \left[1 + 0.34\,\alpha_1(x)\,\frac{2R/3}{\lambda_s}\right]^{-1} \qquad \text{for } R \ll \lambda_s , \tag{11}$$

where R is the radius of the disk, λ_s is the scattering mean free path, and the other quantities are as previously defined.

Tittle[7] recommended that the scattering mean free path be replaced by the transport mean free path, and that the factor 2/3 be deleted. With these changes, and noting that

$$\lambda_{tr} \cong 3L^2\Sigma_a ,$$

(10) and (11) may be rearranged to obtain:

$$F_f(x) = \left[1 + \frac{\alpha_1(x)}{4\Sigma_a L}\,\frac{R}{R + L} - \frac{\alpha_1(x)}{2}\right]^{-1} \qquad \text{for } R \gg L \tag{12}$$

---

[10] W. Bothe, *The Use of Neutron Detectors*, CP-G-2964 (1945) [from *Z. Physik* 120, 437 (1943)].

and

$$F_f(x) = \left[1 + 0.34\, \alpha_1(x)\, \frac{R}{\lambda_{tr}}\right]^{-1} \qquad \text{for } R \ll \lambda_{tr} \ . \qquad (13)$$

In this form it is evident that consideration of a finite radius introduces the factor $R/(R + L)$ in the expression for infinite-radius foils, since $\alpha_1 \cong \alpha_2$. The limiting restriction on (10) and (12) is the assumption that diffusion theory applies with the particular foil size. For a medium of graphite, $L \gg R$, and therefore $F_f(x)$ from (12) can be greater than 1, an obvious absurdity. The limiting restrictions on (11) and (13) are due to the assumptions of no absorption in the medium, no multiple scattering, and negligible third and subsequent flights.

Thermal-Neutron Detectors – Experimental

An experimental determination of the thermal-neutron flux depression factor as a function of foil thickness, for 1.25-in.-dia indium foils in graphite at two distances from the source, is given in Fig. 8.9.6. The data, derived from bare-foil activation minus corrected cadmium-covered-foil activation, was normalized in the following manner: the average normalization factor was established by the use of 36 data points at each of two distances from the source; this factor was used to normalize the data for thin foils (<1.5 mg/cm^2), and a least-squares fit to a straight line was employed to determine the intercept.

Also shown in Fig. 8.9.6 is a theoretical curve obtained by multiplying (13) by the flux-depression factor. (The cross section was assumed to be 0.886 times the 2200-m/sec cross section.) Unfortunately, the flux depression is so small for indium foils in graphite ($\sim$3% for a 5-mil-thick, 1.25-in.-dia foil) that the Bothe expressions are not given a good test. Nearly all the flux-perturbation effect is due to self-shielding.

As reported elsewhere,[11] agreement between theory and experiment appears quite good. However, the poor statistics obtained in the thin-foil measurements compel an uncertainty in the normalization. If, as has been done by previous experimenters, the Bothe equation were normalized to the thick-foil data, the normalization would be shifted by 1 to 2%.

---

[11] T. L. Gallagher, *Nuclear Sci. and Eng.* 3, 110 (1958).

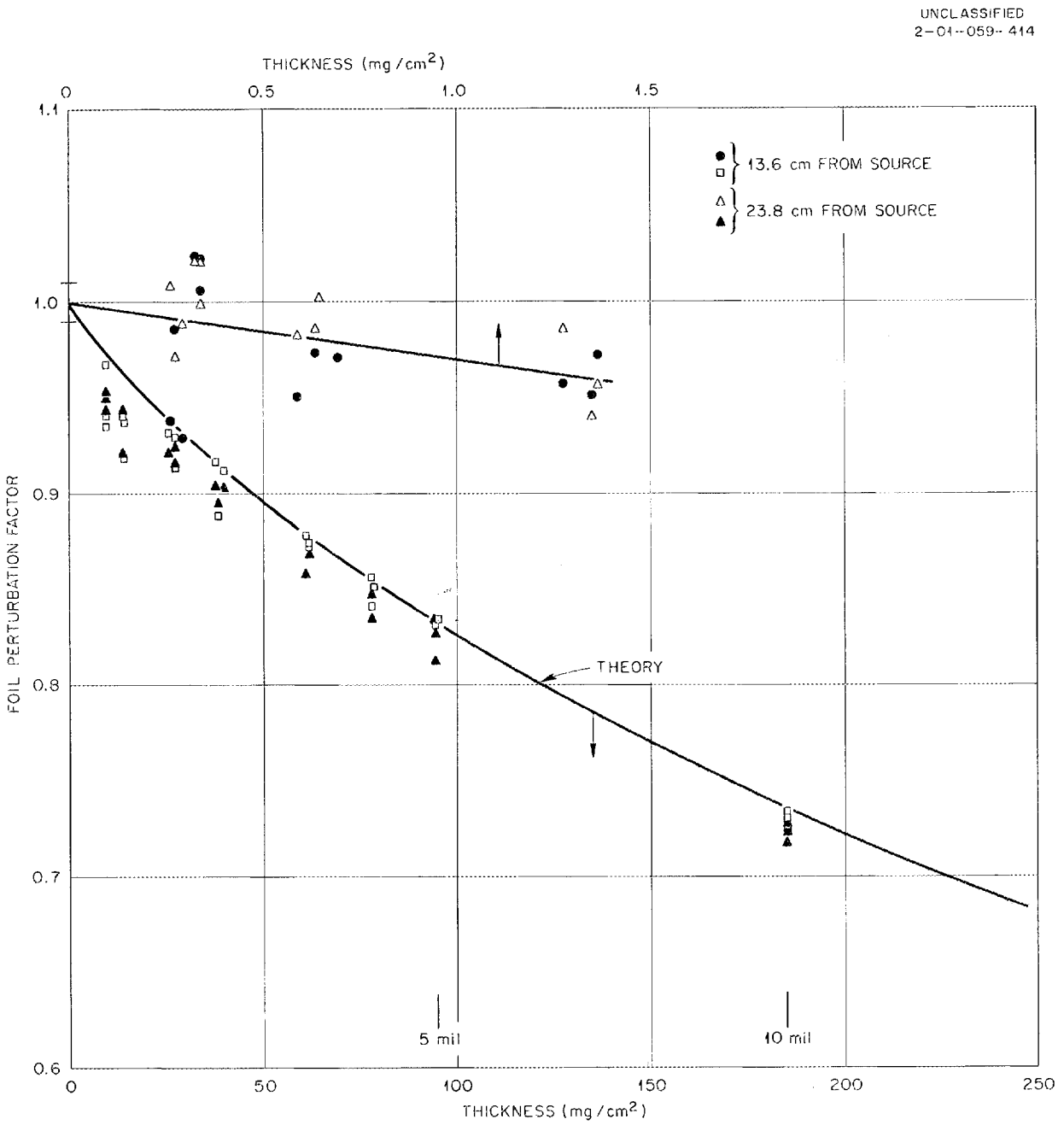

Fig. 8.9.6. Experimental and Theoretical Foil Perturbation Factors for Thermal Neutrons as a Function of the Thickness of 1.25-in.-dia Indium Foils in Graphite, 13.6 and 23.8 cm from the Source.

Part 9

THERMONUCLEAR RESEARCH

Several papers in this chapter consist of abstracts only since longer papers on the same subjects have been included in the *Thermonuclear Project Semiannual Report for Period Ending July 31, 1959*, ORNL-2802.

9.1. ORBIT PRECESSION IN DCX

T. K. Fowler

The possibility of causing ions in the DCX to avoid the arc, once trapped, by introducing precession into their orbits has been investigated. It appears to be impractical to reduce the time spent in the arc by more than a factor of 10.

9.2. ABSOLUTE CONTAINMENT OF IONS IN DCX

T. K. Fowler M. Rankin[1]

The study of orbits of single ions in the azimuthally symmetric DCX magnetic field is being carried out and a detailed report concerning the absolute containment of ions encircling the symmetry axis of the field has been issued.[2] In summary, the report presents a derivation of the absolute-containment criterion together with plots of the regions in space and momentum space to which absolutely contained particles are confined.

[1] Member of Thermonuclear Experimental Division.

[2] T. K. Fowler and M. Rankin, *Containment Properties of DCX*, ORNL CF-59-6-32 (1959).

9.3. CODE FOR CALCULATIONS OF ENERGY DISTRIBUTIONS OF PARTICLES IN THE DCX

T. K. Fowler M. Rankin[1]

A previously discussed IBM-704 code[2,3] designed to solve coupled Fokker-Planck transport equations for the energy distributions of ions and electrons in the DCX, having been found too slow, is being revised. The difficulty in the original code, which followed the distributions in time through the transient phase toward a steady state, lay in the fact that ion and electron relaxations occur at greatly different rates. Within time steps short enough to properly handle changes in the coldest part of the electron distribution, virtually nothing happened to the ions. The new code, which retains most of the old one, including the difference scheme,[2] circumvents this problem by solving directly for the steady state. Since the equations are nonlinear, an iterative scheme of solution is being attempted. Efforts to determine in advance the convergence of the procedure have not proved decisive.

[1] Member of Thermonuclear Experimental Division.

[2] A. Simon, T. K. Fowler, and M. Rankin, *Thermonuclear Semiann. Rep. Jan. 31, 1959*, ORNL-2693, p 25.

[3] T. K. Fowler, M. Rankin, and A. Simon, *Boundary Conditions and Conservation Properties of FOPP, a Plasma Fokker-Planck Code*, ORNL CF-59-2-75 (1959).

9.4. MICROWAVE DIAGNOSTICS UTILIZING THE FARADAY EFFECT

T. K. Fowler

The possibility for density measurements in the DCX utilizing Faraday rotation of microwaves has been analyzed.[1,2] It may be feasible to measure electron densities as low as $N \sim 10^9$ cm^{-3} and to measure the electron collision frequency, ν, as well. The method hinges on the fact that an initially plane-polarized wave launched parallel to the magnetic field confining the plasma separates into two waves, left and right circularly polarized, which propagate through the plasma with different (complex) indices of refraction. Thus the two circular waves, initially of the same phase and amplitude, emerge from the plasma with different phase and amplitude and recombine to form an elliptical wave which, if absorption is negligible, is almost plane-polarized but rotated by an angle θ with respect to the original plane of polarization.

It is the rotation θ which is to be measured, θ being proportional to the density, N. The rotation is greatly enhanced by a resonance at microwave frequencies ω near the cyclotron frequency of the electrons (Ku band). Of course, in the highly nonuniform magnetic field of the DCX, cyclotron resonance can be maintained over only a short path length, just an inch or two around the heart of the plasma at the midplane. Even so, in a given plasma the rotation angle obtainable is greater than the phase shift of conventional microwave methods of measuring the density by a factor $> \sqrt{\omega/(\omega_0 - \omega)}$, ω_0 being the electron cyclotron frequency at the midplane. This factor can easily be made ~ 10 without violating an auxiliary requirement that $\omega < \omega_0 - \nu$ in order to avoid a dependence of θ upon ν. Then a density of $N = 10^9$ cm^{-3} would produce a measurable rotation $\theta \sim 1°$, as compared with a phase shift $\sim 0.1°$ which would be swamped by the background in the DCX.

In order to see that ν also can be measured, two cases must be distinguished: first, the case independent of ν, already discussed,

$$\theta \cong \frac{\pi}{2} \frac{L\omega}{c} \frac{\omega_p^2}{\omega^2} \sqrt{\frac{\omega}{\omega_0 - \omega}} ,$$

$$\text{off resonance, } \omega < \omega_0 - \nu , \quad (1)$$

and also

$$\theta \cong \frac{L\omega_0}{c} \frac{\omega_p^2}{\omega_0^2} \sqrt{\frac{\omega_0}{\nu}} ,$$

$$\text{on resonance, } \omega = \omega_0 . \quad (2)$$

Here ω_p is the plasma frequency and is proportional to $\sqrt{N}$, L is the length between magnetic mirrors in the DCX (the actual path length through the plasma does not appear), and c is the speed of light. Equations (1) and (2) have been derived for the DCX magnetic field–mirror ratio of 2:1 under the assumptions that the path length through the plasma is several times that over which resonance can be maintained (a few inches) and that, when $\omega < \omega_0 - \nu$, $\omega_p^2/\omega(\omega_0 - \omega) < 1$, the latter being valid for the low-density measurements contemplated.

In order to measure ν, it is first necessary to determine ω_p (hence N) from a measurement of θ off resonance, where (1), independent of ν, is applicable. A measurement of θ on resonance, combined with the value of ω_p, then yields ν from (2).

It has been implicitly assumed here that waves will be launched parallel to the magnetic symmetry axis. Effects due to the radial field component, ignored here, can in fact be eliminated by launching the wave with its electric vector directed radially.

---

[1] A detailed report of this investigation will appear in *Thermonuclear Semiann. Rep. July 31, 1959*, ORNL-2802 (to be published).

[2] Application of this method to the DCX was suggested by R. A. Dandl of the Thermonuclear Experimental Division. H. O. Eason and H. W. Shields, also of that division, have contributed greatly. Density measurements utilizing Faraday rotation have previously been made in the Russian thermonuclear machine, OGRA.

9.5. CRITICAL CURRENT FOR BURNOUT IN AN OGRA-TYPE DEVICE

A. Simon

A complete algebraic analysis has been obtained for the variation of the steady-state ion density n_+ with injected current I in an OGRA-type fusion device (i.e., a device based on trapping of ions by breakup of energetic molecular ions on collision with either the background gas or trapped ions). The most general variation of n_+ with I is shown to be an s curve with at most three roots of n_+ for a given input I. A physical interpretation of these three roots has been obtained. In addition, algebraic expressions have been derived for the two currents at which the bends in the s curve occur. It will be necessary to attain the larger current in order to build up a high-density plasma when the density is being increased from below. On the other hand, once the high density has been achieved, it may be maintained by steady injection of a current larger than the lower value.

9.6. COHERENT RADIATION FROM A PLASMA

E. G. Harris[1] A. Simon

By beginning with the Liouville equation and treating both the plasma particles and the electromagnetic field in a completely statistical fashion (the single approximation involved being that all pair correlations vanish), the so-called "collisionless Boltzmann equation" or "Vlasov equation" is deduced, as well as a companion equation for each field oscillator. It is shown, as a consequence of this companion equation, that the entropy of the electromagnetic field is a constant and that, in general, a plasma obeying the Vlasov equation can only radiate coherently.

[1]Consultant, University of Tennessee.

9.7. PLASMA INSTABILITIES ASSOCIATED WITH ANISOTROPIC VELOCITY DISTRIBUTIONS

E. G. Harris[1]

In an earlier discussion of the instabilities of an infinite homogeneous plasma in a uniform magnetic field which were due to anisotropies in the velocity distributions of the ions and electrons[2] the following set of equations was used:

$$\frac{\partial f_i}{\partial t} + \mathbf{v} \cdot \frac{\partial f_i}{\partial \mathbf{r}} + \frac{e_i}{M_i}\left(\mathbf{E} + \frac{1}{c}\mathbf{v} \times \mathbf{B}\right) \cdot \frac{\partial f_i}{\partial \mathbf{v}} = 0 \ , \tag{1}$$

$$\nabla \cdot \mathbf{E} = 4\pi \sum e_i \int f_i d^3v \ , \tag{2}$$

where $f_i(\mathbf{r}, \mathbf{v}, t)$ is the distribution function for the ith species of particle, e_i and M_i are its charge and mass, respectively, and $\mathbf{E}$ is the electric field intensity. It is assumed that $\mathbf{E}$ is the gradient of a scalar potential. Perturbations of the magnetic field are neglected.

[1]Consultant, University of Tennessee.

[2]E. G. Harris, *Unstable Plasma Oscillations in a Magnetic Field*, ORNL-2728 (1959).

Since we did not take into account the remaining Maxwell equations, our treatment suffered from two defects: (1) only longitudinal waves in the plasma were considered, that is, transverse waves were not included, and (2) the coupling which in reality exists between longitudinal and transverse waves was neglected. Neglecting the coupling limits the validity of the treatment to waves with phase velocity much less than the velocity of light.

The previous work has now been extended in order to remedy these defects. We continue to use (1) for the particles but now use the complete set of Maxwell equations. The electric and magnetic fields are derived in the usual way from a scalar potential ϕ and a vector potential **A**. These potentials satisfy the equations

$$\frac{1}{c^2}\frac{\partial^2 \mathbf{A}}{\partial t^2} - \nabla^2 \mathbf{A} = \frac{4\pi}{c}\sum_i e_i \int \mathbf{v} f_i d^3v \ , \tag{3}$$

and

$$\frac{1}{c^2}\frac{\partial^2 \phi}{\partial t^2} - \nabla^2 \phi = 4\pi \sum_i e_i \int f_i d^3v \ . \tag{4}$$

The usual assumption of an infinite homogeneous plasma in a uniform magnetic field is made. The equations are linearized and then Fourier-analyzed in both space and time. Equation (1) becomes a differential equation in velocity space which can be solved. The solution is substituted into (3) and (4), and a set of four homogeneous algebraic equations results. These equations have the form

$$\begin{aligned} \left(-\frac{\omega^2}{c^2} + k^2\right) A_k &= \mathcal{A}_{k0}\phi + \mathcal{A}_{k1}A_1 + \mathcal{A}_{k2}A_2 + \mathcal{A}_{k3}A_3 \ , \\ \left(-\frac{\omega^2}{c^2} + k^2\right) \phi &= \mathcal{A}_{00}\phi + \mathcal{A}_{01}A_1 + \cdots \ . \end{aligned} \tag{5}$$

The $\mathcal{A}_{ij}$'s are very complicated functions and will not be written here. They involve integrals over the unperturbed distribution functions for the electrons and ions. The dispersion relation is obtained by setting the determinant of the coefficients in (5) equal to zero.

We are particularly interested in unperturbed distribution functions which through their effects on the $\mathcal{A}_{ij}$'s cause the dispersion relation to have complex solutions for ω, indicating instabilities. The dispersion relation is very complicated and has not had the thorough study it requires. Only three of the instabilities of transverse waves, which were not reported in our previous work, will be mentioned here.

If the wave vector k is parallel to the magnetic field (which is taken to be in the z direction), then the terms which couple ϕ to A_1 and A_2 vanish and the dispersion relation factors into

three factors. One of these corresponds to longitudinal waves along the lines of **B** and will not further be considered here. Setting each of the other two factors equal to zero gives

$$\omega^2 = k^2c^2 + \sum \omega_p^2 \int f_0 \left[\frac{\omega + kv_z}{\omega + kv_z \pm \omega_c} + \frac{k^2 v_\perp^2}{(\omega + kv_z \pm \omega_c)^2} \right] d^3v \ . \tag{6}$$

(In one of the factors a plus sign occurs and in the other factor a negative sign occurs.) In (6) the summation is over the ions and electrons, the f_0's are unperturbed distribution functions, and ω_p and ω_c are plasma and cyclotron frequencies, respectively. The waves described by (6) are circularly polarized. Whether the polarization of the waves is left-handed or right-handed determines the sign that precedes ω_c. The instabilities discussed below are based on this equation.

If f_0 has the form of one stream of charged particles passing through another, then it may be shown from (6) that hydromagnetic waves with amplitudes which grow exponentially in time can occur.[3] This is similar to the well-known excitation of longitudinal waves by streams of charged particles.

If f_0 has the form

$$f_0 \approx \exp - \left(\frac{v_\perp^2}{\alpha_\perp^2} - \frac{v_z^2}{\alpha_z^2} \right) \ , \tag{7}$$

other interesting instabilities may be found. Weibel[4] has found that, when α_z is sufficiently smaller than $\alpha_\perp$, instabilities occur even in the absence of an external magnetic field. Examination of these instabilities shows that the particles are giving up their kinetic energy to the electromagnetic field.

Rosenbluth[5] has found another interesting instability that occurs for distributions of the form of (7). It involves a resonance between the frequency of a hydromagnetic wave and the cyclotron frequency, and occurs whenever $\alpha_z < \alpha_\perp$.

The recent extension of our work includes the three instabilities mentioned above and also allows the consideration of waves with k at an arbitrary angle to the field. This work will be published elsewhere.[6]

---

[3] I. Bernstein and J. Dawson, *Papers Presented at the Controlled Thermonuclear Conference, Washington, D.C., 1958*, TID-7558, p 360 (1958).

[4] E. S. Weibel, *Phys. Rev. Letters* 2, 83 (1959).

[5] M. Rosenbluth, *Recent Theoretical Developments in Plasma Stability*, paper presented at the meeting of the Fluid Dynamics Division of the American Physical Society, San Diego, November 1958.

[6] In *International Journal of Plasma Physics – Accelerators-Thermonuclear Research.*

9.8. CALCULATION OF THE CROSS SECTION FOR DISSOCIATION OF D_2^+ BY A CARBON ARC

R. G. Alsmiller, Jr.

The cross section for the dissociation of the D_2^+ molecule by a particle of charge ze has been calculated. The calculation is carried out in Born approximation using exact two-center wave functions, the Frank-Condon principle, and a classical average over molecule orientations.[1]

The calculated cross sections divided by z^2 are shown in Fig. 9.8.1. These include the cross section for the excitation of the first excited state, $1s\sigma_g \rightarrow 2p\sigma_\mu$ transition; the cross section for the excitation of the second excited state, $1s\sigma_g \rightarrow 2p\pi_\mu$ transition; and the sum of these cross sections, which is approximately the total dissociation cross section. Also shown in Fig. 9.8.1 are experimental results obtained from the dissociation of H_2^+ and D_2^+ by a vacuum carbon arc. The experimental and theoretical results are found to agree within a factor of 2 over the velocity range considered. However, the Born approximation cross section is much more reliable at the high velocities than at the low velocities, and thus the agreement at low velocities may be fortuitous.

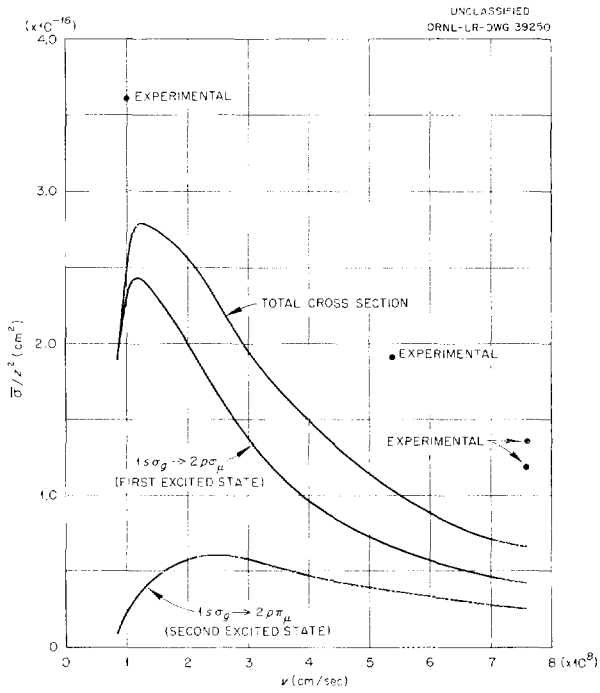

Fig. 9.8.1. Calculated Dissociation Cross Section as a Function of Velocity.

[1] R. G. Alsmiller, Jr., *Cross Sections for the Dissociation of H_2^+ and D_2^+ by a Vacuum Carbon Arc*, ORNL-2766 (1959).

9.9. DIFFUSION OF PLASMA PARTICLES ACROSS A MAGNETIC FIELD

A. Isihara A. Simon

A previous calculation[1] of the rate of diffusion of like charged particles across a magnetic field has been generalized. No a priori assumption as to the relative magnitude of certain terms was made, and spatial density gradients were permitted in both directions perpendicular to the field. The final result agrees with that given earlier. Details will be available in a forthcoming report.[2]

[1] A. Simon, *Phys. Rev.* 100, 1557 (1955).

[2] A. Isihara and A. Simon, *Diffusion of Plasma Particles Across a Magnetic Field*, ORNL-2826 (in press).

9.10. SOME EXACT RADIATING SOLUTIONS IN VLASOV'S EQUATIONS

L. C. Biedenharn[1]

A class of exact solutions to Vlasov equations which show electromagnetic radiation has been constructed. Since velocities larger than c appear to be possibly of importance in these solutions, an exact radiating solution to the relativistic Vlasov equations was constructed, which, though much more specialized than the nonrelativistic solutions, shows that unphysically large velocities in the nonrelativistic solutions are not essential for the radiation there obtained. Details of this calculation, as well as a discussion of a typical example, will be published elsewhere.[2]

---

[1]Summer visitor (1959) and consultant. Permanent address, The Rice Institute, Houston, Texas.

[2]L. C. Biedenharn, *Some Exact Radiating Solutions in Vlasov's Equations*, ORNL-2838 (to be published).

Part 10

THEORETICAL NUCLEAR PHYSICS

10.1. SPACINGS OF NUCLEAR ENERGY LEVELS

L. Dresner

In the last few years a wealth of experimental data concerning the widths and spacings of nuclear energy levels has become available.[1] The initial theoretical response to the information these data supplied was directed toward the understanding of the statistical properties of the neutron widths,[2] and these investigations culminated in the very successful paper of Porter and Thomas.[3] These authors inferred a normal distribution for the reduced neutron width from the plausible assumption of a highly complex, rapidly varying wave function for compound nuclear states, which is not highly correlated with the wave functions of nearby states. In their paper, Porter and Thomas show their inference to be strongly supported by experimental evidence.

With the success of this simple approach in mind, Wigner suggested an analogous examination of the distribution of level spacings.[4] In particular, he pointed out that the distribution of spacings between adjacent eigenvalues of matrices whose elements were randomly chosen would show a deficiency of small spacings, contrary to the expectation if the eigenvalues themselves were uncorrelated. This so-called "level-repulsion" effect has been observed experimentally in connection with the nuclear resonance levels.[5] Blumberg and Porter[6] demonstrated the level repulsion effect numerically by diagonalizing random matrices of fairly large order, all of whose elements had the same normal distribution. Rosenzweig[7] made more accurate numerical calculations of the same type and obtained a rather detailed histogram which agreed very well with the distribution of spacings originally suggested by Wigner [see Eq. (8) in ref 8], except for the largest spacings. [Note added in proof: Wigner pointed out to the author that this slight disagreement arose from a failure to account for the dependence of the local average level spacing on the eigenvalue (energy). When Rosenzweig's results were corrected for this effect, the disagreement for large spacings were removed.]

The author has suggested a simple statistical model, in terms of which the general features of the level spacing distribution can be understood; it involves no special assumptions other than that of Porter and Thomas.[3] This model has been described elsewhere.[8]

---

[1] J. A. Harvey and D. J. Hughes, *Phys. Rev.* **109**, 471 (1958), and refs cited therein.

[2] J. A. Harvey and D. J. Hughes, *Phys. Rev.* **99**, 1032 (1955), and refs cited therein.

[3] C. E. Porter and R. G. Thomas, *Phys. Rev.* **104**, 483 (1956).

[4] E. P. Wigner, *Conference on Neutron Physics by Time-of-Flight Held at Gatlinburg, Tennessee, November 1 and 2, 1956*, ORNL-2309, p 67 (June 17, 1957).

[5] J. A. Harvey, *Phys. Rev.* **98**, 1162 (1955); I. I. Gurevich and M. I. Pevsner, *Zhur. Eksptl. i Teoret. Fiz.* **31**, 162 (1956) [*J. Exptl. Theoret. Phys. U.S.S.R.* **4**, 278 (1957)]; also *Nuclear Phys.* **2**, 575 (1957).

[6] S. Blumberg and C. E. Porter, *Phys. Rev.* **119**, 786 (1958).

[7] N. Rosenzweig, *Phys. Rev. Letters* **1**, 24 (1958).

[8] L. Dresner, *Phys. Rev.* **113**, 633 (1959).

10.2. OPTICAL MODEL OF INELASTIC SCATTERING FROM NUCLEI

T. K. Fowler

Inelastic scattering from a complex nucleus can be regarded as a collision with a single nucleon, a direct interaction, if the multiple scattering within the nucleus prior to this final collision is treated as propagation in a medium characterized by a complex potential V_I. If "nuclear medium" were an unambiguous concept, V_I would equal V_c, the usual optical potential describing the propagation of elastic waves. However, in an analysis of the scattering of 14- to 185-Mev protons from carbon, Levinson and Banerjee[1] found that, while they could equate the imaginary (absorptive) parts of V_I and V_c, they were forced to take $ReV_I = \frac{2}{3}ReV_c$. In a recent letter,[2] it is argued that ReV_I should indeed be smaller in magnitude than ReV_c by an amount x varying with incident energy in the manner found by Levinson and Banerjee; x corresponds to the excitation energy given to the nucleus prior to the one final inelastic scattering under scrutiny in the direct interaction calculation.

That an inelastic correction should arise to the complex potential used in calculating distorted waves, usually considered to represent elastic scattering, is justified as follows: The point of view is taken that, while ostensibly a direct interaction calculation treats a single collision with the nucleus in a definite state (taken to be the ground state), the adjustment of parameters to obtain a best fit to experimental data is in fact a mockup of the coupling between the various virtual states just prior to this final collision and thus introduces virtual excitation. In effect, one best linear combination of virtual target states, γ, is being chosen to represent the state of the nucleus prior to the final scattering. The distorted wave to be used in the direct interaction calculation is just that arising from an elastic scattering from the nucleus in the mixed state, γ. The optical potential to be used is approximately the same as that appropriate to the ground state, V_c. However, the energy of the projectile would be taken as $E - x$, E being the true initial energy and x the mean excitation in state γ. Equivalently, as Levinson and Banerjee did, the distortion can be calculated as elastic scattering from the ground state, with incident energy E and optical potential $V_I = V_c + x$.

The correction x is, of course, important only for projectiles heavy enough to impart considerable energy per collision. In impulse approximation, x is estimated to be

$$x \sim \left(\frac{4}{3}\frac{m}{M}\frac{\bar{K}}{E}\right)^{1/2} |ImV_c| \ , \qquad (1)$$

where m is the projectile mass, M the nucleon mass, and $\bar{K}$ the mean kinetic energy of nucleons bound in the nucleus. The correction x is negligible for pions and electrons incident, but not for nucleons. In Table 10.2.1, x is compared with the comparable correction found by Levinson and Banerjee, $\frac{1}{3}ReV_c$.

Since γ will not be known in detail, the interpretation of distorted-wave, direct interaction calculations presented here is useful only at energies high enough that most quantum details of the target states are unimportant. Even so, when transitions to a definite final state are involved, the quantum selection rules imposed by angular momentum conservation are important at all energies. However, at sufficiently high energies, it is only necessary to consider the angular momentum of the initial and final states, as Levinson and Banerjee did. Then, many virtual states being involved, the numerous alternative transitions provide an essentially classical linkage from initial to final state without hindrance due to selection rules operative in the virtual stage of the transition.

Table 10.2.1. Comparison* of $\frac{1}{3}ReV_c$ with x

E (Mev)	ImV_c (Mev)	$\frac{1}{3}ReV_c$ (Mev)	x (Mev)
17	8.5	15.1	11.9
20	9	12.7	11.6
31.5	15	11.7	15.4
50	12.6	9.3	10.1
100	7.7	6.5	4.5
150	7.4	5.0	3.5
200	8.0	4.7	3.2

*V_c data taken from W. B. Riesenfeld and K. M. Watson, *Phys. Rev.* 102, 1157 (1956).

[1] C. A. Levinson and M. K. Banerjee, *Ann. Phys.* 3, 67 (1958).

[2] T. K. Fowler, *Phys. Rev. Letters* 1, 371 (1958).

10.3. THE QUASI-ELASTIC SCATTERING OF FAST PARTICLES BY ATOMIC NUCLEI[1]

T. K. Fowler K. M. Watson[2]

The nuclear pair correlation function, $G(\mathbf{r}_1 - \mathbf{r}_2)$, defined by

$$P_2(\mathbf{r}_1, \mathbf{r}_2) = P_1(\mathbf{r}_1)\, P_2(\mathbf{r}_2)\, [1 + G(\mathbf{r}_1 - \mathbf{r}_2)]$$

$$P_j(\mathbf{r}_1, \mathbf{r}_2, \ldots, \mathbf{r}_j) = \int \prod_{i \neq 1, 2, \ldots, j} d\mathbf{r}_i \, |\psi_N(\mathbf{r}_1, \mathbf{r}_2, \ldots, \mathbf{r}_A)|^2 \quad , \qquad (1)$$

where ψ_N is the nuclear wave function, plays a central role in the Brueckner theory of nuclear structure[3] and is important in the calculation of many high-energy processes. By methods entirely analogous to x-ray diffraction studies of pair correlations in liquids,[4] inelastic scattering data for high-energy electrons, protons, and pions incident upon various light and medium nuclei have been Fourier-analyzed to yield $G(\mathbf{r}_1 - \mathbf{r}_2)$. Results from the various experiments have been found to be quite consistent. Correlation effects are localized to a range $< 10^{-13}$ cm, as expected, and seem definitely to indicate a repulsive force between nucleons over and above Pauli exclusion.

The method makes use of the interference at large distances of waves which have scattered once within the nucleus and imparted to the nucleus a small excitation. For sufficiently fast projectiles, the scattering process happens so fast that the nucleus remains statically in its initial state during the encounter, and thus interference patterns reflect the structure in the initial (ground) state of the target nucleus. This and other approximations peculiar to the nuclear problem are justified in our paper.[1] Also, correlations due to the exclusion principle are separated from those due to nucleon-nucleon forces. We apply a previously developed sum rule[5] which limits consideration to "quasi-elastic" transitions in order to eliminate from the data multiple scattering events likely to be involved in large energy transfers.

---

[1]Submitted for publication to *Nuclear Phys.*

[2]Physics Department and Lawrence Radiation Laboratory, University of California, Berkeley.

[3]K. A. Brueckner, J. L. Gammel, and H. Weitzner, *Phys. Rev.* **110**, 430 (1958).

[4]See, for instance, R. W. James, *The Optical Principles of the Diffraction of X-Rays*, p 465–80, Bell, London, 1948.

[5]T. K. Fowler, *Phys. Rev.* **112**, 1325 (1958).

Part 11

EXPERIMENTAL NUCLEAR PHYSICS

11.1. MEASUREMENTS OF Y^{88}, Zn^{65}, AND Mn^{54} GAMMA-RAY ENERGIES BY SCINTILLATION SPECTROSCOPY TECHNIQUES

R. W. Peelle T. A. Love

The isotope Y^{88}, which decays with a half life of 104 days, is frequently used as a gamma-ray source for the study of scintillation spectrometer response functions and calibration in the energy region above 1.4 Mev. Two gamma rays with energies of about 1.8 and 0.9 Mev occur between the states of the Sr^{88} daughter with nearly equal intensity.[1] The energies of these gamma rays have not been measured by precise methods, however, and since a Y^{88} source was used as an energy standard in a lengthy ORNL experiment to determine the spectra of fission-associated gamma radiation,[2] it was decided to measure these energies as accurately as possible, using the scintillation techniques available. In addition, efforts were made to check the energies of the 1.1- and 0.8-Mev gamma rays in the decays of Zn^{65} and Mn^{54}, respectively.

Table 11.1.1 shows the energies which have been reported for the more intense gamma-ray

[1] N. H. Lazar *et al.*, *Phys. Rev.* 101, 727 (1956); F. M. Tomnovec, *Bull. Am. Phys. Soc.* 1, 391 (1956).

[2] F. C. Maienschein *et al.*, *Proc. U.N. Intern. Conf. Peaceful Uses Atomic Energy, 2nd, Geneva, 1958*, P/659; see also sec 4.1 of this report.

Table 11.1.1. Published Energies for the More Intense Gamma Rays of Y^{88}

Author(s)	Method[a]	Energies and Errors Reported (Mev)	
Downing *et al.*[b]	sl pe, ce	1.890 ± 0.050	0.908 ± 0.020
Scharff-Goldhaber[c]	Be(γ,n) and proton recoil	1.870 ± 0.050[d]	
Richardson[e]	cloud chamber, ce	1.920 ± 0.030	0.950 ± 0.050
Peacock and Jones[f]	sl, ce	1.853 ± 0.037	0.908 ± 0.018
Lazar *et al.*[g]	scin	1.850 ± 0.008	0.909 ± 0.004
Tomnovec[h]	scin	1.850 ± ?	
O'Kelley and Johnson[i]	scin	1.832 ± 0.006	0.899 ± 0.004
Heath[j]	scin	1.830 ± ?	0.900 ± ?
Weighted average[k] [using reasonable (0.5%) errors where none are given]		1.842 ± 0.004	0.903 ± 0.003

[a] scin: scintillation spectrometer; sl: magnetic lens β-spectrograph; ce: internal conversion electrons measured; pe: photoelectrons measured (external conversion).

[b] J. R. Downing, M. Deutsch, and A. Roberts, *Phys. Rev.* 60, 470 (1941).

[c] G. Scharff-Goldhaber, *Phys. Rev.* 59, 937A (1941).

[d] A recalculation of this energy, in which more recent values of the ThC″ gamma ray and the photonuetron thresholds of the deuteron and Be^9 were used, yields a value of about 1.890 ± 0.021 Mev.

[e] J. R. Richardson, *Phys. Rev.* 60, 188 (1941).

[f] W. C. Peacock and J. W. Jones, *Decay Scheme of Y-88 (104 d)*, AECD-1812 (also CNL-14) (n.d.; declassified in 1948).

[g] N. H. Lazar, E. Eichler, and G. D. O'Kelley, *Phys. Rev.* 101, 727 (1956).

[h] F. M. Tomnovec, *Bull. Am. Phys. Soc.* 1, 391 (1956).

[i] G. D. O'Kelley and N. R. Johnson, "The Decay of I^{136}," *Phys. Rev.* (to be published); the present work was performed prior to existence of these values.

[j] R. L. Heath, *Scintillation Spectroscopy; Gamma-Ray Spectrum Catalogue*, IDO-16408, p 22 (July 1, 1957).

[k] These averages have been obtained by using all listed errors as standard errors. Chi-square tests show the listed values to be internally inconsistent for the Y^{88} 1.8-Mev line, where the probability of greater deviations is $P = 5 \times 10^{-3}$.

transitions in the decay of Y^{88}. Only in the work of O'Kelley and Johnson,[3] performed after the present effort was under way, does a serious effort seem to have been made to determine the photon energies. The apparent uncertainty in the Y^{88} 1.8-Mev line was not tolerable for a calibration source, especially since the measurements on this line quoted in Table 11.1.1 are inconsistent with the quoted errors if reasonable errors are assigned where none were quoted.

In the work reported here, extensive experimental precautions were employed to minimize the errors inherent in scintillation spectroscopy. Low phototube gain and low count rates were used to reduce phototube gain shifts, all experiments contained sufficient repetition to display the effects of any drifts, subtractions were performed to eliminate shifts in peak positions caused by pulse-height distributions from interfering gamma rays, data from a mercury-switch precision pulser were used to correct for nonlinearity of the electronic apparatus, and a variety of scintillation crystal configurations and calibration sources were used to avoid systematic errors.

The pulse-handling equipment was basically standard. It included a DD-2 amplifier[4] feeding a slightly modified Argonne-type 256-channel pulse-height analyzer.[5] A simple coincidence circuit[6] employing special timing circuits[7] and a 40-mμsec resolving time was used to permit coincidence measurements designed to enhance peaks in the pulse-height distribution corresponding to escape of annihilation photons from the spectrometer crystal.

Table 11.1.2 lists the calibration sources used and the energy values averaged from the literature. Most of these sources were encapsuled in quartz ampoules within soldered brass cylinders ¼ in. in OD and 1 in. in length.

Table 11.1.2. Calibration-Source Energies Used in the Analysis

Source	Energy (Mev)[a]	References
m_e (annihilation radiation)	0.5109764 ± 0.000007	*b*
Na^{22}	1.275 ± 0.0005	*c*
Na^{24}	1.368 ± 0.001	*d*
Na^{24}	2.7535 ± 0.001	*d*
$(Na^{24} - 2m_e)$	1.7325 ± 0.001	*d*
Bi^{207}	0.5696 ± 0.0001	*e*
Bi^{207}	1.0637 ± 0.0003	*e*
Cs^{137}	0.6616 ± 0.0002	*f*

[a]The values given have been averaged from the values in the referenced papers and compilations. The errors quoted are estimated standard errors based on errors given in these papers and the scatter between the values quoted.

[b]J. W. M. Dumond and E. R. Cohen, p 7–170 in *Handbook of Physics*, ed. by E. U. Condon and H. Odishaw, McGraw-Hill, New York, 1958.

[c]F. Ajzenberg and T. Lauritsen, *Revs. Modern Phys.* 27, 156 (1955). A larger uncertainty should have been assigned to the Na^{22} energy, based on scatter between the various observations. This oversight is quite unimportant because the source was infrequently used.

[d]A. Hedgran and D. Lind, *Arkiv Fysik* 5, 177 (1952).

[e]K. Way *et al.*, *Nuclear Data Sheets*, NRC 58-2-66, National Academy of Sciences, National Research Council.

[f]K. Way *et al.*, *Nuclear Data Sheets*, NRC 58-4-31, National Academy of Sciences, National Research Council.

Three different scintillator-phototube arrangements were used in the course of the 13 experiments performed. Two single-crystal spectrometers were employed, one using a 1.5-in.-dia by 2-in.-long NaI(Tl) crystal and another using a 3-in.-dia by 3-in.-long crystal. In addition, a double-crystal spectrometer, which enhanced the relative importance of the single and double escape of annihilation radiation, was used. The two crystals were approximately ⅞ by ⅞ in. and 1.8 by 1.8 in., pulses in the smaller crystal being recorded when they were in coincidence with a pulse in the larger crystal corresponding to the absorption of an annihilation quantum. Two experiments were performed with the smaller single crystal, four with the double-crystal coincidence spectrometer, and

[3]G. D. O'Kelley and N. R. Johnson, "The Decay of ^{136}," *Phys. Rev.* (to be published).

[4]E. Fairstein, *Rev. Sci. Instr.* 27, 475 (1956).

[5]R. W. Schumann and J. P. McMahon, *Rev. Sci. Instr.* 27, 675 (1956).

[6]T. A. Love, R. W. Peelle, and F. C. Maienschein, *Electronic Instrumentation for a Multiple-Crystal Gamma-Ray Scintillation Spectrometer*, ORNL-1929 (1955).

[7]R. W. Peelle and T. A. Love, *Appl. Nuclear Phys. Ann. Prog. Rep. Sept. 1, 1957*, ORNL-2389, p 259.

seven with the larger single crystal. The major advantage of the coincidence arrangement was that the 1.8-Mev Y^{88} line could be compared with standards in the region below 1 Mev, but a disadvantage was that apparatus was not available to allow simultaneous recording of the singles and coincidence spectra.

Results were obtained by an analysis procedure which placed heavy stress upon estimated experimental errors and upon adequate statistical procedures for their combination. Input errors were estimated for the position of each observed peak in the pulse-height spectra and for the magnitude of the nonlinearity correction obtained from the precision pulser data. Identical runs were averaged to obtain the results for each experiment. In order to obtain the energies corresponding to the peaks from unknown energies, linear interpolation between the nearest calibration points was employed to minimize any possible residual nonlinear effects. Estimated random errors were properly propagated through this interpolation process so that an error could be quoted for each energy measurement.

Since as many as ten independent measurements were performed for a given gamma-ray line, proper combination of experimental results was essential. Output values were obtained as weighted averages of the results of the several experiments, the weights being taken in each case as the inverse square of the standard error assigned to the individual measurements. This procedure naturally resulted in a best value, a standard error in this value (assuming all input errors to be random), and a chi-square test of the consistency among the various experimental results. For the over-all experiment, this consistency test indicated that random errors were underestimated by no more than 20%. In the individual cases of the Y^{88} 1.8-Mev line and the Zn^{65} 1.1-Mev line, the calculated chance was about 2% that another set of measurements with the quoted errors would be as scattered; so the final quoted errors in these two cases have been enlarged by an amount (1.5 and 2 times, respectively) sufficient to cover this degree of inconsistency.

Table 11.1.3 lists the final results from this series of experiments along with the standard errors obtained in the manner indicated above. In addition to the unknowns, data are shown for some of the standards. These latter results, when compared with the accepted values of Table 11.1.2, provide a valuable guide as to the credibility of the errors quoted for the unknown energies, since these values and errors were obtained from the same sets of data as the unknowns. Moreover, the data analysis for these checks required interpolations of the calibration data over greater ranges of energy and pulse height than for the unknowns. A chi-square test comparing the data on standard sources against the accepted values indicates a probability of 0.15 that greater deviations would occur if the quoted errors hold. The degree of agreement suggests that the standard errors quoted for the unknown energies in Table 11.1.3 are reliable guides to the degree of accuracy of the energy measurements.

Table 11.1.3. Gamma-Ray Energies Determined by Scintillation Spectroscopy Techniques

Source	Energy (Mev)	Standard Error (Mev)
Y^{88}	0.8988	0.0012
Y^{88}	1.8400	0.002
Mn^{54}	0.8347	0.0011
Zn^{65}	1.1140	0.004
Cs^{137}	0.6643	0.0013
Bi^{207}	1.0670	0.0021
Na^{24}	1.3688	0.0016
$Na^{24} - 2m_e$	1.7320	0.0030

Though for readily available long-lived radionuclide sources scintillation spectroscopy can seldom compete with more precise methods for measurement of photon energies, reasonably good results can be obtained if sufficient care is taken. The errors in the measurements reported here are smaller than previously published values for the Y^{88} gamma rays. Since Y^{88} is a useful source, the energies of its strong gamma rays should be determined by a more precise method with sufficient accuracy ($\sim$0.5 kev) to allow its general use as a calibration source.

To produce measurements with the internal consistency obtained in this work, it was necessary to compensate for the nonlinearities of the pulse-height analysis system by a simple method adequate only for energy analysis. This compensation appears to have been quite successful, but more precise results could have been attained if such nonlinearity were unobservably small.

A complete report of this work has been published elsewhere.[8]

[8]R. W. Peelle and T. A. Love, *Scintillation Spectroscopy Measurements of Gamma-Ray Energy from Sources of Y^{88}, Mn^{54}, and Zn^{65}*, ORNL-2790 (1959).

11.2. CROSS SECTION FOR THE $Li^6(n,\alpha)H^3$ REACTION FOR 1.2 Mev $\leq E_n \leq$ 8.0 Mev

R. B. Murray H. W. Schmitt[1] J. J. Manning

A measurement of the $Li^6(n,\alpha)H^3$ reaction cross section in the neutron energy region from 1.2 to 8.0 Mev has been reported previously.[2] This cross section was based on measurements of the ratio of the (n,α) cross section to the fission cross sections of U^{238} and Np^{237}. In the analysis of the (n,α) cross-section data, the Np^{237} fission cross section was taken from BNL-325.[3]

A recent measurement of the Np^{237} fission cross section given elsewhere in this report (Sec 11.3) permits a re-evaluation of the $Li^6(n,\alpha)H^3$ data. The revised $Li^6(n,\alpha)H^3$ cross section as a function of energy is shown in Fig. 11.2.1. The principal difference between the revised data of Fig. 11.2.1 and those given previously[2] occurs in the 1- to 3-Mev region. The previous data were lower in this energy region and indicated a plateau in the neighborhood of 2 Mev.

It is of interest to compare the revised cross section, Fig. 11.2.1, with the results of other experiments, namely, those of Ribe[4] and Gabbard *et al.*[5] It may be noted that it was necessary for Ribe to apply a correction to all his measured cross sections except two, at 2.50 and 14.1 Mev, in order to account for the energy dependence of the long-counter detection efficiency. According to a recent communication[6] the long-counter correction factor as used in Table I of his report[4] was applied inversely. Thus his corrected cross section at a neutron energy of 0.88 Mev should read 323 ± 34 mb, that at 6.52 Mev should read 55 ± 10 mb, etc. With this revision, the results of Ribe's experiment and those of the present experiment are in quite good agreement. The data of Gabbard *et al.*[5] are somewhat lower in the 1- to 3-Mev region.

[1]Physics Division.

[2]R. B. Murray, H. W. Schmitt, and J. J. Manning, *Neutron Phys. Ann. Prog. Rep. Sept. 1, 1958*, ORNL-2609, p 145.

[3]D. J. Hughes and R. B. Schwartz, *Neutron Cross Sections*, 2d ed., BNL-325 (July 1, 1958).

[4]F. L. Ribe, *Phys. Rev.* 103, 741 (1956).

[5]F. Gabbard, R. H. Davis, and T. W. Bonner, *Phys. Rev.* 114, 201 (1959).

[6]F. L. Ribe, private communication, 1959.

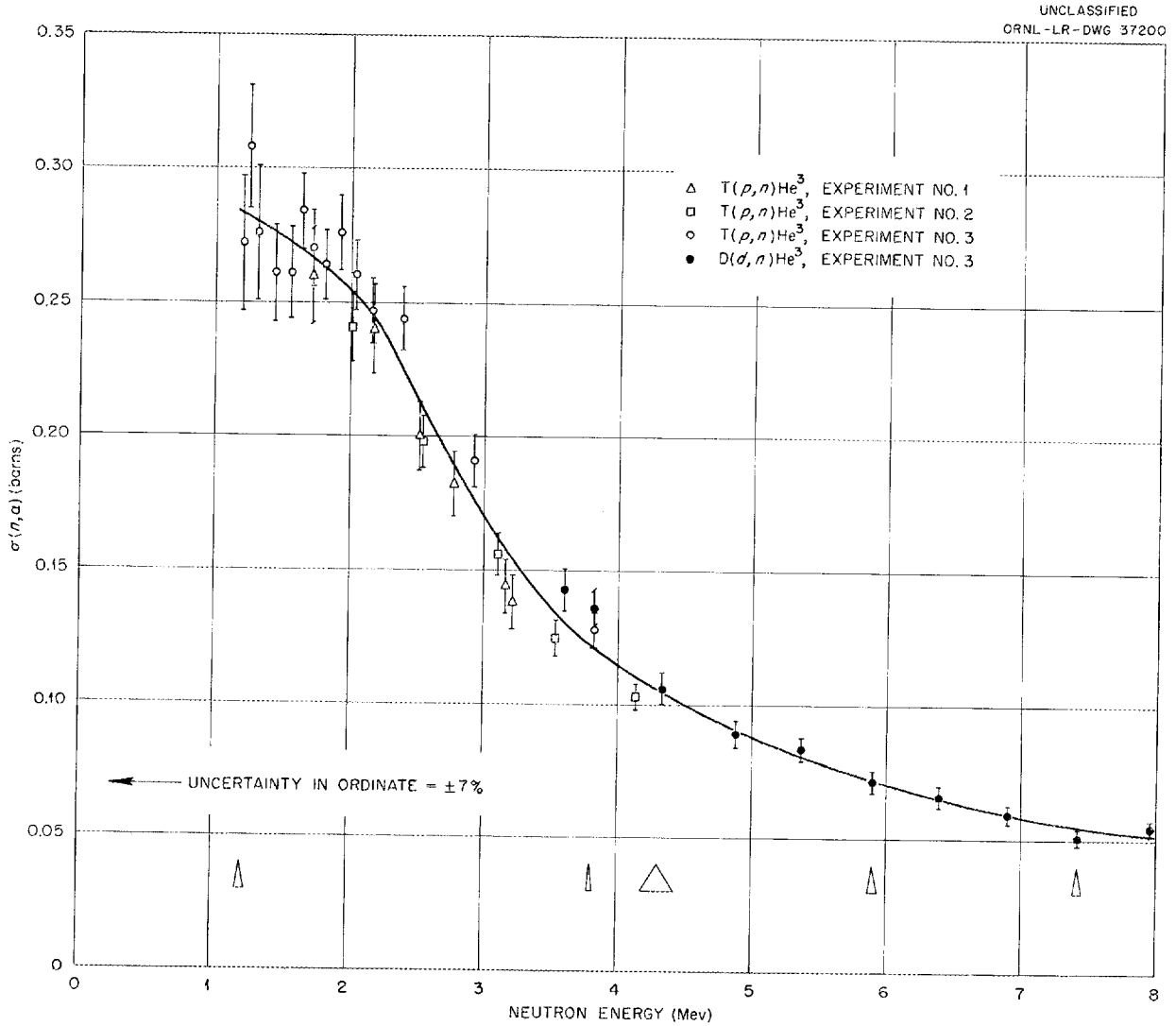

Fig. 11.2.1. Measured Values of the $Li^6(n,\alpha)H^3$ Cross Section as a Function of Neutron Energy. The bases of the triangles represent typical target thickness, that is, full neutron energy spread.

11.3. NEUTRON-INDUCED FISSION CROSS SECTION OF Np^{237}

H. W. Schmitt[1] R. B. Murray J. J. Manning

Knowledge of the fission cross section as a function of neutron energy, for each of the various fissionable nuclei, is of interest in studies of the mechanism of the fission process. In the case of Np^{237} the fission cross section is of further interest by virtue of the use of Np^{237} fission in the measurement of fast-neutron fluxes. Early measurements of $\sigma_f(Np^{237})$ as a function of neutron energy were made relative to the response of a long counter,[2] under the assumption that this response was flat with respect to incident neutron energy, and were normalized to an absolute measurement of Klema.[3] In a later compilation[4] the original data were corrected for the energy dependence of the long-counter detection efficiency, a correction amounting to as much as 20%. The resulting curve of cross section vs energy was considered to be uncertain in both shape and normalization to at least 15% (ref 5).

In view of the uncertainties inherent in previous measurements of the Np^{237} fission cross section and in view of the interest in this reaction as indicated above, a new determination is of value. This paper reports a measurement of the Np^{237} fission cross section as a function of neutron energy from 0.9 to 8.0 Mev. The basis of this measurement is a determination of the ratio $\sigma_f(Np^{237})/\sigma_f(U^{238})$ combined with previously determined values of $\sigma_f(U^{238})$ (ref 6).

Method and Apparatus

Monoenergetic neutrons were obtained from the $T(p,n)He^3$ and $D(d,n)He^3$ reactions, using the ORNL 5.5-Mv Van de Graaff generator to accelerate the incident charged particles. Neutrons emitted in a small cone about 0° with respect to the incident beam were used; the neutron energy was varied by changing the incident charged-particle energy. Loss of energy of the incident particles upon penetration of the target foils and target gas was taken into account; the neutron energy was then determined from published tables.[7]

Fragments from the neutron-induced fission of U^{238} and Np^{237} were counted in 2π geometry, with thin deposits of U^{238} and Np^{237} situated back to back in a thin-walled ionization chamber. Fission events were identified as counts above the integral pulse-height discriminator levels in standard pulse amplifiers. The U^{238} samples were electroplated in the form of U_3O_8 onto 0.010-in.-thick platinum backings; the Np^{237} samples were evaporated in the form of NpF_4 onto platinum backings of the same thickness.

Several Np^{237} and U^{238} deposits were used in the course of the present study. Masses of the fissile deposits were determined by alpha-particle counting, combined with knowledge of the half life of the fissile material. The U^{238} half life was assumed to be $(4.51 \pm 0.02) \times 10^9$ years,[8] and the Np^{237} half life was taken as $(2.14 \pm 0.01) \times 10^6$ years.[9] The mass of fissile material on each of the various deposits was of the order of 1 mg.

Corrections to the observed counts were applied to account for those fission fragments which lost sufficient energy in the deposit of fissile material to give pulses below the discriminator bias setting. The correction for these fragments, determined from integral bias curves, amounted to from 2 to 3% with an estimated uncertainty of 1%.

Background counts throughout the present experiment were measured under conditions and settings identical to those of the fission-counting runs, except that the target gas (tritium or deuterium) was replaced with helium. Backgrounds were negligible for $T(p,n)He^3$ neutrons; for $D(d,n)He^3$ neutrons, backgrounds ranged from a few per cent or less at the lowest deuteron energies to about 20% at the highest deuteron energy.

---

[1] Physics Division.

[2] D. J. Hughes and R. B. Schwartz, *Neutron Cross Sections*, 2d ed., BNL-325 (July 1, 1958); see also D. J. Hughes and J. A. Harvey, BNL-325 (July 1, 1955).

[3] E. D. Klema, *Phys. Rev.* **72**, 88 (1947).

[4] R. L. Henkel, Los Alamos Report LA-2122, 1957 (unpublished).

[5] R. L. Henkel, private communication, 1959.

[6] W. D. Allen and R. L. Henkel, *Progr. in Nuclear Energy, Ser. I* 2, 33 (1958); cross-section values were taken from the smooth curve of Fig. 30.

[7] J. L. Fowler and J. E. Brolley, Jr., *Revs. Modern Phys.* 28, 103 (1956).

[8] A. F. Kovarik and N. I. Adams, Jr., *Phys. Rev.* **98**, 46 (1955); see also D. Strominger, J. M. Hollander, and G. T. Seaborg, *Revs. Modern Phys.* 30, 585 (1958).

[9] Brauer *et al.*, Hanford Atomic Products Operation Report HW-59642, 1959 (unpublished).

A further correction to the observed fission counts arose from the fact that fragments from one of the deposits were emitted in the backward hemisphere; hence a small fraction was lost because of the forward motion of the center of mass. The magnitude of this correction is influenced by the anisotropic emission of the fission fragments[10] and is energy dependent. The net result of calculations and experimental checks at four neutron energies throughout the range of the experiment was a correction of the order of (1 ± 1)%.

In order to determine the shape of the Np^{237} fission cross section as a function of energy in the range below about 1.6 Mev, where the energy dependence of $\sigma_f(U^{238})$ is quite strong, data were obtained relative to the 0° neutron yield from the $T(p,n)He^3$ reaction. In a typical run of this experiment the relative number of incident protons was determined by counting pulses from a beam-current integrator; the relative number of neutrons incident on the deposit was obtained from the product of the known 0° differential cross section for the target reaction[11] and the number of accumulated current-integrator pulses. Relative Np^{237} fission cross sections were obtained in the energy range $0.9 < E_n < 2.8$ Mev and were normalized to the values obtained relative to the U^{238} fission cross section in the range of energy overlap, 1.6 to 2.8 Mev.

Results and Discussion

The results of these measurements are given in Fig. 11.3.1. Uncertainties in the results presented here may be divided into two classes:

1. Standard errors from counting statistics, backgrounds, etc., which vary from point to point. These are computed and appear as flags on the individual points of Fig. 11.3.1; the range is from ±4 to ±10%. In the case of those data based on the $T(p,n)He^3$ yield (open circles), the uncertainty is estimated to be ±10% in every case. In order to avoid confusion in the figure, error flags have been omitted from some of the open circles.
2. Energy-independent uncertainties in absolute value, which arise, for example, from uncertainties in the masses of the fissile deposits or the absolute value of $\sigma_f(U^{238})$. This latter uncertainty is taken to be ±5% (ref 5). The

[10] R. L. Henkel and J. E. Brolley, Jr., *Phys. Rev.* 103, 1292 (1956).

[11] The 0° differential cross section used in this analysis ($E_n > 1.2$ Mev) was obtained recently by J. Perry and S. J. Bame, Jr., based on recoil proton telescope data, and is reported in chap. 1 of *Fast Neutron Physics*, ed. by J. B. Marion and J. L. Fowler (to be published). In the neutron energy interval from 0.9 to 1.2 Mev the differential cross section was taken from the same reference, based on other experiments.

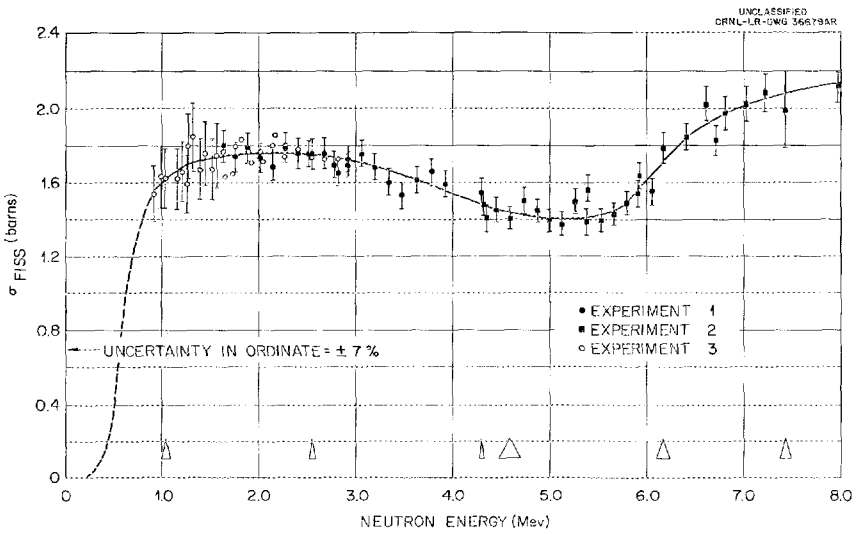

Fig. 11.3.1. Neptunium-237 Fission Cross Section as a Function of Neutron Energy. The bases of the triangles represent the total neutron energy spread at typical points, determined from a calculation of the charged-particle energy loss in passing through the target.

resulting uncertainty in absolute value of $\sigma_f(Np^{237})$ is estimated to be ±7%.

The results derived from the present experiment differ somewhat from the previous (corrected) cross-section curve given in the 1957 compilation of Henkel.[4] The chief difference is in the region from 0.9 to about 4 Mev, where the present results are some 15 to 20% higher; above 4 Mev the two experiments agree rather well, easily within the combined experimental uncertainties. It should be noted, however, that a considerable difference exists between the data from the present experiment and the (uncorrected) cross section given in recent compilations,[2] in both the low- and high-energy regions. For the sake of completeness, the dashed curve in Fig. 11.3.1 is included to indicate the shape of the cross-section curve immediately above threshold. This curve has been taken from previous long-counter measurements[4] and renormalized to the results of the present experiment in the 1.0- to 1.5-Mev region.

INTERNAL DISTRIBUTION

1. C. E. Center
2. Biology Library
3. Health Physics Library
4–6. Central Research Library
7. Reactor Experimental Engineering Library
8–46. Laboratory Records Department
47. Laboratory Records, ORNL R.C.
48. A. M. Weinberg
49. L. B. Emlet (K-25)
50. J. P. Murray (Y-12)
51. J. A. Swartout
52. G. E. Boyd
53. R. A. Charpie
54. W. H. Jordan
55. A. H. Snell
56. C. E. Winters
57–81. E. P. Blizard
82. D. S. Billington
83. F. L. Culler
84. J. L. Fowler
85. J. H. Frye, Jr.
86. C. S. Harrill
87. A. Hollaender
88. A. S. Householder
89. C. P. Keim
90. M. T. Kelley
91. S. C. Lind
92. R. S. Livingston
93. K. Z. Morgan
94. W. Kolink
95. M. L. Nelson
96. H. E. Seagren
97. E. D. Shipley
98. E. H. Taylor
99. R. R. Dickison
100. E. Guth
101. P. F. Kasten
102. A. J. Miller
103. L. C. Oakes
104. G. D. O'Kelley
105. V. K. Pare
106. D. Phillips
107. P. M. Reyling
108. H. W. Schmitt
109. M. J. Skinner
110. K. M. Watson
111. G. C. Williams
112. L. S. Abbott
113. F. S. Alsmiller
114. R. G. Alsmiller, Jr.
115. H. Bertini
116. T. V. Blosser
117. V. R. Cain
118. A. D. Callihan
119. G. T. Chapman
120. R. R. Coveyou
121. D. F. Cronin
122. G. deSaussure
123. L. Dresner
124. J. F. Ellis
125. G. M. Estabrook
126. N. H. Ethridge
127. T. K. Fowler
128. J. K. Fox
129. R. M. Freestone
130. L. W. Gilley
131. R. Gwin
132. V. G. Harness
133. K. M. Henry
134. L. B. Holland
135. J. L. Hull
136. L. Jung
137. E. B. Johnson
138. F. L. Keller
139. R. J. Kerr
140. J. D. Kington
141. W. E. Kinney
142. M. E. LaVerne
143. J. Lewin
144. T. A. Love
145. J. J. Lynn
146. R. J. Mackin
147. R. E. Maerker
148. D. W. Magnuson
149–151. F. C. Maienschein
152. J. J. Manning
153. J. T. Mihalczo
154. J. M. Miller
155. H. S. Moran

156. F. J. Muckenthaler
157. R. B. Murray
158. A. Myer
159. R. W. Peelle
160. S. K. Penny
161. E. R. Rohrer
162. E. G. Silver
163. A. Simon
164. J. G. Sullivan
165. J. T. Thomas
166. D. K. Trubey
167. W. C. Tunnell
168. V. V. Verbinski
169. D. R. Ward
170. C. D. Zerby
171. W. Zobel
172. W. Etzel
173. W. Häfele
174. E. Inönü
175. R. Perez-Belles
176. S. N. Purohit
177. E. G. Harris
178. R. L. Macklin
179. W. S. Lyon
180. M. Rankin
181. C. A. Preskitt
182. F. B. K. Kam
183. F. L. Friedman (consultant)
184. H. Goldstein (consultant)
185. H. Hurwitz, Jr. (consultant)
186. L. W. Nordheim (consultant)
187. R. F. Taschek (consultant)
188. ORNL – Y-12 Technical Library, Document Reference Section

EXTERNAL DISTRIBUTION

189. Division of Research and Development, AEC, ORO
190–799. Given distribution as shown in TID-4500 (15th ed.) under Physics and Mathematics category (75 copies – OTS)